A new Mathematical Framework to Understand Single Neuron Computations

THÈSE N^O 6242 (2014)

PRÉSENTÉE LE 27 NOVEMBRE 2014
À LA FACULTÉ INFORMATIQUE ET COMMUNICATIONS
LABORATOIRE DE CALCUL NEUROMIMÉTIQUE (IC/SV)
PROGRAMME DOCTORAL EN NEUROSCIENCES

ÉCOLE POLYTECHNIQUE FÉDÉRALE DE LAUSANNE

POUR L'OBTENTION DU GRADE DE DOCTEUR ÈS SCIENCES

PAR

Skander MENSI

(EPFL

ÉCOLE POLYTECHNIQUE
FÉDÉRALE DE LAUSANNE

Suisse
2014

Sometimes life is merely a matter of coffee and whatever intimacy a cup of coffee affords.

— Richard Brautigan

Acknowledgements

Abstract

An important feature of the nervous system is its ability to adapt to new stimuli. This adaptation allows for optimal encoding of the incoming information by dynamically changing the coding strategy based upon the incoming inputs to the neuron. At the level of single cells, this widespread phenomena is often referred to as spike-frequency adaptation, since it manifests as a history-dependent modulation of the neurons firing frequency. In this thesis I focus on how a neuron is able to adapt its activity to a specific input as well as on the function of such adaptive mechanisms.

To study these adaptive processes different approaches have been used, from empirical observations of neural activities to detailed modeling of single cells. Here, I approach these problems by using simplified threshold models. In particular, I introduced a new generalization of the integrate-and-fire model (GIF) along with a convex fitting method allowing for efficient estimation of model parameters. Despite its relative simplicity I show that this neuron model is able to reproduce neuron behaviors with a high degree of accuracy.

Moreover, using this method I was able to show that cortical neurons are equipped with two distinct adaptation mechanisms. First, a spike-triggered current that captures the complex influx of ions generated after the emission of a spike. While the second is a movement of the firing threshold, which possibly reflects the slow inactivation of sodium channels induced by the spiking activity. The precise dynamics of these adaptation processes is cell-type specific, explaining the difference of firing activity reported in different neuron types. Consequently, neuronal types can be classified based on model parameters. In Pyramidal neurons spike-dependent adaptation lasts for seconds and follows a scale-free dynamics, which is optimally tuned to encodes the natural inputs that pyramidal neurons receive *in vivo*.

Finally using an extended version of the GIF model, I show that adaptation is not only a spike-dependent phenomenon, but also acts at the subthreshold level. In Pyramidal neurons the dynamics of the firing threshold is influenced by the subthreshold membrane potential. Spike-dependent and voltage-dependent adaptation interact in an activity-dependent way to ultimately shape the filtering properties of the membrane on the input statistics. Equipped with such a mechanism, Pyramidal neurons behave as integrators at low inputs and as a coincidence detectors at high inputs, maintaining sensitivity to input fluctuations across all regimes.

Keywords: Spiking Neuron Models - Fitting - Spike Frequency Adaptation - Threshold Dynamics - Adaptation - Neural Coding

Résumé

Le fonctionnement du cerveau dépend principalement de l'activité électrique de cellules spécifiques appelées neurones. Ces cellules nerveuses communiquent entre elles à l'aide de courtes impulsions électriques, et ce faisant régissent le comportement de notre système nerveux dans son ensemble. Bien que de nombreux aspects de leur structure et des calculs qu'elles effectuent soient connus, la façon dont ces cellules parviennent à transmettre et encoder de l'information restent à ce jour une question ouverte.

Afin d'aborder cette question de nombreuses approches sont envisageables, de l'observation empirique de leur activité, à l'examen minutieux de leur structure moléculaire. Pendant ma thèse je me suis intéressé au fonctionnement de ces cellules nerveuses d'un point de vue mathématique.

Avec un certain degré d'abstraction, il est concevable d'assumer que le travail effectué par un neurone peut se résumer à son activité électrique. Il est alors possible de décrire cette activité à l'aide d'équations mathématiques, construisant ainsi un modèle simple de neurone. Bien que cette approche soit réductive et néglige de nombreux facteurs régulant le fonctionnement des cellules nerveuses, elle permet une compréhension des mécanismes fondamentaux entrant en jeu lors de fonctions neurales spécifiques.

Ces modèles peuvent êtres de différentes sortes, incorporant toutes les connaissances à disposition et créant ainsi un modèle biophysique détaillé ou en laissant de coté la plupart, afin de construire un modèle relativement simple, mais capable d'expliquer comment un neurone peut communiquer et transmettre de l'information sous la forme d'impulsions électriques.

Durant ma thèse, je me suis intéressé à un type de modèle mathématique relativement peu détaillé mais permettant d'expliquer de façon précise l'activité d'un neurone. Cette classe de modèle m'a permis de montrer par quels mécanismes un neurone est capable de s'adapter aux stimulations qu'il reçoit pour en tirer un maximum d'information. Pour atteindre cet objectif j'ai développé une méthode mathématique générique qui permet d'expliquer de manière détaillée les mécanismes biologiques qui doivent être pris en compte pour effectuer une fonction physiologique simple.

Mots-clés : Modèles de neurones à impulsions - Méthode d'estimation des paramètres - Adaptation de la fréquence de tir - Dynamique du seuil de potentiel d'action - Adaptation - Code neural

Contents

Contents

Contents

List of Figures

List of Tables

1 Introduction: Dynamics of single neurons

Neurons are the fundamental building blocks of the brain, making the dynamics of single neurons a crucial aspect of computational neuroscience. To understand the neuronal dynamics it is essential to develop a relevant and compact mathematical description of their activities. Such a compact model will enable to link the response of individual neurons to higher order phenomena, such as learning and behavior. It will also provide insight into neural computations and the biological mechanisms that underly such computations (Rieke et al., 1999; Koch and Segev, 2000).

Currently, there are many projects aiming to model complex neural networks (Traub et al., 2004; Markram, 2006; Lang et al., 2011; Koch and Reid, 2012; Waldrop, 2012; Kandel et al., 2013). To achieve this goal it is crucial to develop single neuron models that are able to reproduce the main features of neuronal activities at a relatively low computational cost. Moreover, to study the dynamical properties of neural networks, the model of choice should be analytically tractable. Such calculation will facilitate the analysis of the network activity, thereby providing useful explanations for the computations performed by the network (Amit and Brunel, 1997; Brunel, 2000; Naud and Gerstner, 2012). Neural circuits are composed of different cell-types — such as inhibitory and excitatory neurons — with their own distinctive properties (Bota et al., 2003; Markram et al., 2004; Bota and Swanson, 2007), and even in a given cell-type, each neuron exhibits cell-to-cell variability that is known to influence the network dynamics (Padmanabhan and Urban, 2010; Tripathy et al., 2013). Therefore, for realistic brain simulations, a model should be flexible enough to capture cell-type and cell-to-cell variability. Ideally, the single neuron model should allow for robust and fast parameter estimation as to enable the development of comprehensive databases of neuron models.

The above mentioned constraints are not the only ones to consider when designing a single neuron model. One of the major points to consider is the level of detail that has to be taken

into account. Indeed, the level of description needed to capture neuron dynamics is not fixed and depends highly on the specific phenomenon being explained (Herz et al., 2006; Gerstner and Naud, 2009). Several mathematical models exist that capture different aspects of neuronal computations and exhibit diverse degrees of complexity (see Figure 1.1), from simple point neuron models (Stein, 1967; Abbott and van Vreeswijk, 1993; Gerstner, 1995b; Brette and Gerstner, 2005) to more detailed biophysical models (Hodgkin and Huxley, 1952; Rall, 1962; Mainen and Sejnowski, 1996; Hay et al., 2011, 2013). Each of these models captures some aspects of the complex dynamics of neurons. While some focus on spike initiation, others include spike-frequency adaptation, refractoriness or dendritic integration.

In this thesis, I focus on single compartment models of the threshold type. This choice was motivated by results showing that these simplified models capture both the spiking activity and the subthreshold response of single neurons (Keat et al., 2001; Paninski et al., 2005; Jolivet et al., 2008; Kobayashi et al., 2009; Dong et al., 2013). Simplified models are sufficiently flexible to reproduce most of the firing patterns observed *in vitro* (Markram et al., 2004; Naud et al., 2008; Touboul and Brette, 2008; Mihalaş and Niebur, 2009), and can easily be extended with new mechanisms if needed. Compared to detailed Hodgkin and Huxley models, simplified threshold models have very few parameters which allows for fast and efficient parameter estimation. Finally, the low computational complexity of these simplified models enables large network simulations in realistic time (Brainscales; Izhikevich and Edelman, 2008; Gewaltig and Diesmann, 2007).

Due to their simplicity, threshold models have some limitations. First, by containing a single compartment, they neglect any non-linear dendritic computation (Häusser et al., 2000; London and Häusser, 2005; Losonczy and Magee, 2006; Spruston, 2008; Larkum et al., 2009). However it is possible to incorporate such complex dendritic computations, mediated by NMDA spikes, dendritic Calcium spikes or others dendritic non-linearities, by the addition of a few active compartments (Poirazi and Mel, 2001; Poirazi et al., 2003; Legenstein and Maass, 2011; Schoen et al., 2012; Naud et al., 2013; Brunel et al., 2014). Second, in threshold models, ion channel dynamics are approximated by simple effective currents, impairing direct biological interpretations of model parameters. In other words, threshold models are loosely related with the underlying biological machinery. Nevertheless, by means of approximations, one can map model parameters onto interesting biological quantities.

Despite their simplicity, single compartment models have been proven useful in different fields of computational neurosciences. Indeed, they have been successfully used to infer neural receptive field from spiking activity (Pillow et al., 2005, 2008), recover network connectivity from extracellular recordings (Okatan et al., 2005; Eldawlatly et al., 2009; Gerhard et al., 2013), recover input stimuli from neural activities and design efficient decoding tools for neuroprosthetics (Lawhern et al., 2010; Pillow et al., 2011; Shoham et al., 2005), study neural network dynamics (Amit and Brunel, 1997; Brunel, 2000) and study learning and plasticity (see Song et al. (2000); Van Rossum et al. (2000) and reference therein).

In the following introduction I present the main classes of simplified neuron models, starting from the standard leaky integrate-and-fire model (LIF) and moving towards more sophisticated models of spiking activity. The functional properties and biological relevance of each model are discussed. A particular focus is given to the generalized integrate-and-fire (GIF) model which is extensively discussed in this thesis. As its name suggests, the GIF model is a generalization of the classic IF model, that accounts for (i) spike-frequency adaptation, (ii) stochastic spike emission and (iii) dynamical properties of the moving threshold.

The introduction is organized as follows: The first section introduces the notion of a threshold model, mainly in the form of the LIF model. The second section discusses classical extensions of the threshold model. Finally, the third section presents the GIF model, highlighting its flexibility and linking it to other standard models, such as the Generalized Linear Model (GLM).

1.1 Simplified threshold models

In the early 20th century, Lapicque introduced the first mathematical model that describes the electrical activity of single neuron: the leaky integrate-and-fire (LIF) model (Lapicque, 1907). According to this model, a single neuron integrates its input current until a certain threshold is reached, where an action potential is emitted. This simple but powerful model led to the conclusion that single neurons encode information in the number of spikes emitted in a given amount of time (Figure 1.1 **E-G**). The LIF model was later extended to account for more realistic neuronal properties. Nowadays integrate-and-fire models refer to a family of different models, that capture different aspect of neuron properties.

1.1.1 Leaky Integrate-and-Fire model

Mathematically, the LIF model (Lapicque, 1907; Hill, 1936; Stein, 1965; Knight, 1972; Tuckwell, 1988) is defined by the following differential equation of the membrane potential V:

$$C\frac{dV}{dt} = -g_L(V(t) - E_L) + I(t) \tag{1.1}$$

where C is the total membrane capacitance, g_L the leak conductance ($R = g_L^{-1}$ is the membrane resistance) and E_L the reversal potential. Equation 1.1 describes the dynamics of the membrane potential $V(t)$. Whenever $V(t)$ reaches the fixed voltage threshold V_T^*, a spike is emitted and the voltage is reseted to E_R:

$$\text{if:} \qquad V(t) > V_T^* \qquad \Longrightarrow \qquad \begin{cases} \hat{t} \leftarrow t \\ V(t) \leftarrow E_R \end{cases} \tag{1.2}$$
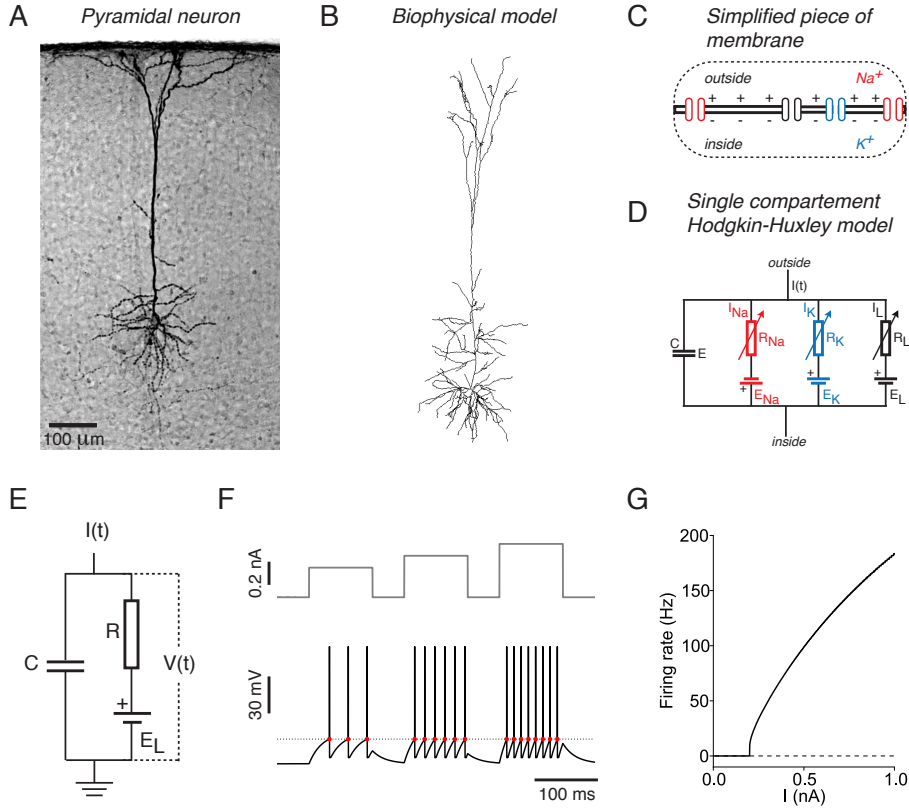
Figure 1.1: **Level of abstraction in single neuron models (A)** Staining of a mouse biocytin-filled L5 pyramidal neuron. Data is a courtesy of Olivier Hagens (LNMC, BMI, EPFL). **(B)** Reconstructed morphology of the L5b pyramidal neuron adapted from the biophysical Hay model (Hay et al., 2011). In this multi-compartmental model, the neural activities is described by more than hundred differential equations and thousands of parameters. **(C-D)** Single compartment Hodgkin-Huxley model describes the electrical properties of a piece of neuron membrane with a simple electrical circuit. **(C)** Schematic representation of a piece of membrane depicting three different ion channels. The sodium channels (red) and potassium channels (blue) mediate spike emissions, and a leak channel (black) models the passive membrane properties. **(D)** Electrical diagram of the Hodgkin-Huxley model. The electrical properties of the membrane is described by a parallel circuit including: C, the membrane capacitance, and three voltage dependent resistors R_{Na}, R_K and R_L in series with individual voltage sources E_{Na}, E_K and E_L, maintaining an equilibrium potential around -70 mV. **(E)** Electrical diagram of the LIF model, where the membrane is described as a parallel RC circuit that converts the input current $I(t)$ into the somatic voltage $V(t)$ (also note the presence of a battery, which maintains the resting potential at E_L). In this framework the membrane acts as a low-pass filter on the input current to produce the somatic voltage. **(F)** Response of the LIF model to three step of currents (grey, top). If the voltage $V(t)$ (black, bottom) reaches the firing threshold V_T^* (dashed line), a spike is emitted (red dots) and the voltage is reset to E_R. **(G)** In response to step of currents of different intensities the LIF model produces different firing frequencies. This relationship between stimuli strength and firing frequency is called f-I Curve and, as proposed by Lapicque (1907) provides a direct representation of an external stimuli in the neuron activities.

Following a spike emission at time $\hat{t}$, the integration of Eq. 1.1 is stopped during an absolute refractory period T_{ref} and then restarted until the next spike is fired. In the LIF model, the

absolute refractory period replaces the spike shape. With this approximation, it is implicitly assumed that the spike shape is stereotypical (i.e. it is always the same) and does not carry information (Hille, 1992; Koch, 1999) (but see (Häusser et al., 2001; de Polavieja et al., 2005; Juusola et al., 2007)).

The LIF model can be rewritten in its integral form[1]:

$$V(t) \quad = \quad E_L + \int_0^\infty \kappa(s) I(t-s) ds - \sum_{\hat{t}_j < t} \eta_R(t - \hat{t}) \tag{1.3}$$

$$\kappa_m(t) \quad = \quad \frac{1}{C} \exp\left(\frac{-t}{\tau_M}\right) \tag{1.4}$$

$$\eta_R(t) \quad = \quad (V_T^* - E_R) \exp\left(\frac{-t}{\tau_M}\right) \tag{1.5}$$

with $\tau_M = RC$ being the membrane timescale and η_R being a refractory kernel induced by the voltage reset. The LIF model captures relative refractoriness in η_R and describes the passive properties of the membrane with an exponential filter $\kappa_m(t)$, which acts as a low-pass filter on the input current. This simple filter has been shown to be a fairly good description of the passive properties of a neuron membrane (Figure 1.1 **E-G**).

1.1.2   Limitations of the LIF model

Due to its simplicity the LIF model does not reproduce some important aspects of the neural dynamics that have been experimentally observed:

1. **Subthreshold resonance**: at subthreshold voltages, different potassium channels mediate particular currents that can in principle affect the single neuron behavior in different ways (Mauro et al., 1970; Izhikevich, 2001, 2007). For example, in response to a subthreshold step of current, certain neurons exhibit damped oscillations in their membrane potential (Figure 1.2 **A**). Subthreshold oscillatory behavior — also called resonance — strongly affects the firing activity of the cell and plays an important role in the types of computation performed by a neuron (Hutcheon and Yarom, 2000; Izhikevich et al., 2003). For example, subthreshold resonance can induce bursts of action potentials (Lampl and Yarom (1997), Figure 1.4 **D**) that are known to signal important events (Larkum (2013) and references therein). Since the LIF membrane filter $\kappa_m(t)$ is strictly exponential, it can not take into account this particular feature.

2. **Spike-history effects**: in response to a constant input, the firing rate of single neurons decays over time (Figure 1.2 **B**). This phenomenon — known as spike-frequency adaptation (SFA) — is ubiquitous in the brain and has been shown to enhance information

---

[1]In its integral form, the LIF model is a special instance of the Spike Response Model, called SRM$_0$ (Gerstner, 1995a)

transfer between cells (Brenner et al., 2000; Wang et al., 2003). SFA can be induced by different ion currents. For example, high-voltage activated, calcium-dependent and sodium-dependent potassium channels create effective spike-triggered currents that accumulate over subsequent spikes and reduce the output firing rate (Baldissera et al., 1976; Madison and Nicoll, 1984; Schwindt et al., 1989; Sawczuk et al., 1997). Also, sodium channel inactivation reduces the number of channels available for spike initiation, effectively increasing the voltage threshold (Fleidervish et al., 1996; Mickus et al., 1999; Melnick et al., 2004; Zeng et al., 2005). Importantly, this second mechanism induces SFA without affecting the membrane potential. In simplified models, the net effect of sodium inactivation is modeled by including a spike-triggered movement of the firing threshold. Since the LIF model does not account for the spike history, it can not account for SFA.

3. **Spike initiation mechanisms**: From a biological point of view, spike emission is governed by the activation of specific sodium channels in the axon hillock that are activated near the voltage threshold (Baranauskas et al., 2010; Debanne et al., 2011). The spike onset is fast, typically in the sub-millisecond range (Naundorf et al., 2006; McCormick et al., 2007) (Figure 1.2 **C**, black), but not instantaneous as it is assumed in the LIF model (Figure 1.2 **C**, red). Theoretical studies have demonstrated that this feature has a major impact on the spiking response of cortical neurons (Fourcaud-Trocme et al., 2003; Brette, 2013).

4. **Spike-timing variability**: when stimulated multiple times with the same input current, spikes do not occur exactly at the same moments in time (Schneidman et al., 1998; Mainen and Sejnowski, 1995), indicating that single neurons are stochastic (Figure 1.2 **D**). This is an important feature since it affects the reliability of signal transmission (Shadlen and Newsome, 1994; Bair and Koch, 1996; Faisal et al., 2008). Whether intrinsic noise is a bug or a feature remains an open question. Recent studies proposed that the brain uses noise as a mechanism to internally represent uncertainty about the state of the external world (Berkes et al., 2011). Since the LIF model is deterministic, it neglects this important aspect.

All these features have been extensively studied in the past, and led to variants of the LIF model. The most important among them will be presented in the next section and are summarized in Table 1.1.

1.1.3 Subthreshold resonance

Certain neuron types exhibit subthreshold resonance. Such behavior has been shown to occur via the activation of specific low-voltage activated potassium channels (Mauro et al., 1970). Typically these channels exhibit nonlinear dynamics and interact with the passive properties of the cell to create oscillations in the subthreshold regime. Phenomenologically, subthreshold resonance can be modeled by extending the LIF model with a linear subthreshold current ω

Mechanism	Model	References
Linearized subthreshold current	Resonate-and-fire	Izhikevich (2001)
	AdEx	Brette and Gerstner (2005)
	Izhikevich model	Izhikevich (2003)
	GIF model	Richardson et al. (2003)
	SRM	Gerstner and Kistler (2002)[1]
	refractory-EIF	Badel et al. (2008)
Spike-triggered current	-	Baldissera et al. (1976)
	-	Treves (1993)
	-	Gerstner et al. (1996)
	-	Liu and Wang (2001)
	SRM	Gerstner and Kistler (2002)[2]
	Izhikevich model	Izhikevich (2003)
	unified SFA model	Benda and Herz (2003)
	GIF	Paninski et al. (2004)
	AdEx	Brette and Gerstner (2005)
	-	Drew and Abbott (2006)
Spike-triggered threshold	-	Fuortes and Mantegazzini (1962)
	-	Geisler and Goldberg (1966)
	-	Holden (1976)
	-	Liu and Wang (2001)
	-	Chacron et al. (2003)
	SRM	Jolivet et al. (2006)
	refractory-EIF	Badel et al. (2008)
	MAT	Kobayashi et al. (2009)
	GIF	Mihalaş and Niebur (2009)
Smooth spike initiation	NLIF	Abbott and van Vreeswijk (1993)
	θ-neuron	Latham et al. (2000)
	QIF	Feng (2001)
	QIF	Hansel and Mato (2001)
	Izhikevich model	Izhikevich (2003)
	EIF	Fourcaud-Trocme et al. (2003)
	AdEx	Brette and Gerstner (2005)
	refractory-EIF	Badel et al. (2008)

Table 1.1: **Extended IF-type models.** This list is not exhaustive, but highlights the vast diversity of simple IF-type model. [1]Formally there is no linearized subthreshold current in the spike response model, however depending on the shape of the linear filter $\kappa(t)$, SRM can be rewritten as a LIF model upgraded with linearized subthreshold current. [2]The SRM does not contains a spike-triggered current, but a spike-triggered voltage describing directly the AHP.

(Izhikevich, 2001; Richardson et al., 2003),

$$C\frac{dV}{dt} = -g_L(V - E_L) + I(t) - \omega \tag{1.6}$$

$$\tau_\omega \frac{d\omega}{dt} = a(V - E_\omega) - \omega \tag{1.7}$$
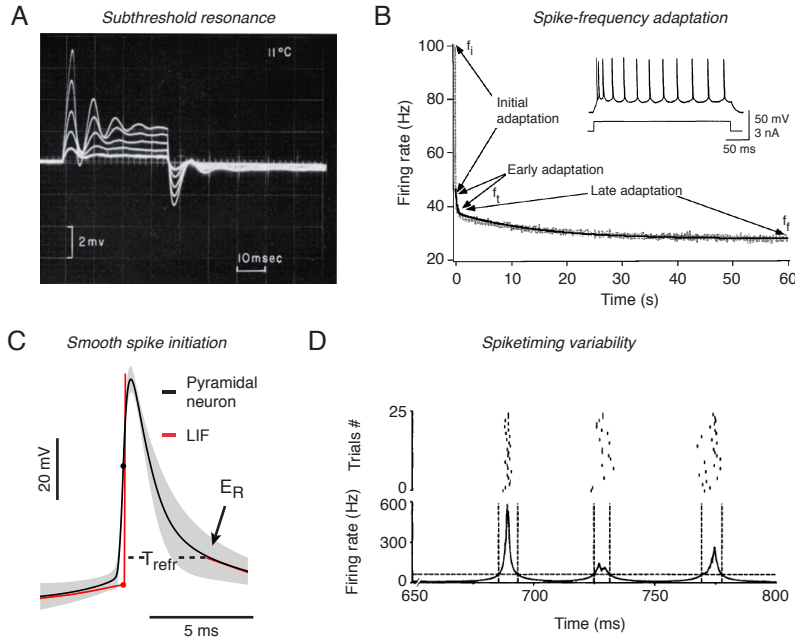
Figure 1.2: **Electrical properties of single neurons.** Four phenomenological features of single cells that are not taken into account by the standard LIF model. **(A)** Subthreshold behavior of the squid giant axon. When stimulated with subthreshold steps of current of different magnitudes, the squid axon responds with a typical oscillatory behavior (adapted from Mauro et al. (1970)). This resonating behavior is present in a vast variety of neurons among the brain (Gutfreund et al., 1995; Lampl and Yarom, 1997; Hutcheon et al., 1996; Hutcheon and Yarom, 2000). **(B)** When a rat hypoglossal motoneuron is stimulated with a suprathreshold step of current, spike-frequency adaptation appears as a slowdown of the neuron firing rate as a function of stimulation time in response (adapted from Sawczuk et al. (1997)). Inset: in response to a step of current, neocortical regular spiking neurons respond with an initial high firing rate that decay to lower sustained firing frequency (top trace: recorded voltage, lower trace: input current, adapted from Connors and Gutnick (1990)) **(C)** Smooth spike initiation in mice cortical neurons. Averaged spike shape from 1157 action potentials (black line, grey area is one standard deviation). Even if the spike onset is fast, it is not instantaneous as in the LIF model (red). Data is a courtesy of Olivier Hagens. This smooth spike initiation is a common features throughout all the cortex. **(D)** Spiketime variability of cortical neurons evoked by 25 repeated injection of the same fluctuating current (raster plot, top panel; PSTH computed by an adaptive filtering of the raster plot, bottom panel), adapted from Mainen and Sejnowski (1995). Spike timing variability is a direct consequence of different intrinsic noise sources and is a common features of all neurons (see (Faisal et al., 2008) and references therein).

with τ_w being the time constant of ω, E_ω being its reversal potential and a controlling its magnitude. Depending on the sign of a, ω can cause subthreshold facilitation or subthreshold resonance. Indeed, for $a < 0$ the impulse response of this system[2] is characterized by an exponential decay with two timescales, while for $a >> 0$, the membrane filter oscillates (resonance).

From a physical point of view, Equations 1.6-1.7 describe a damped oscillator with a driving

---

[2]The impulse response corresponds to the voltage trajectory elicited by the injection of a δ-dirac current $I(t) = \delta(t)$. It corresponds to the linear membrane filter $\kappa(t)$ of the spike response model (SRM).

force $I(t)$. The impulse response of this system can be derived analytically. This topics is further discussed in chapter 3 of this thesis.

In the literature, simplified threshold models augmented with a subthreshold current are often referred to as resonate-and-fire models (Izhikevich, 2001). Linearized subthreshold currents are included in many models: the SRM (Gerstner and Kistler, 2002), the adaptive exponential integrate-and-fire model (AdEx, Brette and Gerstner (2005)), the Izhikevich model (Izhikevich, 2003) and a special variant of the LIF model introduced in Richardson et al. (2003) (Table 1.1). The mechanisms by which subthreshold currents induce burst of action potentials have been studied in Lampl and Yarom (1997), Izhikevich (2001) or Richardson et al. (2003).

1.1.4   Spike-history effects

Spike-triggered currents

As for subthreshold resonance, the LIF model can be extended to account for SFA with a second equation that describes the dynamics of a spike-dependent adaptation current ω:

$$C\frac{dV}{dt} = -g_L(V - E_L) + I(t) - \omega \tag{1.8}$$

$$\tau_\omega\frac{d\omega}{dt} = -\omega + b\tau_\omega \sum_{\hat{t}_j < t} \delta(t - \hat{t}_j) \tag{1.9}$$

According to Eq. 1.9, each time a spike is emitted, the adaptation current is increased by b and exponentially decay with timescale τ_ω. By integrating equation 1.9, one can see that the adaptation current ω consists of a sum of spike-triggered current $\eta_a(t) = b\exp\frac{-t}{\tau_\omega}$:

$$\omega(t) = \sum_{\hat{t}_j < t} \eta_a(t - \hat{t}_j) \tag{1.10}$$

In contrast to η_r, spike-triggered currents induced by different action potential accumulate and can therefore induce SFA, if $b > 0$ (Figure 1.2 **B**, and 1.4 **B**), or facilitation, if $b < 0$ (Figure 1.4 **C**).

A single spike-triggered current of this form is sufficient to account for the after-hyperpolarizing potential (AHP) observed in cortical neurons, but does not fully capture spike-frequency adaptation. Since SFA is mediated by different ion currents, its dynamics is not governed by a single timescale but acts on multiple timescales (Spain and Schwindt, 1991; Gilboa et al., 2005; La Camera et al., 2006; Lundstrom et al., 2008). To account for the multiple timescales of adaptation, a possible solution is to relax the exponential assumption made in Equation 1.9

and describe the spike-triggered current with a arbitrarily shaped current η:

$$C\frac{dV}{dt} \quad = \quad -g_L(V - E_L) + I(t) - \sum_{\hat{t}_j < t} \eta(t - \hat{t}_j) \tag{1.11}$$

where $\eta(t)$ is a causal function of time that summarizes the contribution of multiple channels. Including a shape-free spike-triggered current gives flexibility to the aforementioned model and allows it to capture important aspects of spike-frequency modulation (see Figure 1.4). For example, a biphasic η could mediate relative refractoriness on short timescale and SFA on longer timescales. The role of the functional shape of η is extensively discussed in the chapter 2 and in the Appendix of this thesis. Table 1.1 lists the most important reference threshold models that account for SFA by the means of a spike-triggered current.

Spike-triggered movement of the firing threshold

Regardless of the specific definition of the voltage threshold, it has been shown that spikes do not systematically initiate at the same voltage (Azouz and Gray, 2000, 2003; Wester and Contreras, 2013). Biophysically spike initiation is driven by a sudden influx of sodium ions in the cell. Once sodium channels have been activated and a spike has been emitted, they stay in an inactivated state for a while (Fuortes and Mantegazzini, 1962; Fleidervish et al., 1996; Fleidervish and Gutnick, 1996), decreasing the number of sodium channels which are available for the emission of a second spike. Consequently the voltage threshold is increased by the emission of previous spikes (Henze and Buzsáki, 2001; Melnick et al., 2004). Thus, sodium inactivation constitutes an additional source of SFA, which should be modeled by a spike-triggered movement of the firing threshold γ rather than a spike-triggered current:

$$V_T(t) \quad = \quad V_T^* + \sum_{\hat{t}_j < t} \gamma(t - \hat{t}_j), \tag{1.12}$$

$$\text{if:} \qquad V(t) > V_T(t) \qquad \Longrightarrow \qquad \begin{cases} \hat{t} \leftarrow t \\ V(t) \leftarrow E_R \end{cases} \tag{1.13}$$

In many models, $\gamma(t)$ is assumed to be a single exponential function. In Equation 1.12, $\gamma(t)$ is an arbitrary function of time describing the trajectory of the voltage threshold following spike emission. The dynamics of the spike-triggered movement of the firing threshold is the topics of chapter 2 and the Appendix of the present thesis.

Moving threshold has been introduced in the LIF model in the sixties (Geisler and Goldberg, 1966) to account for adaptation (Figure 1.4 **B**, Chacron et al. (2003); Kobayashi et al. (2009)) and relative refractoriness (Jolivet et al. (2006); Badel et al. (2008) see table 1.1 for references).

Interestingly, recent theoretical and experimental studies have shown that the firing threshold

does not simply depend on previous spikes (Platkiewicz and Brette, 2010, 2011), but also depends on the speed at which the firing threshold is approached (Wester and Contreras, 2013). The complex dynamics of the firing threshold is the topics of the chapter 5 of this thesis.

1.1.5 Spike initiation mechanisms

The voltage threshold is an ill-defined concept, indeed it is hard to say precisely if a spike has been emitted or if it is still in the initiation phase. Spike initiation is not an instantaneous process but occurs on a finite timescale (see Figure 1.2 **C**).

To account for spike initiation, the LIF model has been extended by making the voltage dynamics nonlinear, giving rise to a new class of model: the nonlinear integrate-and-fire model (NLIF, Abbott and van Vreeswijk (1993); Latham et al. (2000); Hansel and Mato (2001); Feng (2001); Izhikevich (2003); Fourcaud-Trocme et al. (2003)):

$$C\frac{dV}{dt} \quad = \quad F(V) + I(t) \tag{1.14}$$

where $F(V)$ is a nonlinear function of the membrane potential. The two most common nonlinearities are: (i) a quadratic function (QIF, Feng (2001)) and (ii) an exponential function (EIF, Fourcaud-Trocme et al. (2003)). These two particular instances of the NLIF family will be described in the next subsections.

Quadratic integrate-and-fire model (QIF)

The QIF model accounts for spike onset with a quadratic voltage nonlinearity:

$$F(V) \quad = \quad a_0(V - E_L)(V - V_T^*) \tag{1.15}$$

where a_0 defines the sharpness of the quadratic function, E_L is the resting potential of the model and V_T^* is the smooth spike threshold[3]. In this model, a spike occurs if the voltage quickly diverges to infinity. In practice, when $V = V_{th}$, where $V_{th} >> V_T^*$.

In the absence of an input current (i.e., when $I(t) = 0$), the QIF model is characterized by the presence of a stable fixed point at $V = E_L$ and an unstable fixed point at $V = V_T^*$ (Figure 1.3 **B**), so that the voltage steady-state is at E_L. When stimulated with a depolarizing step of current, the nullcline is instantaneously shifted upward (Figure 1.3 **B**) and the system loses stability via a saddle-node bifurcation producing tonic spiking (Figure 1.3 **B**, right panel). This particular dynamics leads to a quadratic spike initiation (Figure 1.3 **D**) that capture smooth

---

[3]Even if V_T^* is related to the voltage threshold of the LIF model, it is not a real threshold. As shown in figure 1.3 **B**, it represents the unstable fixed point of Eq 1.15 in absence of input current $I(t)$, so that threshold for spike emission depends on the specific input current (short pulse, step, ramp, ...)

spike initiation.

Importantly, in this model there is no unique definition of the voltage threshold. Indeed, the voltage at which a spike is initiated depends on the stimulation paradigm. For a short current pulse, a spike will be emitted if $V > V_T^*$, whereas for slow depolarization a spike will occur through the saddle node bifurcation at the lower voltage $\tilde{V} = \frac{-(E_L + V_T^*)}{2a_0}$. This creates a positive correlation between the effective firing threshold and the depolarization rate. In other words, the threshold is higher for fast input, than for slow input. The dependency predicted by the QIF model between firing threshold and depolarization rate, is at odd with experimental evidence. Indeed, it has been shown that both *in vitro* and *in vivo* the effective threshold for spike emission is negatively correlated with the rate of depolarization (Azouz and Gray, 2000, 2003; Wilent and Contreras, 2005; Henze and Buzsáki, 2001; Higgs and Spain, 2011). The dynamics of the firing threshold is investigated in the chapter 5 of this thesis.

The exponential integrate-and-fire model (EIF)

Another standard instance of the NLIF model is the exponential integrate-and-fire (EIF) model introduced by Fourcaud-Trocme et al. (2003), where the nonlinearity $F(V)$ is composed of a linear part describing the leaky integration of the membrane and an exponential function capturing the fast onset of spike initiation:

$$F(V) \quad = \quad -g_L(V - E_L) + g_L \Delta T \exp\left(\frac{V - V_T^*}{\Delta T}\right) \tag{1.16}$$

with ΔT being the sharpness of the exponential function and V_T^* being the smooth voltage threshold[4]. As in the QIF model, a spike is emitted if $V \to \infty$. The dynamics of the EIF model is very similar to the QIF dynamics described above, except that the voltage dynamics of the spike onset is exponential (see Figure 1.3 **C** and **D**, red), which is in good agreement with experimental findings (Badel et al., 2008)

Adaptive exponential integrate-and-fire model (AdEx)

In the previous sections, several extensions of the LIF model have been presented independently, however these different extensions have been simultaneously included in two different single neuron models: the Izhikevich model (Izhikevich, 2003) and the adaptive exponential integrate-and-fire model (AdEx, Brette and Gerstner (2005)). These two models are highly flexible and are able to reproduce almost all firing patterns that have been experimentally observed (Markram et al., 2004; Izhikevich, 2007; Naud et al., 2008). The AdEx model and its links with the generalized linear model (GLM) is the topic of chapter 3 of this thesis. A detailed analysis of these two models can be found in Izhikevich (2007); Naud et al. (2008); Touboul

---

[4]As for the QIF model, there is no fixed voltage threshold in the EIF model, and spike emission depends on the stimulation paradigm (see Fourcaud-Trocme et al. (2003))
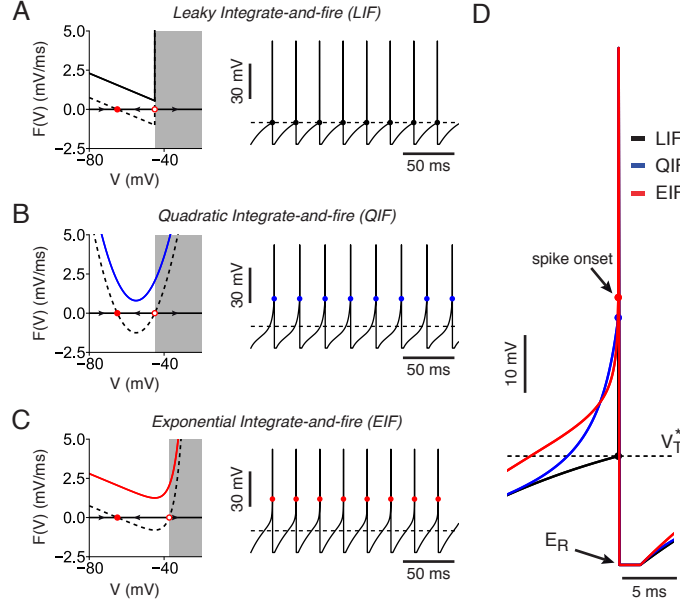
Figure 1.3: **Nonlinear Integrate-and-fire model**. Differences between LIF, quadratic IF and exponential IF models. The dynamics of the nonlinear integrate-and-fire models is better understood by looking at their phase plane ($\dot{V}$ as a function of V). **(A)** Nullcline of the LIF model (dashed line). In absence of input current, the dynamics of the LIF model is governed by two fixed points, a stable one at E_L (full red dot) and an unstable one at V_T^* (open red dot), so that the voltage stays at E_L. When a positive constant current I_0 is applied, the nullcline is shifted upward (blue line), the two fixed points collapse and disappear so that the system loses stability via a saddle node bifurcation, producing spikes. Due to the reset at a constant value, the LIF model produces tonic spiking (right panel). The hard threshold guarantees that in response to a suprathreshold injection of current, spikes are always emitted at the same threshold V_T^* (right panel, dashed line). **(B)** As in **A**, but for the QIF model. The nullcline of the QIF model is a quadratic function with two fixed points, one stable at E_L and one unstable one at V_T^*, when a constant depolarizing current I_0 is applied, the nullcline is shifted upward and the system undergoes a saddle node bifurcation. By contrast to the LIF model, there is no hard threshold and a spike is emitted when the voltage quickly diverges to infinity. As shown in right panel, the QIF model approximates the smooth spike initiation by a quadratic function, leading to more realistic spike onset. In this model the actual firing threshold is ill-defined and depends on the stimulation protocol. **(C)** Same as **B**, but for the EIF model. In contrast to the QIF model, EIF model approximates the spike initiation with an exponential function, leading to a more realistic spike onset (Badel et al., 2008). **(D)** Spike initiation trajectories produced by the three different models. The nonlinearities of the QIF and EIF models start to play role at relatively high voltages (close to V_T^*) and capture smooth spike initiation, while the LIF emits a spike exactly at V_T^* (dashed line).

(2008); Touboul and Brette (2008) and Touboul and Brette (2009).

1.1.6 Spike-timing variability

Neurons are intrinsically noisy, indeed when stimulated several times with the same input current spikes do not occur exactly at the same times (Schneidman et al., 1998; Mainen and Sejnowski, 1995) and voltage trajectories differ between repetitions (Manwani and Koch, 1999;

Faisal et al., 2008). This stochasticity is mainly due to two intrinsic sources of noise: (i) thermal noise due the resistive nature of the neuron membrane (Manwani and Koch, 1999), (ii) channel noise resulting from the stochastic and discrete nature of ion channels[5] (Schneidman et al., 1998; Manwani and Koch, 1999; White et al., 2000; Stiefel et al., 2013). The functional role of single neuron stochasticity is still debated (Shadlen and Newsome, 1994; Bair and Koch, 1996; Faisal et al., 2008; Berkes et al., 2011; Beck et al., 2012).

Trial-to-trial variability can be reproduced by extending IF models with a source of noise in the input current (i.e. diffusive noise; see van Kampen (1992)), or by making the threshold process stochastic (escape rate; Gerstner and van Hemmen (1992); Paninski et al. (2005). The link between IF models extended with diffusive noise and escape rate model is discussed in Plesser and Gerstner (2000) and a particular case is studied in the 3rd chapter of this thesis. In the following I will only focus on the escape rate model, since it is the model used throughout all this thesis.

Escape rate model

In the escape rate model, spikes are produced stochastically according to a point process with conditional firing intensity $\lambda(t|V, V_T^*)$ (also called stochastic intensity), which nonlinearly depends on the distance between the membrane potential $V(t)$ and the firing threshold V_T^* (Gerstner and van Hemmen, 1992; Paninski et al., 2005; Jolivet et al., 2006):

$$\lambda(t|V, V_T) \quad = \quad \lambda_0 \cdot f\left(V, V_T^*\right), \tag{1.17}$$

where λ_0 has units of s^{-1}, so that $\lambda(t)$ is in Hz. According to Equation 1.17 the probability of emitting a spike at time $\hat{t}$ is given by (Gerstner and Kistler, 2002):

$$P(\hat{t} \in [t; t + \Delta t]) \quad = \quad 1 - \exp\left(-\int_t^{t+\Delta t} \lambda(s)\,ds\right) \approx \lambda(t)\Delta t. \tag{1.18}$$

where Δt is an arbitrarily small time step. The choice of the nonlinear function $f(\cdot)$ is free, however it is reasonable to takes into account informations gathered from data. For instance, it seems natural to choose a function $f(\cdot)$ for which probability of spiking vanishes when $V \to -\infty$ and goes to infinity when $V \to \infty$.

Depending on the properties of $f(\cdot)$, the likelihood of the model[6] can be a convex function of

---

[5]Extrinsic sources of noise, such as background synaptic activities or unreliability of synaptic transmission (Allen and Stevens, 1994; Dobrunz and Stevens, 1997) do not play a role when considering somatic injection of current in in-vitro preparation and so, are out of the scope of this thesis.

[6]Following Equation 1.17-1.18, the log-likelihood of observing spikes at times $\hat{t}_j$ for an escape rate model is given by: $\log L(V, \theta) = \sum_{\hat{t}_j} \log \lambda_0 \Delta t f(V, \theta) - \sum_t \log(1 - \lambda_0 \Delta t f(V, \theta))$ and can be interpreted as the probability of the model to generate the observed spiketrain $\{\hat{t}_j\}$.

the model parameters. Convex likelihood is an important criterion to take into account when choosing $f(\cdot)$, since it allows for a fast and robust parameter estimation (Gerstner and van Hemmen (1992); Pillow et al. (2008) and chapters 2, 4, 5 and Appendix). One can mathematically demonstrate that for any convex and log-concave function $f(\cdot)$, the model likelihood becomes a convex function of its parameters (Paninski, 2004). Typical functions fulfilling these requirements are: the linear rectifier function, the quadratic function (Simoncelli and Heeger, 1998) and the exponential function (Pillow et al., 2008). Since the exponential function is in good agreements with experimental data (Jolivet et al., 2006), a good model for stochastic spike emission is given by:

$$\lambda(t|V, V_T^*) \quad = \quad \lambda_0 \cdot \exp\left(\frac{V(t) - V_T^*}{\Delta V}\right), \tag{1.19}$$

where ΔV defines the level of stochasticity of the model. Note that the LIF model is a special case of Equation 1.19. Indeed, in the limit $\Delta V \to 0$, the model becomes deterministic and action potentials are emitted at the precise moment when the membrane potential crosses the firing threshold V_T^*.

The escape rate model defined by Eq. 1.17 shares some interesting links with another statistical class of models called Generalized Linear Models (GLM; Truccolo et al. (2005); Pillow et al. (2008) and also see Dayan and Abbott (2001)), which are introduced in the next section.

1.2 Generalized Integrate-and-fire model

1.2.1 Model definition

The GIF model is obtained by extending the LIF model with a spike-triggered current, a spike-triggered movement of the firing threshold and an exponential escape rate mechanism for stochastic spike emission. The subthreshold voltage $V(t)$ evolves according to the following differential equation:

$$C\dot{V}(t) = -g_{\mathrm{L}}(V(t) - E_{\mathrm{L}}) - \sum_{\hat{t}_j < t} \eta(t - \hat{t}_j) + I(t), \tag{1.20}$$

where the parameters C, g_{L} and E_{L} define the passive properties of the neuron, $I(t)$ is the input current and $\{\hat{t}_j\}$ are the spike times. After each spike, a stereotypical current $\eta(t)$ is triggered[7] that accumulates over subsequent spikes to account for SFA. Each time a spike is emitted, the numerical integration is stopped during a short absolute refractory period T_{ref} and the membrane potential is reset to $V(\hat{t}_j + T_{\mathrm{ref}}) = V_{\mathrm{reset}}$.

Spikes are produced stochastically according to an inhomogenous point process with firing intensity $\lambda(t|V, V_T)$, which exponentially depends on the difference between the membrane

---

[7] the spike-triggered current $\eta(t)$ is hyperpolarizing when its amplitude is positive and depolarizing otherwise.

	PIF	LIF	SRM$_0$	RIF	QIF	EIF	Izhi	AdEx	SRM	GIF
Absolute refractoriness	✓	✓	✓	✓	✓	✓	✓	✓	✓	✓
Relative refractoriness	✗	✓	✓	✓	✓	✓	✓	✓	✓	✓
Subthreshold resonance	✗	✗	✗	✓	✗	✗	✓	✓	✓	✗
After-hyperpolarizing potential	✗	✗	✓	✗	✗	✗	✓	✓	✓	✓
Spike-history effets	✗	✗	✗	✗	✗	✗	✓	✓	✓	✓
Realistic reset value	✗	✗	✗	✗	✗	✗	✗	✗	✓	✓
Smooth spike initiation	✗	✗	✗	✗	✓	✓	✓	✓	✗	✗
Spike-timing variablity	✗	✗	✗	✗	✗	✓	✓[1]	✓[1]	✗	✓

Table 1.2: **Biological features reproduced by different variants of the IF models.** This table summarizes the ability of individual IF model to reproduce a given biological phenomenon. In each column the model is indicate by its acronym: **PIF**: Perfect Integrate-and-Fire, Gerstein and Mandelbrot (1964); **LIF**: Leaky Integrate-and-Fire, Lapicque (1907); **SRM**$_0$: Spike Response Model 0, Gerstner (1995a); **RIF**: Resonate Integrate-and-Fire, Izhikevich (2001); **QIF**: Quadratic Integrate-and-Fire, Feng (2001); **EIF**: Exponential Integrate-and-Fire, Fourcaud-Trocme et al. (2003); **Izhi**: Izhikevitch model, Izhikevich (2003); **AdEx**: Adaptive Exponential Integrate-and-Fire, Brette and Gerstner (2005); **SRM**: Spike Response Model, Gerstner and Kistler (2002); **GIF**: Generalized Integrate-and-Fire as presented in the section 1.2.

Superscript **1**: Depending on its parameters, the NLIF model could exhibit chaotic spiking activity. This chaotic activity is not due to an additional source of noise in the system, but is an emergent properties of this 2-dimensional system of differential equations, mainly induced by the hard reset in the dynamics.

potential $V(t)$ and the firing threshold $V_T(t)$ (Gerstner and van Hemmen, 1992; Paninski et al., 2005; Jolivet et al., 2006):

$$\lambda(t|V, V_T) = \lambda_0 \cdot \exp\left(\frac{V(t) - V_T(t)}{\Delta V}\right).$$ (1.21)

In contrast to Equation 1.19, the firing threshold $V_T(t)$ of the GIF model is dynamic:

$$V_T(t) = V_T^* + \sum_{\hat{t}_j < t} \gamma(t - \hat{t}_j),$$ (1.22)

where V_T^* is the baseline threshold and $\gamma(t)$ describes the stereotypical trajectory of the firing threshold after a spike. Since the contribution of different spikes accumulates, the moving threshold defined in Equation 1.22 constitutes an additional source of adaptation.

In this thesis, I used the GIF model to perform high throughput parameter extraction from *in vitro* recordings (chapter 4), characterize different cell types (chapter 2), predict the spiking activity of different neuron types (chapter 2, 4, 5 and Appendix) and characterize SFA on

multiple timescales (Appendix).

1.2.2 Flexibility of the GIF model

The GIF model is very flexible. Indeed, depending on its parameters, it is able to reproduce most of the firing patterns that have been experimentally observed (Markram et al., 2004). In contrast to the NLIF models, where different firing patterns emerge from different bifurcations (Izhikevich, 2007; Naud et al., 2008; Touboul, 2008; Touboul and Brette, 2008), the type of response of the GIF model to a step of current mainly depends on the time courses of the spike-triggered current $\eta(t)$ and movement of the firing threshold $\gamma(t)$ (Figure 1.4).
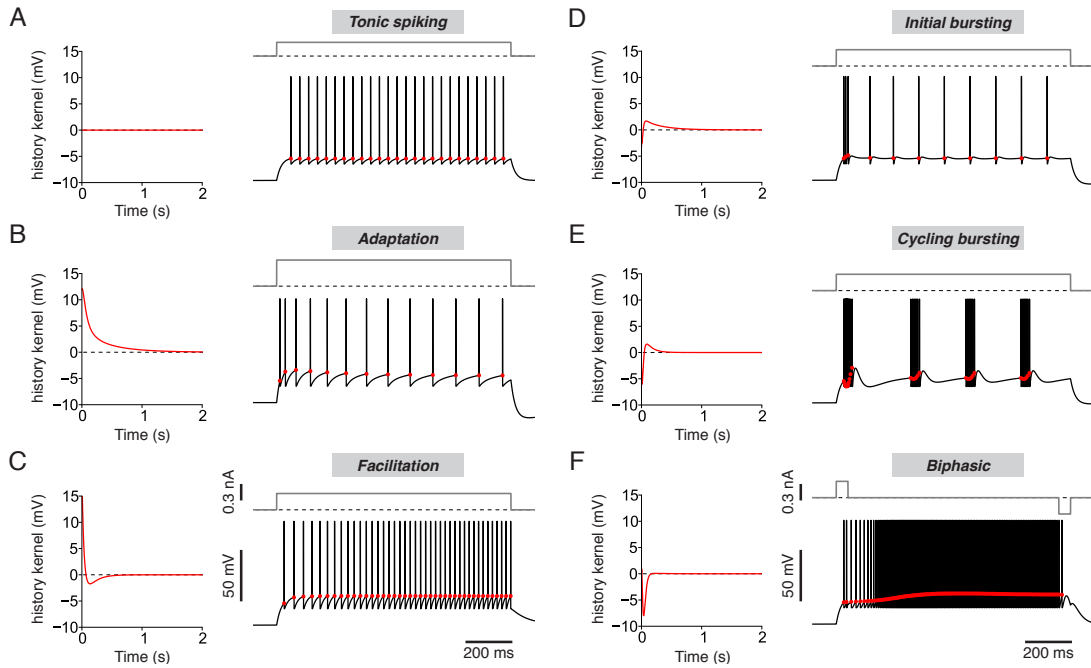
Figure 1.4: **Flexibility of the generalized integrate-and-fire model (GIF). (A-F)** Depending on its parameters, the GIF model produces different firing patterns (right panels, black) in response to a step current (right panels, grey). All the model parameters but the effective *history kernel h(t)* (left panel, red) are kept constant. For illustrating purposes the stochasticity of the GIF model has been set to an arbitrary small value. **(A)** Without spike-triggered process ($h(t) = 0$, left panel, red), the GIF model produces spikes at regular interval (*tonic spiking*). **(B)** When an hyperpolarizing spike-triggered kernel is present, the GIF model produces spike-frequency *adaptation*. **(C)** Conversely, with a depolarizing history kernel, the instantaneous firing rate increases with time, producing *facilitation*. **(D-E)** When $h(t)$ is composed of a first depolarizing part followed by a longer and weaker hyperpolarizing part, the GIF model produces bursts of action potentials. Depending on the precise shape of this biphasic kernel, it can produces an initial burst followed by tonic spiking (**(D)** *initial bursting*), or some volleys of bursts followed by an arbitrary long period of silence (**(E)**, *cycling bursting*). The precise number of spikes in a burst depends on the shape of $h(t)$. **(F)** With the particular biphasic shape of $h(t)$ shown on the left panel, spiking can be switched on by a brief pulse of current and then continue until a brief hyperpolarizing pulse of current occurs. This kind of behavior is referred as *biphasic* firing pattern or *memory* (since it remembers the last depolarizing pulse of current).

1.2.3 Link between GIF and GLM

To establish links between the GIF model and the other models introduced in the previous sections, it is convenient to rewrite the GIF model in its integral form:

$$V(t) \quad \approx \quad E_L + \int_0^t \kappa(s) I(t-s) ds - \sum_{\hat{t}_j < t} \left(\eta_v(t - \hat{t}_j) + \eta_R(t - \hat{t}) \right) \tag{1.23}$$

where $\kappa(t) = \frac{1}{C} \exp\left(\frac{-t}{RC}\right)$ is the exponential membrane filter of the LIF model (Equation 1.4), $\eta_R(t)$ accounts for the relative refractoriness of the LIF induced by the hard reset and $\eta_v(t)$ describes the stereotypical trajectory of the membrane potential induced by the spike-triggered current η:

$$\eta_v(t) \quad = \quad \int_0^\infty \kappa(s) \eta(t-s) ds. \tag{1.24}$$

The approximation in Eq 1.23 comes from the fact that the voltage at which spikes are emitted is not fixed, but depends both on the dynamic nature of $V_T(t)$ and on the escape rate mechanism. To avoid this approximation, one should make the magnitude of the refractory kernel spike-dependent (i.e. $\eta_R(t) = (V_T(\hat{t}) - E_R) \cdot \exp\left(\frac{-t}{RC}\right)$). However, under the assumption of low threshold variability, one can introduce a single refractory kernel η_R given by:

$$\eta_R(t) \quad = \quad (\bar{V}_T^* - E_R) \cdot \exp\left(\frac{-t}{RC}\right) \tag{1.25}$$

where $\bar{V}_T^* = \langle V(\hat{t}_j) \rangle_j$ is the average voltage at which spikes occur. In this form, the GIF model can be interpreted as a Spike Response Model with escape rate (SRM) (Jolivet et al., 2006; Kobayashi and Shinomoto, 2007; Gerstner and Kistler, 2002).

Interestingly, it is possible to reduce the GIF model into a more abstract model that describes the spiking activity without explicitly modeling the subthreshold membrane potential: the Generalized Linear Model (GLM). The GLM provides a statistical description of the single-neuron spiking activity (Simoncelli and Heeger, 1998; Dayan and Abbott, 2001; Paninski, 2004; Truccolo et al., 2005; Pillow et al., 2008) and shares many similitudes with the GIF model. Indeed, the GLM describes the spiking behavior of the neuron by a linear filter κ_{GLM}, followed by an exponential nonlinearity which transforms the filtered input into a spiking intensity $\lambda(t)$ (see equation 1.17). Often, GLMs account for spike-history effects by means of a feedback kernel $h(t)$. Mathematically, the conditional firing intensity of the GLM is given by:

$$\lambda(t) \quad = \quad \lambda_0 \cdot \exp\left(E_0 + \int_0^t \kappa_{\text{GLM}}(s) I(t-s) ds - \sum_{\hat{t}_j < t} h(t - \hat{t}_j) \right), \tag{1.26}$$

where E_0 is a constant. The GIF model can therefore be mapped to a GLM by setting its parameters as follows:

$$E_0 = \frac{1}{\Delta V} \cdot (E_L - V_T^*) \tag{1.27}$$

$$\kappa_{\text{GLM}}(t) = \frac{1}{\Delta V} \cdot \kappa(t) \tag{1.28}$$

$$h(t) = \frac{1}{\Delta V} \cdot (\eta_v(t) + \eta_R(t) + \gamma(t)). \tag{1.29}$$

Despite the strong similarity between these two models, it is important to point out that the biological interpretation of the GLM filters $\kappa_{\text{GLM}}(t)$ and $h(t)$ are not as straightforward as for the GIF model. The linear filter $\kappa_{\text{GLM}}(t)$ does not transform an input current into a voltage and consequently it can not be interpreted as the membrane filter. The same observation stands for the history-dependent filter $h(t)$, which, as shown in Equation 1.29, summarizes the effect of the spike-triggered current η and the moving threshold γ.

In the past, GLMs have been used to: (i) infer the connectivity between cells (Okatan et al., 2005; Eldawlatly et al., 2009; Gerhard et al., 2013), (ii) characterize receptive field of neurons (by directly mapping external sensory stimuli to output spike trains) and (iii) decode the neural code (Lawhern et al., 2010; Pillow et al., 2011; Shoham et al., 2005).

1.3 Structure of the thesis

The following chapters of this thesis regroup 3 peer-reviewed articles, 1 submitted paper and 1 manuscript in preparation, which present novel results in the field of computational neuroscience, simple neuron models, spike-frequency adaptation and neural coding.

Chapter 2 introduces a new version of the Generalized Integrate-and-Fire model along with a convex fitting procedure allowing for efficient parameter extraction from intracellular recordings. We show how cortical neurons of different cell-types implement spike-frequency adaptation by the means of two distinct mechanisms: the spike-triggered current and the moving threshold. We also show that adaptation is cell-type specific and acts on different timescales ranging from milliseconds to seconds. This chapter appeared in *Journal of Neurophysiology*, Mensi et al. (2011b).

Chapter 3 explores the links between the AdEx model with diffusive noise and the GLM. In the first part the GLM linear filters are analytically derived from the AdEX model. In the second part, the GLM nonlinearity is numerically estimated from the AdEX spiking probability distribution. Our results show that the firing activities of the two models are statistically indistinguishable. We therefore concluded that the two are almost equivalent. This chapter was published in *Neural Information Processing Systems (NIPS)*, Mensi et al. (2011a).

In the next years automatic patch-clamp will become available, creating a huge amount of data. To analyze such datasets, fast and efficient tools have to be developed. In Chapter 4, we demonstrate that the GIF model along with its convex fitting procedure is suitable for automatic high-throughput single-neuron characterization. This chapter is under review in *Neuron*, Mensi et al. (2014).

Chapter 5 introduces a new model, the iGIF model, that accounts for enhanced sensitivity to input fluctuations experimentally (Arsiero et al., 2007). The iGIF extends the GIF model by a nonlinear coupling between membrane potential and firing threshold. This new mechanism implements a form of multiplicative adaptation. This chapter reports preliminary results that were presented at Cosyne 2013, 2014 and in INCF 2013.

Finally the Appendix presents a study that extends the work presented in Chapter 2 by looking at longer timescales in the spike-triggered processes. Our results show that, in mice pyramidal neurons, SFA is a scale-free process, correctly described by a power-law. We also show that power-law adaptation is optimally tuned to encode *in vivo*-like input current. This chapter was published in *Nature Neuroscience*, Pozzorini et al. (2013).

My contribution to each of these chapters is detailed in the last chapter of this thesis.

2 Parameter Extraction and Classification of Three Cortical Neuron Types Reveals Two Distinct Adaptation Mechanisms

Cortical information processing originates from the exchange of action potentials between many cell types[1]. In order to capture the essence of these interactions it is of critical importance to build mathematical models that reflect the characteristic features of spike generation in individual neurons. We propose a framework to automatically extract such features from current-clamp experiments, in particular the passive properties of a neuron (i.e. membrane time constant, reversal potential and capacitance), the spike-triggered adaptation currents, as well as the dynamics of the action potential threshold. The stochastic model that results from our maximum likelihood approach accurately predicts the spike times, the subthreshold voltage, the firing patterns, and the type of frequency-current curve. Extracting the model parameters for three cortical cell types revealed that cell types show highly significant differences in the time course of the spike-triggered currents and moving threshold, that is, in their adaptation and refractory properties, but not in their passive properties. In particular, GABAergic fast-spiking neurons mediate weak adaptation through spike-triggered currents only, whereas regular spiking excitatory neurons mediate adaptation with both moving threshold and spike-triggered currents. GABAergic non-fast-spiking neurons combine the two distinct adaptation mechanisms with reduced strength. Differences between cell types are large enough to enable automatic classification of neurons into three different classes. Parameter extraction is performed for individual neurons so that we find not only the mean parameter values for each neuron type, but also the spread of parameters within a group of neurons, which will be useful for future large-scale computer simulations.

---

[1]This text is copied from Mensi et al. (2011b), full citation in the bibliography

Chapter 2. Parameter Extraction and Classification of Three Cortical Neuron Types Reveals Two Distinct Adaptation Mechanisms

2.1 Introduction

Cortical neurons exhibit a variety of different firing patterns in response to step currents (Connors and Gutnick, 1990; Markram et al., 2004) which has led to intricate electrophysiological characterization schemes for three main neuronal cell-types (regular-spiking excitatory neurons (Exc), GABAergic fast-spiking neurons (FS) and GABAergic non-fast-spiking neurons (NFS)). The electrophysiological characterization which reflects the biochemical composition of the cells (Toledo-Rodriguez et al., 2004) is often done manually by visual observation of the firing patterns or, more systematically, by automatic extraction of a few parameters such as the ratio of the first to the second interspike interval, the minimum voltage of the spike afterpotential, the width of an action potential etc. The definition of these parameters is arbitrary and their relevance for neural information processing questionable. The question arises whether a more principled characterization and classification of the cell types is possible based on the properties affecting the conversion of synaptic inputs into a spike.

In the community of computational neuroscience it has been established over the last 20 years that simplified spiking neuron models are capable of reproducing the variety of firing patterns that have been found in experimental preparations, including delayed spike onset, bursting, strong or weak adaptation, refractoriness, etc (Gerstner et al., 1996; Izhikevich, 2004, 2007; Brette and Gerstner, 2005; Naud et al., 2008; Touboul and Brette, 2009; Mihalaş and Niebur, 2009). All of these models belong to the family of generalized integrate-and-fire models, but vary in the way the standard leaky integrate-and-fire model (Lapicque, 1907; Stein, 1967) is generalized. Features to upgrade the simple integrate-and-fire model include spike after-currents (Baldissera et al., 1976; Gerstner et al., 1996; Benda and Herz, 2003; Izhikevich, 2007; Paninski et al., 2004; Brette and Gerstner, 2005), dynamic threshold (Hill, 1936; Fuortes and Mantegazzini, 1962; Chacron et al., 2003; Jolivet et al., 2006; Badel et al., 2007), smooth spike initiation (Latham et al., 2000; Fourcaud-Trocme et al., 2003; Brette and Gerstner, 2005) and linearized subthreshold currents (Richardson et al., 2003; Izhikevich, 2007). Important questions are then: which of these features are needed for basic cortical computation? How many levels of complexity do we have to add to account for relevant features of cortical dynamics? Is the spike-frequency adaptation mediated by moving thresholds or spike-triggered currents?

To answer these questions several groups used what one could call the Turing test for point-stimulated neurons (Keat et al., 2001; Paninski et al., 2005; Jolivet et al., 2006, 2007; Kobayashi et al., 2009; Gerstner and Naud, 2009): a somatic current is injected into a cortical neuron *in-vitro* while its response is being recorded. The modeler then asks how the model response compares with the neuronal response on data that was not used for optimizing the parameters of the model. This is done both qualitatively (for instance by reproducing the firing patterns (Gerstner et al., 1996; Izhikevich, 2004; Naud et al., 2008; Touboul and Brette, 2009; Mihalaş and Niebur, 2009)) and quantitatively. The quantitative test consists of predicting the correct spike-timing and subthreshold voltage of the real neuron. Obviously, a simplified neuron model is not expected to work across the whole range of stimuli that one can artificially design and apply to electrophysiological experiments. The optimal version of this test would therefore

use for a neuron *in-vitro* a stimulus that is similar (Poliakov et al., 1997; Monier et al., 2008) to the one a real neuron receives in an *in-vivo* situation, so that the activity of the neuron is within a range that can be expected in-vivo (Crochet and Petersen, 2006; Poulet and Petersen, 2008; Gentet et al., 2010). The optimal stimulus will appear as a noisy time-series reminiscent but not identical to the white noise previously used for characterizing the input/output relationship (Bryant and Segundo, 1976; Marmarelis and Marmarelis, 1978; Van Steveninck and Bialek, 1988). We say that the model is 'good enough' if a neutral expert is not able to distinguish the activity of the model from that of the real neuron. We call this the '*Turing Test*' of point-stimulated neuron models in analogy to the test of intelligence in computer programs suggested by Alan Turing over sixty years ago (Turing, 1950). A similar framework was also used to test the validity of neuron models in the visual pathway following light stimulation (Keat et al., 2001; Pillow et al., 2005; Carandini et al., 2007; Pillow et al., 2008)

The aim of this paper is three-fold. Firstly, we present a systematic method for extracting the parameters that control the conversion of synaptic input into spike emission at the level of the soma. The method relies on the separation of the parameters affecting the subthreshold voltage and those affecting the firing threshold and its dynamics. Our method improves previously described methods for extracting spike-triggered currents (Paninski et al., 2004; Jolivet et al., 2006; Badel et al., 2007) and dynamic threshold (Azouz and Gray, 2000; Chacron et al., 2003; Badel et al., 2007). We use this method to fit experimental data from fast spiking GABAergic neurons (FS), non-fast spiking GABAergic neurons (NFS) and excitatory cells (Exc). For each neuron type, we find the simplest model that reproduces the activity of neurons on data that was not used for parameter optimization. The models we extract reproduce the excitability type of GABAergic FS, GABAergic NFS and Exc neurons (Connors and Gutnick, 1990; Tateno et al., 2004; Markram et al., 2004). Moreover above 80% of the spikes can be predicted on average while the mismatch in subthreshold voltage prediction is less than 2 mV. Secondly, we ask which are the features essential for the neuron model to pass the Turing Test for point-stimulated neurons. We consider subthreshold resonance, conductance- versus current-based adaptation as well as current- versus threshold-based adaptation. Our results reveal the importance of adaptation currents and of a moving threshold with time constants that can be as long as hundreds of milliseconds. We find that different types of neurons use moving thresholds and spike-triggered currents differently to mediate refractoriness and spike-frequency adaptation.

Finally, we show that the parameters of the adaptation currents and dynamic threshold can be used for an automatic classification of the electrophysiological traces into three well-separated classes, whereas the passive parameters alone do not contain a sufficient amount of information to do so. We observe that the three neuron types have very different threshold dynamics and that efficient classification can be done using the parameters regulating the dynamics of the threshold.

We expect that applying the automatic fitting method on a larger database could allow an unsupervised classification of the extracted computational properties, which would open the possibility to detect the potential spread of parameters within a given class of neurons and therefore avoid a forced classification if in reality parameters are continuous. Finally, we expect

that our method of parameter extraction once combined with similar results for synapses, dendrites and connectivity patterns will enable us to build network models where neuronal parameters and firing patterns reproduce not only the mean 'typical' firing of different neuron types, but also the spread of firing characteristics within and between classes of neurons.

2.2   Material and Methods

2.2.1   *In vitro* Two-photon Microscopy and Whole-cell Recordings

All animal experiments were carried out under authorisation from the Swiss Federal Veterinary Office. Brains of 17-22 day old GAD67-GFP knock-mice (Tamamaki et al., 2003) were removed and quickly placed into an ice-cold modified ACSF (Bureau et al., 2006) (containing in mM: 110 choline chloride, 25 $NaHCO_3$, 25 D-glucose, 11.6 sodium ascorbate, 7 $MgCl_2$, 3.1 sodium pyruvate, 2.5 KCl, 1.25 NaH_2PO_4 and 0.5 $CaCl_2$). 300 μm oblique slices (parasagittal 35° away from vertical) were cut with a vibrating slicer (Leica VT1000S, Germany) and subsequently transferred into standard ACSF (containing in mM: 125 NaCl, 25 $NaHCO_3$, 25 D-glucose, 2.5 KCl, 1.25 NaH_2PO_4, 2 $CaCl_2$ and 1 $MgCl_2$) aerated with 95% O_2 / 5% CO_2 at 35°C for 15 minutes. Afterwards slices were maintained at room temperature for at least 30 minutes prior to use to allow for recovery from the slicing procedure. GFP-expressing neurons were visualized using a two-photon microscope (Prairie Technologies, USA). Infrared two-photon excitation light of 880 nm was generated by a MaiTai laser (Spectra-Physics, France) and focused into the slice tissue through a 40x 0.8NA water immersion objective (Olympus, Japan). Detection of bandpass-filtered green fluorescence (525 ± 35 nm) was achieved using PMTs above the objective and below the condenser. Infrared light was passed through a Dodt contrast element (Luigs & Neumann, Germany) and detected by an additional PMT to allow creation of a high contrast view of the brain tissue. Whole-cell recordings were carried out at 33°C in standard ACSF. Borosilicate pipettes of 5-7 MΩ resistance were used. The patch-pipette intracellular solution contained (in mM): 135 K-gluconate, 4 KCl, 4 Mg-ATP, 10 Na_2-phosphocreatine, 0.3 Na-GTP, 10 HEPES (pH 7.3, 280 mOsm). A Multiclamp 700A amplifier (Molecular Devices, USA) was used for whole-cell recordings. Data were low-pass Bessel filtered at 10 kHz and digitized at 20 kHz with an ITC-18 acquisition interface (HEKA Electronics, Germany). The measured membrane potential was not corrected for the liquid junction potential.

The bridge balance feature of Multiclamp was not used during the recordings. Access resistance values were in the range of 10-15 MOhm. If there was an increase in access resistance or a drift in the resting membrane potential during the recording, traces were discarded. Moreover background synaptic activity was not blocked (e.g. with CNQX/AP5). Under our recording conditions, miniature and spontaneous EPSPs are present but neurons do not show spontaneous spiking.

Cortical layers 2/3 GABAergic inhibitory neurons were distinguished from excitatory neurons (Exc) by their expression of GFP (Gentet et al., 2010). GFP-expressing GABAergic neurons were further classified into fast-spiking (FS) and non-fast-spiking (NFS) neurons with respect to their action-potential (AP) kinetics upon somatic current pulse injection. An AP half-width

lower than 0.75 ms was used as a selection criterion for GABAergic FS neurons.

2.2.2 Stimulation Protocol: Synaptic-like current

We construct input currents $I_{syn}(t)$ as a weighted sum of six impinging spike trains constructed from independent inhomogeneous Poisson processes (see also (Poliakov et al., 1997)). Three spike-trains are convolved with a mono-exponential filter with time constant of 2 ms mimicking spike arrival at excitatory synapses and summed with weight $w_{1,2,3}$, while the three remaining ones are convolved with a 10 ms mono-exponential filter for the inhibitory spike trains and summed with weight $w_{4,5,6}$. The unitary weights of the PSCs $w_{1,2,3,4,5,6} = \left(\begin{array}{cccccc} 20.00 & 34.14 & 5.86 & -1.60 & -3.89 & -2.51 \end{array} \right)$ are then rescaled by a global factor w_0 that was chosen for each cell individually in order to drive the neuron to a mean firing frequency between 2 and 15 Hz. In our data set w_0 is on average 0.89, 0.65 and 0.72 for the GABAergic FS neurons, the GABAergic NFS neurons and the Exc neurons, respectively. Finally all the Poisson processes shared the same time-dependent intensity (firing rate) which is a concatenation of blocks of 300-500 ms duration each with a constant intensity chosen randomly from a uniform distribution between 0 and 50 Hz. The duration of the blocks was drawn from a uniform distribution (Figure 2.1 *A, B, C*). Note that this procedure produces a colored-noise current with time-dependent mean and standard deviation. We call the time-dependent input constructed by the above procedure a synaptic-like current $I_{syn}(t)$.

This synaptic-like current has the advantage that it produces voltage traces with ISI distributions that cover a wide range of timescales, from a few ms to more than 1 second (see Figure 2.8 *G, H* and *I*). This enables the extraction of threshold mechanisms that span different timescales, from milliseconds to seconds.

One minute of this synaptic-like current is injected in the cortical neurons repeatedly, interrupted by silent periods of 10 seconds. Each independent injection is called a 'repetition'. Note that in each repetition the cell received exactly the same time course of synaptic-like current which enables us to study peri-stimulus time histograms (PSTH) and reliability of neuronal spiking. In order to compare experimental results with our models, we used the first 30 seconds of all repetitions for fitting and reserved the last 30 seconds for testing the performance of the models. These two subsets of the data are called training and test sets, respectively.

2.2.3 Other Stimulation Protocol

To assess the robustness of our fitting procedure on surrogate data, we also test it on 4 different stimulation paradigms applied only to model neurons but not to real neurons. First we use a gradually increasing ramp of current of 30 seconds. Second we construct an input current as a series of 300 ms step current interleaving with 200 ms of silence, with increasing intensities. Third we used as a stimulation current a white noise with 0 mean that lasts for 30 seconds. Finally we construct a 30 seconds long input current made of colored noise, generated according to an Ornstein-Uhlenbeck process with correlation time constant of 4 ms.
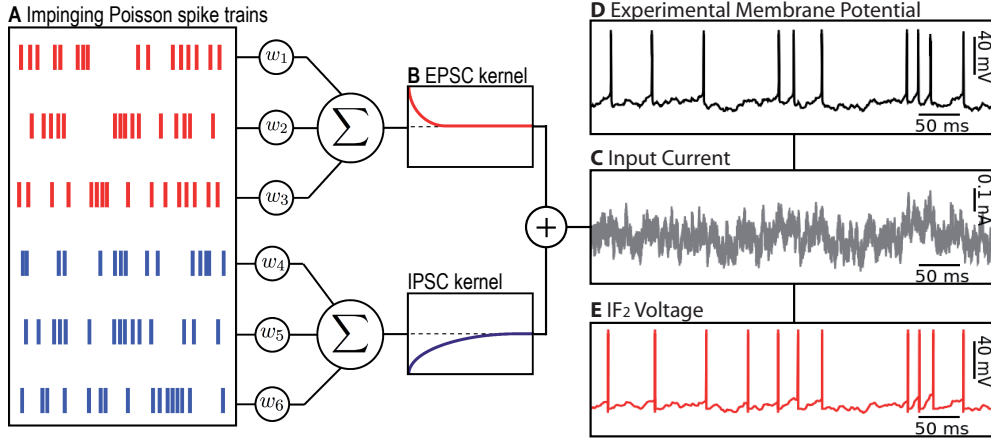
Figure 2.1: **Stimulation protocol and dynamics of an IF model.** *A*: Six spike trains are generated by an inhomogeneous Poisson process with piecewise constant rates. Rates are switched simultaneously for all input spike trains. The rate changes at intervals chosen randomly between 300 - 500 ms. *B*: The excitatory spike trains are convolved with an excitatory postsynaptic current (EPSC) kernel that has a time constant of 2 ms to mimic AMPA-receptor dynamics and the inhibitory spike trains are convolved with an inhibitory postsynaptic current (IPSC) kernel with a time constant of 10 ms to mimic GABA-receptor dynamics. *C*: The six current traces are combined in a weighted sum, with weight w_1 to w_6 to produce the final input current. The weights are chosen to drive the neuron to a mean firing frequency between 5 and 15 Hz (see panel *D*), but in a segment of 100 ms the momentary rate can be above 30 Hz. *D*: Experimental membrane potential as a function of time of a GABAergic FS neuron stimulated with the input current in panel *C*. *E*: An example of a model voltage trace generated by the injection of the input current from panel *C*. Here the model has $N = 2$ spike-triggered currents (IF$_2$).

All the parameters of these currents are chosen so that the resulting input current produced an averaged firing frequency of approximatively 15 Hz.

2.2.4   Performance Measurements

Since we are assessing the performance on the test set, the performance of the model will not increase by merely increasing the number of parameters because over-fitting would occur on the training set and lower the performance on the test set. Two distinct criteria are used to evaluate the performance of our IF models: (i) the precise spike time prediction and (ii) the subthreshold voltage prediction.

Spike Train Similarity

Neurons, as well as stochastic models, have some trial-to-trial variations due to intrinsic noise. In neurons, this intrinsic noise is mainly due to channel noise and spontaneous synaptic events (Faisal et al., 2008). To quantify the spike time prediction we used a method that corrects the bias due to the small number of available repetitions (Naud et al., 2011). We first use our optimal stochastic model to generate $R_m = 1000$ spike-time predictions. The

next step is to compute a quantity between zero and one that measures how well the set of R_m model spike trains matches the set of R_r experimental spike trains, where R_r is the number of repetitions available for the specific cell (lower index r for real neuron). To do so, we first count the total number of spikes of the model that fall within +/- 4 ms of a spike in the recorded spike train and average the count over all repetitions. We call the resulting raw measure of comparison between model (lower index m) and real neuron (lower index r): n_{mr}. Next we count the average number of coincidences between distinct repetitions of the model spike trains and average the results across all available repetitions. We call this quantity n_{mm}. Similarly, n_{rr} is the analogous quantity evaluated over the available repetitions recorded in the real neuron. Finally, we combine these numbers into the measure:

$$M_d^* = \frac{n_{mr}}{\frac{1}{2}(n_{mm} + n_{rr})} \tag{2.1}$$

which is an estimate of the fraction of spikes that are correctly predicted with a precision of +/- 4 ms. It can be shown that this quantity corresponds to a normalized distance between PSTHs (Naud et al., 2011).

Subthreshold Voltage Trace Similarity

The subthreshold voltage prediction is evaluated using the root mean square error on the voltage (RMSE) defined by

$$\widetilde{\text{RMSE}} \quad = \quad \sqrt{\frac{1}{T_1} \int_{\psi_1} \left(V_{\text{ref}}(t|I) - V_{\text{predicted}}(t|I,\theta,\{\hat{t}_{\text{ref}}\}) \right)^2 dt} \tag{2.2}$$

where $V_{\text{ref}}(t|I)$ is the recorded voltage given an input current I, $V_{predicted}(t|I,\theta,\{\hat{t}_{\text{ref}}\})$ is the voltage predicted by a model with the set of parameters θ and the same input current. The index $\{\hat{t}_{\text{ref}}\}$ indicates that for the voltage comparison we force spikes at exactly the same time as in the recorded voltage trace. In other words, we ask: how close is the voltage of the model to that of the data, given the input and the firing times in the recent past. The squared error is integrated over a subset ψ_1 of the available data defined in the Appendix. T_1 is the total time for which the squared error is considered, $T_1 = \int_{\psi_1} dt$. Forcing the spikes at the observed spike times disentangles the subthreshold voltage prediction from the spike time prediction.

To estimate the RMSE solely due to intrinsic noise, we compute the root-mean-squared error between repetitions only on the subset of data ψ_4 (defined in the Appendix), RMSE_{ψ_4} which is restricted to voltage recordings sufficiently far away from the spikes to avoid the effect of adaptation currents due to spikes emitted at different times across repetitions (Fellous et al., 2004). RMSE_{ψ_4} is clearly an overestimation of the true subthreshold fluctuations because it still contains some long-lasting spike-triggered effects. Nevertheless it can give some insights on how well our models have to predict the subthreshold voltage. To quantify the ability of the models to replicate subthreshold voltage fluctuations we use the normalized 'Root

Mean Square Error Ratio': RMSER $= \frac{\overline{\text{RMSE}}}{\text{RMSE}_{\psi_4}}$, so that RMSER ≈ 1 for a good reproduction of the subthreshold voltage and RMSER > 1 for inaccurate reproduction.

2.3 Results

We stimulated an experimental neuron with a time-dependent input current that mimics stochastic spike arrival (see Figure 2.1 and Methods) and drives the neuron through episodes of high and low firing rates. We adapted parameters of generalized integrate-and-fire models so as to explain the data and predict spike times and subthreshold voltage for novel sitmuli not used during parameter optimization. The results section is organized as follows. First, we describe the model class and parameter extraction strategy. Second, we quantify the performance of the extracted neuron model and dicuss differences between different cell types. Third, we perform automatic classification of the different neuron types based on the extracted parameters.

2.3.1 Model Dynamics

In order to describe subthreshold voltage and spike generation we studied a family of integrate-and-fire models augmented with a spike-triggered current $\eta(t)$, a moving threshold $\gamma(t)$ and stochastic spike emission via escape noise.

Subthreshold Voltage Dynamics

The somatic voltage is deterministic and follows the differential equation:

$$C\dot{V}(t) = -g_l(V(t) - E_l) + \sum_{\{\hat{t}_j\}} \eta(t - \hat{t}_j) + I(t) \tag{2.3}$$

C, g_l and E_l are the passive membrane parameters of the neuron: the membrane capacitance, leak conductance and the resting potential, respectively. $I(t)$ is a time-dependent input current. Adaptation of the subthreshold membrane potential is mediated by an adaptation current η which is triggered at the firing time $\hat{t}_j$; contributions from previous spikes in the spiking history accumulate by summation of the contributions of $\eta(t - \hat{t}_j)$ over all spike times $\{\hat{t}_j\} = \{\hat{t}_1, \hat{t}_2, \ldots\}$. By convention, the current η in Eq. 2.3 is depolarizing when its amplitude is positive and hyperpolarizing otherwise. A short hyperpolarizing current mediates refractoriness, while a current with a long time constant leads to spike frequency adaptation because the effect of multiple spikes can accumulate. Even though the reset of the voltage after a spike is equivalent to a short hyperpolarizing pulse, we use an explicit reset that is discussed below. We approximate the adaptation current $\eta(t - \hat{t}_j)$ sometimes by a single exponential (IF$_1$) or by two exponentials (IF$_2$), or we keep the time course arbitrary (IF$_\eta$).

Stochastic Spike Emission

The deterministic voltage dynamics of Equation 2.3 is integrated so as to yield a voltage $V(t) = V(t|I, \theta, \{\hat{t}_j\})$ which depends on the input current $I(t')$ for $t' < t$; on the past firing times $\hat{t}_1, \hat{t}_2, \hat{t}_3, \ldots < t$, as well as the set of parameters (denoted as θ) chosen for the model. This deterministic voltage is the central variable for the stochastic spike generation. Using the escape-rate picture (Plesser and Gerstner, 2000; Gerstner and Kistler, 2002; Paninski et al., 2005), the conditional probability intensity of emitting a spike is a nonlinear function of the instantaneous distance from the voltage threshold. More precisely the stochastic spiking process follows an inhomogeneous point process with conditional firing intensity $\lambda(t|V, V_T)$ given by:

$$\lambda(t|V, V_T) = \lambda_0 \exp\left(\frac{V(t) - V_T(t)}{\Delta V}\right) \tag{2.4}$$

where λ_0 has units of s^{-1}, so that $\lambda(t)$ is in Hz, $V(t)$ is the membrane potential, $V_T(t)$ is the voltage threshold and ΔV describes the sharpness of the exponential function. In principle, any function of $V - V_T$ would be possible, but it was shown previously that the exponential function explains experimental data well (Jolivet et al., 2006). Note that the value of λ_0 can be chosen arbitrarily since a scaling $\lambda_0 = a\lambda_1 = \lambda_1 \exp(\log a)$ can be compensated in Eq. 2.4 by a shift of the threshold V_T by $\Delta V \log(a)$.

When a spike is emitted the numerical integration is stopped and after a short absolute refractory period T_{refr}, V is reset to E_{reset}. This voltage reset is typical for a large class of Integrate-and-Fire (IF) models.

Moving Threshold

The voltage threshold $V_T(t)$ can be either a constant threshold, with $V_T(t) = V_0$ or a time-dependent sliding threshold that implements an additional source of refractoriness (Gerstner and Kistler, 2002; Chacron et al., 2003; Badel et al., 2007). In our model, the dynamic threshold is a cumulative function of previous spike times:

$$V_T(t) \quad = \quad V_0 + \sum_{\{\hat{t}_j\}} \gamma(t - \hat{t}_j) \tag{2.5}$$

where V_0 is the threshold baseline, $\{\hat{t}_j\}$ the set of spike times that were emitted before t and $\gamma(t)$ is the spike-triggered shift in voltage threshold (see Appendix A3 for details). When a dynamic threshold $V_T(t)$, as specified in Eq. 2.5, is used instead of the constant threshold, we denote it with '+dyn'. For example, $IF_2 + \text{dyn}$ is an IF model with two exponential spike-triggered currents and the dynamic threshold defined by $\gamma(t)$.

2.3.2 Fitting Procedure

To extract all the parameters of the neuron model a four-step procedure is applied. The main steps of the method are illustrated in Figure 2.2. For the details of the fitting procedure and the definition of appropriate subsets of the available data see Appendix.

Step 1. We measure the average spike shape by computing the spike-triggered average voltage (Jolivet et al., 2004). The refractory period T_{refr} and reset potential E_{reset} are defined by the value of the minimum of the after hyper-polarization (AHP), see Figure 2.2 *B*, left panel. For Excitatory neurons the AHP trace does not have any local minimum, and we arbitrarily chose $T_{\text{refr}} = 4$ ms, and fixed E_{reset} to the corresponding voltage at this moment. As long as it remains short, the exact value of T_{refr} has no impact on the quality of the fit.

Step 2. We extract from the experimental voltage traces the first-order estimate of the time derivative using the finite difference: $\dot{V}_t = (V_{t+1} - V_t)/dt$. Here, V_t denotes the binned voltage time-series as obtained from the recordings, using a bin size dt of 0.05 ms. We use the data set ψ_2 where spikes are removed (see Appendix C) so as to optimize the parameters by minimizing the sum square error between the observed voltage time-derivative $\dot{V}_t$ and that of the model. The integrate-and-fire model given in Eq. 2.3 with $\eta(t)$ expressed as a linear combination of rectangular basis functions is linear in the parameters and it is straightforward to obtain the optimal set of parameters with a multi-linear regression on the derivative of the voltage ((Weisberg, 2005; Paninski et al., 2005; Huys et al., 2006); see Appendix A1 and D1 for details).

Step 3. To extract the cumulative dynamic threshold $\gamma(t)$ from the data, we maximize the likelihood of generating the experimental spike train by our model. The log-likelihood for a spike train can be written in terms of the probability p_t of observing no spike in an experimental time bin by using Bayes theorem recursively in time (Paninski, 2004):

$$\log L(\vec{\theta}_3) = \sum_{\{\hat{t}_j\}} \log(1 - p_t) + \sum_{\tilde{\psi}_2} \log(p_t) \tag{2.6}$$

where the set of spike times $\{\hat{t}_j\}$ is taken to be 0.5 ms before the peak of the spike and $\tilde{\psi}_2$ contains segments of the voltage trace with the spike times removed (see Appendix C). The optimal set of parameters $\hat{\theta}_3$ is obtained by convex maximization of the log-likelihood function with respect to the parameters (Paninski et al., 2005). The probability to spike $(1 - p_t)$ or not to spike p_t is calculated from the parameters of the model via Eq. 2.4, see Appendix A3 and D2 for details.

Step 4. At this point all the parameters have been extracted, but in order to obtain an optimal spike time prediction in terms of the spike train similarity measure M_d^* (see Methods Section 'Spike Train Similarity'), we recompute the baseline threshold V_0 so that it

maximizes $M_d^*(V_T)$. To do so we find the parameter V_0 that maximizes M_d^* through an exhaustive search over a large range of parameters V_0.
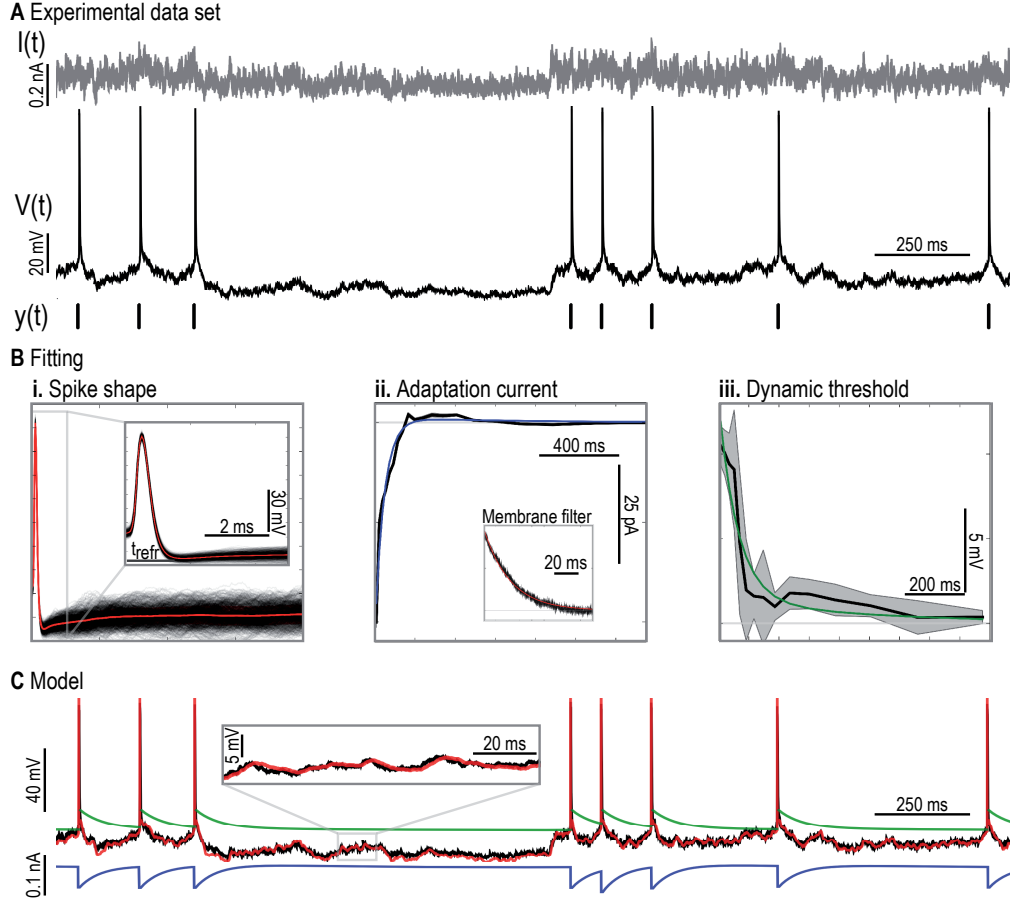
Figure 2.2: **Fitting protocol.** *A*: Experimental data set, injected current $I(t)$ (top panel), recorded voltage trace $V(t)$ (middle panel) and extracted spike times $y(t)$ (bottom panel). *B*: Example of extracted parameters. (i) All the spikes are aligned (black) and averaged (red) to obtain the spike shape. The inset shows the first 5 ms on an extended time scale. (ii) Adaptation current η (black) and a double exponential fit (blue). Inset, membrane filter extracted with a Wiener-Hopf optimal filter method (black) and single exponential fit (red). (iii) Dynamic threshold γ (black) and a double exponential fit (green), the grey area represents one standard deviation. *C*: An example of a model voltage trace (IF$_2$ + dyn) produced by the injection of the input current $I(t)$ and the corresponding experimental voltage. Experimental data (black), predicted voltage trace (red), voltage threshold (green) and adaptation current (blue). The inset shows the subthreshold voltage over 100 ms in a region far away from any spikes.

2.3.3 Efficiency and Accuracy of the Fitting Method on Surrogate Data

Before turning to experimental data obtained from cortical neurons, we checked the consistency of our parameter extraction method on artificially generated data. We first generated 60 seconds of surrogate data from an IF model augmented with a spike-triggered current

decaying exponentially with two time constants and a dynamic threshold ($IF_2 + \texttt{dyn}$) and used our fitting method to retrieve its parameters. Thus we used an $IF_2 + \texttt{dyn}$ model to fit data from another $IF_2 + \texttt{dyn}$ model. The error in the estimated parameters and thus the prediction performance of the model depends on the amount of data used for fitting.

Figure 2.3 shows how the fitting quality evolves as a function of the amount of data used for parameter extraction. We observe that the voltage prediction of the fitted model becomes better when a larger amount of data is used (see Figure 2.3 *A* and *C*). But even with a small amount of data (1 second), the predicted voltage is relatively accurate, producing a RMSE of 0.43 mV (the RMSE obtained with 15 seconds of data is 0.26 mV). The spike time prediction also depends on the size of the training set, leading to a spike train similarity M_d^* of 0.79 with 1 second of data while $M_d^* = 0.99$ when 15 seconds are used. Furthermore the relative error ϵ in the parameter estimate (computed according to $\epsilon = \langle |\frac{\theta - \hat{\theta}}{\theta}| \rangle$, with θ the true parameters and $\hat{\theta}$ the extracted parameters) also shows a strong decrease as a function of training set size, from $\epsilon(1s) = 0.13$ to $\epsilon(15s) = 0.03$. Thus with less than 20 seconds of data our method enables us to retrieve the reference parameters to a high degree of accuracy (Fig. 2.3).

To be sure that parameters have reached their steady-state, we systematically compare RMSE, M_d^* and ϵ at each training set size. We find that if less than 14 seconds of recordings are used (Figure 2.3 *C*, shaded area) parameters are significantly different from their steady-state value as quantified by ϵ (two-sample t-test, $\alpha = 0.05$). So, when our reference model is fitted to itself, 14 seconds of recordings with 10 Hz firing frequency are sufficient to obtain a good fit in terms of RMSE, M_d^* and ϵ.

Since fitting a model to data (model extraction) is more difficult than fitting to itself (model identification), for the fits to real neurons (as done in the next subsection) we always use a training set of at least 20 seconds and a separated test set that contains at least 100 spikes with firing frequencies from 0.1 to 40 Hz.

We checked that the fitting procedure works for other stimulation protocols. To study this we used the stimulated $IF_2 + \texttt{dyn}$ model with various kinds of widely used currents: series of steps, ramp, white noise and colored noise. We tested the fitted models on a test set made with the synaptic-like current. The results are shown in Table 2.1. We conclude that step currents or synaptic-like currents are more informative and enable a more reliable parameter extraction than ramp currents and (white or colored) noise injection. This can be explained by two facts. First, constant mean noise yields models with almost constant firing rate. The produced ISI distributions do not span a sufficient range of timescales to allow a fair extraction of the threshold parameters that potentially act on long timescales. Second, since we use a training set of fixed length, the distribution of the spike times (i.e. the spiking pattern) plays an important role in the total amount of available data for the parameter extraction. Indeed, for the estimation of the model parameters we have to remove a period of time around each spike, thus there is more available data when the model fires irregularly with long period of silence interleaved with short period of high activity (which is the case with synaptic-like current and series of steps) than when the model fires regularly (white and colored noise). Both facts together explain why parameter extractions fails with white noise stimuli with constant
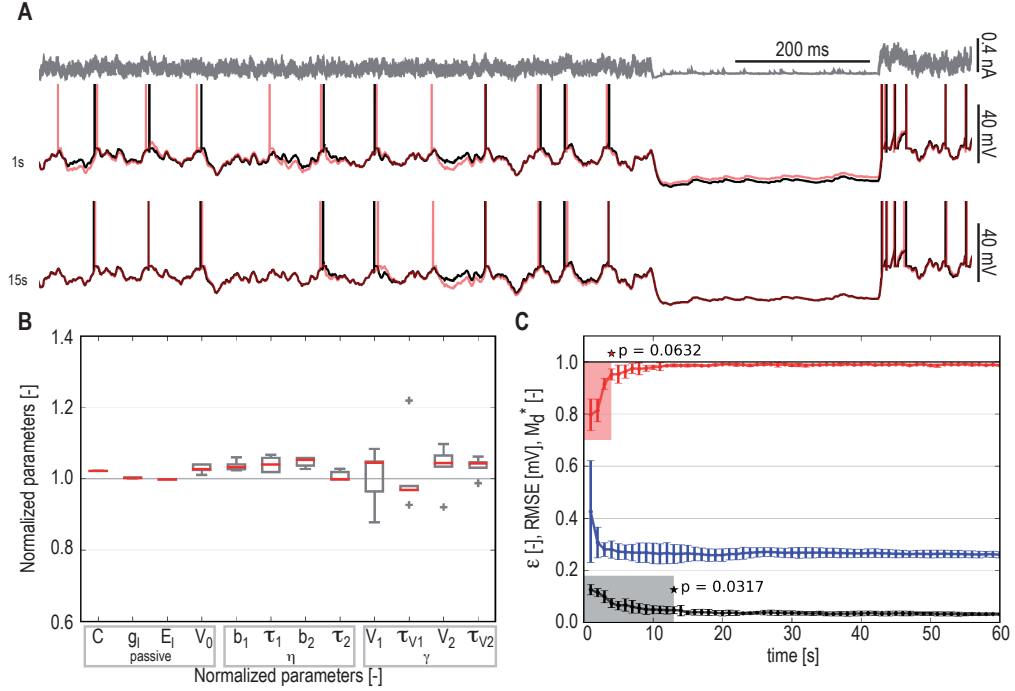
Figure 2.3: **Assessment of the fitting procedure by fitting a model to a model.** *A*: Upper panel: Example of injected current used as part of the test data set. Lower Panel: Corresponding voltage trace of the reference data (black) and a modeled voltage trace (red), the upper traces are obtained with a training set of 1 second and the lower traces with a training set of 15 seconds. *B*: Boxplot of the normalized parameters extracted with a training set of 15 seconds. A perfect fit of the reference parameters would lead to normalized parameters equal to units. All the parameters are within 5% of their target value. Crosses denote outliers. *C*: The spike train similarity measure M_d^* (red) as a quality measure of spike time prediction, RMSE (blue) as a quality measure of subthreshold voltage prediction, and the relative error in the parameters estimates ϵ (black) as a function of the size of the training set, error bars are one standard deviation. The shaded areas correspond to training set size insufficient to reliably extract the optimal parameters. Stars denote last significant difference between M_d^* (or ϵ) at a given training set size and the final values obtained with the full training set (two sample t-test, $\alpha = 0.05$).

mean and standard deviation. The problem occurring with the ramp is of another nature. Indeed the ramp stimuli do not carry enough information to allow a fair parameter extraction: the time-derivative is almost constant, which is insufficient to evaluate the membrane time constant τ and the passive conductance g_l.

2.3.4 Quantitative and Qualitative Accuracy of Fitted Models on FS, NFS and Exc

The accuracy of the fitting method is summarized in Fig. 2.4 for exemplars of FS, NFS and Exc neurons. With voltage prediction consistently below the intrinsic RMSE of the data (estimated across several repetitions, see 'Material and Methods'), and spike time prediction above a spike train similarity of $M_d^* = 0.78$ we conclude that the simple neuron models, in combination with

Type of Stimuli	RMSE	M_d^*	Relative Error
	$[mV]$	$[-]$	$[-]$
ramp	0.15	0.81	0.14
step	0.42	0.97	0.04
white noise	1.77	0.90	0.11
colored noise	0.26	0.88	0.12
synaptic-like noise	0.29	0.98	0.04

Table 2.1: **Evaluation of the fitting procedure on different common types of stimulation.** We evaluate the ability of our methods to extract parameters from various types of stimulation in the training set. After parameter extraction the model is evaluated on a test set consisting of synaptic-like current as defined in section 'Stimulation Protocol: Synaptic-like current'. The evaluation criteria are: the RMSE on the voltage, the M_d^* factor as a quality measure for spike time prediction, and the relative error in the parameter estimates. Step current and synaptic-like current are the most informative stimulation protocols.

our fitting method accurately model the three different cell types.

Our neuron models extracted by the above procedure are able to reproduce the typical behavior of the different cell types in terms of their firing patterns in response to step currents. To show this we reproduce an experiment done by (Tateno et al., 2004), where the authors stimulate GABAergic FS and Exc neurons with step currents of 1 second at various amplitudes and classify cells as a function of their frequency-intensity curves (f-I Curve). Using this method the authors conclude that GABAergic FS neurons have a step in the f-I curve (Type-II excitability) whereas Exc neurons exhibit a smooth f-I curve (Type-I excitability).

Figure 2.5 *A, B* and *C*, which have been generated using our optimal models for GABAergic FS, GABAergic NFS and Exc neurons, are analogous to Figure 4 of the paper of (Tateno et al., 2004). Our model of FS neurons is of Type-II exhibiting a minimal frequency at a critical input amplitude, with f_c = 15.5 Hz (when f_c is computed as the inverse of the first interspike interval) and a steady-state critical frequency of 5.45 Hz. When constant currents are used, smaller frequencies are possible but the f-I curve always exhibits a finite jump. The critical frequency and emergence of Type-II behaviour can be traced back to the facilitating component of the effective moving threshold (see inset of Figure 2.5 *A* and Discussion for details). If the amplitude of the stimulation current is sufficient to evoke a spike, then the facilitating part of $\eta(t)$ causes repetitive firing at non-zero frequency that is maintained as long as the stimulating current is maintained. For NFS and Exc models we obtain a smooth transition of the f-I curve between silence and repetitive firing, which is the behavior of the Type-I neurons consistent with experiments of (Tateno et al., 2004). Links between the type of f-I curve and the bifurcation theory have been previously established (Izhikevich, 2007; Naud et al., 2008). These relations are discussed in the Section 'Links with Bifurcation Theory' of the Discussion. Finally Figure 2.5 *D-F* provides examples of firing patterns from our optimal models for each cell type, analogous to the examples provided in Figure 5 of (Tateno et al., 2004).

We conclude that the fitted models predict quantitatively the subthreshold voltage and the spike times as well as qualitatively features such as the firing patterns and the type of excitabil-
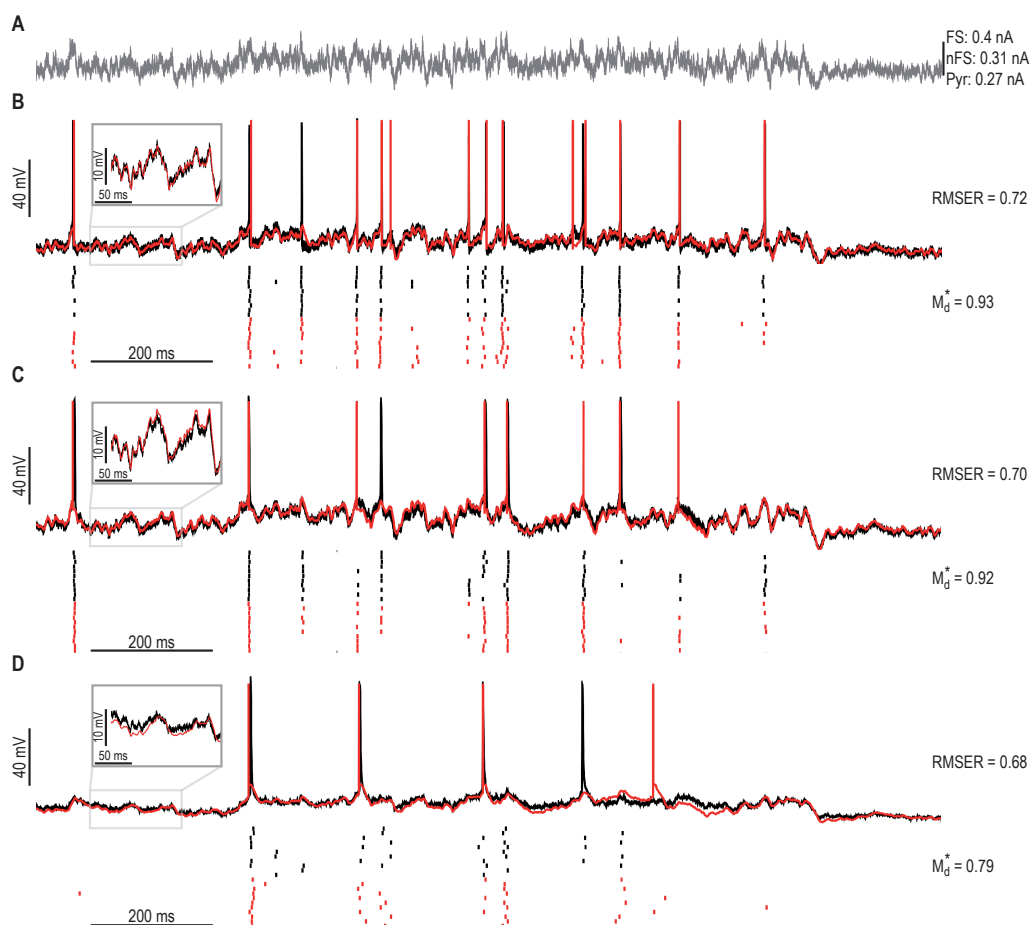
Figure 2.4: **Examples of voltage traces and spike train predictions for the 3 neuron classes.** *A*: Injected current. The waveform of the injected current is the same for the 3 neurons but we rescale it (note the different scale bars for each neuron) to achieve an average firing frequency between 5 and 15 Hz when averaged across 30 seconds of stimulation, segments of 200 ms can have much higher firing rates, see 'Material and Methods' for details. *B*: Upper panel: left, experimental voltage trace (black) and modeled voltage trace (red) for a GABAergic FS neuron. Inset: zoom on 150 ms of subthreshold voltage. Subthreshold voltage prediction is quantified by the measure RMSER (see Methods). Lower panel: Raster plot of the emitted spikes during 11 repetitions for the experimental data (black) and for the model prediction (red). Spikes that occur reliably in the neuron are reliably reproduced by the model. Spike timing prediction is quantified by the measure M_d^*. *C*, as in *B* but for a GABAergic NFS neuron. *D*, as in *B* but for an Excitatory neuron.

ity.

2.3.5 Essential features for Subthreshold Voltage Prediction

The membrane filter $\kappa(t)$ (described in the Appendix Section 'Model-free Extraction of Membrane Filter') for each neuron type is well approximated by a single exponential function (Figure 2.6*A-C*). Since the extraction method of the filter (see Appendix B) is flexible enough to extract resonances, or multiple exponentials, the absence of resonances and the presence of a
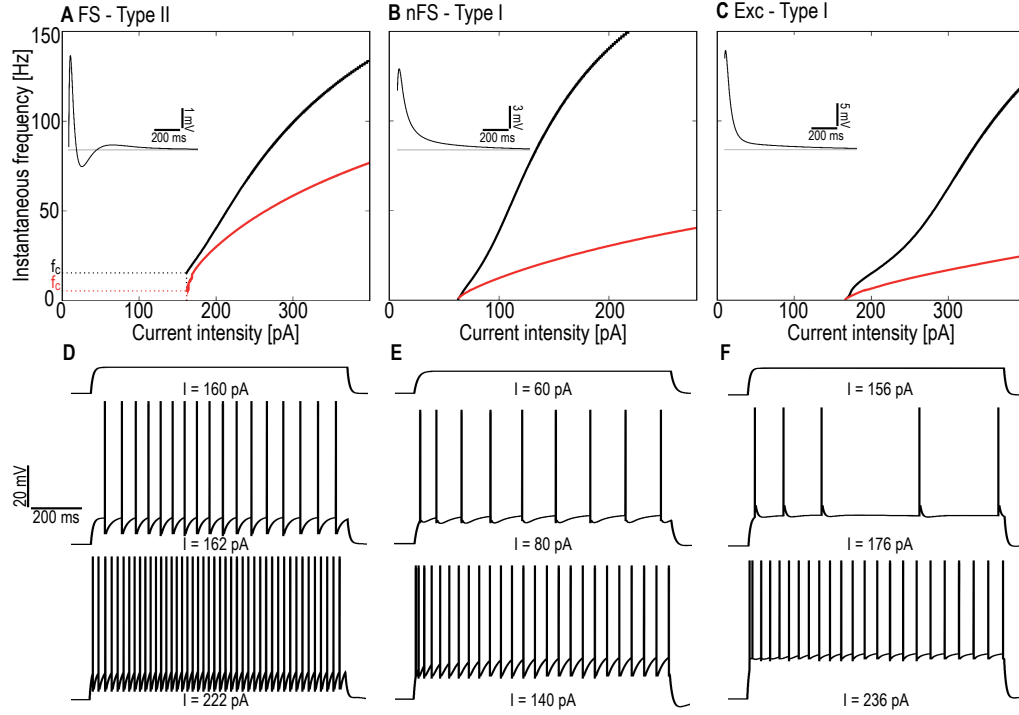
Figure 2.5: **Instantaneous firing frequency of models as a function of the intensity of a step current, (f-I curve).** *A*: f-I curve for a model of GABAergic FS neuron: black trace - inverse of the 1st interspike interval; red trace - steady state. Since there is a non-zero onset firing frequency f_c (critical frequency) at the threshold value of the step current amplitude, the FS model has a type-II excitability according to the definition of (Tateno et al., 2004). Inset: the effective moving threshold in voltage η_v as extracted by our method and fully described and discussed in Section 'Effective Moving Threshold'. The blue horizontal axis is at 0 mV. Around 100 ms after a spike, the effective threshold is lower than its resting value so that generation of a further spike is facilitated. *B*: As in *A* but for a model of a GABAergic NFS neuron. Note the smooth transition between quiescence and spiking activity, so the NFS model is type-I. *C*: As in *B* but for a model of an Exc neuron. Here again the Exc model is a type-I model. *D-F*: Examples of different firing pattern of the three models, FS (*D*), NFS (*E*) and Exc (*F*) neurons, for three different intensities of the step current.

single timescale shows that voltage-dependent subthreshold currents (Richardson et al., 2003; Izhikevich, 2007) are small and can be neglected. Moreover it follows from this finding that, for the neuron types studied here, subthreshold resonance is not the most important factor for accurate prediction of the voltage traces. Specific spike-triggered currents, however, are necessary to reproduce the subthreshold voltage.

The spike-triggered current $\eta(t)$ corresponds to the stereotypical current that flows into the neurons after a spike. After the onset of the spike, the dominant features of the spike-triggered currents consist of (i) the current that produces the spike (i.e. the spike shape), (ii) a short refractory current that follows the end of the AP (just a few milliseconds after the spike onset) and (iii) a long cumulative current that can adapt the spike-frequency of the neurons. Here, we consider only parts (ii) and (iii) since these currents are the most important part for the processing of information done by the neuron (Koch, 1999; Hille, 1992; Jolivet et al., 2007). To

investigate the shape of the spike-triggered currents, we measure the cumulative adaptation current $\eta(t)$ for each neuron and group these by cell type. Figure 2.6 *D-F* shows the mean adaptation current $\eta(t)$ (black lines), one example for each neuron class.

Once we have $\eta(t)$ in terms of rectangular basis functions, we want to test whether a simpler model made of a combination of a small number of exponential processes also works. To this end we fit N exponentially decaying functions with different amplitude b_i and time constant τ_i on the extracted $\eta(t)$. An integrate-and-fire model made with N exponential adaptation currents will be called IF_N, so that IF_2 means an integrate-and-fire model with two adaptation currents. A model where the shape η comes from the raw fit of η is called IF_η. We explore the voltage prediction in terms of RMSER mentioned in Materials and Methods, where the lower the RMSER, the better the prediction. A RMSER < 1 is possible, because we systematically overestimate the intrinsic $\widetilde{\text{RMSE}}$. Here we investigate models with static thresholds, since the dynamic threshold has no impact on the predicted voltage when the spikes of the model are enforced at the correct spike times.

Figure 2.6 *D* shows the average spike-triggered current of the 9 GABAergic FS neurons. We observe that this spike-triggered current has two main parts, a strong and fast hyperpolarization that prevents repetitive firing during the first 40 ms, followed by a weaker but longer depolarization that lasts for 350 ms. This resonance is distinct from strictly subthreshold (resonating) membrane currents (Hutcheon and Yarom, 2000) since, as discussed above, no resonance was observed in the membrane filter $\kappa(t)$. Note that the shape of the spike-triggered current is similar to the feedback kernel of the FS neurons observed in (Tateno and Robinson, 2009). The time course $\eta(t)$ of the spike-triggered current can be well approximated by a double exponential decay (IF_2 with $b_1 = -111.61$ pA, $\tau_1 = 36.86$ ms and $b_2 = 72.64$ pA, $\tau_2 = 61.76$ ms). The membrane potential prediction also shows that $N = 2$ time constants are necessary and sufficient for optimal RMSER (Fig. 2.6 *G*).

The NFS GABAergic neurons show a simpler spike-triggered current that only mediates hyperpolarization, and which can be fitted with a single exponential function (IF_1 with amplitude and time constant $b_1 = -29.02$ pA, $\tau_1 = 34.58$ ms (figure 2.6 *E*, blue trace)). This current produces the relatively weak adapting behavior of the GABAergic NFS neurons, characteristic of their firing patterns (Kawaguchi and Hama, 1987). The membrane potential prediction also shows that a single time constant ($N = 1$) is necessary and sufficient for optimal RMSER (Fig. 2.6 *H*).

Excitatory neurons have a stronger and longer adaptation current $\eta(t)$ (Fig. 2.6 *F*) than the GABAergic NFS and the GABAergic FS cells, which mediates the regular spiking (accommodating) behavior of these cells. Again this current is well approximated with a mono-exponential function, with $b_1 = -48.35$ pA, $\tau_1 = 44.89$ ms. Moreover we observe more variability in $\eta(t)$ across individual cells for Exc neuron than for the two other groups. The membrane potential prediction also shows that a single time constant ($N = 1$) is necessary and sufficient for optimal RMSER (Fig. 2.6 *I*).

From these results, we conclude that the shape and dimensions of the adaptation current $\eta(t)$ are cell-type specific. Moreover, we observe that $\eta(t)$ in GABAergic NFS and Exc differs only by their time scale and amplitude whereas $\eta(t)$ in GABAergic NFS and Exc have a shape

distinct from $\eta(t)$ in GABAergic FS. We also notice that independent of the neuron type, spike-triggered currents extend for a few hundred milliseconds, so that due to the cumulative effect, the spike-triggered current influence the spike-frequency adaptation of the neurons on long timescales. This suggests that adaptation currents might mediate some aspect of cell-type specific behavior (i.e. firing patterns).

In summary we found that (i) the adaptation currents of different neuron classes reflect their typical firing behavior (see Figure 2.5), (ii) adaptation currents act on multiple timescales (FS: 37 and 62 ms, NFS: 35 ms, Exc: 45 ms) and (iii) NFS and Exc have strictly hyperpolarizing currents (leading to spike-frequency adaptation), but FS have both hyperpolarizing and depolarizing currents. From these results it is clear that spike-triggered currents can cause different types of spike-frequency adaptation. However some others mechanisms can also contribute to adaptation such as a fatigue of action potential (AP) initiation mechanisms (Kobayashi et al., 2009; Benda et al., 2010). This is discussed in the next section.

In the previous paragraphs, we discussed the importance of spike-triggered currents. However we know that these mechanisms are mediated by a spike-triggered change in conductance rather than current (Schwindt et al., 1988b,a). To address this issue we fit spike-triggered conductances instead of spike-triggered currents and look at the magnitude of the improvements that follow (see Appendix A2 and D1 for a description of the conductance-based spike-triggered adaptation).

Figure 2.7 *A* shows the movement of the cumulative change in conductance η_{cond} following each spike for excitatory neurons. The $R\tilde{M}SE$ depends on the reversal potential E_{rev} and shows a minimum at $\hat{E}_{\text{rev}} = -51.89$ mV (Figure 2.7 *B*). Note that E_{rev} could be attributed to the reversal potential of potassium since most of the spike-triggered currents are mediated by potassium ion channels. However the high value we found indicates that E_{rev} reflects a mixed ion reversal, which in addition to potassium, also includes sodium and calcium.

The shape of the spike-triggered conductances η_{cond} is more difficult to interpret than the standard spike-triggered current η, because of its dependency on the reversal potential E_{rev}. In fact, the effect of η_{cond} on voltage depends on the instantaneous difference between the actual membrane potential and the reversal potential. Furthermore one can observe that given the mean voltage reset $E_{\text{reset}} = -35.56$ mV of the Exc neurons – that is above E_{rev} – the effect of the spike-triggered conductance after a spike is to hyperpolarize the membrane potential and thus η_{cond} also mediates spike-frequency adaptation.

Figure 2.7 *C* and *D* shows the averaged RMSER of voltage prediction as well as the spike train similarity measure M_d^*, for the three cell types and with the two model variants, IF_η and $\text{IF}_{\eta_{\text{cond}}}$. One can observe that conductance-based adaptation does not lead to any significant improvements in terms of spike trains similarity measure M_d^* and the subthreshold voltage prediction RMSER (two sample t-test, $p > 0.2$ for M_d^* and $p > 0.07$ for RMSER). Thus we conclude that conductance- or current-based spike-triggered events make equally valid models.
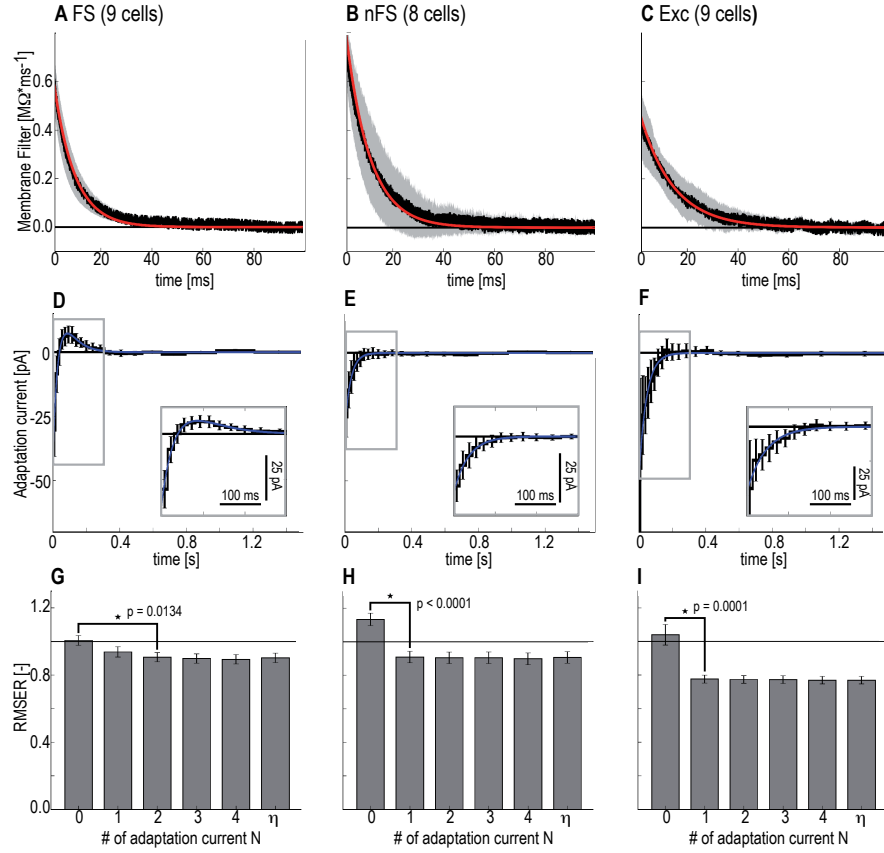
Figure 2.6: **Essential Model Features for Subthreshold Voltage Prediction in GABAergic FS, GABAergic NFS and Exc neurons.** *A*: Membrane filter κ extracted with the Wiener-Hopf method individually for each GABAergic FS cell (9 cells) are averaged to obtain the mean membrane filter of the GABAergic FS neurons (black) and its standard deviation (grey area). A single exponential (red) is fitted on the mean κ. A single exponential is sufficient to approximate the membrane filter and no resonance is present in any of the 9 GABAergic FS cells or the 8 GABAergic NFS (*B*) or the 9 Exc neurons (*C*). *D*: The adaptation current η extracted individually for each Fast Spiking GABAergic neuron (9 FS cells) is averaged to obtain the mean η current (black). The error bars represent one standard deviation. Note that a positive current represents a depolarizing drive and negative current a hyperpolarizing drive. A double exponential (blue) is fitted to this mean η current. Inset: zoom on the first 300 ms. *E* and *F*: same Figures with the 8 non-Fast Spiking GABAergic neurons (NFS) and the 9 Exc neurons (Exc), respectively. Note that for the NFS and the Exc, a single exponential fit (blue trace) is sufficient to approximate the mean η current. *G*: Mean RMSER for the 9 GABAergic FS cells as a function of the number of exponential function used to describe the adaptation current η (0 to 4), and for an arbitrary shaped spike-triggered current η (last column). Error bars are one standard deviation. Black stars denote a significant difference (two sample t-test). *H*: and *I*: same Figures with the 8 non-Fast Spiking GABAergic neurons (NFS) and the 9 Exc neurons (Exc), respectively.

2.3.6   Essential Features for Spike Time Prediction

To explore the spike time prediction of our models, we compute the spike train similarity measure M_d^* (see Materials and Methods) averaged across all neurons of a given type. For
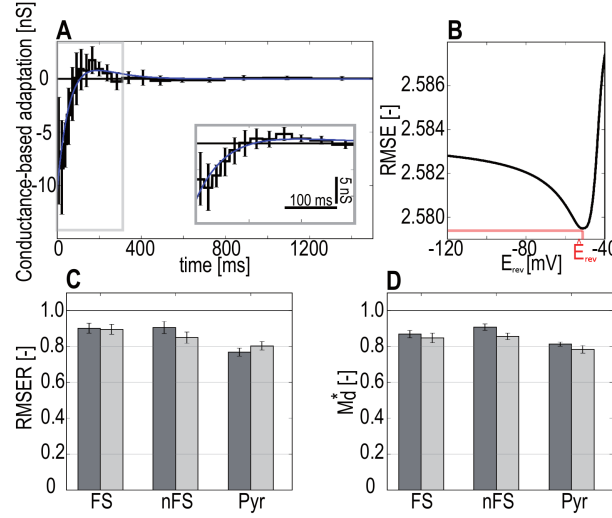
Figure 2.7: **Conductance vs current-based adaptation.** *A*: Conductance-based adaptation extracted individually for each Excitatory neuron (9 Exc cells) is averaged to obtain the mean η_{cond} (black). Error bars represent one standard deviation. A double exponential (blue) is fitted on η_{cond}. Inset: zoom on the first 300 ms. *B*: $R\tilde{M}SE$ as a function of the reversal potential E_{rev} of η_{cond}. The optimal $RMSE$ is obtained with $\hat{E}_{\mathrm{rev}}$. *C*: Mean RMSER for the 9 GABAergic FS, 8 GABAergic NFS and 9 Exc cells for models with current-based adaptation (IF$_\eta$, dark grey) and similar model with conductance-based adaptation (IF$_{\eta_{\mathrm{cond}}}$, light grey), error bars represent one standard deviation. There are no significant differences between IF$_\eta$ and IF$_{\eta_{\mathrm{cond}}}$ for a given cell type (two-samples t-test). *D*: Spike time prediction measured by the mean spike train similarity M_d^* for the 9 GABAergic FS, 8 GABAergic NFS and 9 Exc cells using a model with current-based adaptation (IF$_\eta$ + dyn, dark grey) or a model with conductance-based adaptation (IF$_{\eta_{\mathrm{cond}}}$ + dyn, light grey). Error bars represent one standard deviation. There are no significant differences between current and conductance-based models for a given cell type (two-sample t-test).

example, as mentioned in the Methods section, a value of $M_d^* = 0.8$ indicates that 80% of the PSTH is correctly predicted by the model. In order to compare the effects of adaptation current η and sliding threshold γ, we show the spike time prediction for models with and without spike-triggered currents as well as with or without sliding threshold. Figure 2.8*D-F*, show our results for GABAergic FS, GABAergic NFS and Exc neurons, respectively. The dynamic thresholds were in each case described as a double exponential, consistent with the results of Figure 2.8 *A-C* (green traces).

For the GABAergic FS cells (Figure 2.8 *A*), we find that there is almost no movement of the threshold. The small fluctuations in the extracted moving thresholds are presumably due to noise in the estimation. This implies that all the adaptive behavior of GABAergic FS cells is mediated by the spike-triggered current and not by any changes in the AP threshold. We did not find that adding a moving threshold yields any significant improvement in terms of spike-time prediction ($p > 0.07$ for all pairs, with 2 sample t-test with $\alpha = 0.05$). Nevertheless when IF$_0$ is augmented with bin-based spike-triggered currents η (IF$_\eta$), we obtain a minor gain in spike time predictions ($\Delta M_d^* = 0.05$). There is negligible increase in M_d^* when augmenting the model further with sliding threshold (IF$_\eta$ + dyn; $\Delta M_d^* = 0.007$). The optimal model for

GABAergic FS neurons is $IF_\eta + \mathtt{dyn}$ producing a M_d^* of 0.87 ± 0.06, but the gain compared to other model variants is marginal.

The moving threshold $\gamma(t)$ of GABAergic NFS neurons follows a double exponential decay, with parameters $b_1 = 3.64$ mV, $\tau_1 = 21.88$ ms for the fast component, and $b_2 = 1.24$ mV, $\tau_2 = 336.50$ ms for the late component (2.8 *B*, green trace). After half a second to a second, $\gamma(t)$ is weak but by cumulating over multiple spikes the late component can contribute to spike-frequency adaptation. When comparing the value of spike time prediction M_d^*, a model IF_0 performs always worse than models augmented with spike-triggered currents η or dynamic AP threshold γ. More precisely, adding a sliding threshold produces a highly significant gain in the spike prediction measure of $\Delta M_d^* = 0.10$. Adding a spike-triggered current produces a net gain of $\Delta M_d^* = 0.07$ compared to IF_0. This leads us to the optimal model for GABAergic NFS cells being $IF_\eta + \mathtt{dyn}$ with a value of spike time prediction $M_d^*(IF_\eta + \mathtt{dyn})$ that indicates that more than 90% of the spikes in the PSTH are indeed predicted by the model.

The excitatory neurons also exhibit a dynamic threshold with a double exponential decay with $b_1 = 12.45$ mV, $\tau_1 = 37.22$ ms and $b_2 = 1.98$ mV, $\tau_2 = 499.80$ ms (2.8 *C*, green trace) with an amplitude that is at least twice as strong as for GABAergic NFS cells. The effect of the spikes on the threshold lasts for more than 1 second. The case of the excitatory neurons is special because they show a voltage reset to a value above the threshold baseline ($E_{\mathrm{reset}} > V_T$). Therefore all models with static threshold produce repetitive firing at very high and unrealistic frequencies, which leads to a very low M_d^*, as one can observe on Figure 2.8 *F*. Thus models upgraded with a sliding threshold always generate a significantly higher M_d^* than similar models with static threshold ($\Delta M_d^* = 0.48$). We also observe a small increase of $\Delta M_d^* = 0.07$ for models upgraded with spike-triggered currents. Thus the adaptation process is dominated by the effect of the sliding threshold (also see Figure 2.11 *C*). The optimal model for excitatory neurons is an $IF_\eta + \mathtt{dyn}$ that produces $M_d^* = 0.81 \pm 0.04$. The ISI distributions of the data (Fig. 2.8 *G-I*) agree with the ones coming from the optimal models, but not with those from the simples model without spike-triggered adaptation.

We summarize results from Figure 2.6 and 2.8 by observing that the minimal optimal model for GABAergic FS cells must have two spike-triggered currents and a static threshold (IF_2), whereas for GABAergic NFS and Exc neurons the minimal model must have only one spike-triggered current, but a dynamic threshold ($IF_1 + \mathtt{dyn}$). These minimal models reproduce the subthreshold voltage traces of the experiments (RMSER $\leqslant 1$) and at least 80% of the spikes (scaled to experimental reliability).

We observe that GABAergic NFS and Exc neurons have AP threshold dynamics that extend from milliseconds to more than 500 milliseconds. Moreover, due to its cumulative property, the moving threshold can tune the neuron's firing frequencies, and thus the PSTH, on timescales beyond 1 second. Finally AP threshold dynamics are only present in some cell types and – when present – act on very long timescales. We also note that it is the effect of the dynamic threshold $\gamma(t)$ combined with the spike-triggered current $\eta(t)$ that produces the effective adaptation behavior of a given neuron.
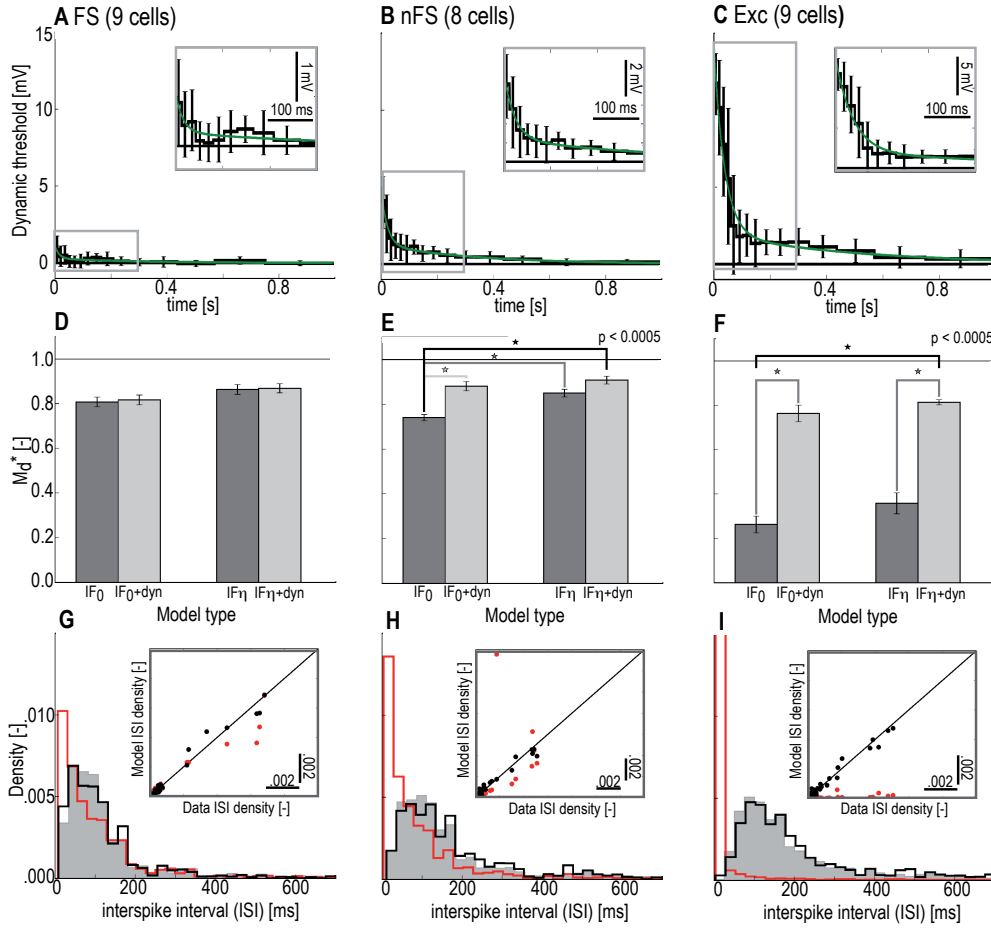
Figure 2.8: **Essential Model Features for Spike Time Prediction in GABAergic FS, GABAergic NFS and Exc.** *A*: The dynamic threshold γ extracted individually for each GABAergic FS cell (9 cells) is averaged to obtain the mean threshold dynamics for GABAergic FS neurons (black) and its standard deviation (error bars). A double exponential (green) is fitted on the mean threshold. Inset: zoom on the first 300 ms. *B* and *C*: same Figures as in *A* but with the the 8 non-Fast Spiking GABAergic neurons (NFS) and the 9 Exc neurons (Exc), respectively. *D*: Quality of the spike time prediction quantified by the mean M_d^* for the 9 GABAergic FS cells as a function of the model types, static threshold (dark grey), dynamic threshold (light grey). Error bars correspond to one standard deviation. *E* and *F*: as in *D* but for the 8 non-Fast Spiking GABAergic neurons (NFS) and the 9 Excitatory neurons, respectively. Black stars represent a significant difference between different IF models, (two-sample t-test). *G*: Experimental ISI distribution (grey), ISI distribution for a model without adaptation current (IF_0, red) and ISI distribution for a model with adaptation currents and a dynamic threshold ($IF_\eta + \mathtt{dyn}$, black). Inset: ISI density of the data as a function of the ISI density of the models (IF_0, red and $IF_\eta + \mathtt{dyn}$, black). For perfect fit of the experimental ISI distribution all dots will lie on the diagonal (black line). *H*: As in *G* but for the 8 non-Fast Spiking GABAergic neurons (NFS). *I*: As in *G* but for the 9 Excitatory neurons (Exc).

Dependency of the Extracted Parameters on the State of the Neurons

Given the intricate voltage-dependence of ion channels, it is clear that spike-triggered currents as well as passive parameters of neurons change as a function of the instantaneous state of the

neurons. It is conceivable that the intensity and the time course of the spike-triggered currents would be affected by the instantaneous firing frequency of the neuron (Tateno and Robinson, 2009). To investigate this point, we apply our method to subsets of the data that differ in mean firing rate and in mean membrane potential. In other words we study the dependence of the extracted parameters on the state of the neuron.

To do so we split the 60-second long experiments in 6 classes of 10 seconds and compute the mean firing frequencies and the mean voltage of these classes. Note that we use only 6 classes because as mentioned in Section 'Efficiency and Accuracy of the Fitting Method on Surrogate Data' we need at least 10 seconds of recordings to obtain a fair estimate of the parameters. Moreover as mentioned in Section 'Fitting Procedure' our method requires data that covers a large range of ISIs to obtain a good estimate of the threshold parameters γ. With 6 classes both requirements are fulfilled. In Figure 2.9 *A* one can observe that a single 10-second class contains high and low rate episodes interleaved with periods of silence. This produces an ISI distribution covering a wide range of instantaneous rates (from 0 to 25 Hz, Figure 2.9 *B*, lower panel) estimated from episodes of 0.5 seconds. If averaged over segments of 10 seconds, the apparent range of firing frequency is smaller (from 1 to 6 Hz, Figure 2.9 *B*, upper panel) but contains the exact same episodes. The 6 classes of 10 seconds enable us to investigate the dependency of extracted parameters on the neuronal regime.

Using these 6 classes we could not find important dependencies of the spike-triggered current η (Figure 2.9 *C* and *D*) or the passive parameters C, τ and E_l (Figure 2.9 *E* to *J*) on the firing rate or on the mean voltage. Moreover it is impossible to distinguish parameters extracted on a single class from parameters extracted on the whole 60-second long experiment.

These results suggest that over the range of firing frequencies that we have studied, the parameters of the neurons do not change significantly. This tends to justify our assumptions that a unique set of parameters per neuron is sufficient to capture its dynamics. This does not exclude that a neuron behaves differently when driven to some exotic regime (in fact, it definitely will), but over the range studied here, our method did not indicate important parameter changes. Other experiments, where rates vary more drastically would be needed to investigate these points in a more systematic way.

2.3.7 Cell-type Classification

In the last sections we showed that the membrane filter, the time course of adaptation and the AP dynamics strongly depend on the neuron type. Here we ask whether we can characterize cell types solely on their extracted parameters. We classify cell types based on (i) their passive parameters C, g_l and E_l (ii) the parameters describing the adaptation current including the value of voltage reset E_{reset} (note that here we use a combination between η and E_{reset}, because the extracted spike-triggered current depends on the voltage reset, and in this view, E_{reset} is a part of the adaptation process), (iii) the parameters describing the shape of the dynamic threshold γ, or (iv) all the parameters. To do so we perform standard Principal Component Analysis (PCA) using (i) only the passive parameters for each cells, (ii) only the parameters of adaptation current, (iii) only the parameters of the dynamic threshold and (iv)
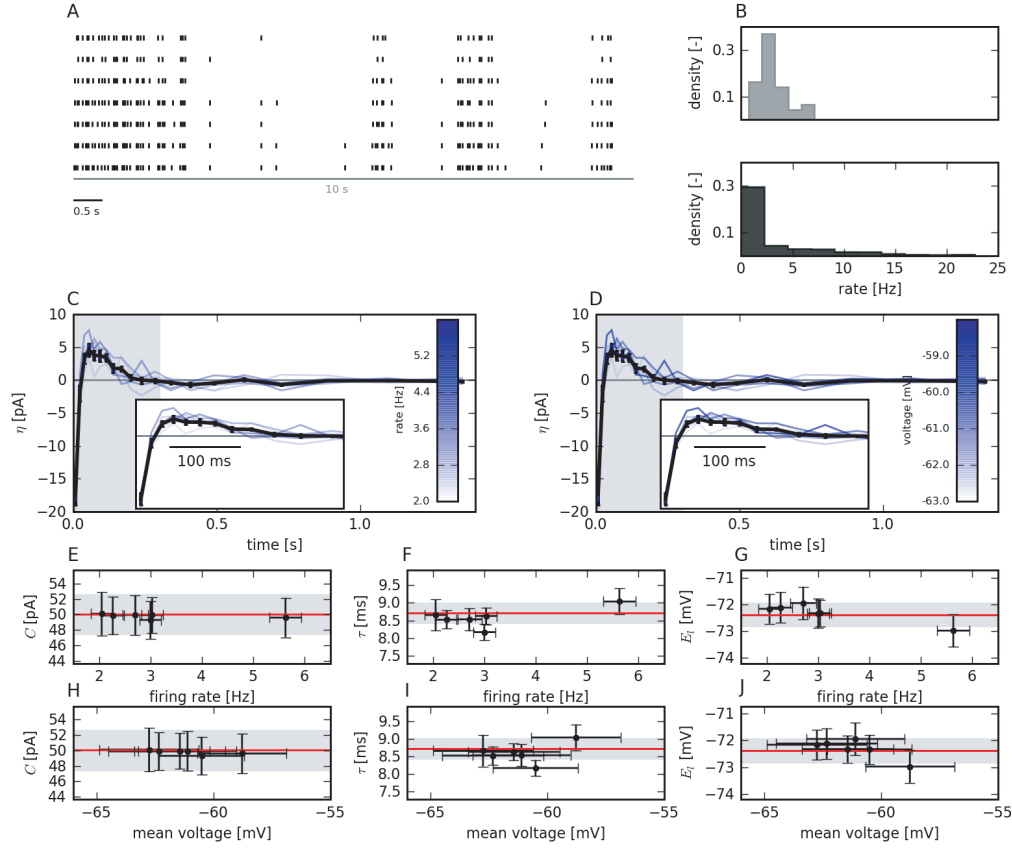
Figure 2.9: **Dependency of the extracted parameters upon the instantaneous firing rates and the mean voltage of the neurons.** *A*: Raster plot (7 repetitions) of the first 10 seconds of a typical GABAergic FS cells (grey line is 10 seconds and black line 0.5 seconds). *B*: Distribution of the mean firing rate of one experiment of 60 seconds where the rate is computed on 10-second bins (upper panel) or 0.5-second bins (lower panel). The distribution strongly depends on the bin size, so even if the mean firing rate (averaged over 60 seconds) is at 3 Hz, the data contains episodes of high firing rate (> 20 Hz). *C*: Spike-triggered current η extracted on 6 different subsets of 10 seconds and sorted by the mean firing frequency of the subset used (shaded blue lines). The black line shows η extracted on the whole experiment of 60 seconds. *D*: As in *C* but η are sorted according to the mean membrane potential of the subset. *E* to *G*: Extracted parameters C, g_l and E_l as a function of the mean firing frequency of the data subset. Red line shows the value of the parameters extracted on the whole experiments with its standard deviation (grey area). The horizontal and vertical error bars correspond to one standard deviation. *H* to *J*: As in *E, F, G* but the parameters are sorted according to the mean voltage of the data subset.

using all the parameters.

Using any subset of parameters is sufficient for classification with the first two principal components (Figure 2.10 *B-D*) except when passive parameters only are used (Figure 2.10 *A*). Classification based on passive parameters fails because GABAergic FS and NFS neurons do not differ in a significant way in their capacitance, their leak conductance or their reverse potential. However, if PCA is applied on the parameters that characterize the adaptation current and/or the dynamic threshold, we can successfully classify neurons. Moreover we also

observe that the variance between the different cells is mainly explained by the reset value E_{reset} and the dynamic threshold (2.10 *D*, right panel).
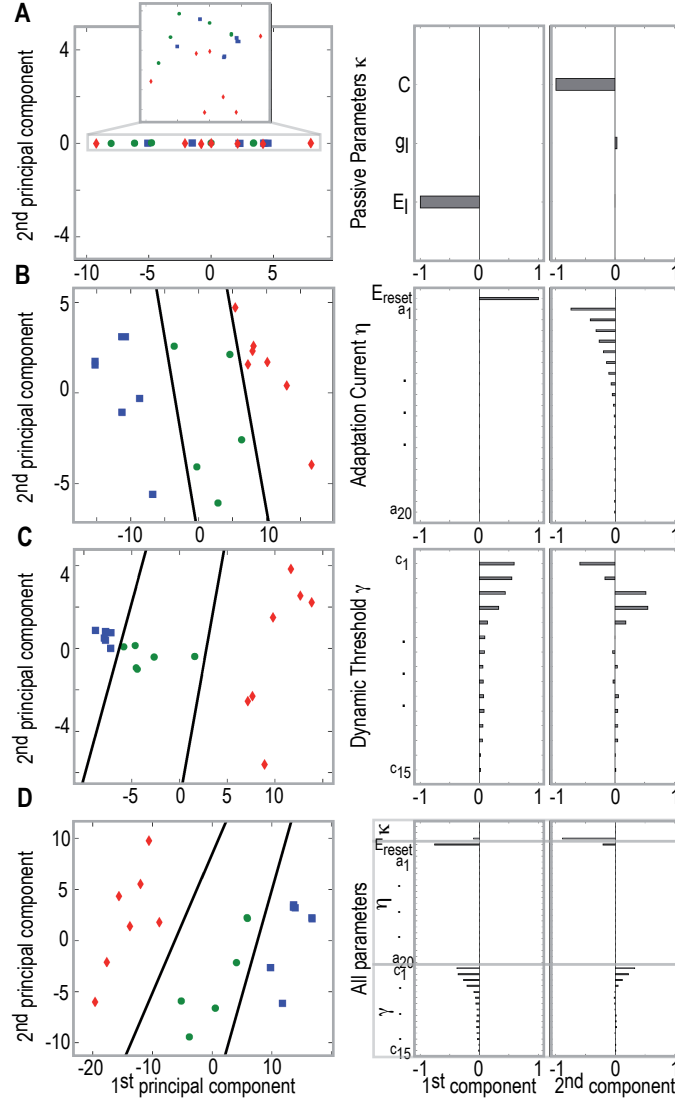
Figure 2.10: **Principal components of the 3 studied cell types.** Principal components are obtained with standard principal component analysis (PCA) for all the cells. *A*: PCA applied on the passive parameters C, g_l and E_l of the modeled neurons. Left panel: projection of all the passive parameters from all the cells (blue square: FS, green circle: NFS, red losange: Exc) onto the space defined by the two first principal components. Inset: zoom on the outlined region. Right panel: Loadings of the first and the second principle component, respectively. The same method is applied to the adaption current η, the AP dynamics γ and all the parameters of a model $\text{IF}_\eta + \text{dyn}$, *B*, *C* and *D*, respectively. In these cases black lines are lines that separate each group, obtained by a standard linear classifier.

2.4 Discussion

2.4.1 Automatic Fitting Method

There is a rich history of fitting neuron models to intra-cellular recordings of real neurons (Vanier and Bower, 1999; Rauch et al., 2003; Keren et al., 2005; Achard and De Schutter, 2006; Huys et al., 2006; Jolivet et al., 2006; Kobayashi and Shinomoto, 2007; Druckmann et al., 2007; Badel et al., 2008; Kobayashi et al., 2009). The variety of approaches arises from the choice of neuron model and the fitting method. Still, not all methods yield models that can predict the spike times and membrane potential with high accuracy (Jolivet et al., 2007; Gerstner and Naud, 2009). To predict the membrane potential with Hodgkin-and-Huxley compartmental models, one needs prior knowledge on the dynamics of the ion channels present in the recorded cell (Huys et al., 2006; Druckmann et al., 2008). Without knowledge of the ion channels, fitting Hodgkin-and-Huxley compartmental models becomes plagued with local minima, and there are often multiple parameters that share the same fitting quality (Achard and De Schutter, 2006). The only hope for a fitting method that can easily be applied to multiple systems for which we have insufficient knowledge of the ion channel dynamics is to use convex fitting methods in combination with IF models (Paninski, 2004). Earlier work (Jolivet et al., 2006) had an efficient fitting method for the subthreshold voltage but the black-box fitting of the adaptive threshold was not convex. The method of (Badel et al., 2008) may have been convex, but it applied only to models without spike-frequency adaptation. The method of (Paninski, 2004) was convex but did not use the information contained in the voltage trace while the method of (Paninski et al., 2005) was convex and used the voltage trace but lacked the moving threshold required for efficient spike prediction. In this paper we have used a method that improves upon the earlier multi-linear regression method (Paninski et al., 2005) by adding a second fitting step for the moving threshold taken from the literature on generalized linear models (McCullagh and Nelder, 1998). The method is sure to find only one set of optimal parameters because it is made of two convex fitting methods (multiple linear regression and generalized linear model with Poisson or Bernoulli probability distribution, but see constraints for the convexity in (Paninski et al., 2004)). We expect the method to generalize well to many cell types because the total time of the spike-triggered current, number and size of the basis functions is not expected to depend on the cell types.

The notion of a dynamic threshold affecting neuronal computation also has a long history (Hill, 1936; Azouz and Gray, 1999, 2000; Gerstner and Kistler, 2002; Chacron et al., 2003). So far, the methods for fitting the dynamics of the firing threshold have relied on the measurement of the effective threshold for each spike (Azouz and Gray, 2000; Chacron et al., 2003). Instead, the method presented in this article uses the whole voltage trace, providing information about the firing threshold each time a transient increase in the membrane potential is not followed by a spike. We expect this method to be more precise since the number of data points used to constrain the moving threshold is not proportional to the number of spikes but to the number of data points constituting the subthreshold voltage trace in the regime close to threshold. Since the choice of model will affect the prediction performance the question arises, why we

omit the non-linearity responsible for spike initiation in IF-type models (Fourcaud-Trocme et al., 2003; Badel et al., 2008). An exponential non-linearity in integrate-and-fire models was shown to be crucial for accurate processing of the inputs at high frequency (Fourcaud-Trocme et al., 2003). Such a non-linear term can interact with subthreshold currents to produce a variety of firing patterns (Izhikevich, 2004, 2007; Naud et al., 2008). The IF models used here assume strictly linear voltage dynamics and are fitted away from the spikes so that the increased non-linearity close to a spike does not bias the parameter estimation. It is not trivial to generalize the present convex method to include an exponential non-linearity for spike initiation. However, in the present model the spike initiation is stochastic with an exponential non-linearity for the probability of spiking as a function of voltage as extracted from experimental data (Jolivet et al., 2006). This exponential non-linearity should not be confused with the exponential non-linearity in the Adaptive Exponential integrate-and-fire (AdEx) model (Brette and Gerstner, 2005) or the model of (Badel et al., 2008). Nevertheless, there are some links between the exponential spike-initiation of the AdEx model and the exponential transfer function of the generalized integrate-and-fire models discussed here, so that the AdEx model can be approximately mapped onto a generalized integrate-and-fire model (Mensi et al., 2011a). The escape-noise IF models discussed here can reproduce all the main firing patterns, except delayed spike-initiation upon pulse current input (see below).

Another feature of some neurons that is not present in our model is a subthreshold resonance. A strong subthreshold resonance has been observed in the dendrites of large excitatory neurons (Cook et al., 2007) and in 'mes V' neurons (Izhikevich, 2007). Subthreshold resonance is thought to be mediated by an additional current linearly coupled with the membrane potential. Similarly, delayed spiking upon step current injection has also been attributed to an additional current linearly coupled with the membrane potential (Naud et al., 2008). One can check the presence of such an additional effect by looking at the shape of the membrane filter $\kappa(t)$ extracted with a method that does not force an exponential shape (i.e. the Wiener-Hopf optimal filter method described in Appendix B and in (Jolivet et al., 2004)). Indeed, a resonance corresponds to a filter with a negative undershoot, while a delayed onset corresponds to a filter with a double exponential decay. Both cases can be described by an additional current having linear coupling with the soma to take into account resonance or delayed spiking. We have tested a method which involves adding the term $ae^{-t/\tau_w} * V(t)$ to Eq. 2.3. Multi-linear regression can still be applied to determine the strength of the coupling a when a time constant τ_w is assumed. Iterating through a large range of possible τ_w by repeating the multi-linear regression usually yields a convex function of the MSE as a function of τ_w. This method enables us to fit the parameters mediating subthreshold resonance or delayed spiking, but this was not necessary here since the neuron types studied have no resonance or do not display delayed spiking.

The choice of an appropriate input stimulus is of crucial importance for all model identification methods. Here we have successfully tested our method on different kinds of input currents, injected in current-clamp mode. However, *in-vivo* neurons receive excitatory and inhibitory synaptic inputs acting in conductance. It is possible to mimic this complex input scenario *in-vitro* by patching neurons in dynamic-clamp mode, where excitatory and

inhibitory conductances are dynamically injected in a patched neuron. We do not directly investigate the robustness of our method in this particular input scenario in this study. However we have shown that our fitting procedure can handle dynamic-clamp input by participating in an international competition in 2008, where the goal was to predict the spike times of a single neuron stimulated in dynamic-clamp (see (Jolivet et al., 2008) and (Jolivet et al., 2007) for details and results). For this competition we used a related model and fitting procedure and obtained similar results.

2.4.2 Effective Moving Threshold

We have seen that the effects of spike-triggered currents and dynamic threshold merge to produce spike-frequency adaptation. The effect of the spike-triggered adaptation current $\eta(t)$ on the voltage is simply given by the convolution of the spike-triggered current $\eta(t)$ with the membrane filter κ ($\eta_v(t) = -\kappa * \eta$). The effective moving threshold $\zeta(t)$ arises from the combination of the threshold dynamics $\gamma(t)$ and the effect in voltage of the spike-triggered current. Since spikes are triggered when the membrane potential hits the threshold, the relevant variable is the difference $\zeta(t)$ between the change in dynamic threshold (increasing after a spike) and the contribution of the adaptation current to the voltage trace.

$$\zeta(t) = \gamma(t) - [\kappa * \eta](t) \tag{2.7}$$

To answer the question of whether the spike-frequency adaptation is dominantly mediated by spike-triggered currents or moving threshold, we can look at the respective contribution of $\gamma(t)$ and $\eta_v(t)$ towards the effective adaptation $\zeta(t)$. Figure 2.11 *A* shows that the effective moving threshold of GABAergic FS cells are clearly dominated by spike-triggered currents. For the Exc cells, $\zeta(t)$ is dominated by the moving threshold (see figure 2.11 *C*), whereas for the GABAergic NFS cells the effective adaptation process $\zeta(t)$ (Figure 2.11 *B*) is a combination of η and γ, where each spike-triggered mechanism mediates approximatively half of the effective moving threshold. Therefore, we conclude that the adaptation is mediated by different processes in different cell types: adaptation is dominated by the moving threshold for the Exc neurons; caused entirely by spike-triggered currents for the FS neurons; and consists of an equal mix of threshold and current for the NFS neurons.

The effective moving threshold for GABAergic FS cells has the particularity of crossing zero after 30-80 ms and remaining negative (*i.e.* facilitating) thereafter. The zero-crossing then determines the type of excitability: Under constant current injection, after the neuron model fires its first spike, the effective threshold is first high, decreases and eventually crosses the membrane potential, and hence forcing a spike after a period approximatively equal to the first zero-crossing in the function $\zeta(t)$. One can see that under constant current injection this type of neuron will not fire with a period longer than the time of the minimum of the effective threshold $\zeta(t)$: $f_c \approx 12 - 33$ Hz, in agreement with Fig. 2.5. The facilitating tail of the effective adaptation must lead to spike-frequency facilitation as observed in the firing patterns of Fig. 2.5. Moreover, the peak of the facilitating part in $\eta(t)$ will indicate a preferred

frequency around 10 Hz. On the other hand, strictly decaying functions $\zeta(t)$ as in NFS and Exc will produce adapting firing patterns and type I excitability.
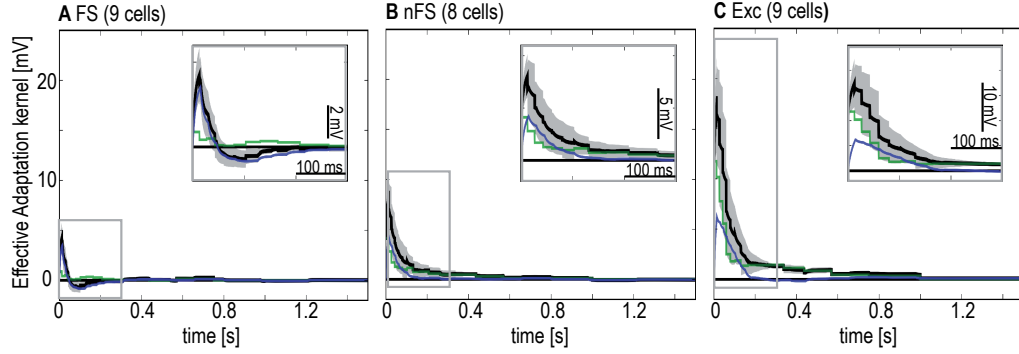
Figure 2.11: **Effective spike-triggered adaptation for the three neuron classes.** As discussed in the main text the effective moving threshold is the sum of the dynamic threshold and of the adaptation current η convolved with the membrane filter. *A*: Effective moving threshold for each GABAergic FS cells (9 cells) are averaged to obtain the mean effective adaptation (black) and its standard deviation (grey shaded area). Mean threshold dynamics (green) and mean η_v (blue). Inset: zoom on the first 300 ms. *B* and *C*: same Figures with the 8 non-Fast Spiking GABAergic neurons (NFS) and the 9 Exc neurons (Exc), respectively.

2.4.3 Links with Bifurcation Theory

We observe that our FS models have a Type-II exctitability, whereas our Exc and NFS models are of Type-I. In the literature these Type-I and Type-II behaviors are known to occur via different types of bifurcations (Koch, 1999; Gerstner and Kistler, 2002; Izhikevich, 2007; Naud et al., 2008; Touboul and Brette, 2009). For instance Type-I may occur via a saddle-node bifurcation onto an invariant circle, whereas Type-II typically occurs through an Hopf bifurcation or a saddle-node bifurcation off invariant circle. The presence of the hard reset and multiple timescales in the spike-triggered adaptation means that standard theorems of bifurcation theory in continuous 2 dimensions do not apply. In spite of this we can draw analogies with two-dimensional bifurcation theory.

Hopf bifurcations are associated with subthreshold resonances: When a neuron model is stimulated with a slowly increasing current ramp, subthreshold oscillations would be observed in response to a short current pulse before stability is lost through the Hopf bifurcation. These oscillations hch2:appen even before the neuron has fired a first spike and are therefore strictly subthreshold. Our fitted FS models do not generate such subthreshold oscillations as can be deduced from the absence of any resonance in the membrane filter $\kappa(t)$. Nevertheless, the FS neuron model exhibits resonance in the spike-triggered currents. These spike-triggered currents, which are summarized in the adaptation current $\eta(t)$ are responsible for the minimal firing frequency that is characteristic of Type-II behavior. We note that spike-triggered currents result in membrane potential oscillations after an action potential, i.e., they give rise to a non-monotonic spike-afterpotential. Such an oscillatory SAP should not be confused with

pure subthreshold oscillations. Let us describe in more detail how the Type-II behavior arise in a simplified version of our fitted models.

We simplify our models such that adaptation is mediated by a single exponential spike-triggered current of amplitude b, that mediates spike-frequency adaptation ($b > 0$) for Exc and NFS neurons and facilitation ($b < 0$) for FS neurons. This can be done by coupling a second differential equation $\tau_w \dot{w} = -w$ to the main voltage Equation 2.3 and to add a constant value b to w each time a spike is emitted (Izhikevich, 2007). Note that this makes a w-nullcline that is independent of the membrane potential V, as expected from the fact the membrane filter is a single exponential (as shown in Figure 2.6 *A-C*). Under these assumptions, the only difference between Type-I and Type-II models is the sign of the spike-triggered current. A schematic of the phase plane of these simplified Type-I and Type-II models is shown in figure 2.12. Before application of a depolarazing step current, the membrane potential is at rest (Fig. 2.12 *A*). The stable fixed point looses its stability through a saddle-node bifurcation. The simple model can still create Type-I or Type-II excitability depending on whether the saddle node bifurcation is on or off the limit cycle. Facilitating spike-triggered adaptation ($b < 0$) implies that the limit cycle stays away from the location of the saddle node bifurcation in phase space, because the reset of the w variable restarts at lower value (Type II, Figure 2.12 *B*). True adaptation ($b > 0$), however leads to the classic saddle-node bifurcation onto invariant circle (Type-I, Figure 2.12 *C*).

We have argued that our fitted FS models loose stability via a saddle-node bifurcation which causes Type-II excitability because it is off the invariant circle. We have discarded the Hopf bifurcation because of the absence of subthreshold resonance. It is possible, however, that the fitting procedure did not capture a subthreshold resonance that appears only at voltages close to the threshold, and there are exactly the type of resonances that would be expected when stability is lost via a Hopf bifurcation. Therefore the present analysis can not draw conclusions on the type of bifurcation responsible for firing in real FS neurons.

2.4.4 Interpretation of Model Parameters

We extract a set of parameters for a typical model of each neuron class. The parameters are related to the underlying biophysics (density, distribution and dynamics of ion channels, membrane capacitance, resistance), but the exact relationship is unclear. For instance, the extracted membrane time constants (τ_m ranged from 5 ms to 20 ms) are slightly shorter than the typical membrane time constant measured in experiments with voltage recording of the response to subthreshold step current injection at rest. This discrepancy can be explained by the fact that we measure passive parameters of neurons when they are stimulated instead of at rest. The different working regime of membrane potential will activate differently the subthreshold conductances (spike-triggered or not) and thus modify the effective membrane time constant (Richardson et al., 2003; Jolivet et al., 2004; Kobayashi et al., 2009). The presence of the electrode may also bias our estimate of the membrane membrane capacitance as discussed in (Badel et al., 2008). Similarly, the reversal potential, voltage threshold and voltage reset may depend on the bath solution, and the intra-pipette solution. The amplitude and
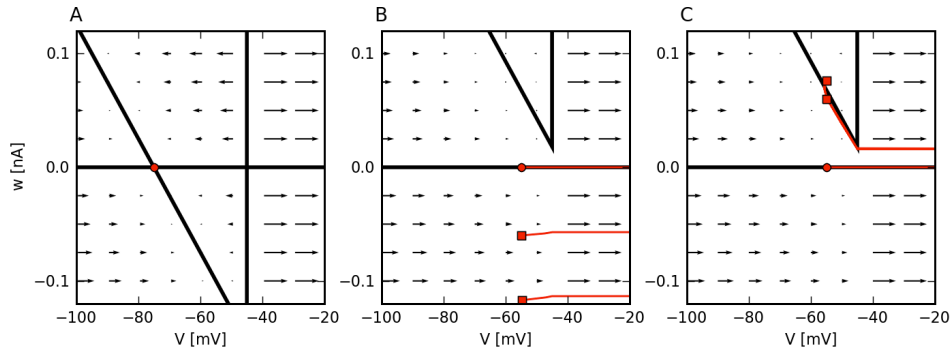
Figure 2.12: **Phase plane of the Type II (FS) and Type I (NFS and Exc) neurons.** Schematics of the phase plane of our simplified models, assuming a single depolarizing or hyperpolarizing exponential spike-triggered current of amplitude w (as decribed in Discussion Section 'Links with Bifurcation Theory') for Type II and Type I models, respectively. *A*: Phase portrait at rest (resting state marked by a red circle). *B*: Phase plane of the Type II (FS) model after injection of a depolarizing step current. Black lines; nullclines $\dot{V} = 0$ and $\dot{w} = 0$. Red traces; trajectories of the first three spikes caused by the step current. Red circle; initial conditions. Red square; first and second reset. Arrows indicate the direction and the strength of the flow. *C*: As in *B* but for a Type I (NFS or Exc) model.

time scale of the spike-triggered adaptation, should not be affected by the electrode or the bath solution, but the temperature at which the experiment was performed can affect the dynamics of the underlying ion channels.

We also investigated the dependency of the extracted parameters (i.e. the membrane filter and the spike-triggered current) on the regime of the neuron. Somewhat surprisingly we did not observe significant dependencies, in spite of what has been already observed (Tateno and Robinson, 2009). Our results could be explained by the limited range of firing rates that we studied and the nature of our stimulation protocol. Indeed we have restricted our analysis to current-clamp experiments and it is known that neurons exhibit different behaviors under *in-vivo* conditions (Prescott et al., 2006, 2008). Those *in-vivo* conditions can be approximated *in-vitro* by dynamic-clamp. The dynamic-clamp allows the study of the neuron behavior as a function of the relative strength and nature of the input conductances (i.e. balance between excitatory and inhibitory conductances, shunting). For instance the integration properties of Exc neurons change drastically depending on the conductance state (Jolivet et al., 2004; Prescott et al., 2008). Moreover these changes also affect the adaptation mechanisms of the neurons. The method presented in this article can be applied to dynamic-clamp recordings to address these issues.

The effect of the spike-triggered current on the voltage $\eta_v(t)$ is closely related to the spike-after potential (SAP; (Sah, 1996)). The spike-after potential may differ from $\eta_v(t)$ since it is measured around the resting potential while $\eta(t)$ is an average of the spike-triggered current under synaptic-like current injection. Furthermore, the spike-after potential is measured after a spike that was artificially triggered by a large and short current injection. The amount of charge that was injected to produce the spike will leak out of the membrane on a time

scale given by the membrane time constant. The spike-after current extracted by standard experimental protocols (Sah, 1996) is thus biased by the current used for stimulating the spike. Yet, the close relationship between the SAP and $\eta_v(t)$ indicate that $\eta(t)$ should be mediated by the same ion channels mediating the SAP, namely: the M-type current I_M (Adams et al., 1982), the after-hyperpolarization current I_{AHP} (Madison and Nicoll, 1984) or any other calcium-dependent ion channels (Hille, 1992; Sah, 1996; Koch, 1999; Wang et al., 2003). Moreover, spike-triggered events in the dendrites can also shape the spike-triggered current (Doiron et al., 2007).

The movement of the threshold after a spike has been proposed to depend on sodium channel de-inactivation (Fleidervish et al., 1996; Fleidervish and Gutnick, 1996; Kobayashi et al., 2009). Following a spike, a portion of the Na^+ channels responsible for the spike initiation stay inactivated, which leads to a higher effective threshold. The sodium channels then de-inactivate which results in a gradual decay of the spiking threshold (Henze and Buzsáki, 2001; Platkiewicz and Brette, 2011). It has been proposed that only a subtype of sodium channels are inactivating (Martina and Jonas, 1997). Thus, in our framework, the observed dynamic threshold must be related to the proportion and the type (inactivating or non-inactivating) of the sodium channel. Our results corroborate this hypothesis since only the GABAergic NFS and Exc types have a moving threshold, which suggest that the GABAergic FS neurons do not express the inactivating sodium channels.

Finally it would be possible to investigate the biological mechanisms underlying spike-triggered adaptation by the use of specific pharmacological experiments. For instance, by blocking some specific ion channels one can study how the shape of the spike-triggered current is affected by calcium-channels or high-voltage activated potassium channels. Similarly, if one can block specific sodium channels, like the inactivating Na^+ channels, it is possible to investigate the dependency of the dynamic threshold on the type of sodium channels expressed in a given neuron type.

2.4.5 Classification

Classification of neuron types can be done on multiple features: firing pattern, spike shape, morphology, expression of molecular markers (Markram et al., 2004). Here we classify based on the computational properties of the neurons, that is, the parameters regulating how the neuron encodes the incoming current into spike trains. These computational properties are determined by the expression of ion channels and lead to firing patterns that depend on the neuron type. We have shown that the classification of neuron types relates to a classification of the computational properties beyond the classification of firing patterns (GABAergic NFS and Exc cell-types are both regular spiking, and accommodating neurons). In other terms classification is possible even if the shape of the spike used traditionally for the distinction between GABAergic NFS and Exc neuron is not taken into account, since the different neuron types encode the incoming current differently.

We found that the passive properties of the neurons (capacitance, input resistance, membrane time-constant) are not sufficient to efficiently distinguish between the neurons types. It is the

adaptation properties (voltage reset, spike-triggered current, moving threshold) that distinguishes the different cell types. These results would indicate that the strength and time-scale of adaptation are important parameters of cortical network computation, indicating a direction for investigating the importance of micro-circuitry in cortical networks.

We have studied only three types of neurons, but more types of excitatory neurons (Connors and Gutnick, 1990) and GABAergic neurons (Markram et al., 2004) have been described. Further work is needed to check that such extensive classification can be done on the properties affecting the conversion of synaptic inputs to a spike. Classification on a greater pool of neurons would also enable to study how distinct the computational properties of different neuron types are and if a finer classification can be inferred. We expect that one would need on the order of one hundred recorded neurons under synaptic-like current injection to study in detail the classification of cortical neurons, and perform unsupervised clustering on the computational properties.

Neurons recorded *in vitro* can show very different properties from their alter ego in the intact, awake and behaving animal. In the awake animal it is not yet possible to know the input a neuron receives from its synaptic connection, but the somatic voltage can be recorded (Crochet and Petersen, 2006). In such an experiment it is not possible to apply this part of the fitting method for the spike-triggered current and passive properties because the method requires the knowledge of the stimulating current arriving at the soma. The moving threshold, on the other hand, can be extracted since our fitting method only requires the voltage trace and the time of the spike. It remains to be tested if moving thresholds can effectively be extracted from *in vivo* recordings. It is an interesting avenue for further research since this would allow to study the correspondence of *in vitro* and *in vivo* threshold dynamics and its classification across cell types.

2.4.6   How Good is Good?

Depending on the neuron type, the optimal IF model is able to predict between 81 and 91% of the spikes and reproduce the subthreshold voltage fluctuations with a precision in the range of millivolts. One can then ask: Why can we not achieve a perfect prediction (i.e. $M_d^* = 100\%$ and a $RMSE$ close to 0 mV)? What is missing? We can think of three possible explanations.

First, the experimental data suffers from some unavoidable drifts that are not due to the neuron itself and that we do not model. These drifts are presumably due to some additional currents that flow out of the neuron near the patch junction and so affect the recorded membrane potential in a non-systematic manner. The experimental drifts can greatly limit the maximum prediction performance.

Second, it is known that injecting current through the same electrode used for recording the voltage corrupts the recorded voltage (Brette et al., 2007). This artifact manifests itself as a high-frequency component of the recorded voltage that is correlated with the current being injected. Since we are fitting on the voltage trace, the artifactual component of the voltage will bias the estimated parameters. Mainly, the electrode artifact will affect the estimation of the membrane time-constant (Brette et al., 2007). We can also speculate that the average current triggering a

spike (the so-called spike-triggered averaged current, or STA) will contribute erroneously to the measured spike-triggered current. However we expect these effects to be small and to affect only very small time scales since the time-constant of the electrode contribution was measured to be below the millisecond range (Badel et al., 2008). Similarly, the erroneous high-frequency component of the voltage can bias our estimation of the threshold and its dynamics. The extent to which the bias in membrane time-constant and spike-triggered adaptation affects the prediction performance would have to be studied in details, but we have preliminary results showing that the effect is negligible. In any case, the artifact due to simultaneous current injection can be greatly reduced by the use of active electrode compensation methods (Brette et al., 2007; Badel et al., 2008).

Third, by modeling neurons with simple IF models, we neglect some non-linearities that are present in the neurons. For instance, the voltage dynamics close to a spike become strongly non-linear due to the activation of sodium channels (Naundorf et al., 2006; Badel et al., 2008). Saturation in the open/close fraction of the ion-channels can cause the spike-triggered current of spikes in a burst to differ from the spike-triggered current of isolated spikes, leading to higher-order dependencies on the spiking history. Furthermore, we know that ion channels mediating the spike-triggered currents have time-constants which depend non-linearly on the voltage, while our formalism imposes voltage-independent time-constants. Similarly, the escape-noise formalism is only an approximation to the full dynamics entailed by stochastic activation of a limited number of voltage-dependent ion channels. For injection of synaptic-like current into the soma of a cortical neuron all these approximations prove to be very good since the spike-time prediction is high and would be even higher if experimental drifts and electrode artifacts could be completely removed.

2.5   Appendix

2.5.1   A: Variants of the Family of IF Models

We studied different variants of the main model described by Eq. 2.3, 2.4 and 2.5 (see Section 'Model Dynamics'). Here we describe more precisely how these models are built and some variants of the standard models considered in this study.

A1. Shape of the Spike-triggered Current

As mentionned in the results Section 'Subthreshold Voltage Dynamics', the spike-triggered current $\eta(t)$ could be any function of time, and for fitting purposes we implemented this spike-triggered current as a linear combination of rectangular basis function, so that $\eta(t)$ is

given by:

$$
\begin{aligned}
\eta(t) &= \sum_{k=1}^{K} a_k f^{(k)}(t) & (2.8)\\
f^{(k)}(t) &= \mathrm{rect}\left(\frac{t - T_k}{\delta T_k}\right) = \Theta(t - (T_k - \frac{\delta T_k}{2})) \cdot \Theta(T_k + \frac{\delta T_k}{2} - t)
\end{aligned}
$$

where $f^{(k)}(t)$ are rectangular basis functions centered at T_k and of width δT_k, and where Θ denotes the Heaviside step function. Since we expect the spike-triggered current to change faster close to the previous spike and slower far from it, we spaced the rectangular basis function logarithmically. The index k runs from 1 to K where K is the total number of rectangular functions used for fitting. The parameters T_k, δT_k and K are meta-parameters fixed *a priori* so that the shape of the spike after-currents is controlled by the coefficient a_k (see also (Paninski et al., 2005)). Parameters T_k, δT_k and K are chosen to give sufficient freedom to span all plausible shapes of η while avoiding overfitting. Equation 2.8 will be used to extract the precise shape of the spike after-current $\eta(t)$ without assumptions with respect to its shape (single exponential, double exponential, etc.).

A2. Conductance-based Adaptation

As a variant of the model defined in Eq. 2.3, we can turn the spike-triggered current $\eta(t)$ into a spike-triggered conductance. This is done by replacing η in Eq. (2.3) by $\eta_{\mathrm{cond}}(V - E_{\mathrm{rev}})$, where η_{cond} has now units of conductance and E_{rev} is the reversal potential. If the model's adaptation is based on conductance as opposed to an adaptation current, we call the model $\mathrm{IF}_{\eta_{\mathrm{cond}}}$.

A3. Shape of the Dynamic Threshold

The dynamic threshold $\gamma(t)$ described in Eq. 2.5 (see Section 'Model Dynamics' for details) is expressed as a linear combination of rectangular basis functions:

$$
\begin{aligned}
\gamma(t) &= \sum_{p=1}^{P} c_p f^{(p)}(t) & (2.9)\\
f^{(p)}(t) &= \mathrm{rect}\left(\frac{t - T_p}{\delta T_p}\right)
\end{aligned}
$$

Then the shape of $\gamma(t)$ is defined by the coefficients c_p which control the amplitude of a set of the rectangular basis $f^{(p)}(t)$.

2.5.2 B: Extraction of Membrane Filter

The passive properties of a neuron, such as the reversal potential E_l, the leak conductance g_l and the capacitance C, characterize the linear response of a neuron to current injection and define the membrane filter κ of the neurons. The standard exponential membrane filter arises from the solution of Eq. 2.3 using the initial condition $V(0) = E_l$:

$$V(t) - E_l = \int \kappa(t-s)I(s)ds + \int \kappa(t-s)\sum_{\{\hat{t}\}}\eta(s-\hat{t})ds \tag{2.10}$$

where $\kappa(t)$ acts as a low-pass filter on the current I and on the spike-triggered currents:

$$\kappa(t) = \frac{1}{C}\exp\left(\frac{-t}{\tau_\mathrm{m}}\right) \tag{2.11}$$

with the membrane time constant $\tau_m = \frac{C}{g_l}$. Eq. 2.10 is known as the Spike-Response Model (SRM; (Gerstner et al., 1996)). It summarizes the dynamics of the membrane potential as made of two parts: the effect of the input current (first term on the right-hand side of Eq. 2.10) and the effect of the afterpotential following each spike (second term on the right-hand side of Eq. 2.10). The functions $\kappa(t)$ and $\eta(t)$ are *response kernels* which depict the membrane filter and the shape of the spike-after currents, respectively. Eq. 2.10 taken without restrictions on the shape on $\eta(t)$ and $\kappa(t)$ is very general and can take into account the effect of multiple subthreshold or spike-triggered ion-channels.

In practice, the linear filter $\kappa(t)$ may or may not consist of a single exponential decay. It is known that subthreshold currents, like I_m or I_h (Sabah and Leibovic, 1969; Mauro et al., 1970; Koch, 1984) generate subthreshold resonances or delayed spiking responses to steps (Naud et al., 2008; Izhikevich, 2004). These subthreshold currents give rise to a current-to-voltage filter κ exhibiting a negative bump (for resonances) or an exponential decay with two time constants (for delayed firing onset). Thus, to make sure that our assumption of an exponential filter is not too restrictive, we extract the shape-free membrane filter κ defined in Equation 2.10. To do so, we compute this filter by extracting the Wiener-Hopf optimal filter (Jolivet et al., 2004) on the spike-free subset of data ψ_3 (see Appendix C for details), such that we are left with only the last term on the right-hand side of Eq. 2.10. Note that we take only subset of the data that are far from the spike to ensure that the resulting κ filter does not take into account some spike-triggered effects, or non-linearities of the spike onset, that will corrupt the estimation of the membrane filter.

2.5.3 C: Data Preprocessing

To extract all the parameters of the models it is convenient to define appropriate subsets of the available data. Since we do not want to model the exact shape of the action potential we cut out, around each spike time $\hat{t}$, a small segment of the data which we ignore. In the experimental data the spike time $\hat{t}$ is defined to be the time when the membrane potential crosses a given voltage V_detect from below, here we set the detection threshold V_detect to 0 mV.

Let us, at each moment t, refer to the last spike time as $\hat{t}^{(\text{last})}$ and to the forthcoming spike time as $\hat{t}^{(\text{next})}$. The subsets of the data that we use for fitting are:

$$\psi_1 = \{t \quad | \quad t > \hat{t}^{(\text{last})} + T_{\text{refr}} \text{ and } t < \hat{t}^{(\text{next})}\} \tag{2.12}$$

$$\psi_2 = \{t \quad | \quad t > \hat{t}^{(\text{last})} + T_{\text{refr}} \text{ and } t < \hat{t}^{(\text{next})} - 2\,\text{ms}\} \tag{2.13}$$

with T_{refr} the absolute refractory period. Thus ψ_1 represents a set of recording times where the voltage is subthreshold and outside the absolute refractory period. ψ_2 further removes 2 ms of data before each spike. We will also use two other subsets of the data:

$$\psi_3 = \{t \quad | \quad t > \hat{t}^{(\text{last})} + T_{\text{adapt}} \text{ and } t < \hat{t}^{(\text{next})} - 2\text{ms}\} \tag{2.14}$$

$$\psi_4 = \{t \quad | \quad \psi_3^{(1)} \cap \psi_3^{(2)} ... \cap \psi_3^{(R)}\} \tag{2.15}$$

Thus ψ_3 removes a period of time T_{adapt} after the spikes where $T_{\text{adapt}} > T_{\text{refr}}$. We use for T_{adapt} a period of 200 ms when the recording has a high average firing frequency (> 5 Hz) but we use $T_{\text{adapt}} = 500$ ms otherwise. For our recordings made of multiple repetitions, we only consider the subset of times ψ_4 that are separated by a period of at least T_{adapt} from any previous spike, from any repetition. This subset is therefore the intersection between the subsets $\psi_3^{(k)}$ of all repetitions $1 \leqslant k \leqslant R$. Each subset ψ_1, ψ_2, ψ_3, ψ_4 will be used in different steps of the fitting procedure.

2.5.4   D: Estimation of the Models Parameters

The fitting procedure to extract all the parameters of the model from a single voltage trace and the input current is a four-step method presented in the Section 'Fitting Procedure'. Here we describe in details two critical steps of this method, (i) the linear regression method that allows the estimation of the optimal parameters governing the dynamics of subthreshold voltage and (ii) the maximum likelihood method used to estimate the optimal parameters governing the firing activity of the model. Along with these descriptions some possible variants of the standard fitting protocol are briefly explained.

D1. Estimation of the subthreshold voltage parameters

As discussed in the step 2 of the Section 'Fitting Protocol', the model parameters $\vec{\theta}_2 = \{-\frac{g_l}{C}, \frac{g_l E_l}{C}, \frac{1}{C}, \frac{a_1}{C}, \ldots, \frac{a_K}{C}\}$ act linearly on the model's voltage time-derivative $\dot{V}_t^{(\text{mod})}$, so that:

$$\dot{V}_t^{(\text{mod})} = -\frac{g_l}{C}(V_t - E_l) + \frac{1}{C}I_t + \sum_{k=1}^{K} \frac{a_k}{C} \sum_{\{\hat{t}_j\}} f_{t-\hat{t}_j}^{(k)} \tag{2.16}$$

The voltage V, the time-derivative of the voltage $\dot{V}$, the input current I and the basis function are known the only unknown in Eq. 2.16 are the parameters. For notational convenience, we will write the above equation as a matrix equation, defining $\dot{\vec{V}}^{(\text{mod})}$ as the vector of the binned voltage time-derivatives and $\mathbf{X}$ as a matrix with the vector of voltage $\vec{V}_t$ (binned as a function of time) in the first column, a vector $\vec{1}$ of ones in the second column, the vector of input current $\vec{I}_t$ (binned as a function of time) in the third column, and the value $\sum_{\hat{t}_j} f^{(k)}_{t-\hat{t}_j}$ for $1 \leqslant k \leqslant K$ evaluated at the known spike times $\hat{t}$ in the remaining K columns, such that the differential equation 2.16 becomes:

$$\dot{\vec{V}} = \mathbf{X}\vec{\theta}_2 \qquad (2.17)$$

The parameters can be estimated by minimizing the sum of squared errors $SSE(\vec{\theta}_2) = \|\dot{\vec{V}}_{\psi_2} - \mathbf{X}_{\psi_2}\vec{\theta}_2\|^2$ between the voltage derivative of the experimental trace V_{ψ_2} and that of the model, $X_{\psi_2}\theta_2$, summed over all points in the data set ψ_2 that comprise the voltage trace in the subthreshold regime. According to multi-linear regression theory (Weisberg, 2005), the optimal set of parameters is then given by

$$\hat{\vec{\theta}}_2 = (\mathbf{X}_{\psi_2}^T\mathbf{X}_{\psi_2})^{-1}\mathbf{X}_{\psi_2}^T\dot{\vec{V}}_{\psi_2} \qquad (2.18)$$

This method was used in (Paninski et al., 2005) as a linear method to maximize the likelihood of observing the measured $\dot{V}$ time series. This step gives the passive parameters of the neurons and the adaptation current η (figure 2.2 B, middle panel, inset). Note that here we voluntarily discard the spikes from the data (because we only consider the subset ψ_2, see Appendix C), but it is straightforward to apply the same linear regression method on the whole recording (including the spikes). To do this we put $T_{\text{refr}} = 0$ so that the first bins in $\eta(t)$ model the shape of the spike and an explicit reset of the voltage is no longer be necessary.

We presented a method to extract the coefficients a_k that govern the shape of the spike-triggered current η from the data. However, when a model IF_N is considered, the time constants τ_i and the amplitude b_i of the adaptation currents w_i are extracted from $\eta(t) = \sum_k a_k f^{(k)}(t)$ by fitting N exponential functions to the time course $\eta(t)$. When a model $\text{IF}_{\eta_{\text{cond}}}$ is considered, we observe that if E_{rev} is known a priori, then exactly the same protocol can be applied. So we perform the linear regression defined by Eq. 2.18 iteratively for a set of $\{E_{\text{rev}}\}$ and chose the optimal $\hat{E}_{\text{rev}}$ to be the one that minimizes the SSE of the regression (see Figure 2.7 A and B).

D2. Estimation of the voltage threshold parameters

As discussed in step 3 of the Section 'Fitting Protocol', it is possible to extract the cumulative dynamic threshold γ from the data by maximizing the likelihood of generating the experimental spike train by our model. The log-likelihood for a spike train can be written in terms of the probability p_t of observing no spike in an experimental time bin by using Bayes theorem

recursively in time (Paninski, 2004):

$$\log L(\vec{\theta}_3) = \sum_{\{\hat{t}_j\}} \log(1 - p_t) + \sum_{\tilde{\psi}_2} \log(p_t) \tag{2.19}$$

where the set of spike times $\{\hat{t}_j\}$ is taken to be 0.5 ms before the peak of the spike and $\tilde{\psi}_2$ contains segments of the voltage trace with the exact spike times removed (see Appendix C). Given the model defined by Eq. 2.3, 2.4 and 2.5, the probability of having no spike in a time bin $[t, t + \Delta_T)$ is (Gerstner and Kistler, 2002):

$$p_t = \exp\left(-\int_t^{t+\Delta_T} \lambda(t')dt'\right) \approx e^{-\lambda_t \Delta_T} \tag{2.20}$$

where the approximation holds for small Δ_T (here $\Delta_T = 0.05$ ms). λ_t is the discretized version of $\lambda(t)$. Using Eq. 2.4 we have:

$$\lambda_t = \lambda_0 \exp(\vec{X}_t \vec{\theta}_3) \tag{2.21}$$

where the vector $\vec{X}_t$ is made of V_t, one, and $\sum_{\{\hat{t}_j\}} f_t^{(p)}$, and the parameters are $\vec{\theta}_3 = [\frac{1}{\Delta V}, -\frac{V_0}{\Delta V}, -\frac{c_1}{\Delta V}, \ldots, -\frac{c_P}{\Delta V}]^T$. Note that to avoid correlations between the parameters for subthreshold voltage and the parameters that describe the spike emission process, we use the recorded voltage V_t and not the modeled voltage, as it would be done with a purely generative model. Now, using λ_t defined in Eq. 2.21 with $\lambda_0 = 1/\Delta_T$ and using the fact that $\lambda_t \Delta_T$ is small, the optimal set of parameter $\hat{\vec{\theta}}_3$ is simply given by:

$$\hat{\vec{\theta}}_3 = \text{argmax}_{\vec{\theta}_3}\left(\sum_{\{\hat{t}_j\}} \vec{X}_t \vec{\theta}_3 - \sum_{\tilde{\psi}_2} \exp(\vec{X}_t \vec{\theta}_3)\right) \tag{2.22}$$

With the exponential link-function in Eq. 2.21 we are sure that the log-likelihood is a convex function of the parameters $\vec{\theta}_3$ (Paninski et al., 2005).

In Section 'Fitting Procedure' we mentionned that in order to extract the optimal parameters V_0, ΔV and c_p governing the threshold dynamics $\gamma(t)$, one has to maximize the log-likelihood of a spike train with a gradient-ascent. To perform the gradient-ascent of the log-likelihood function, the simplest method is perhaps to use a pre-programmed script (for instance `fminunc.m` in Matlab), but we used the iteratively re-weighted least-square method, also called Fischer's scoring method (McCullagh and Nelder, 1998).

All numerical computations have been done in Matlab (The Mathworks, Natwick, MA) on a desktop computer. In practice our fitting procedure is straightforward and fast; it takes only a few minutes on a desktop computer to extract all the parameters of a model from 10 seconds of voltage recordings and current injection producing a firing frequency of 10 Hz. The Matlab code used to extract the model parameters along with a subset of our data will be available on ModelDB: http://senselab.med.yale.edu/modeldb/.

3 From Stochastic Nonlinear Integrate-and-Fire to Generalized Linear Models

Variability in single neuron models is typically implemented either by a stochastic Leaky-Integrate-and-Fire model or by a model of the Generalized Linear Model (GLM) family [1]. We use analytical and numerical methods to relate state-of-the-art models from both schools of thought. First we find the analytical expressions relating the subthreshold voltage from the Adaptive Exponential Integrate-and-Fire model (AdEx) to the Spike-Response Model with escape noise (SRM as an example of a GLM). Then we calculate numerically the link-function that provides the firing probability given a deterministic membrane potential. We find a mathematical expression for this link-function and test the ability of the GLM to predict the firing probability of a neuron receiving complex stimulation. Comparing the prediction performance of various link-functions, we find that a GLM with an exponential link-function provides an excellent approximation to the Adaptive Exponential Integrate-and-Fire with colored-noise input. These results help to understand the relationship between the different approaches to stochastic neuron models.

3.1 Motivation

When it comes to modeling the intrinsic variability in simple neuron models, we can distinguish two traditional approaches. One approach is inspired by the stochastic Leaky Integrate-and-Fire (LIF) hypothesis of Stein (1967) (Stein, 1967), where a noise term is added to the system of differential equations implementing the leaky integration to a threshold. There are multiple versions of such a stochastic LIF (Gerstner and Kistler, 2002). How the noise affects the firing probability is also a function of the parameters of the neuron model. Therefore, it is important to take into account the refinements of simple neuron models in terms of

---

[1] This text is copied from Mensi et al. (2011a), full citation in the bibliography

subthreshold resonance (Izhikevich, 2001; Richardson et al., 2003), spike-triggered adaptation (Izhikevich, 2003; Mensi et al., 2011b) and non-linear spike initiation (Fourcaud-Trocme et al., 2003; Izhikevich, 2003). All these improvements are encompassed by the Adaptive Exponential Integrate-and-Fire model (AdEx (Brette and Gerstner, 2005; Badel et al., 2007)).

The other approach is to start with some deterministic dynamics for the the state of the neuron (for instance the instantaneous distance from the membrane potential to the threshold) and link the probability intensity of emitting a spike with a non-linear function of the state variable. Under some conditions, this type of model is part of a greater class of statistical models called Generalized Linear Models (GLM (McCullagh and Nelder, 1998)). As a single neuron model, the Spike Response Model (SRM) with escape noise is a GLM in which the state variable is explicitly the distance between a deterministic voltage and the threshold. The original SRM could account for subthreshold resonance, refractory effects and spike-frequency adaptation (Gerstner et al., 1996). Mathematically similar models were developed independently in the study of the visual system (Hubel and Wiesel, 1968) where spike-frequency adaptation has also been modeled (Pillow et al., 2005). Recently, this approach has retained increased attention since the probabilistic framework can be linked with the Bayesian theory of neural systems (Doya et al., 2007) and because Bayesian inference can be applied to the population of neurons (Gerwinn et al., 2008).

In this paper, we investigate the similarity and differences between the state-of-the-art GLM and the stochastic AdEx. The motivation behind this work is to relate the traditional threshold neuron models to Bayesian theory. Our results extend the work of Plesser and Gerstner (2000) (Plesser and Gerstner, 2000) since we include the non-linearity for spike initiation and spike-frequency adaptation. We also provide relationships between the parameters of the AdEx and the equivalent GLM. These precise relationships can be used to relate analog implementations of threshold models (Schemmel et al., 2008) to the probabilistic models used in the Bayesian approach.

The paper is organized as follows: We first describe the expressions relating the SRM state-variable to the parameters of the AdEx (Sect. 3.3.1) in the subthreshold regime. Then, we use numerical methods to find the non-linear link-function that models the firing probability (Sect. 3.3.2). We find a functional form for the SRM link-function that best describes the firing probability of a stochastic AdEx. We then compare the performance of this link-function with the often used exponential or linear-rectifier link-functions (also called half-wave linear rectifier) in terms of predicting the firing probability of an AdEx under complex stimulus (Sect. 3.3.3). We find that the exponential link-function yields almost perfect prediction. Finally, we explore the relations between the statistic of the noise and the sharpness of the non-linearity for spike initiation with the parameters of the SRM.

3.2   Presentation of the Models

In this section we present the general formula for the stochastic AdEx model (Sect. 3.2.1) and the SRM (Sect 3.2.2).

3.2.1 The Stochastic Adaptive Exponential Integrate-and-Fire Model

The voltage dynamics of the stochastic AdEx is given by:

$$\tau_m \dot{V} = E_l - V + \Delta_T \exp\left(\frac{V - \Theta}{\Delta_T}\right) - Rw + RI + R\epsilon \tag{3.1}$$

$$\tau_w \dot{w} = a(V - E_l) - w \tag{3.2}$$

where τ_m is the membrane time constant, E_l the reverse potential, R the membrane resistance, Θ is the threshold, Δ_T is the shape factor and $I(t)$ the input current which is chosen to be an Ornstein-Uhlenbeck process with correlation time-constant of 5 ms. The exponential term $\Delta_T \exp(\frac{V-\Theta}{\Delta_T})$ is a non-linear function responsible for the emission of spikes and ϵ is a diffusive white noise with standard deviation σ (i.e. $\epsilon \sim \mathcal{N}(0, \sigma)$). Note that the diffusive white-noise does not imply white noise fluctuations of the voltage $V(t)$, the probability distribution of $V(t)$ will depend on Δ_T and Θ. The second variable, w, describes the subthreshold as well as the spike-triggered adaptation both parametrized by the coupling strength a and the time constant τ_w. Each time $\hat{t}_j$ the voltage goes to infinity, we assumed that a spike is emitted. Then the voltage is reset to a fixed value V_r and w is increased by a constant value b.

3.2.2 The Generalized Linear Model

In the SRM, The voltage $V(t)$ is given by the convolution of the injected current $I(t)$ with the membrane filter $\kappa(t)$ plus the additional kernel $\eta(t)$ that acts after each spikes (here we split the spike-triggered kernel in two $\eta(t) = \eta_v(t) + \eta_w(t)$ for reasons that will become clear later):

$$V(t) = E_l + [\kappa * I](t) + \sum_{\{\hat{t}_j\}} \left(\eta_v(t - \hat{t}_j) + \eta_w(t - \hat{t}_j)\right) \tag{3.3}$$

Then at each time $\hat{t}_j$ a spike is emitted which results in a change of voltage described by $\eta(t) = \eta_v(t) + \eta_w(t)$.
Given the deterministic voltage, (Eq. 3.3) a spike is emitted according to the firing intensity $\lambda(V)$:

$$\lambda(t) = f(V(t)) \tag{3.4}$$

where $f(\cdot)$ is an arbitrary function called the *link-function*. Then the firing behavior of the SRM depends on the choice of the link-function and its parameters. The most common link-function used to model single neuron activities are the linear-rectifier and the exponential function.

3.3 Mapping

In order to map the stochastic AdEx to the SRM we follow a two-step procedure. First we derive the filter $\kappa(t)$ and the kernels $\eta_v(t)$ and $\eta_w(t)$ analytically as a function of AdEx parameters. Second, we derive the link-function of the SRM from the stochastic spike emission of the AdEx.
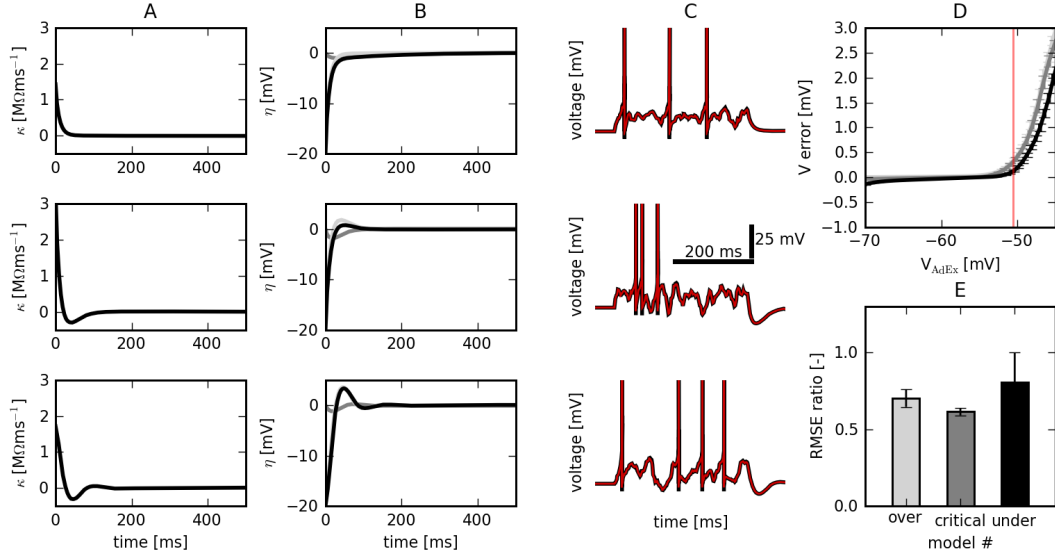
Figure 3.1: **Mapping of the subthreshold dynamics of an AdEx to an equivalent SRM.** *A*: Membrane filter $\kappa(t)$ for three different sets of parameters of the AdEx leading to over-damped, critically damped and under-damped cases (upper, middle and lower panel, respectively). *B*: Spike-Triggered $\eta(t)$ (black), $\eta_v(t)$ (light gray) and η_w (gray) for the three cases. *C*: Example of voltage trace produced when an AdEx is stimulated with a step of colored noise (black). The corresponding voltage from a SRM stimulated with the same current and where we forced the spikes to match those of the AdEx (red). *D*: Error in the subthreshold voltage ($V_{\mathrm{AdEx}} - V_{\mathrm{GLM}}$) as a function of the mean voltage of the AdEx, for the three different cases: over-, critically and under-damped (light gray, gray and black, respectively) with $\Delta_T = 1$ mV. Red line represents the voltage threshold Θ. *E*: Root Mean Square Error (RMSE) ratio for the three cases with $\Delta_T = 1$ mV. The RMSE ratio is the RMSE between the deterministic V_{SRM} and the stochastic V_{AdEx} divided by the RMSE between repetitions of the stochastic AdEx voltage. The error bar shows a single standard deviation as the RMSE ratio is averaged accross multiple value of σ.

3.3.1 Subthreshold voltage dynamics

We start by assuming that the non-linearity for spike initiation does not affect the mean subthreshold voltage of the stochastic AdEx (see Figure 3.1 D). This assumption is motivated by the small Δ_T observed in *in-vitro* recordings (from 0.5 to 2 mV (Brette and Gerstner, 2005; Badel et al., 2007)) which suggest that the subthreshold dynamics are mainly linear except very close to Θ. Also, we expect that the non-linear link-function will capture some of the dynamics due to the non-linearity for spike initiation. Thus it is possible to rewrite the deterministic subthreshold part of the AdEx (Eq. 3.1-3.2 without ϵ and without $\Delta_T \exp((V - \Theta)/\Delta_T)$) using

matrices:

$$\dot{\mathbf{x}} = A\mathbf{x} \tag{3.5}$$

$$\text{with } \mathbf{x} = \begin{pmatrix} V \\ w \end{pmatrix} \text{ and } A = \begin{bmatrix} -\frac{1}{\tau_m} & -\frac{1}{g_l\tau_m} \\ \frac{a}{\tau_w} & -\frac{1}{\tau_w} \end{bmatrix} \tag{3.6}$$

In this form, the dynamics of the deterministic AdEx voltage is a damped oscillator with a driving force. Depending on the eigenvalues of A the system could be over-damped, critically damped or under-damped. The filter $\kappa(t)$ of the GLM is given by the impulse response of the system of coupled differential equations of the AdEx, described by Eq. 3.5 and 3.6. In other words, one has to derive the response of the system when stimulating with a Dirac-delta function. The type of damping gives three different qualitative shapes of the kernel $\kappa(t)$, which are summarized in Table 3.1 and Figure 3.1 A. Since the three different filters also affect the nature of the stochastic voltage fluctuations, we will keep the distinction between over-damped, critically damped and under-damped scenarios throughout the paper. This means that our approach is valid for at least 3 types of diffusive voltage-noise (i.e. the white noise ϵ in Eq. 3.1 filtered by 3 different membrane filters $\kappa(t)$).

To complete the description of the deterministic voltage, we need an expression for the spike-triggered kernels. The voltage reset at each spike brings a spike-triggered jump in voltage of magnitude $\Delta = V_r - V(\hat{t})$. This perturbation is superposed to the current fluctuations due to $I(t)$ and can be mediated by a Delta-dirac pulse of current. Thus we can write the voltage reset kernel by:

$$\eta_v(t) = \frac{\Delta}{\kappa(0)} [\delta * \kappa](t) = \frac{\Delta}{\kappa(0)} \kappa(t) \tag{3.7}$$

where $\delta(t)$ is the Dirac-delta function. The shape of this kernel depends on $\kappa(t)$ and can be computed from Table 3.1 (see Figure 3.1 B).

Finally, the AdEx mediates spike-frequency adaptation by the jump of the second variables w. From Eq. 3.2 we can see that this produces a current $w_{\text{spike}}(t) = b\exp(-t/\tau_w)$ that can cumulate over subsequent spikes. The effect of this current on voltage is then given by the convolution of $w_{\text{spike}}(t)$ with the membrane filter $\kappa(t)$. Thus in the SRM framework the spike-frequency adaptation is taken into account by:

$$\eta_w(t) = [w_{\text{spike}} * \kappa](t) \tag{3.8}$$

Again the precise form of $\eta_w(t)$ depends on $\kappa(t)$ and can be computed from Table 3.1 (see Figure 3.1 B).

At this point, we would like to verify our assumption that the non-linearity for spike emission can be neglected. Fig. 3.1 C and D shows that the error between the voltage from Eq. 3.3

Membrane Filter: $\kappa(t)$		
over-damped if: $(\tau_m + \tau_w)^2 > \frac{4\tau_m\tau_w(g_l+a)}{g_l}$	critically-damped if: $(\tau_m + \tau_w)^2 = \frac{4\tau_m\tau_w(g_l+a)}{g_l}$	under-damped if: $(\tau_m + \tau_w)^2 < \frac{4\tau_m\tau_w(g_l+a)}{g_l}$
$\kappa(t) = k_1 e^{\lambda_1 t} + k_2 e^{\lambda_2 t}$ $\lambda_1 = \frac{1}{2\tau_m\tau_w}\left(-(\tau_m+\tau_w) + \sqrt{(\tau_m+\tau_w)^2 - 4\frac{\tau_m\tau_w}{g_l}(g_l+a)}\right)$ $\lambda_2 = \frac{1}{2\tau_m\tau_w}\left(-(\tau_m+\tau_w) - \sqrt{(\tau_m+\tau_w)^2 - 4\frac{\tau_m\tau_w}{g_l}(g_l+a)}\right)$ $k_1 = \frac{-(1+(\tau_m\lambda_2))}{C\tau_m(\lambda_1-\lambda_2)}$ $k_2 = \frac{1+(\tau_m\lambda_1)}{C\tau_m(\lambda_1-\lambda_2)}$	$\kappa(t) = (\alpha t + \beta)e^{\lambda t}$ $\lambda = \frac{-(\tau_m+\tau_w)}{2\tau_m\tau_w}$ $\alpha = \frac{\tau_m-\tau_w}{2C\tau_m\tau_w}$ $\beta = \frac{1}{C}$	$\kappa(t) = (k_1 \cos(\omega t) + k_2 \sin(\omega t))e^{\lambda t}$ $\lambda = \frac{-(\tau_m+\tau_w)}{2\tau_m\tau_w}$ $\omega = \sqrt{\left|\left(\frac{\tau_w-\tau_m}{2\tau_m\tau_w}\right)^2 - \frac{a}{g_l\tau_m\tau_w}\right|}$ $k_1 = \frac{1}{C}$ $k_2 = \frac{-(1+\tau_m\lambda)}{C\omega\tau_m}$

Table 3.1: **Analytical expressions for the membrane filter** $\kappa(t)$ in terms of the parameters of the AdEx for over-, critically-, and under-damped cases.

and the voltage from the stochastic AdEx is generally small. Moreover, we see that the main contribution to the voltage prediction error is due to the mismatch close to the spikes. However the non-linearity for spike initiation may change the probability distribution of the voltage fluctuations, which in turn influences the probability of spiking. This will influence the choice of the link-function, as we will see in the next section.

3.3.2 Spike Generation

Using $\kappa(t)$, $\eta_v(t)$ and $\eta_w(t)$, we must relate the spiking probability of the stochastic AdEx as a function of its deterministic voltage. According to (Gerstner and Kistler, 2002) the probability of spiking in time bin dt given the deterministic voltage $V(t)$ is given by:

$$p(V) = \text{prob\{spike in [t, t+dt]\}} \quad = \quad 1 - \exp\left(-f(V(t))dt\right) \tag{3.9}$$

where $f(\cdot)$ gives the firing intensity as a function of the deterministic $V(t)$ (Eq. 3.3). Thus to extract the link-function f we have to compute the probability of spiking given $V(t)$ for our SRM. To do so we apply the method proposed by Jolivet *et al.* (2004) (Jolivet et al., 2004), where the probability of spiking is simply given by the distribution of the deterministic voltage

estimated at the spike times divided by the distribution of the SRM voltage when there is no spike (see figure 3.2 A). One can numerically compute these two quantities for our models using N repetitions of the same stimulus.

The standard deviation σ of the noise and the parameter Δ_T of the AdEx non-linearity may affect the shape of the link-function. We thus extract $p(V)$ for different σ and Δ_T (Fig. 3.2 B). Then using visual heuristics and previous knowledge about the potential analytical expression of the link-funtion, we try to find a simple analytical function that captures $p(V)$ for a large range of combinations of σ and Δ_T. We observed that the $\log(-\log(p))$ is close to linear in most studied conditions Fig. 3.2 B suggesting the following two distributions of $p(V)$:

$$p(V) \quad = \quad 1 - \exp\left(-\exp\left(\frac{V - V_T}{\Delta V}\right)\right) \tag{3.10}$$

$$p(V) \quad = \quad \exp\left(-\exp\left(-\frac{V - V_T}{\Delta V}\right)\right) \tag{3.11}$$

Once we have $p(V)$, we can use Eq. 3.4 to obtain the equivalent SRM link-function, which leads to:

$$f(V) = \frac{-1}{dt}\log\left(1 - p(V)\right) \tag{3.12}$$

Then the two potential link-functions of the SRM can be derived from Eq. 3.10 and Eq. 3.11 (respectively):

$$f(V) \quad = \quad \lambda_0 \exp\left(\frac{V - V_T}{\Delta V}\right) \tag{3.13}$$

$$f(V) \quad = \quad -\lambda_0 \log\left(1 - \exp\left(-\exp\left(-\frac{V - V_T}{\Delta V}\right)\right)\right) \tag{3.14}$$

with $\lambda_0 = \frac{1}{dt}$, V_T the threshold of the SRM and ΔV the sharpness of the link-function (i.e. the parameters that governs the degree of the stochasticity). Note that the exact value of λ_0 has no importance since it is redundant with V_T. Eq. 3.13 is the standard exponential link-function, but we call Eq. 3.14 the log-exp-exp link-function.

3.3.3 Prediction

The next point is to evaluate the fit quality of each link-function. To do this, we first estimate the parameters V_T and ΔV of the GLM link-function that maximize the likelihood of observing a spike train generated with an AdEx. Second we look at the predictive power of the resulting SRM in terms of Peri-Stimulus Time Histogram (PSTH). In other words we ask how close the spike trains generated with a GLM are from the spike train generated with a stochastic AdEx when both models are stimulated with the same input current.

For any GLM with link-function $f(V) \equiv f(t|I, \theta)$ and parameters θ regulating the shape of $\kappa(t)$,
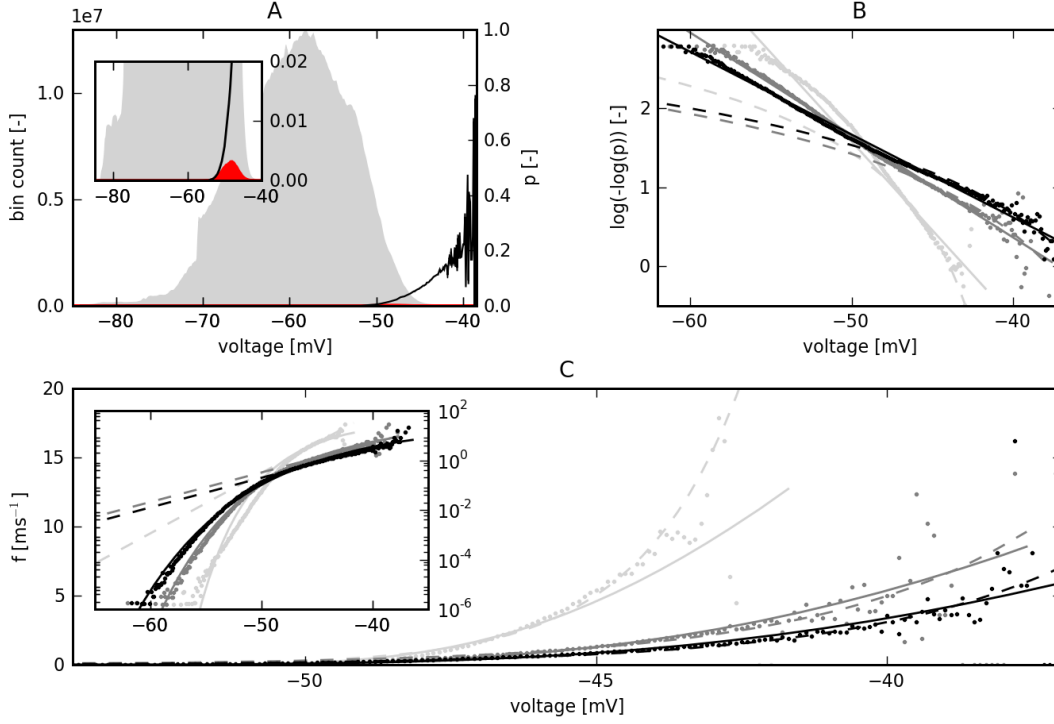
Figure 3.2: **SRM link-function.** *A*: Histogram of the SRM voltage at the AdEx firing times (red) and at non-firing times (gray). The ratio of the two distributions gives $p(V)$ (Eq. 3.9, dashed lines). Inset, zoom to see the voltage histogram evaluated at the firing time (red). *B*: $\log(-\log(p))$ as a function of the SRM voltage for three different noise levels $\sigma = 0.07, 0.14, 0.18$ nA (pale gray, gray, black dots, respectively) and $\Delta_T = 1$ mV. The line is a linear fit corresponding to the log-exp-exp link-function and the dashed line corresponds to a fit with the exponential link-function. *C*: Same data and labeling scheme as *B*, but plotting $f(V)$ according to Eq. 3.12. The lines are produced with Eq. 3.14 with parameters fitted as described in *B*. and the dashed lines are produced with Eq. 3.13. Inset, same plot but on a semi-log(y) axis.

$\eta_v(t)$ and $\eta_w(t)$, the Negative Log-Likelihood (NLL) of observing a spike-train $\{\hat{t}\}$ is given by:

$$\text{NLL} \quad = \quad -\left(\sum_{\hat{t}} \log(f(t|I,\theta)) - \sum_{t} f(t|I,\theta) \right) \tag{3.15}$$

It has been shown that the negative log-likelihood is convex in the parameters if f is convex and log-concave (Paninski, 2004). It is easy to show that a linear-rectifier link-function, the exponential link-function and the log-exp-exp link-function all satisfy these conditions. This allows efficient estimation of the optimal parameters $\hat{V}_T$ and $\hat{\Delta V}$ using a simple gradient descent. One can thus estimate from a single AdEx spike train the optimal parameters of a given link-function, which is more efficient than the method used in Sect. 3.3.2.
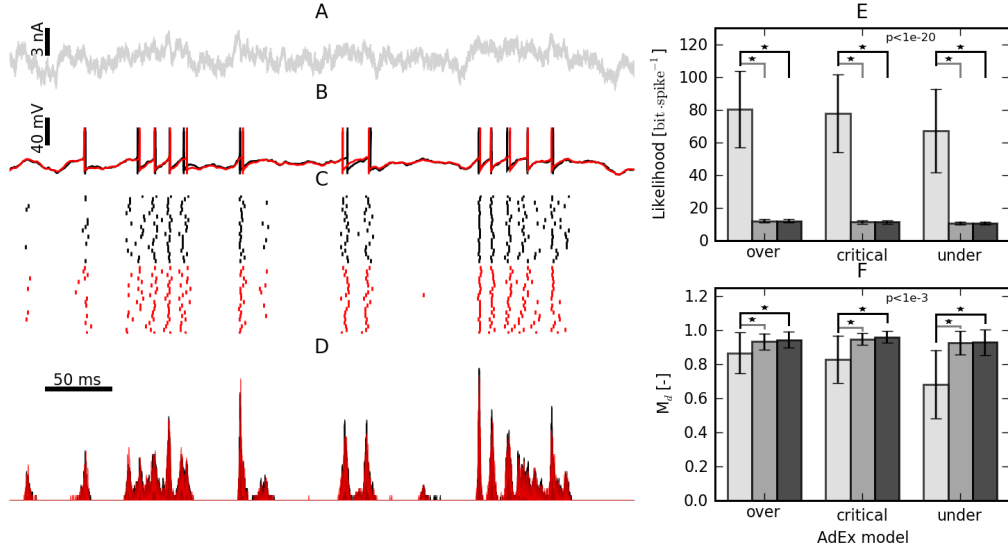
Figure 3.3: **PSTH prediction.** *A*: Injected current. *B*: Voltage traces produced by an AdEx (black) and the equivalent SRM (red), when stimulated with the current in *A*. *C*: Raster plot for 20 realizations of AdEx (black tick marks) and equivalent SRM (red tick marks). *D*: PSTH of the AdEx (black) and the SRM (red) obtained by averaging 10,000 repetitions. *E*: Optimal log-likelihood for the three cases of the AdEx, using three different link-functions, a linear-rectifier (light gray), an exponential link-function (gray) and the link-function defined by Eq. 3.14 (dark gray), these values are obtained by averaging over 40 different combinations σ and Δ_T (see Fig. 3.4). Error bars are one standard deviation, the stars denote a significant difference, two-sample t-test with $\alpha = 0.01$. *F*: same as *E*. but for M_d (Eq. 3.16).

The minimal NLL resulting from the gradient descent gives an estimation of the fit quality. A better estimate of the fit quality is given by the distance between the PSTHs in response to stimuli not used for parameter fitting . Let $v_1(t)$ be the PSTH of the AdEx, and $v_2(t)$ be the PSTH of the fitted SRM, then we use $M_d \in [0, 1]$ as a measure of match:

$$M_d = \frac{2\int (v_1(t) - v_2(t))^2 \, dt}{\int v_1(t)^2 \, dt + \int v_2(t)^2 \, dt} \tag{3.16}$$

$M_d = 1$ means that it is impossible to differentiate the SRM from the AdEx in terms of their PSTHs, whereas a M_d of 0 means that the two PSTHs are completely different. Thus M_d is a normalized similarity measure between two PSTHs. In practice, M_d is estimated from the smoothed (boxcar average of 1 ms half-width) averaged spike train of 1 000 repetitions for each models. We use both the NLL and M_d to quantify the fit quality for each of the three damping cases and each of the three link-functions.

Figure 3.3 shows the match between the stochastic AdEx used as a reference and the derived GLM when both are stimulated with the same input current (Fig. 3.3 A). The resulting voltage traces are almost identical (Fig. 3.3 B) and both models predict almost the same spike trains and so the same PSTHs (Fig. 3.3 C and D). More quantitalively, we see on Fig. 3.3 E and F, that the linear-rectifier fits significantly worse than both the exponential and log-exp-exp

link-functions, both in terms of NLL and of M_d. The exponential link-function performs as well as the log-exp-exp link-function, with a spike train similarity measure M_d being almost 1 for both.

Finally the likelihood-based method described above gives us the opportunity to look at the relationship between the AdEx parameters σ and Δ_T that governs its spike emission and the parameters V_T and ΔV of the link-function (Fig. 3.4). We observe that an increase of the noise level produces a flatter link-function (greater ΔV) while an increase in Δ_T also produces an increase in ΔV and V_T (note that Fig. 3.4 shows ΔV and V_T for the exponential link-function only, but equivalent results are obtained with the log-exp-exp link-function).
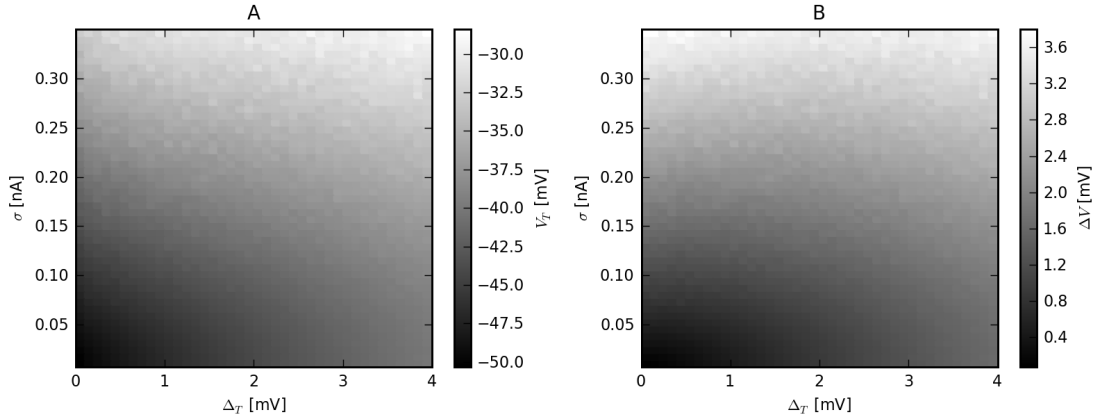
Figure 3.4: **Influence of the AdEx parameters on the parameters of the exponential link-function.** *A*: V_T as a function of Δ_T and σ. *B*: ΔV as a function of Δ_T and σ.

3.4 Discussion

In Sect. 3.3.3 we have shown that it is possible to predict with almost perfect accuracy the PSTH of a stochastic AdEx model using an appropriate set of parameters in the SRM. Moreover, since the subthreshold voltage of the AdEx also gives a good match with the deterministic voltage of the SRM, we expect that the AdEx and the SRM will not differ in higher moments of the spike train probability distributions beyond the PSTH. We therefore conclude that diffusive noise models of the type of Eq. 3.1-3.2 are equivalent to GLM of the type of Eq. 3.3-3.4. Once combined with similar results on other types of stochastic LIF (*e.g.* correlated noise), we could bridge the gap between the literature on GLM and the literature on diffusive noise models. Another noteworthy observation pertains to the nature of the link-function. The link-function has been hypothesized to be a linear-rectifier, an exponential, a sigmoidal or a Gaussian (Plesser and Gerstner, 2000). We have observed that for the AdEx the link-function follows Eq. 3.14 that we called the log-exp-exp link-function. Although the link-function is log-exp-exp for most of the AdEx parameters, the exponential link-function gives an equivalently good prediction of the PSTH. This can be explained by the fact that the difference between log-exp-exp and exponential link-functions happens mainly at low voltage (i.e. far from the threshold),

where the probability of emitting a spike is so low (Figure 2 C, until -50 mv). Therefore, even if the exponential link-function overestimates the firing probability at these low voltages it rarely produces extra spikes. At voltages closer to the threshold, where most of the spikes are emitted, the two link-functions behave almost identically and hence produce the same PSTH. The Gaussian link-function can be seen as lying in-between the exponential link-function and the log-exp-exp link-function in Fig. 3.2. This means that the work of Plesser and Gerstner (2000) (Plesser and Gerstner, 2000) is in agreement with the results presented here. The importance of the time-derivative of the voltage stressed by Plesser and Gerstner (leading to a two-dimensional link-function $f(V, \dot{V})$) was not studied here to remain consistent with the typical usage of GLM in neural systems (Doya et al., 2007).

Finally we restricted our study to exponential non-linearity for spike initiation and do not consider other cases such as the Quadratic Integrate-and-fire (QIF, (Izhikevich, 2003)) or other polynomial functional shapes. We overlooked these cases for two reasons. First, there are many evidences that the non-linearity in neurons (estimated from *in-vitro* recordings of Pyramidal neurons) is well approximated by a single exponential (Badel et al., 2007). Second, the exponential non-linearity of the AdEx only affects the subthreshold voltage at high voltage (close to threshold) and thus can be neglected to derive the filters $\kappa(t)$ and $\eta(t)$. Polynomial non-linearities on the other hand affect a larger range of the subthreshold voltage so that it would be difficult to justify the linearization of subthreshold dynamics essential to the method presented here.

4 Automated high-throughput parameter extraction for Generalized Integrate and Fire models

In order to perform realistic large-scale simulations of brain activity, mathematical models need to be developed that accurately capture the spiking activity of individual neurons[1]. To account for the large variety of behaviors observed in different neuronal types, single-neuron models should be flexible and allow efficient parameter extraction from experimental recordings. Here we demonstrate that, using a convex optimization procedure we previously introduced, a Generalized Integrate and Fire model capable of predicting both the spiking activity and the subthreshold dynamics of different cell types, can be accurately fitted with a limited amount of data. Based on our results, a procedure is proposed that, combined with a recently developed technology for automatic patch-clamp recordings, allows automated high-throughput characterization of single neurons.

4.1 Introduction

In the field of computational neuroscience, the last years have been characterized by the announcements of several large-scale projects aimed to build realistic models of the electrical activity of entire brains (Markram, 2006; Koch and Reid, 2012; Waldrop, 2012; Kandel et al., 2013; Lang et al., 2011). To achieve this ambitious goal, it is of crucial importance to build accurate models of the brain's fundamental building blocks: the single neurons.

Ideally, a single-neuron model should be sufficiently complex and flexible to capture the spiking activity of real neurons, but also relatively simple to allow large-scale simulations and robust parameter estimation (Herz et al., 2006; Gerstner and Naud, 2009). Detailed biophysical models with stochastic ion channel dynamics can in principle account for every aspect of the single-neuron activity; however, due to their complexity, they require high computational

---

[1]This text is copied from (Mensi et al., 2014), full citation in the bibliography

power (Herz et al., 2006; Markram, 2006; Lang et al., 2011). While systematic fitting of detailed biophysical models is possible (Gold et al., 2006; Huys et al., 2006; Druckmann et al., 2007; Hay et al., 2011; Vavoulis et al., 2012), a computationally efficient solution to this problem is not known (Gerstner and Naud, 2009). Parallel to efforts of large scale biophysical modeling (Markram, 2006; Lang et al., 2011), there exist also large scale simulations approaches based on simplified threshold models in which the biophysical mechanisms relevant for neural computation are accounted for by phenomenological descriptions (Brainscales; Izhikevich and Edelman, 2008; Gewaltig and Diesmann, 2007). These approaches are supported by several studies showing that simplified spiking models are able to accurately predict the single-neuron activity with millisecond precision (Keat et al., 2001; Paninski et al., 2005; Jolivet et al., 2008; Kobayashi et al., 2009; Dong et al., 2013), at least for the case of single-electrode somatic stimulation; but see (Häusser et al., 2000; Larkum et al., 2009).

On the experimental side, a new *in vivo* technology has recently been developed that allows for automatic single-neuron intracellular recordings (Kodandaramaiah et al., 2012). With this method, a robot can establish a whole-cell patch-clamp seal in approximatively five minutes. In the near future, *in vitro* automatic patch-clamp techniques combined with genetic labeling will probably make high-throughput electrophysiology from identified neuronal types possible (Dunlop et al., 2008). In order to make sense of the resulting large dataset expected from such high-throughput methods, adequate computational tools have to be developed.

Here we demonstrate that a Generalized Integrate-and-Fire (GIF) model capable of predicting both the spiking activity and the subthreshold dynamics of different neuronal types (Mensi et al., 2011b; Pozzorini et al., 2013), can be robustly fitted using only 100 seconds of *in vitro* recordings. To validate parameter extraction, a short protocol is proposed in which the ability of GIF models in predicting the spiking response to new inputs is quantified. Overall, we found that fitting and validating a GIF model takes approximatively five minutes. Considering the time required to automatically establish a patch-clamp seal, the complete characterization of a single neuron can therefore be achieved in around ten minutes. We therefore conclude that modern computational tools are suitable for high-throughput modeling of single neurons.

4.2 Results

The Results section is organized as follows. In the first two sections, we respectively define the GIF model and the procedures used for parameter extraction and model validation. Using artificial data generated by the GIF model itself, we then determine the amount of data and the computing time required to perform accurate parameter extraction and model validation. Based on these results, an experimental protocol is established that enables automated high-throughput characterization of single neurons. In the last sections, the validity of this protocol is verified using *in silico* recordings obtained by simulating the activity of a multi-compartmental conductance-based model (Hay et al., 2011) as well as *in vitro* recordings from layer 5 (L5) pyramidal neurons obtained with standard patch-clamp technique. The GIF

model performance is finally compared against that of a standard Generalized Linear Model (GLM) (Truccolo et al., 2005; Pillow et al., 2008).

4.2.1 Generalized Integrate and Fire model

The GIF model discussed in this study (Mensi et al., 2011b; Pozzorini et al., 2013) is a leaky integrate-and-fire model augmented with a spike-triggered current $\eta(t)$, a moving threshold $\gamma(t)$ and the escape rate mechanism (Gerstner and Kistler, 2002; Jolivet et al., 2006) for stochastic spike emission (Figure 4.1 **A**). This model is able to predict both the spiking activity and the subthreshold dynamics of individual neurons (Figure 4.1 **B**) and it is flexible enough to capture the behavior of different neuronal types (Mensi et al., 2011b).
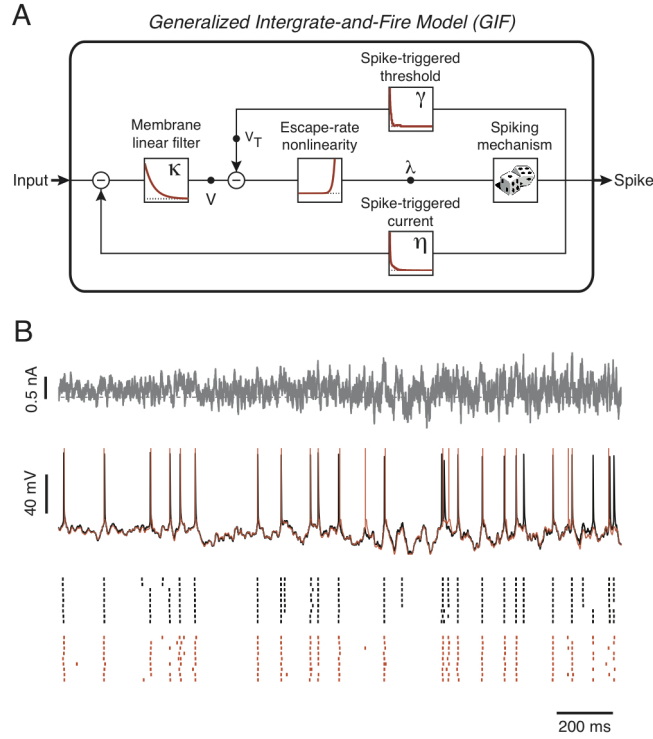
Figure 4.1: **The GIF model accurately predicts both the subthreshold and the spiking activity of cortical neurons. (A)** Block representation of the GIF model. The membrane acts as a low-pass filter $\kappa(t) = \frac{1}{C}\exp\left(-\frac{g_L t}{C}\right)$ on the input current $I(t)$ to produce the modeled potential $V(t)$. The exponential nonlinearity (escape-rate) transforms this voltage into an instantaneous firing intensity $\lambda(t)$, according to which spikes are generated. Each time a spike is emitted, both a current $\eta(t)$ and a movement of the firing threshold $\gamma(t)$ are triggered. **(B)** The GIF model accurately predicts the occurrence of individual spikes with millisecond precision. To evaluate the predictive power of the GIF model, the response of a L5 pyramidal neuron to a fluctuating input current (top) has been recorded intracellularly (middle, black). The same protocol was repeated nine times to assess the reliability of the neural response (bottom, black raster). The GIF model (with parameters extracted using a different dataset) was able to accurately predict both the subthreshold (middle, red) and the spiking response (bottom, red raster) of the cell.

In the model, the subthreshold membrane potential $V(t)$ evolves according to the following differential equation:

$$C\dot{V}(t) = -g_\mathrm{L}(V(t) - E_\mathrm{L}) - \sum_{\hat{t}_j < t} \eta(t - \hat{t}_j) + I(t),\tag{4.1}$$

where the parameters C, g_L and E_L define the passive properties of the neuron, $I(t)$ is the input current and $\{\hat{t}_j\}$ are the spike times. According to Equation 4.1, each time an action potential is fired, an intrinsic current with stereotypical shape $\eta(t)$ is triggered. By convention, the spike-triggered current $\eta(t)$ is hyperpolarizing when its amplitude is positive and depolarizing otherwise. Currents triggered by different spikes accumulate and produce spike-frequency adaptation, if $\eta(t) > 0$ (or facilitation, if $\eta(t) < 0$). The functional shape of $\eta(t)$ varies among neuron types (Mensi et al., 2011b). Consequently the time course of $\eta(t)$ is not assumed *a priori* but is extracted from intracellular recordings. Each time a spike is emitted, the numerical integration is stopped during a short absolute refractory period T_ref and the membrane potential is reset to $V(\hat{t}_j + T_\mathrm{ref}) = V_\mathrm{reset}$.

Spikes are produced stochastically according to a point process with conditional firing intensity $\lambda(t|V, V_T)$, which exponentially depends on the momentary difference between the membrane potential $V(t)$ and the firing threshold $V_\mathrm{T}(t)$ (Gerstner and van Hemmen, 1992; Paninski et al., 2005; Jolivet et al., 2006):

$$\lambda(t|V, V_T) = \lambda_0 \cdot \exp\left(\frac{V(t) - V_T(t)}{\Delta V}\right),\tag{4.2}$$

where λ_0 has units of s^{-1}, so that $\lambda(t)$ is in Hz and ΔV defines the level of stochasticity. According to Equation 4.2, if $\Delta V \neq 0$, the probability of a spike to occur at a time $\hat{t} \in [t; t + \Delta t]$ is given by:

$$P(\hat{t} \in [t; t + \Delta t]) = 1 - \exp\left(-\int_t^{t+\Delta t} \lambda(s)\,ds\right) \approx \lambda(t)\Delta t.\tag{4.3}$$

In the limit $\Delta V \to 0$, the model becomes deterministic and action potentials are emitted at the precise moment when the membrane potential crosses the firing threshold. Importantly, the value of ΔV is extracted from experimental data.

Finally, the dynamics of the firing threshold $V_T(t)$ is given by:

$$V_T(t) = V_T^* + \sum_{\hat{t}_j < t} \gamma(t - \hat{t}_j),\tag{4.4}$$

where V_T^* is a constant and $\gamma(t)$ describes the stereotypical time course of the firing threshold after the emission of an action potential. Since the contribution of different spikes accumulates, the moving threshold defined in Equation 4.4 constitutes an additional source of adaptation (or facilitation). Similar to $\eta(t)$, the functional shape of $\gamma(t)$ is not assumed *a priori* but is extracted from intracellular recordings. To help the readers, all model parameters and

mathematical symbols used are summarized at the end of this chapter in table 4.1.

4.2.2 GIF model parameter extraction

Given the intracellular voltage response $V_{\text{data}}(t)$ evoked *in vitro* by a controlled input current $I_{\text{tr}}(t)$, all of the GIF model parameters are extracted from experimental data (*training set*) using a three-step procedure (Figure 4.2 **A**) that we previously introduced (Mensi et al., 2011a; Pozzorini et al., 2013). A detailed description of the fitting procedure can be found in the Experimental Procedures section.

In *Step 1* (Figure 4.2 **A**, Step 1), the experimental spike-train $S_{\text{data}} = \{\hat{t}_j\}$ is first defined as the collection of instants $\hat{t}_j$ at which $V_{\text{data}}(t)$ crossed a certain threshold from below. The average spike-shape $V_{\text{STA}}(t)$ is then obtained by computing the spike-triggered average (STA) of $V_{\text{data}}(t)$. Depending on the cell type (that is, depending on the average spike-shape), the absolute refractory period T_{ref} is fixed to a certain value and the reset potential is computed as $V_{\text{reset}} = V_{\text{STA}}(T_{\text{ref}})$. In the GIF model, a period of absolute refractoriness can alternatively be implemented by setting the first milliseconds of the spike-triggered threshold movement $\gamma(t)$ to very large values. For this reason, as long as T_{ref} remains smaller than the shortest interspike-interval observed in the data, its precise value is not crucial. A sensible choice is to set T_{ref} about twice the spike width at half maximum.

In *Step 2* (Figure 4.2 **A**, Step 2), the first-order temporal derivative of the experimental voltage $\dot{V}_{\text{data}}(t)$ is estimated by finite differences and the parameters θ_{sub} determining the membrane potential dynamics are extracted by fitting Equation 4.1 on $\dot{V}_{\text{data}}(t)$. This is done by exploiting the knowledge of the experimental voltage $V_{\text{data}}(t)$ and the external input $I_{\text{tr}}(t)$. To avoid *a priori* assumptions on the functional shape of the spike-triggered current, $\eta(t)$ is expanded in a linear combination of rectangular basis functions. Consequently, optimal parameters minimizing the sum of squared errors between $\dot{V}(t)$ and $\dot{V}_{\text{data}}(t)$ can be efficiently obtained by solving a multilinear regression problem (Paninski et al., 2005) (cf. Equations 4.18-4.19).

In *Step 3* (Figure 4.2 **A**, Step 3), the parameters estimated so far are first used to compute the subthreshold membrane potential of the model $\hat{V}_{\text{model}}(t)$. For that, Equation 4.1 is numerically solved by enforcing adaptation currents $\eta(t)$ at all the observed spike-times $\{\hat{t}_j\}$. Given $\hat{V}_{\text{model}}(t)$, the parameters θ_{th} defining the firing threshold dynamics (cf. Equations 4.2-4.4) are then extracted by maximizing the probability (i.e., the *log-likelihood*) of the experimental spike-train $S_{\text{data}}(t)$ being produced by the GIF model (cf. Equations 4.21-4.22). Similar to $\eta(t)$, the spike-triggered threshold movement is extracted nonparametrically by expanding $\gamma(t)$ in a linear combination of rectangular basis functions. With the exponential function in Equation 4.2, the *log-likelihood* to maximize is guaranteed to be a concave function of θ_{th} (Paninski, 2004) and the optimization problem can be solved using standard gradient ascent techniques. The method used in this last step closely resembles the standard GLM fitting procedure (Truccolo et al., 2005; Pillow et al., 2008). However, here, by exploiting the information contained in the subthreshold dynamics of the membrane potential, the maximum likelihood approach is

specifically used to infer the dynamics of the firing threshold. In contrast to GLMs, the GIF model can consequently disentangle adaptation processes mediated by intrinsic currents and threshold movements.
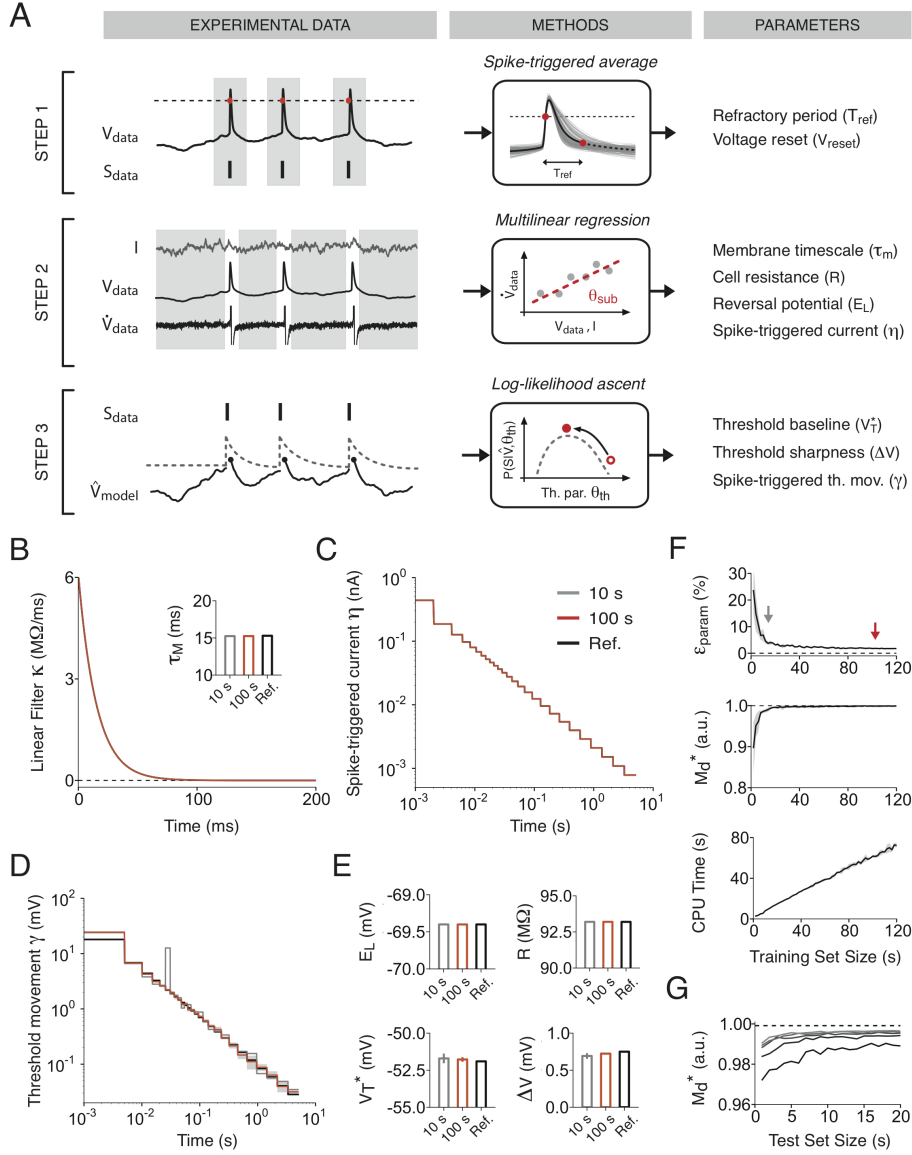
Figure 4.2: **GIF model parameter extraction.** **(A)** Schematic representation of the three-step procedure used to extract GIF model parameters from *in vitro* intracellular recordings. In *Step 1* (first row), the experimental spike-train $S_{data}(t)$ is extracted from the voltage trace $V_{data}(t)$ using a standard threshold-crossing method (left, dashed line). Parameters related to absolute refractoriness are extracted from the average spike-shape (middle). In *Step 2* (second row), given the injected current $I_{tr}(t)$ and the recorded potential V_{data}, all the parameters θ_{sub} defining the dynamics of the subthreshold membrane potential (Equation 4.1) are extracted by performing a least-square multilinear regression on the membrane potential derivative $\dot{V}_{data}(t)$. Since Equation 4.1 does not describe the membrane potential dynamics during action potentials, all the data close to spikes are discarded. In *Step 3* (third

row), the subthreshold parameters θ_{sub} are first used to compute the subthreshold voltage of the model $\hat{V}_{\mathrm{model}}(t)$. The parameters θ_{th} defining the dynamics of the firing threshold (left, dashed gray) are then extracted by maximizing the probability (i.e., the *log-likelihood*) that the experiential spike-train $S_{\mathrm{data}}(t)$ was produced by the model, given the subthreshold dynamics $\hat{V}_{\mathrm{model}}(t)$. **(B-E)** GIF model parameters used to generate the artificial data (black) and recovered using a training set of $T_{\mathrm{tr}} = 10$ seconds (gray) and $T_{\mathrm{tr}} = 100$ seconds (red). Error bars and shaded areas represent one standard deviation obtained using 5 different data sets. In case of perfect agreement, black lines, gray lines and shaded areas are not visible. **(B)** Membrane filter $\kappa(t)$. Inset: membrane timescale $\tau_{\mathrm{m}} = C/g_{\mathrm{L}}$. **(C)** Spike-triggered current $\eta(t)$. **(D)** Spike-triggered movement of the firing threshold $\gamma(t)$. **(E)** Reversal potential (E_{L}, top left); cell resistance ($R = g_{\mathrm{L}}^{-1}$, top right); threshold baseline (V_{T}^*, bottom left) and threshold sharpness (ΔV, bottom right). **(F)** Estimation error $\epsilon_{\mathrm{param}}$ on model parameters (upper panel), performance on spike-timing prediction M_d^* (middle panel) and computing time required for parameter extraction (lower panel) as a function of the training set size T_{tr}. Gray areas indicate one standard deviation across different artificial datasets generated using the same reference parameters. Gray and red arrows indicate the performance obtained with a training set of 10 s and 100 s, respectively. **(G)** Reliability of the validation procedure as a function of the number of repetitions n_{test} and the duration T_{test} of the test current. For different values of n_{test} and T_{test}, M_d^* was computed 1000 times using different test currents. Consistent with the result that M_d^* corrects the small-sample bias, the mean value of M_d^* obtained across repetitions of different test currents did not depend on n_{test} and T_{test} and was of $M_d^* = 0.998$ (dashed line). The continuous lines represent the 0.25-quantiles of the M_d^* distribution obtained with $n_{\mathrm{test}} = \{3, 6, 9, 12, 15\}$ (from dark to light gray) and indicate that the reliability of the measure increases with n_{test} and T_{test}.

4.2.3 GIF model validation

To obtain a high-throughput pipeline for GIF model parameter extraction, the method described in the previous section has to be complemented with a validation protocol designed to automatically detect and discard trials in which the fitting procedure fails. Good spiking neuron models should be able to accurately predict the occurrence of individual action potentials with millisecond precision (Gerstner and Naud, 2009). To take into account the stochastic nature of single neurons (Mainen and Sejnowski, 1995), we designed a validation protocol based on the measurement of the model performance in predicting spike emission probability. After the acquisition of the *training dataset* used for parameter extraction, a new set of recordings (*test dataset*) is performed in which single neurons are stimulated repetitively with a test current $I_{\mathrm{test}}(t)$. The resulting set of experimental spike-trains is then compared against a set of spike-trains predicted by repetitive simulations of the GIF model. To obtain a quantitative measure of the model's predictive power, the similarity M_d^* (Naud et al., 2011) between the two sets of spike-trains is computed (Experimental Procedures). M_d^* takes values between 0 and 1, where $M_d^* = 0$ indicates that the model is unable to predict any of the experimental spikes and $M_d^* = 1$ indicates a perfect match. Importantly, M_d^* avoids the *small-sample bias* known to occur when measuring the similarity between small groups of spike-trains as well as the *deterministic bias* known to favor noise-free models (Naud et al., 2011).

4.2.4 Testing GIF model parameter extraction and validation on artificial data

To estimate the amount of data required to perform GIF model parameter extraction, we first tested our fitting procedure on an artificial training set generated by simulating the response of a GIF model to a fluctuating current $I(t)$. The choice of reference parameters (Figure 4.2 **B-E**, black) was based on previous results (Pozzorini et al., 2013). In particular, both the spike-triggered current $\eta(t)$ and the threshold movement $\gamma(t)$ were defined as a linear combination of $K = 26$ log-spaced rectangular basis functions approximating a power-law decay over 5 seconds (Pozzorini et al., 2013; Lundstrom et al., 2008). Overall, the reference model had 59 parameters: 31 were related to the subthreshold dynamics and 28 to the firing threshold.

The input current $I(t)$ used to build the artificial training set was generated at $\Delta T^{-1} = 20$ kHz by numerically solving the stochastic differential equation $\tau \dot{I} = -I + I_0 + \sqrt{2\tau}\sigma(t)\xi(t)$ in discrete time

$$I(t + \Delta T) = I(t) + \frac{I_0 - I(t)}{\tau} \cdot \Delta T + \sqrt{\frac{2\sigma^2 \Delta T}{\tau}} \cdot \mathcal{N}(0, 1), \tag{4.5}$$

where $\xi(t)$ is a Gaussian white-noise process generated by independently sampling from a Normal distribution $\mathcal{N}(0, 1)$, $\tau = 3$ ms is the characteristic timescale on which the input fluctuates, I_0 defines the mean input and $\sigma(t)$ is the time-dependent standard deviation of $I(t)$. Ornstein-Uhlenbeck processes (i.e. stationary filtered Gaussian processes) have been extensively used to model the input current received *in vivo* at the soma of neocortical neurons (Destexhe and Pare, 1999). Here, we relaxed the assumption of stationarity by modulating the variance of the input with a periodic oscillation (Lundstrom et al., 2008) given by:

$$\sigma(t) = \sigma_0(1 + \Delta\sigma \sin(2\pi f t)), \tag{4.6}$$

where σ_0 and $\Delta\sigma$ are constants and $f = 0.2$ Hz is the modulation frequency. An input current with non-stationary statistics drives the neurons through different regimes producing broad ISI distributions that better constrain the fit of adaptation processes. The input parameters I_0, σ_0 and $\Delta\sigma$ were adjusted to generate an artificial training set in which the GIF model emitted spikes at an average firing rate of 10 Hz oscillating over 5 seconds between 7 and 13 Hz.

The fitting procedure illustrated in Figure 4.2 **A** was then applied to recover the reference parameters of the GIF model used to generate the artificial dataset (Figure 4.2 **B-E**, black). To estimate the amount of data required to guarantee a high degree of accuracy, this operation was repeated several times by varying the size of the training set T_{tr} (that is, the duration of the input current $I(t)$). 4.2 **B-E** shows a comparison between the reference parameters and the results obtained by fitting a training set of $T_{tr} = 10$ seconds (gray) and $T_{tr} = 100$ seconds (red). Overall, we found that 100 seconds were sufficient to accurately recover the reference parameters. To quantify the accuracy of the fit, we computed the mean error ϵ_{param} on model parameters (see Experimental Procedures) as a function of T_{tr} and found that 100 seconds were sufficient to limit the error to $\epsilon_{param} < 2.0\%$ (Figure 4.2 **F**, top). The great accuracy with which

the fitted model was able to predict the spiking activity of the reference model ($M_d^* = 0.998$) confirmed the goodness of this fit (Figure 4.2 **F**, middle). To achieve high-throughput and perform parameter extraction *on the fly*, it is crucial to minimize the computing time (CPU time) required for the fit. We measured the CPU time as a function of the training set duration T_{tr} (Figure 4.2 **F**, bottom) and we found that accurate parameter extraction from a training set of $T_{tr} = 100$ seconds requires around 60 seconds of computing. We concluded that GIF model parameter extraction is suitable for high-throughput.

A second time-consuming procedure that has to be analyzed is the validation protocol. To quantify the predictive power of the fitted model, the reference model was stimulated with repetitive injections of a test current $I_{test}(t)$ generated according to Equations 4.5-4.6. To estimate the number of repetitions n_{test} and the duration T_{test} of the test current required to obtain a reliable estimate of the model predictive power, the similarity measure M_d^* was computed multiple times using different values of n_{test} and T_{test} (Figure 4.2 **G**). On average, the value of M_d^* was independent of both the input current duration and the number of repetitions, confirming that the spike-train metrics M_d^* successfully eliminates the *small-sample bias* (Naud et al., 2011). We measured the variability of M_d^* across validation procedures performed with different realizations of $I_{test}(t)$ and found that the reliability of M_d^* increased with both the number of repetitions n_{test} and the duration of the test current T_{test} (Figure 4.2 **G**). Spike-triggered processes can last for several seconds (Pozzorini et al., 2013; Lundstrom et al., 2008). This sets a constraint on the minimal duration of both the test current $I_{test}(t)$ and the interstimulus interval. By taking into account these constraints, we concluded that, while respecting high-throughput constraints, a validation protocol based on 9 injections of a 10-second current guarantees a reliable estimation of the model's predictive power (Figure 4.2 **G**).

4.2.5 A protocol for automated high-throughput single-neuron characterization

Based on the results reported in the previous section, we designed a protocol for the fit and the validation of GIF models on *in vitro* intracellular recordings (Figure 4.3). The protocol is conceptually divided in two phases. In the first part, a *training set* is acquired by recording the single-neuron response to a fluctuating input $I_{tr}(t)$ lasting for $T_{tr} = 100$ seconds and generated according to Equations 4.5-4.6. These data are then used for parameter extraction. In the second part of the protocol, 9 repetitive injections of a new 10-second current $I_{test}(t)$ are performed with an interstimulus interval of 10 seconds, so as to allow the cell to recover. These data (*test set*) are then used to quantify the predictive power of the GIF model with the spike-train similarity measure M_d^*. Since all the computations required for parameter extraction and model validation can be performed *on the fly*, the whole protocol requires 5 minutes and is suitable for high-throughput.

Current-clamp experiments in which the same electrode is used both for stimulating and recording from single neurons are biased due to the voltage drop across the electrode (Brette

et al., 2007). To remove this bias, intracellular recordings are preprocessed using a technique called Active Electrode Compensation (AEC, refs. (Brette et al., 2007; Badel et al., 2008), see Experimental Procedures). To perform AEC, the filtering properties of the electrode have to be estimated. For that, an additional 10-second-long subthreshold injection is performed before the acquisition of the *training set* (Figure 4.3).
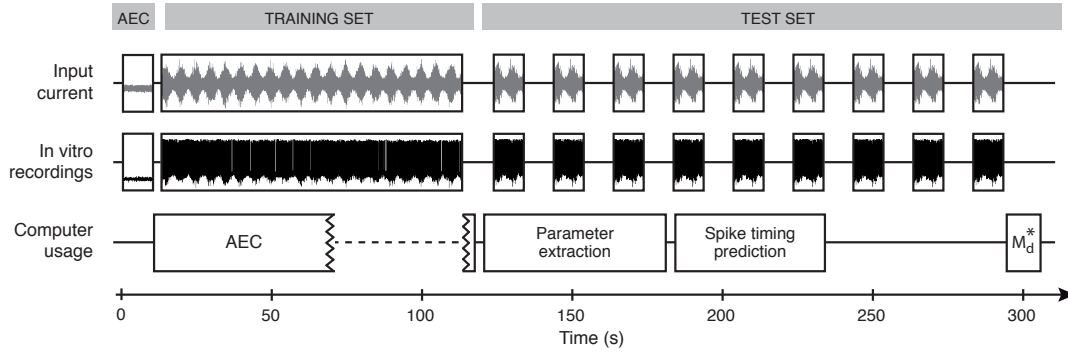
Figure 4.3: **Schematic representation of the protocol for high-throughput single-neuron characterization.** To characterize the properties of the electrode required for AEC, the experimental protocol starts with the injection of a short subthreshold current. While the filtering properties of the patch clamp are estimated (AEC left), the training dataset is collected. After training set collection, the raw data are preprocessed with AEC (AEC right). Then, in parallel with GIF model parameter extraction and successive spike timing prediction, the test dataset is collected by injecting 9 repetitions of the same time-dependent current. Finally, after complete acquisition of the test set, the similarity measure M_d^* between the observed and the predicted spike-trains is computed. Overall, GIF model parameter extraction and validation requires around 5 minutes.

4.2.6 Testing the high-throughput protocol on *in silico* recordings

A different class of models used to describe the electrical activity of individual neurons includes the so called multi-compartment conductance-based models (or detailed biophysical models). In contrast to point-neuron models, detailed biophysical models account for the intricate morphology of both dendritic and axonal arborizations and explicitly describe the dynamics of a large variety of ion channels mediating active currents. Both aspects are likely to play a role in single neuron information processing (Koch and Segev, 2000; London and Häusser, 2005). A detailed biophysical model (DBM) has recently been proposed that captures several features of L5b thick-tufted pyramidal neurons (Hay et al., 2011). In particular, this model includes active dendrites and describes the interactions between Na^+ spiking at the soma, back-propagating action potentials and Ca^{2+} spikes generated at the distal apical dendrites.

To validate our procedure for high-throughput single-neuron characterization, the protocol described in Figure 4.3 was tested *in silico* by simulating the DBM response to a set of current injections (Figure 4.4 **A**, see Experimental Procedures). The input parameters were calibrated to obtain an average firing rate of 10 Hz with slow rate fluctuations between 7 and 13 Hz (see Figure 4.4 **H**). Moreover, to model stochastic spike emission, a source of noise was introduced

by corrupting the input current with some additive white-noise (see Experimental Procedures). Capturing the DBM spiking response to dendritic injections goes beyond the scope of this study. Since we are ultimately interested in automatic somatic patching, all *in silico* experiments were preformed by delivering the current at the somatic compartment (Figure 4.4 **A**). DBM somatic recordings were then used to perform GIF model parameter extraction (Fig. 4B-D). Compared with previous results from *in vitro* recordings in L5 pyramidal neurons (Mensi et al., 2011a; Pozzorini et al., 2013), the membrane filter $\kappa(t)$ was characterized by a relatively short timescale ($\tau_m = 6.7$ ms, s.d. 0.1 ms, Figure 4.4 **B**). GIF model parameter extraction also revealed the presence of a long-lasting adaptation current (Figure 4.4 **C**) as well as a long-lasting spike-triggered movement of the firing threshold (Figure 4.4 **D**). Consistent with the tendency of L5b pyramidal neurons to produce bursts of action potentials (ref. (Hay et al., 2011) and Figure 4.4 **G**), the activation of the spike-triggered current was not instantaneous.
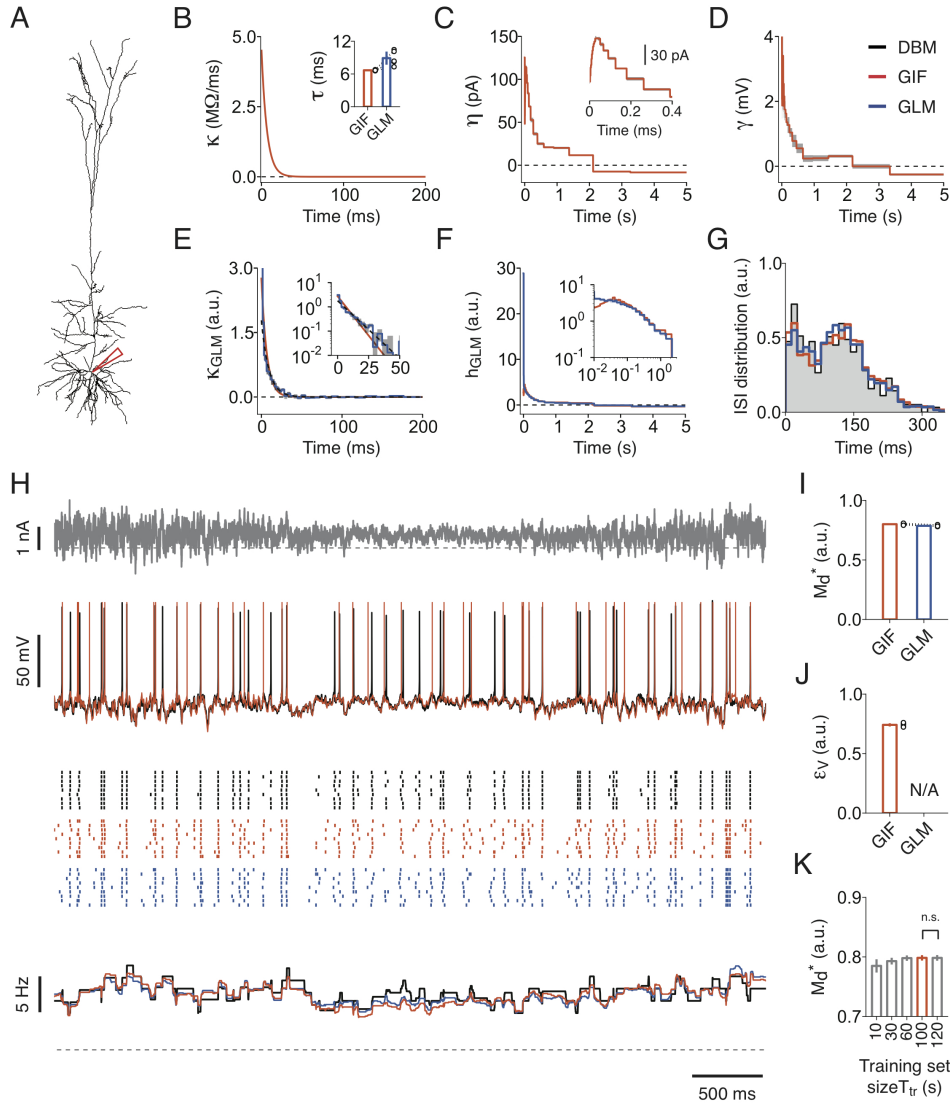
Figure 4.4: **Testing GIF model parameter extraction on *in silico* recordings from a detailed biophysical model. (A)** Reconstructed morphology of the detailed biophysical model (DBM, ref. (Hay et al., 2011)) used to validate the protocol for high-throughput single-neuron characterization. The recording site is indicated by the red pipette. **(B-D)** GIF model parameters extracted from *in silico* recordings obtained by simulating the DBM response to a somatic current injection. The filters obtained by averaging the parameters extracted from 5 independent training sets of $T_{tr} = 100$ s each are shown in red. Gray areas indicate one standard deviation. **(B)** Membrane filter $\kappa(t)$. Inset: comparison between the membrane timescale extracted using a GIF model and the timescale of the GLM linear filter (cf, exponential fit of $\kappa_{GLM(t)}$ in panel E). Each couple of open circles indicates the timescale extracted from a specific training set. Bar plots represent the mean and one standard deviation across training sets ($\tau_m = 6.7$ ms, s.d. 0.1 ms, GIF; $\tau_m = 8.9$ ms, s.d. 1.3 ms, GLM). **(C)** Spike-triggered current $\eta(t)$. **(D)** Spike-triggered movement of the firing threshold $\gamma(t)$. **(E-F)** GLM parameters extracted from the same *in silico* recordings used to fit the GIF model. Average filters are shown in blue. Gray areas indicate one standard deviation across training sets. **(E)** Linear filter $\kappa_{GLM}(t)$ (blue) and exponential fit (dashed black). For comparison, a rescaled version of the membrane filter $\kappa(t)$ is shown in red. Inset: same data displayed on semi-logarithmic scales. **(F)** History filter $h_{GLM}(t)$. For comparison, a rescaled version of the GIF model effective filter $h(t)$ (Equation 4.8) is shown in red. Inset: same data displayed on double-logarithmic scales. **(G)** Interspike-interval (ISI) distributions computed using the *test set* data (black) the GIF model prediction (red) and the GLM prediction (blue). **(H)** Fraction of the input current $I_{test}(t)$ (top, gray) used for model validation; typical DBM response evoked by a single current injection (middle, black); DBM spiking activity in response to nine repetitive injections of the same input (bottom, black raster); PSTH constructed by averaging the nine spike-trains smoothed with a rectangular 500-ms window (bottom, black line). GIF model and GLM predictions are shown in red and blue, respectively. Dashed black lines represent 0 nA (top) and 0 Hz (bottom). **(I-K)** Performance comparison between GIF model (red) and GLM (blue) in predicting the DBM activity. Parameter extraction and model validation were repeated five times using different datasets. Each couple of open circles indicates the performance obtained by both models on a specific dataset. Bar plots indicate the mean one standard deviation across repetitions. **(I)** Spike-timing prediction as quantified by M_d^* with precision $\Delta = 4$ ms. **(J)** Mean prediction error ϵ_V on subthreshold membrane potential fluctuations. The GLM does not explicitly model the subthreshold membrane potential dynamics and is therefore not applicable (N/A). **(K)** GIF model spike-timing prediction (M_d^*, with precision $\Delta = 4$ ms) as a function of the training set size used for parameter extraction. Increasing the duration of the training set from 100 s to 120 s does not improve the GIF model predictive power ($M_d^* = 0.80$, s.d. 0.01, $T_{tr} = 100$ s; $M_d^* = 0.80$, s.d. 0.01, $T_{tr} = 120$ s; n=10, paired Student t-test, $t_4 = 0.05$, $p = 0.97$; n.s. > 0.05).

In the GIF model, the passive properties of the membrane are described by a single exponential filter (see Figure 4.1 **A**):

$$\kappa(t) = \frac{R}{\tau_m} \cdot \exp\left(-\frac{t}{\tau_m}\right) \tag{4.7}$$

According to cable theory (Rall, 2011), the large number of dendritic branches explicitly modeled in the DBM, is expected to manifest itself in a linear filter decaying over multiple timescales. To verify the accuracy of the single-exponential assumption and to compare the GIF model performance against a reference model, we also used the *in silico* recordings to fit a Generalized Linear Model (GLM, (Truccolo et al., 2005; Pillow et al., 2008), Figure 4.4 **E-F**). In the GLM, the linear filter $\kappa_{GLM}(t)$ is not assumed *a priori* to be an exponential function and its shape is extracted from experimental data using a non-parametric method (see Experimental Procedures). We found that the GLM filter $\kappa_{GLM}(s)$ and the membrane filer $\kappa(t)$ of the GIF

model were in good agreement (Figure 4.4 **E**), suggesting that complex dendritic morphologies weakly affect temporal integration at the somatic compartment. Further quantitative evidence was provided by fitting $\kappa_{\text{GLM}}(t)$ with a single exponential function and comparing the resulting timescale against τ_{m} (Figure 4.4 **B**, inset). The GLM spike-history filter $h_{\text{GLM}}(t)$ extracted from *in silico* recordings (Figure 4.4 **F**) was also in good agreement with the effective adaptation filter $h(t)$ of the GIF model (Mensi et al., 2011b; Pozzorini et al., 2013):

$$h(t) = \int_0^\infty \kappa(s)\eta(t-s)ds + \gamma(s). \tag{4.8}$$

This result confirmed that $h_{\text{GLM}}(t)$ combines, but can not disentangle, the effects of the adaptation current $\eta(t)$ and the movement of the firing threshold $\gamma(t)$. In contrast to GIF models, GLMs do not model absolute refractoriness with a dead time followed by a voltage reset. This explains why, during the first milliseconds, $h_{\text{GLM}}(t)$ is much larger than $h(t)$ (Figure 4.4 **F**). Consistent with previous results that in L5 pyramidal neurons spike-frequency adaptation occurs on multiple timescales (Lundstrom et al., 2008; Pozzorini et al., 2013), we finally noticed that both $h(t)$ and $h_{\text{GLM}}(t)$ were approximatively linear on double logarithmic scales (Figure 4.4 **F**, inset).

The predictive power of both the GIF model and the GLM was then assessed on a *test set* obtained by simulating the DBM response to nine repetitive injections of a new 10-second-long current (Figure 4.4 **H**). Both models achieved a similar performance and were able to predict around 80% of the spikes emitted by the DBM ($M_d^* = 0.80$, s.d. 0.01, GIF; $M_d^* = 0.79$, s.d. 0.01, GLM; Figure 4.4 **I**). Compared to the GLM, the GIF model presented two advantages. First, the GIF model, but not the GLM, explicitly modeled the dynamics of the membrane potential and could therefore explained 74.3 ± 1.1 % (Figure 4.4 **J**) of the DBM subthreshold variance. Second, the time required to perform parameter extraction was faster for the GIF model than for the GLM ($T_{\text{CPU}} = 86$ s, GIF; $T_{\text{CPU}} = 143$ s, GLM).

Repeating the entire protocol by varying the duration of $I_{\text{tr}}(t)$ confirmed that a training set of $T_{\text{tr}} = 100$ seconds was sufficient to ensure convergence of the fitting procedure (Figure 4.4 **K**). Overall, these results suggest that, despite their simplicity, modern point-neuron models are capable of predicting most of the spikes emitted by a detailed biophysical model in response to complex somatic current injections.

4.2.7 Testing the high-throughput protocol on *in vitro* patch clamp recordings

To confirm the results reported in the previous section, the protocol for high-throughput single-neuron characterization was further tested using standard current-clamp *in vitro* recordings from L5 pyramidal neurons (see Experimental Procedures). At the beginning of the experiment, the input current was calibrated to obtain an average firing rate of 10 Hz with amplitude fluctuations between 7 and 13 Hz.

Since the same patch-clamp electrode was used to simultaneously stimulate and record
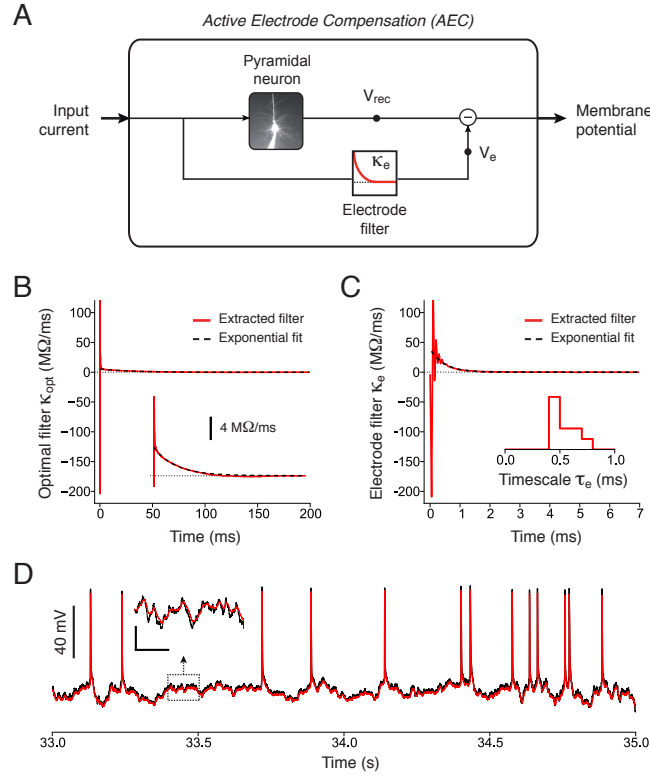
Figure 4.5: **Data preprocessing: Active Electrode Compensation. (A)** Schematic representation of the Active Electrode Compensation technique used to correct for the experimental bias known to occur when the same patch-clamp electrode is used to simultaneously inject and record from a single neuron. The artifactual voltage $V_e(t)$ across the pipette is estimated by filtering the input current $I(t)$ with the electrode filter $\kappa_e(t)$. The intracellular membrane potential $V_{data}(t)$ if finally obtained by subtracting the artifactual voltage $V_e(t)$ from the recorded signal $V_{rec}(t)$. **(B)** Typical optimal linear filter $\kappa_{opt}(t)$ between the subthreshold input current $I_{sub}(t)$ and the recorded signal $V_{sub}(t)$. To estimate the electrode filter, an exponential fit is performed on the tail of $\kappa_{opt}(t)$ (dashed black). Inset: Magnification of the y-axis illustrating the good accuracy of the exponential fit (dashed black) on the tail of the optimal linear filter $\kappa_{opt}(t)$ (red). **(C)** Typical electrode filter $\kappa_e(t)$ obtained by subtracting the exponential fit from the optimal linear filter $\kappa_{opt}(t)$ (see panel B). Since *in vitro* recordings were performed with the standard bridge compensation technique, the electrode filter $\kappa_e(t)$ is characterized by a strong initial negative peak. The characteristic timescale of the electrode filter τ_e was measured by performing an exponential fit (dashed black) on $\kappa_e(t)$. Inset: distribution of the electrode timescales τ_e measured in 10 different recordings included in the study. **(D)** Comparison between recorded signal $V_{rec}(t)$ (black) and membrane potential $V_{data}(t)$ (red) obtained after AEC. Inset: zoom indicating that AEC operates as a low-pass filter by removing high-frequency components from the acquired signal. Scale bars: 30 ms, 5 mV.

from single neurons, the acquired signal $V_{rec}(t)$ is a biased version of the real membrane potential $V_{data}(t)$ (Brette et al., 2007; Badel et al., 2008). This bias, due to the voltage drop $V_e(t)$ across the patch-clamp electrode, was removed using a technique called Active Electrode Compensation (AEC, see Experimental Procedures and Figure 4.5 **A**). In AEC (Brette et al., 2007; Badel et al., 2008), the electrode is modeled as an arbitrarily complex linear filter $\kappa_e(t)$

estimated at the beginning of the experiment from the optimal linear filter $\kappa_{\mathrm{opt}}(t)$ between a 10-second subthreshold current $I_{\mathrm{sub}}(t)$ and the recorded response $V_{\mathrm{sub}}(t)$ (Figure 4.5 **B**). Consistent with previous results (Pozzorini et al., 2013), the electrode filter $\kappa_{\mathrm{e}}(t)$ decayed on a very rapid timescale $\tau_{\mathrm{e}} = 0.54 \pm 0.11$ ms (Figure 4.5 **C**). For all subsequents injections, the voltage drop across the electrode $V_{\mathrm{e}}(t)$ is estimated by convolving the input current with the electrode filter $\kappa_{\mathrm{e}}(t)$. The membrane potential $V_{\mathrm{data}}(t)$ is finally recovered by subtracting $V_{\mathrm{e}}(t)$ from the recorded signal $V_{\mathrm{rec}}(t)$ (Figure 4.4 **A,D**):

$$V_{\mathrm{data}}(t) = V_{\mathrm{rec}}(t) - V_{\mathrm{e}}(t). \tag{4.9}$$

According to our high-throughput protocol, the training set was compensated only after its complete acquisition. With this strategy, the time-consuming procedure required to estimate the electrode filter can be performed during the acquisition of the training set (see Figure 4.3), limiting the total duration of the protocol.

After preprocessing by AEC, the *in vitro* recordings acquired from 10 different L5 pyramidal neurons (Figure 4.6 **A**) were used to perform GIF model parameter extraction (Figure 4.6 **B-E**). All of the extracted parameters were consistent with the ones previously obtained by fitting the GIF model on *in vitro* recordings from L5 pyramidal neurons responding to a mean-modulated input (Pozzorini et al., 2013). To allow for a comparison, we also used the *in vitro* recordings to perform GLM parameter extraction (Figure 4.6 **F-G**, see Experimental Procedures). Confirming the results reported in the previous section, the effective spike-history filter $h(t)$ of the GIF model obtained by combining the spike-triggered current $\eta(t)$ and threshold movement $\gamma(t)$ was in nice agreement with the GLM spike-history filter $h_{\mathrm{GLM}}(t)$ (Figure 4.6 **F**). The linear filters $\kappa_{\mathrm{GLM}}(t)$ and $\kappa(t)$ were also in good agreement (Figure 4.6 **B** and **F**, τ_{m}= 20.9 ms , s.d. 6.5 ms GIF; τ_{slow}= 22.5 ms , s.d. 3.0 ms GLM). However, the large values observed in the first two bins of $\kappa_{\mathrm{GLM}}(t)$ indicated the presence of a second rapid component (τ_{fast} = 1.9 ms, s.d. 0.5 ms), which is neglected in the GIF model (Figure 4.6 **F**, inset).

We tested the predictive power of both the GIF model and the GLM on a new set of recordings (*test set*) in which a test current $I_{\mathrm{test}}(t)$ that was repetitively injected (Figure 4.6 **I**). In terms of mere spike-timing prediction, the GIF model and the GLM achieved similar results ($M_d^* = 0.79 \pm 0.04$, GIF; $M_d^* = 0.81 \pm 0.04$, GLM; Figure 4.6 **J**). Moreover, the GIF model, but not the GLM, could explain 80.1 ± 4.1 % of the subthreshold variance of real neurons (Figure 4.6 **K**).These results suggests that the difference observed between the linear filters $\kappa(t)$ and $\kappa_{\mathrm{GLM}}(t)$ does not play a crucial role in spike-timing prediction.
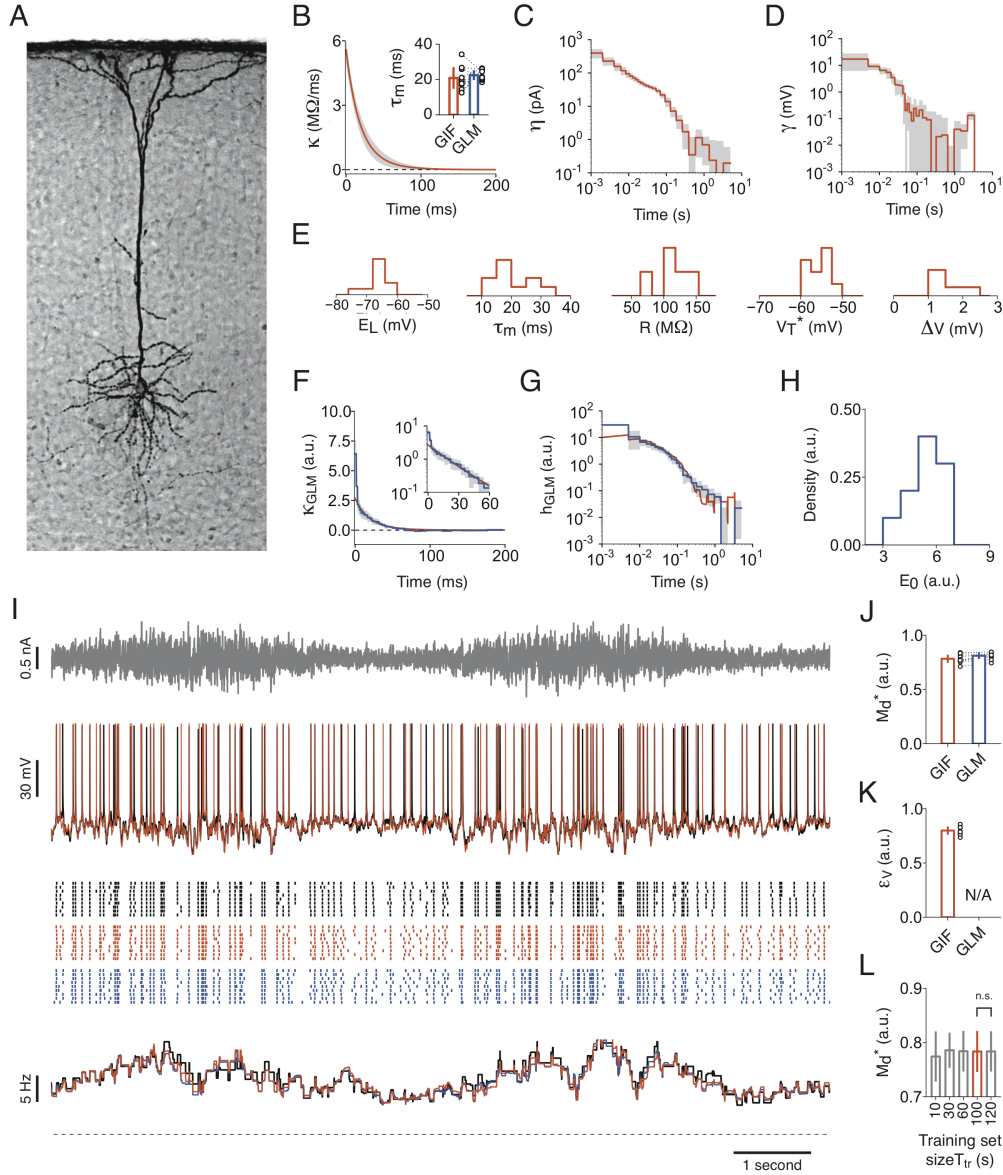
Figure 4.6: **Testing the protocol for high-throughput single-neuron characterization on *in vitro* patch-clamp recordings. (A)** Staining of a biocytin-filled L5 pyramidal neuron included in this study. **(B-E)** GIF model parameters extracted from ten L5 pyramidal neurons. Average filters are shown in red. Gray areas indicate one standard deviation across neurons. **(B)** Membrane filter $\kappa(t)$. Inset: comparison between the characteristic timescale of $\kappa(t)$ and the slow timescale τ_{slow} of $\kappa_{\mathrm{GLM}}(t)$ (see panel F). Each couple of open circles indicates the parameters measured in a single neuron. Bar plots indicate the mean and one standard deviation across neurons. **(C)** Spike-triggered current $\eta(t)$ displayed on double-logarithmic scales. **(D)** Spike-triggered movement of the firing threshold $\gamma(t)$ displayed on double-logarithmic scales. **(E)** Histograms of GIF model parameters extracted from ten L5 pyramidal neurons. From left to right: reversal potential, E_{L}; membrane timescale, $\tau_m = C/g_{\mathrm{L}}$; cell resistance, $R = g_{\mathrm{L}}^{-1}$; firing threshold baseline, V_{T}^*; firing threshold sharpness, ΔV. **(F-G)** GLM parameters extracted from ten L5 pyramidal neurons. Average filters are shown in blue. Gray areas indicate one standard deviation across neurons. **(F)** GLM linear filter $\kappa_{\mathrm{GLM}}(t)$ (blue). For comparison, a rescaled version of the GIF filter $\kappa(t)$ is shown in red. Inset: same data shown on a semi-logarithmic

scales. To quantify the slow τ_{slow} (panel B, inset) and the fast τ_{fast} (see Results section) timescale of $\kappa_{GLM}(t)$, we performed a double exponential fit (not shown for clarity) of $\kappa_{GLM}(t)$. **(G)** GLM spike-history filter $h_{GLM}(t)$ (blue). For comparison, a rescaled version of the effective GIF adaptation filer $h(t)$ (cf, Equation 4.8) is shown in red. **(H)** Distribution of the GLM parameter E_0 extracted from ten L5 pyramidal neurons. **(I)** Input current $I_{test}(t)$ (top, gray) used for model validation, typical L5 pyramidal neuron response evoked by a single current injection (middle, black) spiking activity observed in response to nine repetitive injections of the same input (bottom, black raster) and PSTH constructed by averaging the nine spike-trains within rectangular windows of 500 ms (bottom, black line). GIF model and GLM predictions are shown in red and blue, respectively. **(J-L)** Summary data for the performance of the GIF model and the GLM in predicting the responses of 10 L5 pyramidal neurons. Each couple of open circles indicates the performance on an individual cell. Error plots indicate the mean and one standard deviation across neurons. **(J)** Spike-timing prediction as quantified by M_d^* with precision $\Delta =$ 4 ms. **(K)** Mean prediction error ϵ_V on subthreshold membrane potential fluctuations. The GLM does not explicitly model the subthreshold membrane potential dynamics and is therefore not applicable (N/A). **(L)** GIF model spike-timing prediction (M_d^*, with precision $\Delta = 4$ ms) as a function of the training set size used for parameter extraction. Increasing the duration of the training set from 100 s to 120 s does not improve the GIF model predictive power ($M_d^* = 0.79$, s.d. 0.04, $T_{tr} = 100$ s; $M_d^* = 0.79$, s.d. 0.04, $T_{tr} = 120$ s; n=10, paired Student t-test, $t_9 = 0.25$, $p = 0.8$; n.s. > 0.05).

Finally, comparing the predictive power of different GIF models with parameters extracted from five training sets of different durations ($T_{tr} = 10, 30, 60, 100$ and 120 s; Figure 4.6 **L**), confirmed that 100 seconds of intracellular recordings were sufficient to accurately constrain the GIF model parameters. We concluded that our protocol for GIF model parameter extraction is suitable for high-throughput single-neuron characterization.

4.3 Discussion

In vitro patch-clamp recording is the gold standard used to investigate the intrinsic properties of single neurons. If on one hand this technique is considered to be the most accurate in reliably recording the single-neuron activity, *in vitro* patch-clamp remains labour-intensive and requires a trained experimentalists with high technical skills. In the last years, several platforms have been successfully developed that automatize electrophysiological recordings for ion-channel screening and drug discovery (Dunlop et al., 2008). Most of the existing platforms are however designed to record from mammalian cell lines or oocytes in which ion-channels of interest are artificially expressed (Xu et al., 2003; Finkel et al., 2006). In the next future, this technology will likely be transferred to more complex setups, as for example *in vitro* brain-slices. Confirming the rising interest for high-throughput electrophysiology, a system has recently been developed in which *in vivo* whole-cell patch-clamp recording is, at least partially, automatized (Kodandaramaiah et al., 2012). With this technique, 3-7 minutes are sufficient for a robot to automatically identify a cell and form a gigaohm seal of the same quality as achieved by a trained electrophysiologist. This technological advance represents a big step towards high-throughput electrophysiology from *in vitro* brain-slices, which, in the near future, could open the doors for high-throughput characterization of single neurons. To make sense of the large datasets that automated patch-clamp will make available, adequate

computational tools have to be developed. A powerful method to extract and summarize the most relevant information contained in an intracellular recording, consists of fitting a simplified spiking neuron model able to accurately capture the experimental data using a limited number of parameters. Moreover, spiking neuron models are indispensable tools to study the emergence of complex behaviors from neural circuits.

In this study, we demonstrated that the fitting procedure for GIF models we recently introduced (Mensi et al., 2011b; Pozzorini et al., 2013) (Figures 4.1 and 4.2) is suitable for high-throughput analysis of intracellular patch-clamp recordings. Using an artificial dataset generated by the model itself, we first established that GIF model parameter extraction and validation can be accomplished in around 5 minutes given a limited amount of intracellular recordings (Figure 4.2). Based on these results, we then designed a protocol for the characterization of the electrical activity of single neurons (Figure 4.3). Importantly, all the computations in the protocol can be executed *on the fly*, while electrophysiological recordings are performed. Considering the time required to automatically select a target neuron and form a gigaohm seal, this means that, combined with technologies for automatic patch-clamp, the mathematical tools discussed in this study could be used to implement a high-throughput pipeline performing single-neuron characterization in around 10 minutes. On the experimental side, the proposed protocol relies on *in vitro* injections of rapidly fluctuating currents. To compensate for the artifact known to occur while delivering inputs through the recording pipette, we propose the use of Active Electrode Compensation (Brette et al., 2007; Badel et al., 2008) (Figure 4.5). In AEC, estimating the electrode properties is a potentially time-consuming procedure. For this reason, in our protocol, artifacts resulting from the voltage drop across the patch-clamp electrode are removed only after the complete acquisition of the dataset used for parameter extraction (Figure 4.3). We tested the protocol for high-throughput single-neuron characterization using both *in silico* data (Figure 4.4) as well as *in vitro* recordings obtained with conventional (i.e., manual) patch-clamp technique (Figure 4.6). In both cases we found that a GIF model with parameters extracted from a 100-second-long training set accurately predicted both the subthreshold and the spiking response evoked by a new input. Intriguingly, the GIF model achieved almost identical performances in predicting *in silico* and *in vitro* data (Figures 4.4 and 4.6), indicating that detailed biophysical models could be used in the future to guide the improvement of simplified spiking models. Analyzing the performance of the GIF model in response to dendritic inputs goes beyond the scope of this study. However, as demonstrated by a recent study (Naud et al., 2013), the mathematical framework discussed here is flexible and can in principle be extended to account for dendritic current injections.

To allow for a comparison, both *in silico* and *in vitro* recordings were also fitted with a Generalized Linear Model (GLM, (Truccolo et al., 2005; Pillow et al., 2008)). Despite the fact that GLMs are more flexible than GIF models, we found that, in terms of mere spike timing prediction, the two models achieved similar performance (Figures 4.4 and 4.6). This result can be understood by noting that the *nonparametric* filter $\kappa_{\mathrm{GLM}}(t)$ extracted with the GLM fitting procedure are well approximated by the exponential filter $\kappa(t)$ of the GIF model. GLMs are typically considered as statistical models for spike trains and their parameters are only loosely related

to biophysical properties of the cell. The reason for this is that GLM parameter extraction entirely relies on the likelihood maximization of the spiking data. If on one hand this fact constitutes a big advantage in case of (multielectrode) extracellular recordings (Paninski et al., 2005; Pillow et al., 2008), the standard GLM framework is less appropriate for whole-cell current-clamp data. In contrast to GIF models, GLMs do not explicitly model the membrane potential dynamics, do not exploit all the information available in intracellular recordings and, consequently, are unable to predict the subthreshold activity of single neurons. Moreover, compared to GLMs, we found that parameters extraction for GIF models was faster.

A voltage-dependent plasticity rule has recently been proposed (Clopath et al., 2010) in which the subthreshold dynamics of the membrane potential plays a crucial role in explaining a large variety of experimental results obtained using different induction protocols for long-term potentiation (or depression). Among others, this finding highlights the need of spiking neuron models that accurately capture the subthreshold membrane potential dynamics. The GIF model accounts for spike-dependent adaptation using two distinct filters: a spike-triggered current $\eta(t)$ and a spike-triggered movement of the firing threshold $\gamma(t)$. At first glance, having two spike-dependent processes might seem redundant and not necessary. However, while the firing threshold only affects spike probability, adaptation currents also alter the dynamics of the subthreshold membrane potential. By noting that, one can understand why the correct distinction between these two forms of adaptation is key to correctly predict the subthreshold response of single neurons. Supporting this claim, a reduced GIF model, in which the two processes mediating spike-frequency adaptation are combined into a single effective filter $h(t)$ (Equation 4.8), has been shown to systematically overestimate the membrane potential (Pozzorini et al., 2013).

Since GLM parameter extraction entirely relies on spiking data (see Experimental Procedures), the linear filter $\kappa_{\mathrm{GLM}}(t)$ also includes the effects of all biophysical processes that affect spike emission without altering the subthreshold membrane potential. In particular, the filter $\kappa_{\mathrm{GLM}}(t)$, but not the filter $\kappa(t)$ of the GIF model, is expected to capture an eventual coupling between membrane potential and firing threshold (Mihalaş and Niebur, 2009; Platkiewicz and Brette, 2010). Possibly explaining the difference we found between $\kappa_{\mathrm{GLM}}(t)$ and $\kappa(t)$ (Figure 4.6 **F**), both direct (Higgs and Spain, 2011) and indirect (Azouz and Gray, 2003) experimental evidence has been provided that such a coupling exists in cortical pyramidal neurons. Extending the GIF model to account for a coupling between membrane potential and firing threshold goes behind the scope of this study and will be presented in a separate publication. It is however worth noting that the threshold equation of the GIF model can be easily augmented as follows:

$$V_T(t) = V_T^* + \sum_{\hat{t}_j < t} \gamma(t - T_{\mathrm{ref}} - \hat{t}_j) + \int_{\hat{t}_{\mathrm{last}}}^{t} \kappa_\theta(t - s) V(s) ds, \tag{4.10}$$

with $\kappa_\theta(t)$ being an arbitrarily shaped filter that, with a straightforward extension of the maximum likelihood method used in Step 3 (see Figure 4.2 **A**, *Step 3*), could be extracted from

intracellular recordings.

In contrast to the GIF model, popular point-neuron models like the adaptive exponential integrate-and-fire (ADEX, (Brette and Gerstner, 2005)) or the adaptive quadratic integrate-and-fire (AQIF, (Izhikevich, 2003)) feature a subthreshold adaptation current $w(t)$ governed by the following differential equation

$$\tau_w \dot{w} = -w + a(V - E_L). \tag{4.11}$$

Extending the GIF model with Equation 4.11 would relax the assumption of having a single exponential membrane filter $\kappa(t)$ and, depending on the parameter choice, the subthreshold dynamics of the resulting model could account for two-timescale decay or resonance (Mensi et al., 2011a). In ADEX and AQIF, this current has been shown to play an important role in explaining the variety of firing patterns emitted by single neurons in response to a step of current (Naud et al., 2008; Touboul and Brette, 2008). In GIF, the lack of subthreshold adaptation is, at least partially, compensated by the fact that the spike-triggered current is not assumed to be exponential, but can have an arbitrary shape. For example, the GIF model can capture the *resonate-and-fire* behavior by means of a biphasic spike-triggered current that, during the first milliseconds hyperpolarizes the membrane and then rapidly becomes positive, favoring the emission of spikes with a particular interspike interval (Mensi et al., 2011b). Our results suggest that, while increasing the complexity, extending a GIF model with a subthreshold current $w(t)$ does not significantly improve the model's performance in predicting the activity of the three main neuronal types of the mouse barrel cortex (Mensi et al., 2011a). However, this might not hold true for neurons in other brain regions or in case of more involved stimulation paradigms. Performing parameter extraction with a GIF model extended with Equation 4.11 is possible. Once the timescale τ_w is known, performing a least-square regression similar to Equation 4.18 is indeed sufficient to recover all the other parameters. Extended GIF parameter extraction can therefore be performed by iterating on τ_w and looking for the timescale that minimizes the sum of squared errors on the voltage derivative. Since line-search (i.e., brute-force) algorithms can be efficiently executed using parallel computing, extending a GIF model with a subthreshold adaptation current does not necessarily imply a dramatic increase of the CPU time required for parameter extraction.

The intrinsic dynamics of individual neurons strongly depends on the cell type and the brain area (Markram et al., 2004). This heterogeneity is increasingly considered as a critical feature of the brain and not as the consequence of biological imprecision (Padmanabhan and Urban, 2010; Tripathy et al., 2013). Taking into account single-neuron variability might therefore be crucial to understand the way in which neural tissues support computation. For that, high-throughput platforms have to be developed for both data acquisition and data analysis. Previous results have shown that simplified neurons are surprisingly good in predicting the spiking activity of single-neurons (Gerstner and Naud, 2009). Here, we demonstrated that, if combined with automatic patch-clamp recordings, the fitting technique

we recently introduced (Mensi et al., 2011b; Pozzorini et al., 2013) can be used to build a high-throughput pipeline for the fitting and the validation of GIF models on a cell-by-cell basis. In the future, these methods could contribute to the development of realistic large-scale models of the central nervous system (Koch and Reid, 2012; Waldrop, 2012; Kandel et al., 2013; Lang et al., 2011; Markram, 2006).

4.4 Experimental procedures

4.4.1 Electrophysiological recordings

All procedures in this study were conducted in conformity with the Swiss Welfare Act and the Swiss National Institutional Guidelines on Animal Experimentation for the ethical use of animals. The Swiss Cantonal Veterinary Office approved the project following an ethical review by the State Committee for Animal Experimentation.

In vitro electrophysiological recordings were performed on 300 μm thick parasagittal acute slices from the right hemispheres of male P13-15 C57Bl/6J mouse brains, which were quickly dissected and sliced (HR2 vibratome, Sigmann Elektronik, Germany) in ice-cold artificial cerebrospinal fluid (ACSF) (in mM: NaCl 124, KCl 2.5, $MgCl_2$ 10, NaH_2PO_4 1.25, $CaCl_2$ 0.5, D-(+)-Glucose 25, $NaHC0_3$ 25; pH 7.3 $\pm$ 0.1, aerated with 95% O_2, 5% CO_2), followed by a 15 minute incubation at 34 °C in standard ACSF (in mM: NaCl 124, KCl 2.5, $MgCl_2$ 1, NaH_2PO_4 1.25, $CaCl_2$ 2, D-(+)-Glucose 25, $NaHC0_3$ 25; pH 7.4, aerated with 95% O_2, 5% CO_2), equally used as bath solution. Cells were visualized using infrared differential interference contrast video microscopy (VX55 camera, Till Photonics, Germany and BX51WI microscope, Olympus, Japan). Somatic whole-cell current clamp recordings of layer 5 pyramidal cells in the primary somatosensory cortex were performed at 32 $\pm$ 1 °C with an Axon Multiclamp 700B Amplifier (Molecular Devices, USA) using 6.5-7.5 MΩ borosilicate pipettes, containing (in mM): K^+-gluconate 110, KCl 10, ATP-Mg^{2+} 4, Na_2^+-phosphocreatine 10, GTP-Na^+ 0.3, HEPES 10, biocytin 5 mg/ml; pH 7.3, 300 mOsm). To ensure intact axonal and dendritic arborisation, recordings were conducted in slices cut parallel to the apical dendrites.

Data were acquired at ΔT^{-1} = 20 kHz using an ITC-18 digitising board (InstruTECH, USA) controlled by a custom-written software module operating within IGOR Pro (Wavemetrics, USA). Voltage signals were low-pass filtered (Bessel, 10 kHz) and not corrected for the liquid junction potential. Only cells with an access resistance < 25 MΩ (20.2 $\pm$ 3.2 MΩ, n = 10), which was compensated throughout the recording, and a drift in the resting membrane potential < 2.5 mV (1.2 $\pm$ 0.8 mV, n = 10) between the start and the end of the recording were retained for further analysis.

4.4.2 *In silico* recordings: multi compartemental model simulations

In silico recordings were performed by simulating a multi compartmental model of a L5b pyramidal neuron (Hay et al., 2011). The model was obtained from Model DB (accession number 139653) and all simulations were performed in Neuron (Carnevale and Hines, 2006). Similar to the *in vitro* experiments, input currents $I(t)$ were generated according to Equations 4.5-4.6 (with sampling frequency $\Delta T^{-1} = 20$ kHz) and were delivered at the somatic compartment. To obtain an average firing rate fluctuating between 7 and 13 Hz, the input parameters were set to $I_0 = 520$ pA, $\sigma_0 = 320$ pA and $\Delta\sigma = 0.5$. To reproduce spike timing variability between responses to repetitive injections of the same current $I(t)$, a source of noise was included in the model by adding a zero-mean white-noise signal $\xi_{\text{w.n.}}(t)$ to $I(t)$. In order to capture the autocorrelation function between spike trains recorded *in vitro* in response to different repetitions of the test set current, the magnitude of the noise was set to $\sqrt{\langle \xi_{\text{w.n.}}(t)^2 \rangle} = 160$ pA. The same amount of noise was also used to generate the training dataset. GIF model and GLM parameter extraction was performed by treating the noise current $\xi_{\text{w.n.}}(t)$ as being unknown.

4.4.3 Data preprocessing: Active Electrode Compensation

All the *in vitro* recordings included in this study were preprocessed with AEC (Brette et al., 2007) according to the following four-step procedure (Badel et al., 2008; Pozzorini et al., 2013).

Step 1: Shortly before the acquisition of the *training dataset* (see Figure 4.3), we recorded the intracellular response $V_{\text{sub}}(t)$ evoked by the injection of a short subthreshold current $I_{\text{sub}}(t)$. The input was generated according to Equation 4.5 with parameters $I_0=0$ pA, $\sigma(t)=75$ pA and $\tau=3$ ms and evoked small-amplitude subthreshold fluctuations around the resting potential. With this parameter choice, the standard deviation of $V_{\text{sub}}(t)$ was around 2-3 mV.

Step 2: We then estimated the optimal linear filter $\kappa_{\text{opt}}(t)$ between the subthreshold input $I_{\text{sub}}(t)$ and the recorded signal $V_{\text{sub}}(t)$ (Figure 4.4 **B**). To reduce computing time, $\kappa_{\text{opt}}(t)$ was defined over a finite interval $[0, 200 \text{ ms}]$ as

$$\kappa_{\text{opt}}(t) = \sum_{m=1}^{M} b_m f^{(m)}(t), \tag{4.12}$$

with $\{f^{(m)}(t)\}$ being a set of M=202 rectangular basis functions of linearly increasing width. The parameters $b = [b_1, \ldots, b_M]$ determining the shape of $\kappa_{\text{opt}}(t)$ were then estimated by solving the following multilinear regression:

$$b = (Z^T Z)^{-1} Z^T \dot{V}, \tag{4.13}$$

where, using the discrete-time notation $x_t = x(t \cdot \Delta T)$ and by removing the subscripts *sub* for clarity, $\dot{V}$ is a vector whose t-th element is given by the membrane potential derivative

$\dot{V}_t = (V((t+1)\Delta T) - V(t\Delta T)) / \Delta T$ and Z is a matrix made of vectors z_t^T defined as:

$$z_t^T = \left[\sum_{s=0}^{t} f_s^{(1)} \dot{I}_{t-s} \Delta T, \ \dots \ , \sum_{s=0}^{t} f_s^{(M)} \dot{I}_{t-s} \Delta T \right],$$

(4.14)

with $\dot{I}_t = (I((t+1)\Delta T) - I(t\Delta T)) / \Delta T$ being the first-order temporal derivative of the input current $I_{sub}(t)$.

Step 3: An exponential function $f(t; a_1, a_2) = a_1 \exp(-t/a_2)$ was then fitted to the tail of $\kappa_{opt}(t)$ by minimizing the error $E(a_1, a_2) = \int_{T_{min}}^{\infty} (\kappa_{opt}(s) - f(s; a_1, a_2))^2 ds$ (Figure 4.4 **B**). In AEC, the electrode is assumed to operate on fast timescales (< 1 ms) and the slow decay in $\kappa_{opt}(t)$ is attributed to the cell. For this reason the fit was performed with $T_{min} = 5$ ms, and the electrode filter was estimated as

$$\kappa_e(t) = \kappa_{opt}(t) - f(t; \hat{a}_1, \hat{a}_2),$$

(4.15)

with $\hat{a}_1$ and $\hat{a}_2$ being the optimal parameters minimizing $E(a_1, a_2)$. To improve accuracy, Steps 2 and 3 were repeated 15 times by resampling from the available data and the final electrode filter used for AEC was obtained by averaging the results across repetitions (Figure 4.4 **C**).

Step 4: Finally, for all subsequent current-clamp injections, the membrane potential $V_{data}(t)$ was estimated as follows (Figure 4.4 **A,D**):

$$V_{data}(t) = V_{rec}(t) - \int_{0}^{\infty} \kappa_e(s) I_{ext}(t-s) ds,$$

(4.16)

where $I_{ext}(t)$ is the injected current, $V_{rec}(t)$ is the recorded signal and the convolution integral on the right-hand side of Equation 4.16 approximates the voltage drop $V_e(t)$ across the electrode.

Expanding $\kappa_{opt}(t)$ in rectangular basis functions drastically reduces the computing time required in Step 2. Overall, Steps 1-3 were performed in around 62 seconds and can in principle be executed while the training set is being acquired. Step 4 requires less than 1 second and can be performed after training set collection without compromising high-throughput (Figure 4.3). Since in our protocol model validation only relies on spike-timing prediction, AEC only has to be applied to the training dataset. Here, in order to asses the prediction error on the subthreshold membrane potential, we also performed AEC on all test set recordings.

4.4.4 GIF model parameter extraction

Given the intracellular membrane potential $V_{data}(t)$ measured at a sampling frequency ΔT^{-1} in response to a known input current $I_{tr}(t)$, as well as the spike times $\{\hat{t}_j\}$ defined as instants at which $V_{data}(t)$ crosses 0 mV from below, all the GIF model parameters are extracted following a three-step procedure (Mensi et al., 2011b; Pozzorini et al., 2013) (Figure 4.2 **A**).

Chapter 4. Automated high-throughput parameter extraction for Generalized Integrate and Fire models

Step 1: The absolute refractory period T_{ref} is fixed to an arbitrary value and the voltage reset is estimated by the average membrane potential recorded T_{ref} milliseconds after a spike $V_{\text{reset}} = \langle V_{\text{data}}(\hat{t}_j + T_{\text{ref}}) \rangle_j$. Since absolute refractoriness can be captured by a spike-triggered movement of the firing threshold, the particular choice of T_{ref} is not crucial and the only constraint is given by the shortest interspike interval in the dataset. Here, for L5 pyramidal neuron, we set the refractory period to $T_{\text{ref}} = 4$ ms.

Step 2: The parameters determining the subthreshold dynamics of the membrane potential are extracted. To allow convex optimization, the spike-triggered current $\eta(t)$ is expanded as a linear combination of basis functions (Paninski et al., 2005):

$$\eta(t) = \sum_{k=1}^{K} \eta_k f^{(k)}(t), \tag{4.17}$$

where $\{\eta_k\}$ is a set of parameters controlling the time course of $\eta(t)$. The parameters $\theta_{\text{sub}}^T = C^{-1} \cdot [g_L, E_L g_L, \eta_1, ..., \eta_K, 1]$ are then extracted by minimizing the sum of squared errors between the observed voltage derivative $\dot{V}_{\text{data}}$ and that of the model (i.e., Equation 4.1). Since all subthreshold parameters θ_{sub} act linearly on the observables, this optimization problem can be efficiently solved by computing the following multilinear regression (Paninski et al., 2005; Huys et al., 2006):

$$\hat{\theta}_{\text{sub}} = (X^T X)^{-1} X^T \dot{V}_{\text{data}}, \tag{4.18}$$

where X is a matrix whose rows are given by the vectors

$$x_t^T = \left[-V_{\text{data}}(t), 1, -\sum_j f^{(1)}(t - T_{\text{ref}} - \hat{t}_j), ..., -\sum_j f^{(K)}(t - T_{\text{ref}} - \hat{t}_j), I(t) \right], \tag{4.19}$$

and $\dot{V}_{\text{data}}$ is a column-vector containing the voltage first-order derivative estimated by finite differences $\dot{V}_{\text{data}}(t) = (V_{\text{data}}(t + \Delta T) - V_{\text{data}}(t)) / \Delta T$. Since the GIF model does not capture the subthreshold dynamics during spike initiation, all the data points close to action potentials $\{t | t \in [\hat{t}_j - 5 \text{ ms}; \hat{t}_j + T_{\text{ref}}]\}$ are excluded from the regression.

Step 3: The parameters defining the dynamics of the firing threshold are extracted. To determine the functional shape of the spike-triggered movement of the firing threshold, we first expand $\gamma(t)$ as a sum of basis functions:

$$\gamma(t) = \sum_{p=1}^{P} \gamma_p f^{(p)}(t). \tag{4.20}$$

Given the parameters obtained in the first two steps and the spike times observed in the experiment, the subthreshold membrane potential $\hat{V}_{\text{model}}(t)$ is then computed by numerical integration of Equation 4.1. All threshold parameters $\theta_{\text{th}}^T = \Delta V^{-1} \cdot [1, V_T^*, \gamma_1, ..., \gamma_P]$ are finally extracted by maximizing the log-likelihood of the experimental spike train (Brillinger, 1988;

Truccolo et al., 2005; Pillow et al., 2008):

$$\hat{\theta}_{\text{th}} = \underset{\theta_{\text{th}}}{\operatorname{argmax}} \left\{ \sum_{t \in \{\hat{t}_j\}} y_t^T \theta_{\text{th}} - \Delta T \cdot \sum_{t \in \Omega} \exp\left(y_t^T \theta_{\text{th}}\right) \right\}, \tag{4.21}$$

where $\Omega = \{t | t \notin [\hat{t}_j, \hat{t}_j + T_{\text{ref}}]\}$ is a set that excludes all the data points falling in the absolute refractory periods, the vectors y_t^T are defined as

$$y_t^T = \left[\hat{V}_{\text{model}}(t), -1, -\sum_j f^{(1)}(t - T_{\text{ref}} - \hat{t}_j), \dots, -\sum_j f^{(P)}(t - T_{\text{ref}} - \hat{t}_j) \right], \tag{4.22}$$

and, without loss of generality, we set $\lambda_0 = 1 \ s^{-1}$. With the exponential function in Equation 4.2, the log-likelihood to maximize is a convex function of θ_{th} (Paninski, 2004) and both its gradient and Hessian can be computed analytically. Consequently, the optimization problem of Equation 4.21 can be efficiently solved using the Newton-Raphson method. Alternatively, *Step 3* can be performed using the recorded potential $V_{\text{data}}(t)$ instead of $\hat{V}_{\text{model}}(t)$ in Equation 4.22. Since small inaccuracies in *Step 2* can be compensated in *Step 3*, performing the fit using $\hat{V}_{\text{model}}(t)$ generally improves spike-timing prediction.

Further details on the fitting procedure can be found in refs. (Mensi et al., 2011b; Pozzorini et al., 2013) and a Matlab implementation is available on ModelDB (http://senselab.med.yale.edu/modeldb/ShowModel.asp?model=143148).

4.4.5 Generalized Linear Model

All GIF model performance included in this study are compared against the ones of a standard Generalized Linear Model (GLM) (Truccolo et al., 2005; Pillow et al., 2008). In the GLM, spikes are emitted stochastically according to the following conditional intensity

$$\lambda_{\text{GLM}}(t|I, \{\hat{t}_j\}) = \lambda_0 \cdot \exp\left(E_0 + \int_0^t \kappa_{\text{GLM}}(s) I(t - s) ds + \sum_{\hat{t}_j} h_{\text{GLM}}(t - \hat{t}_j)\right). \tag{4.23}$$

In the GLM, the linear filter $\kappa_{\text{GLM}}(t)$ is not assumed to be exponential but is extracted from experimental data through linear expansion in rectangular basis functions. Moreover, the GLM accounts for spike-history effects with a unique filter $h_{\text{GLM}}(t)$. GLM also differs from the GIF model because it has neither an absolute refractory period nor an explicit voltage reset after the emission of a spike. To obtain a fair comparison between the two models, the filter $h_{\text{GLM}}(t)$ was expanded using the same basis functions as used for $\gamma(t)$ in the GIF and the number of basis functions used for $\kappa_{\text{GLM}}(t)$ was such that, in total, the two models had the same number of parameters. Given the input current $I(t)$ and the observed spike-train $S_{\text{data}}(t)$, GLM parameters θ_{GLM} were extracted with standard methods (Truccolo et al., 2005; Pillow et al., 2008) by maximizing the model log-likelihood $L(\theta_{\text{GLM}}) = \log p(S_{\text{data}}|I, \theta_{\text{GLM}})$. Without loss of generality, we set $\lambda_0 = 1 \ s^{-1}$. Importantly, the GLM fitting procedure does not exploit

the information available in the subthreshold membrane potential fluctuations.

4.4.6 Similarity measure M_d^* between sets of spike-trains

To quantify the model performance in predicting spikes, we used the normalized, bias-corrected metrics M_d^* (Naud et al., 2011). M_d^* relies on a measure of the distance between the experimental and the predicted spike-emission probability, which are in turn inferred from the responses to a limited number of repetitive current injections. Importantly, M_d^* resolves the *small sample* bias known to affect most of the similarity measures when the number of available spike-trains is small. Also, in contrast to previous measures based on naive pairwise comparisons (e.g., the Γ coincidence factor used in ref. (Jolivet et al., 2007)), M_d^* does not suffer from the so-called *deterministic bias* known to favor noise-free models and is therefore well suited for the evaluation of stochastic spiking models (Naud et al., 2011). Moreover, in contrast to many other correlation-based measures, M_d^* is sensitive to the accuracy with which both the shape and the amplitude of the spike probability is predicted.

Given a small set of experimental spike trains $S_i^{(\mathrm{d})} = \sum_f \delta(t - \hat{t}_f)$ recorded in response to N_d repetitive injections $i = 1, \ldots, N_\mathrm{d}$ of the same input current $I_\mathrm{test}(t)$, as well as a large set of spikes trains $S_j^{(\mathrm{m})} = \sum_f \delta(t - \hat{t}_f)$ predicted by N_m repetitive simulations $j = 1, \ldots, N_\mathrm{m}$ of a stochastic model, the similarity M_d^* between the two sets of spike trains is defined as (Naud et al., 2011):

$$M_d^* = \frac{2 \cdot \langle \nu_\mathrm{d}, \nu_\mathrm{m} \rangle}{\frac{2}{N_\mathrm{d}(N_\mathrm{d}-1)} \sum_{i=1}^{N_\mathrm{d}} \sum_{i'=i+1}^{N_\mathrm{d}} \left\langle S_i^{(\mathrm{d})}, S_{i'}^{(\mathrm{d})} \right\rangle + \langle \nu_\mathrm{m}, \nu_\mathrm{m} \rangle}, \tag{4.24}$$

where $S_i^{(\mathrm{d})}$ denotes the i-th experimental spike-train, $\nu_\mathrm{d} = \frac{1}{N_d} \sum_{i=1}^{N_\mathrm{d}} S_i^{(\mathrm{d})}$ is the average experimental response across trials (that is, the experimental PSTH computed with infinitesimally small bins), $\nu_\mathrm{m} = \frac{1}{N_m} \sum_{i=1}^{N_\mathrm{m}} S_i^{(\mathrm{d})}$ is the average model response and $\langle \nu_\mathrm{m}, \nu_m \rangle$ represents its norm. Due to high-throughput requirements and experimental constraints, only a small number N_d of experimental spike-trains are available. For this reason, the norm of ν_d must be computed using an unbiased estimator (cf. first term in the denominator of Equation 4.24). Finally, the brackets $\langle \cdot, \cdot \rangle$ denote the inner product used to quantify the distance between two spike trains (Naud et al., 2011):

$$\langle S_i, S_j \rangle = \int_0^T \int_{-\infty}^{\infty} \int_{-\infty}^{\infty} K(s, s') S_i(t - s) S_j(t - s') \, ds \, ds' \, dt, \tag{4.25}$$

where $K(s, s')$ is a two-dimensional kernel defining the degree of coincidence between two spikes occurred at times s and s'.

While different windows $K(s, s')$ may be used, the Kistler coincidence kernel $K(s, s') = \delta(s') \cdot \Theta(s + \Delta) \cdot \Theta(-s + \Delta)$ was chosen with $\Delta = 4$ ms as in refs.(Mensi et al., 2011a; Pozzorini et al., 2013). With this particular choice, the inner product $\langle S_i, S_j \rangle$ equals the number of spikes in S_i

that fell $\pm\Delta$ ms apart to one of the spikes in S_j and, consequently, M_d^* becomes:

$$M_d^* = \frac{2n_{\mathrm{dm}}}{n_{\mathrm{dd}}^* + n_{\mathrm{mm}}},\tag{4.26}$$

with n_{dm} being the average number of coincident spikes between data (d) and model (m), n_{mm} being the average number of coincident spikes computed across $N_{\mathrm{m}} = 500$ repetitions generated by the model and n_{dd}^* being the bias-corrected average number of coincident spikes between different experimental spike trains (that is, the number of coincident spikes between experimental spike-trains $S_i^{(d)}$ and $S_j^{(d)}$ averaged across $(i, j) \in [1, N_{\mathrm{d}}] \times [1, N_{\mathrm{d}}]$ with $i \neq j$, see Equation 4.25).

4.4.7   Performance evaluation

For each repetition i in the *test set*, we computed the coefficient of determination R_i^2 between the experimental membrane potential $V_i^{(\mathrm{data})}(t)$ and the GIF model prediction $\hat{V}_i^{(\mathrm{model})}(t)$ obtained by solving Equation 4.1 and forcing the spikes to occur at the same time as in the experiment.

$$R_i^2 = 1 - \frac{\int_0^{T_{\mathrm{test}}} (V_i^{(\mathrm{data})}(t) - \bar{V}_i^{(\mathrm{data})})^2 dt}{\int_0^{T_{\mathrm{test}}} (V_i^{(\mathrm{data})}(t) - \hat{V}_i^{(\mathrm{model})}(t))^2 dt},\tag{4.27}$$

R_i^2 corresponds to the ratio of explained variance to the sample variance, where $R_i^2 = 1$ when the model correctly predicts the voltage fluctuations and $R_i^2 = 0$ when the model is unable to predicts the variance of the subthreshold voltage fluctuations.

The prediction error ϵ_{V} on the subthreshold response was then obtained by averaging the results from each repetition:

$$\epsilon_{\mathrm{V}} = \frac{1}{n_{\mathrm{test}}} \sum_{i=1}^{n_{\mathrm{test}}} R_i^2.\tag{4.28}$$

The parameters T_{test} and n_{test} denote the duration and the number of repetitions in the *test set*, respectively.

The mean error $\epsilon_{\mathrm{param}}$ on the parameters θ extracted from artificial data is defined as

$$\epsilon_{\mathrm{param}} = \left\langle \frac{\Delta\theta_i}{|\theta_i|} \right\rangle_i,\tag{4.29}$$

where $\Delta\theta_i = |\theta_i - \hat{\theta}_i|$ is the $L1$-error between the estimated parameter $\hat{\theta}_i$ and the reference parameter θ_i (used to generate the artificial data). Overall, $\epsilon_{\mathrm{param}}$ measures the absolute percentage error averaged across model parameters.

All the CPU times reported in this study were obtained using an IntelCore i7 CPU920 @ 2.67GHz with 24 GB RAM. Both GLM and GIF model parameters were extracted using custom-written Matlab procedures.

4.5 Appendix

GIF Model		GLM	
Membrane capacitance	C	Stimulus filter	$\kappa_{\mathrm{GLM}}(t)$
Membrane conductance	g_L	Spike-history filter	$h_{\mathrm{GLM}}(t)$
Reverse potential	E_L	Baseline	E_0
Absolute refractory period	T_{ref}		
Voltage reset	V_{reset}	**AEC**	
Voltage threshold baseline	V_T^*	I-V optimal linear filter (Eq. 4.12)	$\kappa_{\mathrm{opt}}(t)$
Threshold sharpness	ΔV	Electrode filter (Eq. 4.15)	$\kappa_e(t)$
Spike-triggered current	$\eta(t)$	Electrode time constant	τ_e
Spike-triggered threshold	$\gamma(t)$		
Membrane resistance	$R = g_L^{-1}$	**Performance evaluation**	
Membrane time constant	$\tau_m = RC$	Spike-trains similarity (Eq. 4.26)	M_d^*
Membrane filter (Eq. 4.7)	$\kappa(t)$	Voltage prediction error (Eq. 4.28)	ϵ_{V}
Effective adaptation filter (Eq. 4.8)	$h(t)$	Parameters prediction error (Eq. 4.29)	$\epsilon_{\mathrm{param}}$

Table 4.1: **Symbols and parameters definitions.**

4.6 Acknowledgments

4.7 Author contributions

S.M., C.P. and C.K. conceived the study. S.M. and C.P. analyzed the data and wrote the initial draft; O.H. performed the electrophysiological experiments; W.G. supervised the project. All of the authors worked on the manuscript.

5 Evidence for a nonlinear coupling between firing threshold and sub-threshold potential

This chapter is an article in preparation that will be submitted under the following title:

Nonlinear threshold dynamics enhances temporal coding in neocortical pyramidal neurons

Skander Mensi[†], Christian Pozzorini[†], Olivier Hagens and Wulfram Gerstner

[†] equal contribution

5.1 Introduction

In agreement with the predictions of the leaky integrate-and-fire model, neocortical neurons have been shown to lose sensitivity to input fluctuations at increasing driving currents (Rauch et al., 2003; Giugliano et al., 2004; La Camera et al., 2006). For this reason, neurons are typically thought to operate as coincidence detectors when the mean input is below threshold and as temporal integrators above rehobase (Gerstner and Kistler, 2002). This view has recently been challenged by *in vitro* recordings demonstrating that, in rat prefrontal cortex (PFC) and in CA1 hippocampus, pyramidal neurons maintain high sensitivity to input fluctuations through a wide range of depolarizing inputs (Arsiero et al., 2007; Fernandez et al., 2011). In particular, the input-output curve of these neurons saturates at relatively low firing rates and the maximal firing rate depends on the input variance (Arsiero et al., 2007). Similar behaviors can be qualitatively reproduced by Hodgkin-Huxley models with decreased sodium conductance (Lundstrom et al., 2008) or augmented with slow sodium inactivation (Arsiero et al., 2007; Fleidervish et al., 1996). However, while these studies suggest that the firing threshold plays a role, the mechanism by which single neurons maintain high sensitivity to input variance remains unclear.

The membrane potential at which spikes are initiated in a given neuron is highly variable both *in vitro* and *in vivo* (Azouz and Gray, 2000, 2003). Threshold variability is not random

but probably results from a complicated dynamics which is likely to play a functional role by enhancing temporal coding (Henze and Buzsáki, 2001; Platkiewicz and Brette, 2011) and stimulus selectivity (Carandini and Ferster, 2000; Wilent and Contreras, 2005; Cardin et al., 2010). Many studies have demonstrated that the voltage threshold for spike initiation depends not only on the average value of the membrane potential (Azouz and Gray, 2003) but also on previous interspike intervals (Henze and Buzsáki, 2001; Chacron et al., 2007; Jolivet et al., 2006; Badel et al., 2008; Mensi et al., 2011b) and on the depolarization rate before a spike (that is, the speed at which the firing threshold is approached) (Azouz and Gray, 2000; Henze and Buzsáki, 2001; Azouz and Gray, 2003; Wilent and Contreras, 2005). In particular, when single neurons are stimulated with current ramps of different slopes, rapid rates of depolarization are often associated with lower thresholds (Higgs and Spain, 2011). While in rat pyramidal neurons this phenomenon results from the activation of low-threshold Kv1 channels (Higgs and Spain, 2011), theoretical studies suggest that a rapid coupling between voltage threshold and subthreshold membrane potential could also result from fast sodium channel inactivation (Hodgkin and Huxley, 1952; Platkiewicz and Brette, 2010; Wester and Contreras, 2013). Regardless of the underlying biophysical mechanism, threshold dependence on the rate of depolarization enhances coincidence detection and temporal coding by increasing the sensitivity to rapid input fluctuations (Azouz and Gray, 2000, 2003; Platkiewicz and Brette, 2011).

Two questions therefore arise. First, is it possible to extract a nonlinear coupling between firing threshold and subthreshold membrane potential directly from intracellular recordings? Second, can a simplified spiking neuron model augmented with such a mechanism explain enhanced sensitivity to input fluctuations?

To answer these questions, we measured the *in vitro* responses to fluctuating currents of both pyramidal and fast spiking neurons in mice L5 somatosensory cortex (SSC). While fast spiking neurons lose sensitivity to input fluctuations at large input, we found that pyramidal neurons are characterized by input-output curves which are very similar to the ones reported for excitatory neurons in PFC (Arsiero et al., 2007). Analysis of firing threshold revealed that, in pyramidal neurons, firing threshold and firing rate were positively correlated. Moreover, while evoking larger responses, we surprisingly found that increased input fluctuations were always associated with reduced firing thresholds.

Using a new convex optimization procedure we found that the firing threshold not only depends on the spike history, but on a shorter timescale is nonlinearly coupled with the subthreshold membrane potential. As revealed by the model, this two mechanisms interact in a non trivial way extending the range of input to which sensitivity to input fluctuations are maintained. Accounting for a nonlinear interaction between firing threshold and membrane potential significantly improves the ability of GIF model in predicting spike timing with millisecond predictions as well as the input-output of the neuron. Our results suggest that the dynamic of the firing threshold is surprisingly complex and plays a non-trivial role in encoding voltage fluctuations into output spike trains transmitted to postsynaptic cells.

Overall our results demonstrate and explain how, depending on the input statistics, neocortical pyramidal neurons adapt their coding strategy operating either as integrators or coincidence detectors.

5.2 Results

5.2.1 Pyr but not Fs neurons maintain sensitivity to input fluctuations in the suprathreshold regime

In the brain, neocortical neurons constantly receive barrages of presynaptic spikes (Destexhe et al., 2003). Single neuron coding can therefore be studied *in vitro* by recording the spiking activity elicited in response to rapidly fluctuating currents modeled as filtered Gaussian processes (see Eq. 5.6). Assuming that the input spikes obey an homogeneous Poisson process and elicit postsynaptic currents (PSCs) that exponentially decay with a characteristic timescale τ_I, the statistics of *in vivo*-like input currents are described by a mean μ_I, corresponding to the average intensity of the driving current, and a standard deviation σ_I, defining the magnitude of input fluctuations. If on one hand the timescale on which PSCs decay *in vivo* is fairly constant, both the mean μ_I and the standard deviation σ_I of inputs occurring in biologically relevant situations are likely to vary in time (Crochet and Petersen, 2006; Poulet and Petersen, 2008).

To characterize the input-output transformation performed by single neurons, we followed the same approach already used in previous studies (Rauch et al., 2003; Arsiero et al., 2007) and we intracellularly measured the single neuron responses evoked *in vitro* by a set of 5-second currents obtained by systematically varying the parameters μ_I and σ_I (Figure 5.1a,b). *In vivo*-like fluctuating currents were generated according to Equation 5.6 and injected at the soma of L5 neurons in the mouse somatosensory cortex (SSC) (see Materials and Methods). In qualitative agreement with the response predicted by the standard leaky integrate-and-fire (LIF) model (Rauch et al., 2003), we found that the steady-state firing rate f of fast spiking (Fs) inhibitory neurons was dependent on the magnitude of input fluctuations σ_I but only in the subthreshold regime, that is, when the mean input μ_I was smaller than the critical magnitude at which step currents (i.e., $\sigma_I = 0$) become sufficiently strong to elicit spikes (Figure 5.1a). At large offsets μ_I, the four f-μ_I curves recorded using different values of σ_I always converged, confirming that, in the suprathreshold regime, Fs neurons lose sensitivity to rapid fluctuations (Figure 5.1c). Moreover, the responses observed in Fs neurons did not saturate even in cases of strong inputs eliciting responses above 100 Hz (Figure 5.1c).

Applying the same protocol in pyramidal (Pyr) neurons from the same brain region led to different results (Figure 5.1b). Similar to what has been observed in Pyr neurons of the rat prefrontal cortex (PFC) (Arsiero et al., 2007; Thurley et al., 2008) and hippocampus (Fernandez et al., 2011), the f-μ_I curves of these cells were indeed always characterized by saturation at low firing rates (f_{max}=20.2 Hz, *s.d.*=2.6 Hz). Moreover, the firing rate at which saturation occurred significantly increased with the amplitude of input fluctuations σ_I (Figure 5.1d). Overall,

these results demonstrate that in mice SSC, Pyr, but not Fs neurons, maintain sensitivity to rapid fluctuations over a wide range of depolarizing offsets. This result suggests that SSC Pyr neurons operate as coincidence detectors over a wide range of inputs (Ratté et al., 2013).

Previous studies found that the particular input-output function we experimentally observed in Pyr neurons (see Figure 5.1b) can be qualitatively reproduced by Hodgking-Huxley models in which the ratio between sodium and potassium maximal conductances is low (Arsiero et al., 2007; Lundstrom et al., 2008). This result suggests that enhanced sensitivity to input fluctuations might be mediated by mechanisms that reduce the number of sodium channels available for spike initiation, and more generally, by processes that regulate the dynamics of the firing threshold. To explore this hypothesis, we analyzed the intracellular recordings performed in both Fs and Pyr neurons and estimated the voltages at which action potentials were initiated (Figure 5.1e,f) (see Methods). Threshold variability was approximatively 2-fold larger in Pyr neurons ($\sigma_\theta^{\text{Pyr}}$=4.5 mV, *s.d.*=0.3 mV) than in Fs neurons ($\sigma_\theta^{\text{Fs}}$=2.2 mV, *s.d.*=0.3 mV) (Figure 5.1g). Moreover, plotting the average threshold observed for different input parameters (μ_I,σ_I), revealed nontrivial dependencies. Consistent with previous results showing that the firing threshold adaptively rises after the emission of previous action potentials (Mensi et al., 2011b; Pozzorini et al., 2013), the voltage threshold measured in Pyr neurons always increased with the mean input μ_I (Figure 5.1f,h). However, at odds with the hypothesis of a threshold dynamics entirely governed by positive spike-triggered changes, we also found that larger input fluctuations, while evoking higher firing rates, significantly reduced the mean voltage threshold (Figure 5.1f,i). Yet, by changing perspective, this result is consistent with enhanced sensitivity to input fluctuations. Lowering the firing threshold, is indeed an effective way of increasing the firing rate. Complicating the picture, we found that the voltage threshold of Fs neurons, while being insensitive to the mean drive μ_I, was also modulated by input fluctuations σ_I (Figure 5.1h,i).

Overall, these results suggest that the dynamics of the voltage threshold of Pyr and Fs neurons is different and that understanding these differences might be a key to explain the origin of enhanced sensitivity to input fluctuations. In the next section, the threshold dynamics is therefore further analyzed.
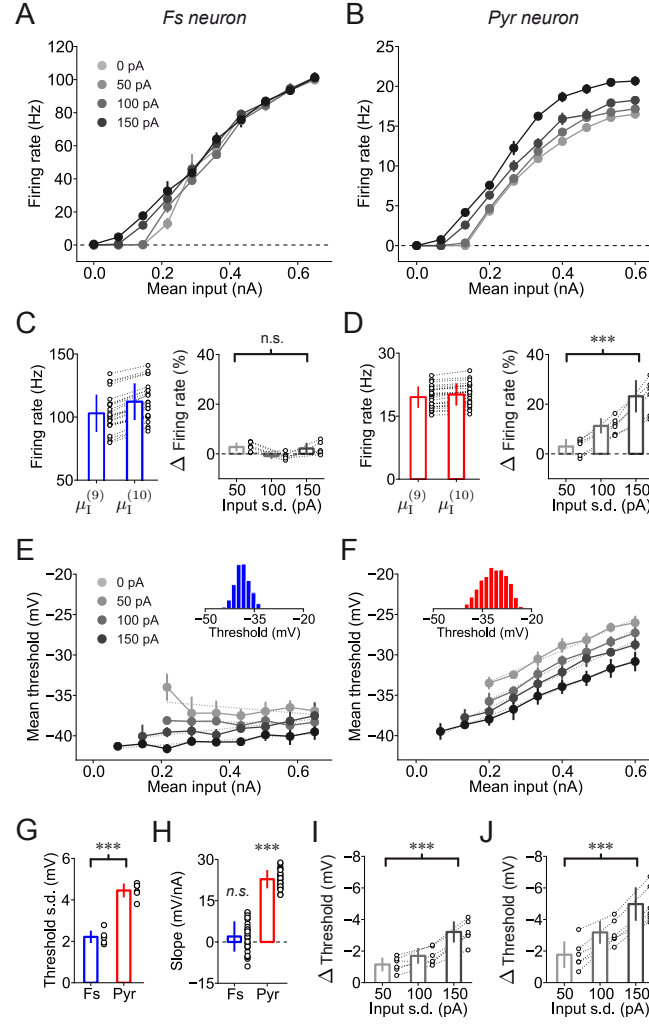
Figure 5.1: **Pyr neurons, but not Fs neurons, maintain sensitivity to rapid input fluctuations over the entire spectrum of depolarizing offsets. A:** Steady-state firing rate f of a typical Fs neuron as a function of the mean input μ_I. Different colors indicate different levels of input fluctuations σ_I. For each combination of input parameters (μ_I, σ_I), three different 5-s-long recordings were performed. Firing rates were estimated by discarding the transient response observed during the first second. Error bars, indicating one standard deviation across repetitions, are small and sometimes not visible demonstrating high reliability. **B:** Same results as in panel *a*, but for a typical Pyr neuron. In contrast to Fs, Pyr neurons maintain sensitivity to input fluctuations through the entire spectrum of depolarized offsets μ_I. **C:** Summary data of results obtained in different Fs neurons (n=6). Left: Comparison of steady-state firing rate in response to the two largest depolarizing offsets. Each couple of open circles represents results obtained in a particular cell for a given standard deviation σ_I. Bar plots represent mean and standard deviation across different cells and different values of σ_I. Right: Percentage change in steady-state firing rate obtained by increasing the input standard deviation σ_I. Changes were computed with respect to σ_I=0 pA by taking the average response to the two strongest inputs $\mu_I^{(9)}$ and $\mu_I^{(10)}$. Each set of open circles represents data from a particular cell. Bar plots represent mean and standard deviation across cells. Changes induced by a 3-fold increase in σ_I were not significant (n =6, paired Student t-test, t=0.62, p=0.52). **D:** Same results as in panel *c*, but for Pyr neurons (n=6). In contrast to Fs, Pyr neurons maintain sensitivity to input fluctuations (n =6, paired Student t-test, t=8.0, p=4.9 $\cdot 10^{-4}$). **E:** Average voltage threshold for spike initiation in a typical Fs neuron (same cell

105

shown in panel *a*) as a function of the mean input μ_I. Different colors indicate different σ_I. The voltage threshold was estimated for each individual spike by measuring the voltage at which the first-order derivative of the membrane potential crossed a certain threshold (see Methods). As in *a*, error bars indicate one standard deviation across recordings. Dashed lines show least squares linear regressions performed on experimental data with different σ_I. *Inset:* Distribution of voltage thresholds estimated for all the spike in a typical Fs neuron. **F:** Same results as in panel *e*, but for a typical Pyr neuron (same cell shown in panel *b*). **G:** Threshold variability observed in *n* =6 Fs and *n* =6 Pyr neurons. Each circle represents the standard deviation σ_θ of the distribution of voltage thresholds observed in a given cell (σ_θ is defined as the standard deviation of the distributions shown in the insets of panels *e* and *f*). Bar plots indicate mean and standard deviation across cells. In Pyr neurons, threshold variability was significantly larger than in Fs neurons (*n* =12, unpaired Student *t*-test, *t*=11.2, $p < 10^{-6}$). **H:** Comparison between regression slopes obtained by least square fits shown in panels *e* and *f*. Circles represent the slopes fitted for different cells and different values of σ_I. Bar plots indicate mean and standard deviation. In Pyr neurons (*n* =6, two-sided Student *t*-test, *t*=32.9, $p < 10^6$), but not in Fs (*n* =6, two-sided Student *t*-test, *t*=1.76, $p = 0.9$), the firing threshold increases with μ_I. **I:** Average change in voltage threshold obtained by increasing the input standard deviation σ_I in Fs neurons. Changes were computed with respect to $\sigma_I = 0$ by averaging the results obtained for all depolarizing offsets μ_I. Conventions are as in panel *c* (right). The firing threshold was significantly reduced by a 3-fold increase in input fluctuations (*n* =6, paired Student *t*-test, *t*=13.1, $p=4.6 \cdot 10^{-5}$). **J:** Same results as in panel *i*, but for Pyr neurons (*n* =6, paired Student *t*-test, *t*=14.2, $p=3.1 \cdot 10^{-5}$).

5.2.2 Steady-state analysis suggests a nontrivial threshold dynamics in both Pyr and Fs neurons

Firing threshold variability unlikely results from channel noise and probably reflects a complex dynamics. Supporting evidence has been provided by different studies showing that firing threshold variability can be at least partially explained by taking into account the average value of the subthreshold membrane potential (Azouz and Gray, 2003), the depolarization rate preceding the emission of an action potential (that is, the speed dV/dt at which the threshold is reached) (Azouz and Gray, 2000, 2003) and, as already mentioned, the emission of previous spikes (Henze and Buzsáki, 2001; Badel et al., 2008; Mensi et al., 2011b). To gain insight into a potential role of firing threshold in enhanced sensitivity to input fluctuations, we analyzed these three dependencies in both Fs and Pyr neurons (Figure 5.2).

Plotting the average firing threshold of Pyr neurons as a function of the steady-state firing rate, revealed an approximatively linear relationship consistent with the hypothesis of slowly decaying threshold movements being induced after each spike (Mensi et al., 2011b; Pozzorini et al., 2013) (Figure 5.2a). Consistent with previous results (Mensi et al., 2011b), the firing threshold of Fs neurons did not significantly correlate with the output firing rate (Figure 5.2a,b). In both Fs and Pyr neurons, the θ-f curves depended on σ_I, confirming that increased input fluctuations always resulted in reduced firing thresholds. Since increased input fluctuations σ_I translates into faster currents, we hypothesized that this result could reflect a dependency of the firing threshold on the membrane depolarization rate. For each input condition, we therefore estimated the average speed dV/dt at which the firing threshold was reached (see Materials and Methods). Consistent with this hypothesis, we found that, on average, rapid membrane depolarizations reduced the voltage threshold for spike initiation in both Fs and

Pyr (Figure 5.2c,d). A recent theoretical result has demonstrated that the latter dependency could in principle result from a nonlinear coupling between firing threshold and subthreshold membrane potential (Platkiewicz and Brette, 2010). As predicted by this theory, we found a clear relationship between the firing threshold of Pyr neurons and the average subthreshold membrane potential measured far from spikes (Figure 5.2e and Methods). Finally, while being significantly weaker, a similar coupling was also present in Fs neurons (Figure 5.2e,f).
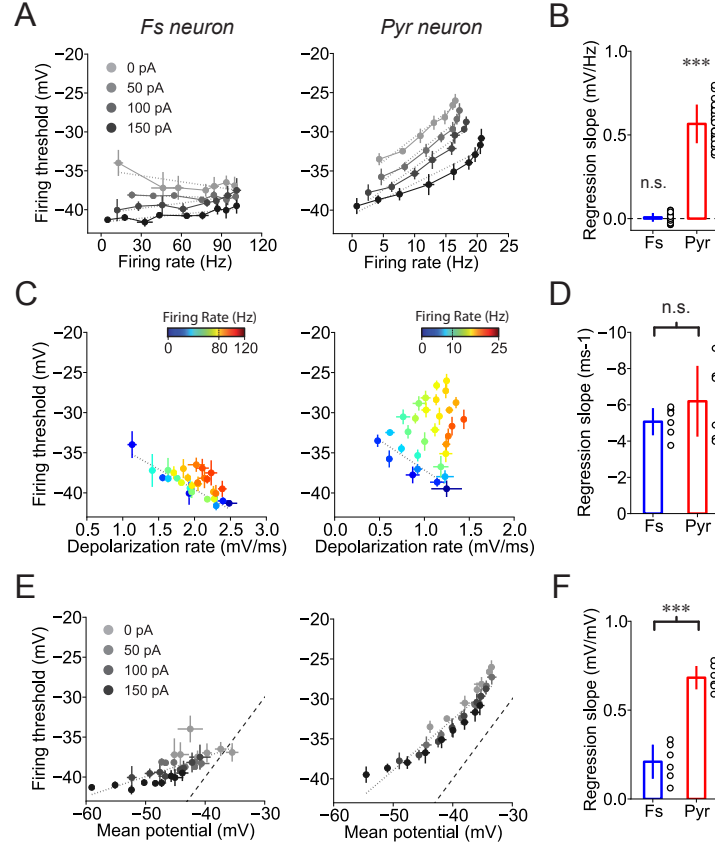
Figure 5.2: **The voltage threshold for spike initiation is variable and depends on several covariates in both Pyr and Fs neurons. A:** Voltage threshold for spike initiation as a function of the output firing rate in a typical Fs (*left*, same cell as in Figure 5.1a) and Pyr (*right*, same cell as in Figure 5.1b) neuron. Different colors represent different levels of input fluctuations σ_I. Dashed lines are least-square regressions fitted for different values of σ_I. **B:** Regression slopes obtained by fitting the firing threshold as a function of the output firing rate (see panel *A*). Open circles show the results obtained in $n=6$ Fs and $n=6$ Pyr neurons stimulated with different σ_I. Bar plots indicate means and standard deviations across cells and σ_I. In Pyr neurons ($n=24$, two-sided Student t-test, $t=23.5$, $p<10^{-6}$), but not in Fs neurons ($n=24$, two-sided Student t-test, $t=1.4$, $p=0.17$), regression slopes were significantly larger than zero, indicating a positive correlation between firing rate and voltage threshold. **C:** Firing threshold as a function of the depolarization rate preceding a spike. Results are shown for the same cells in panel A (Fs, *left*; Pyr, *right*). For each spike i (occurred at time $\hat{t}_i$), the depolarization rate was estimated by performing a linear regression on the membrane potential recorded in the time interval $[\hat{t}_i - 3.5 \text{ ms}, \hat{t}_i]$. The output firing rate is color coded. The dashed line indicates a least-square regression performed on experimental data observed at low firing rates f (Fs: $0 < f < 80$ Hz, Pyr: $0 < f < 10$ Hz, see color

bars). **D:** Regression slopes obtained by fitting the firing threshold as a function of the depolarization rate (see panel *C*) were not significantly different in Fs (*n*=6) and Pyr (*n*=6) neurons (*n*=12, unpaired Student *t*-test, *t*=1.21, *p*=0.25). **E:** Firing threshold as a function of the average subthreshold membrane potential in the recordings. Different colors indicate different σ_I. Results are shown for the same cells in panel *A* (Fs, *left*; Pyr, *right*). The dashed line indicates a least-square regression computed on all the data points. The thick dashed line is the diagonal $x = y$ delimitating the area (light gray) in which the membrane potential is larger than the firng threshold. **F:** The regression slopes obtained by fitting the firing threshold as a function of the mean membrane potential (see panel *E*) were significantly larger in Pyr (*n*=6) than in Fs (*n*=6) neurons (*n*=12, two-sided Student *t*-test, *t*=9.1, $p=3.7{\cdot}10^{-6}$). In panels *A, C* and *E*, each data point *j* was computed by averaging the results obtained by analyzing the responses to three different 5-s-long currents with the same statistics ($\mu_I^{(j)}$, $\sigma_I^{(j)}$). Data recorded in the first second of each repetition were not considered. Error bars indicate one standard deviation across the three repetitions. In panels *D* and *F*, the bar plots indicate means and standard deviations across results obtained in different cells (open circles).

Overall, the results reported in Figure 5.2 demonstrate that threshold variability can in part be explained by considering different covariates. We concluded that the firing threshold evolves according to a nontrivial dynamics, whose understanding requires mathematical modeling. In the next section, we therefore introduce a new spiking model.

5.2.3 Modeling a nonlinear coupling between membrane potential and firing threshold

In the standard Hodgkin-Huxley (HH) model (Hodgkin and Huxley, 1952), the sodium current I_Na responsible for spike initiation is gated by two independent variables m and h that respectively describe Na^+-channel activation and inactivation (Figure 5.3A). Sodium activation occurs on very short timescales and can therefore be approximated as being instantaneous (Fourcaud-Trocme et al., 2003; Badel et al., 2008; Platkiewicz and Brette, 2010). It follows that, at spike onset, the sodium current is correctly described by an exponential function of the membrane potential $I_\mathrm{Na} \propto h\exp\left(\frac{V-V_\mathrm{T}^*}{k_\mathrm{a}}\right) = \exp\left(\frac{V-(V_\mathrm{T}^*-k_\mathrm{a}\log h)}{k_\mathrm{a}}\right)$, where V_T^* is a constant, k_a is a biophysical parameter describing the sharpness of the Na^+-channel activation function $m_\infty(V)$ and $\theta = V_\mathrm{T}^* - k_a\log h$ defines a smooth threshold for spike initiation (Platkiewicz and Brette, 2010). Since in the HH model Na^+-channel inactivation follows a first-order kinetics $\tau_\mathrm{h}\dot{h} = -h + h_\infty(V)$, an accurate model of the voltage threshold for spike initiation θ is given by the following differential equation (Platkiewicz and Brette, 2010, 2011):

$$\tau_\theta\dot{\theta} = -\theta + \theta_\infty(V), \tag{5.1}$$

where $\tau_\theta = \tau_\mathrm{h}$. By modeling the steady-state inactivation curve with an inverse sigmoidal function $h_\infty(V) = \left(1 + \exp\left(\frac{V-V_\mathrm{i}}{k_i}\right)\right)^{-1}$, one can further predict that the coupling between firing threshold and membrane potential resulting from fast sodium inactivation should be correctly described by a smooth rectifier function (Platkiewicz and Brette, 2011) (Figure 5.3B):

$$\theta_\infty^\mathrm{Na}(V) = V_\mathrm{T}^* - k_\mathrm{a}h_\infty(V) = V_\mathrm{T}^* + k_\mathrm{a}\log\left(1 + \exp\left(\frac{V-V_\mathrm{i}}{k_\mathrm{i}}\right)\right). \tag{5.2}$$

Depending on the parameter V_i and on the asymptotic slope $\theta_{\text{slope}}^{\text{Na}} = k_a / k_i$, Equations 5.1 and 5.2 provide a possible theoretical explanation for the negative correlation between the voltage threshold for spike initiation and the depolarization rate of the membrane potential preceding a spike (Platkiewicz and Brette, 2010, 2011; Higgs and Spain, 2011). Indeed, if $\theta_{\text{slope}}^{\text{Na}} > 0$ and $V_i < V_T^*$, all membrane potential depolarizations occurring on a slower rate than the characteristic timescale τ_θ on which Na$^+$-channels inactivate will reduce the number of Na$^+$-channels which are available for spike initiation (Figure 5.3A,B). Consequently, compared to fast inputs, slow depolarizations will induce action potentials that are initiated at larger voltages (Figure 5.3E). On the other hand, if $h_\infty(V)$ is shifted towards more depolarized potentials (Figure 5.3C), Na$^+$-channel will not inactivate at subthreshold potentials and, consequently, spikes will always be initiated at the same voltage threshold V_T^* (Figure 5.3D,E). Overall, to effectively modulate the voltage threshold for spike initiation, the inactivation profile of Na$^+$-channel has to be such that, in the $V - \theta$ plane, the non-constant part of $\theta_\infty^{\text{Na}}(V)$ is not *masked* on the right-hand side of the diagonal $V = \theta$ (compare Figure 5.3A,B with Figure 5.3C,D; see ref. Platkiewicz and Brette (2010)).
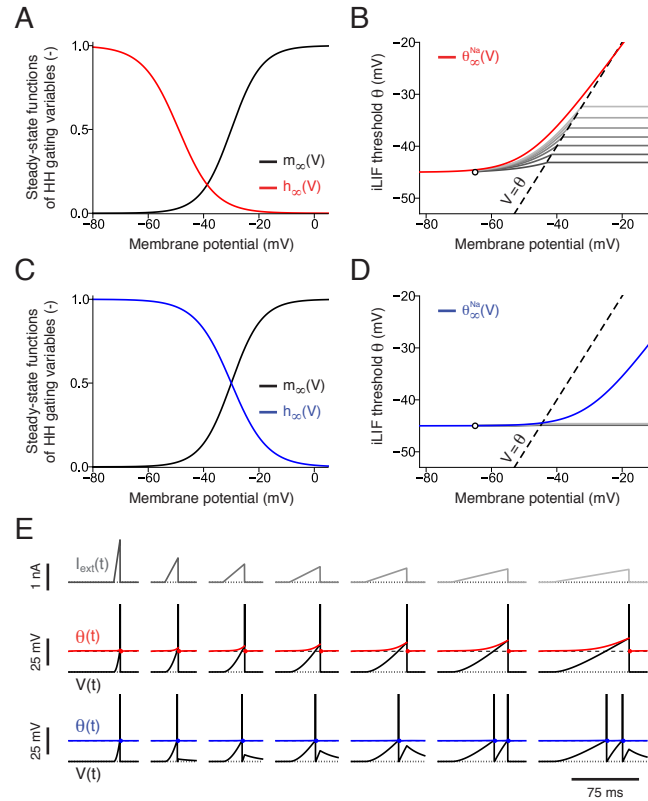
Figure 5.3: **Simplified integrate-and-fire model illustrating firing threshold dynamics modulation by fast Na$^+$-channel inactivation. A:** Steady-state activation ($m_\infty(V)$, black) and inactivation ($h_\infty(V)$, red) functions describing the dynamics of Na$^+$-channels responsible for spike initiation in a Hodgkin-Huxley (HH) model (Hodgkin and Huxley, 1952). **B:** Phase plane analysis illustrating the dynamics of the inactivating leaky integrate-and-fire model (iLIF, (Platkiewicz and Brette, 2010)) consisting of a standard LIF model augmented with a dynamic threshold θ described by Equations 5.1

and 5.2. In the iLIF model, a spike is deterministically emitted each time the membrane potential V crosses the firing threshold θ (dashed black line). After each spike, both V and θ are reset to low values (open circle). The smooth rectifier function defining the steady-state firing threshold $\theta_\infty^{\text{Na}}(V)$ (red) of the iLIF model was obtained by transforming the steady state inactivation function $h_\infty(V)$ shown in panel A according to Equation 5.2. The iLIF model responses to different ramps of current shown in gray. Different gray levels correspond to ramps of current with different slopes (see panel E). **C:** Steady-state activation ($m_\infty(V)$, black) and inactivation ($h_\infty(V)$, blue) functions. Compared to panel A, the inactivation curve is shifted towards more depolarized potentials. **D:** Phase plane analysis illustrating the threshold dynamics of the iLIF model for the case in which Na^+-channel inactivation only occurs after Na^+-channel activation (see panel C). Since the non-constant part of $\theta_\infty^{\text{Na}}(V)$ (blue) lies on the right-hand side of the diagonal $V = \theta$, ramps of current with different slopes elicit spikes that originate around the same voltage V_T^* (gray lines and panel E). Same conventions as in panel B. **E:** iLIF model response to ramps of current $I_{\text{ext}}(t) = s \cdot t$ with slopes s ranging from 0.2 nA/ms (top left, dark gray) to 0.005 nA/ms (top left, dark gray). Top: Input current $I_{\text{ext}}(t)$. The dotted line indicates $I_{\text{ext}} = 0$. Middle: iLIF model responses for the case in which Na^+-channel inactivation starts before Na^+-channel activation (see panels A,B). Membrane potential $V(t)$ and firing threshold $\theta(t)$ are shown in black and red, respectively. Since Na^+-channels inactivation is not instantaneous, but occurs on a characteristic timescale τ_θ, fast inputs (left) elicit spikes that, in comparison to slow inputs (right), initiate at lower membrane potentials (see also panel B). Dotted and dashed lines respectively represent the iLIF model reversal potential E_L and the the lowest possible voltage threshold V_T^* for spike initiation (cf. Eq. 5.2). iLIF model parameters: membrane timescale $\tau_m = 20$ ms; resistance $R = 100$ MΩ; reversal potential $E_L = -65$ mV; $V_T^* = -45$ mV; $V_i = -49$ mV; $\theta_{\text{slope}}^{\text{Na}} = k_a/k_i = 0.85$, $\tau_\theta = 5$ ms (cf. Eqs. 5.1 and 5.2). These parameters were not extracted from data, but where chosen to illustrate the theoretical result of ref. Platkiewicz and Brette (2010) that Na^+-channels inactivation could result in a coupling between firing threshold and membrane potential. Bottom: iLIF model response for the case in which Na^+-channel inactivation starts after Na^+-channel activation (see panels C,D). The same model parameters were used, expect for $V_i = -30$ mV.

To explain the experimental findings reported in Figures 5.1 and 5.2, we fitted the intracellular recordings using a new spiking neuron model obtained by extending the previous Generalized Integrate-and-Fire model (GIF) (Mensi et al., 2011b; Pozzorini et al., 2013) with a nonlinear coupling between firing threshold and membrane potential. We refer to this new model as iGIF, where i stands for *inactivating* (Figure 5.3A, see Materials and Methods). In the iGIF model, spikes are produced stochastically according to a firing intensity which exponentially depends on the instantaneous difference between the membrane potential V and firing threshold V_T (Gerstner and van Hemmen, 1992; Jolivet et al., 2006). As in the GIF model, the dynamics of the membrane potential is modeled as a leaky integrator augmented with a spike-triggered current $\eta(t)$ for spike-frequency adaptation. This function describes the time course of the net current generated by the single-neuron intrinsic dynamics after the emission of an action potential. In the iGIF model, the firing threshold V_T is given by:

$$V_T(t) = \theta(t) + \sum_{\hat{t}_j < t} \gamma(t - \hat{t}_j) \tag{5.3}$$

where the dynamics of $\theta(t)$ is as in Equation 5.1 and implements a nonlinear coupling between V_T and V. In Pyr neurons, the firing threshold has been previously shown to adaptively increase after the emission of previous spikes (Mensi et al., 2011b; Pozzorini et al., 2013). To

capture this phenomenon, the iGIF model also features a spike-triggered movement of the firing threshold $\gamma(t)$. Similar to $\eta(t)$, this function describes changes in V_T induced by previous action potentials and constitutes an additional mechanism for spike-frequency adaptation. A spike-dependent movement of the firing threshold could in principle be accounted for by increasing $\theta(t)$ after each spike. However, such a model would implicitly assume that spike-dependent and spike-independent threshold movements occur on the same timescale τ_θ. To avoid this assumption, in the iGIF model, the variable $\theta(t)$ is reset to V_T^* after each spike and all threshold changes induced by previous spikes are included in $\gamma(t)$. Importantly, the functional shape of $\eta(t)$, $\gamma(t)$ and $\theta_\infty(V)$, along with all other iGIF model parameters, were extracted from intracellular recordings using a new nonparametric fitting procedure (see Materials and Methods). In what follows, we refer to the iGIF model with parameters extracted using the nonparametric method as iGIF-NP, where NP stands for *nonparametric*.

5.2.4 iGIF model parameters extracted from intracellular recordings reveals a nonlinear coupling between V and V_T in Pyr neurons

In agreement with previous results (Mensi et al., 2011b; Pozzorini et al., 2013), we found that, in Pyr neurons, the passive properties of the membrane were characterized by a timescale of $\tau_m = 26.23 \pm 2.52$ ms (Figure 5.4A). When displayed on log-log scales, the decay of both the spike-triggered current $\eta(t)$ and movement of the firing threshold $\gamma(t)$ were approximatively linear over several orders of magnitude (Figure 5.4C,D). This result provides further evidence in support of a previous finding that, in Pyr neurons, spike-frequency adaptation does not have a preferred timescale, but is characterized by scale free dynamics (Lundstrom et al., 2008; Pozzorini et al., 2013). While avoiding *a priori* assumptions about the existence of a coupling between firing threshold and membrane potential, as well as about the underlying biophysical process, our nonparametric method allowed us also to extract $\theta_\infty(V)$ directly from intracellular recordings. We found that, in Pyr neurons, firing threshold and subthreshold membrane potential were indeed nonlinearly coupled (Figure 5.4E, black). Moreover, the functional shape of the inferred threshold coupling was in striking agreement with the theoretical prediction made under the hypothesis of Na^+-channel inactivation (Platkiewicz and Brette, 2010) (cf. Eq. 5.2). Since the value of the coupling timescale $\tau_\theta = 5.83 \pm 0.41$ ms (Figure 5.4F) was also consistent with previous measurements of fast sodium inactivation (Hodgkin and Huxley, 1952), we used the intracellular recordings to fit a new iGIF model, denoted iGIF-Na, in which $\theta_\infty(V)$ was assumed *a priori* to be the smooth rectifier function $\theta_\infty^{Na}(V)$ defined in Equation 5.2. For that, a different maximum likelihood procedure was used allowing the extraction of the biophysical parameters k_a, k_i and V_i (cf. Eq. 5.2), along with all other iGIF-Na model parameters (Figure 5.4G, see Materials and Methods). Both the spike-triggered movement of the firing threshold $\gamma(t)$ (Figure 5.4D, red) and the nonlinear coupling $\theta_\infty^{Na}(V)$ (Figure 5.4E, red) extracted by fitting the iGIF-Na model confirmed the results obtained with the nonparametric method (Figure 5.4D,E, black). Moreover, by fitting the data acquired in different cells, we intriguingly found that the ratio k_a/k_i determining the asymptotic slope of $\theta_\infty^{Na}(V)$ was always very close to one (Figure 5.4G, bottom). Providing additional evidence for the hypothesis that

the biophysical mechanism underlying a nonlinear coupling between firing threshold and membrane potential is fast Na$^+$-channel inactivation, we found that the log-likelihood was always larger for the iGIF-Na model than for the iGIF-NP model (Figure 5.4E, inset).
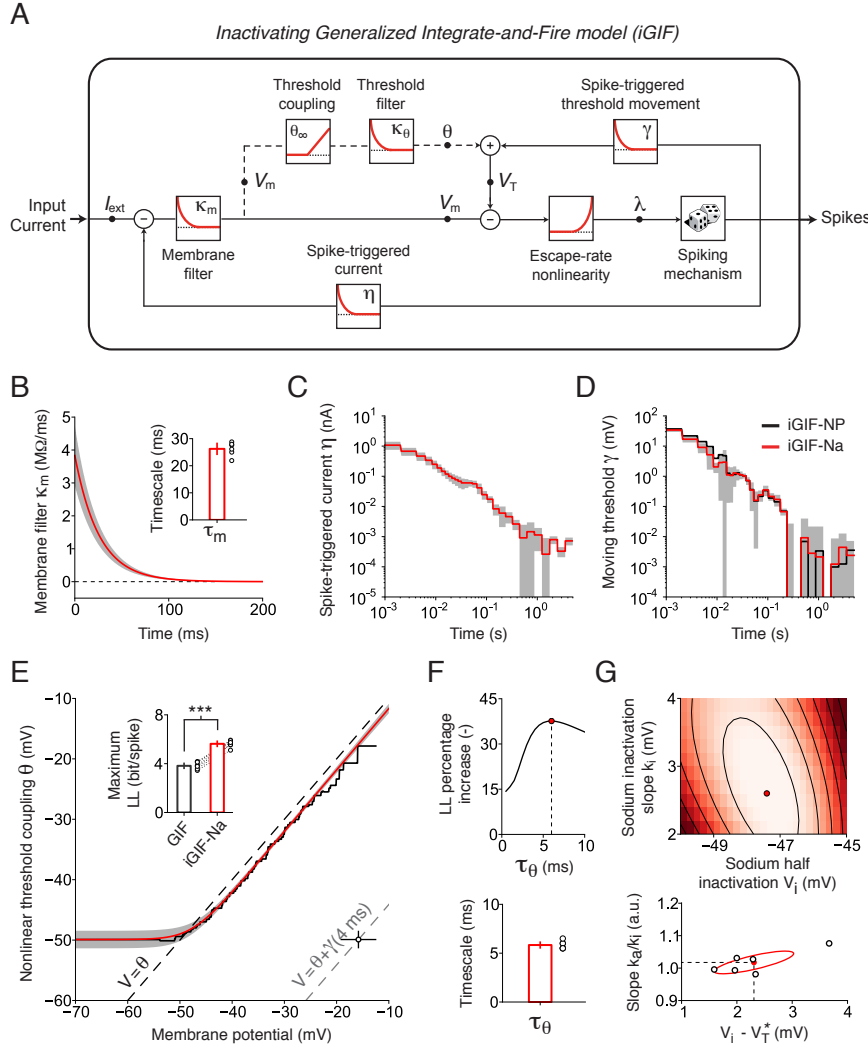
Figure 5.4: **Inactivating Generalized Integrate-and-Fire model (iGIF) with parameters extracted from intracellular recordings performed in Pyr neurons. A:** Schematic representation of the iGIF model. The input current I_{ext} is first low-pass filtered by the *Membrane filter* $\kappa_m(t) = \frac{R}{\tau_m} \cdot e^{-\frac{t}{\tau_m}}$. The resulting signal models the subthreshold membrane potential V_m and, after subtraction of the firing threshold V_T, is transformed into a firing intensity λ by the exponential *Escape-rate nonlinearity*. Spikes are emitted stochastically and elicit both a *Spike-triggered current* $\eta(t)$ and a *Spike-triggered threshold movement* $\gamma(t)$. In the iGIF model, but not in the GIF model, the firing threshold V_T is coupled to the subthreshold membrane potential (dashed circuit). For that, the membrane potential V_m is first passed throught the nonlinear *Threshold coupling* function $\theta_\infty(V)$ and then low-pass filtered by the *Threshold filter* $\kappa_\theta(t) = \frac{1}{\tau_\theta} \cdot e^{-\frac{t}{\tau_\theta}}$. As illustrated in the scheme, the latter mechanism implements a form of feedforward subthreshold adaptation. **B:** Mean (red) and standard deviation (gray area) of the membrane filters $\kappa_m(t)$ extracted from 6 Pyr neurons. Inset: the open circles represent the

characteristic timescale τ_m extracted from 6 Pyr neurons. The bar plot shows the average and one standard deviation across cells. **C:** Log-log plot of the mean (red) and standard deviation (gray area) of the spike-triggered current $\eta(t)$ extracted from 6 Pyr neurons. Asymmetric errors are a result of log-scales. **D:** Log-log plot of the mean spike-triggered threshold movement $\gamma(t)$ extracted from 6 Pyr neurons by fitting the iGIF-NP model (black) and the iGIF-Na model (red). The gray area represents one standard deviation across cells for the iGIF-Na model. Asymmetric errors are a result of log-scales. **E:** Mean nonlinear threshold coupling $\theta_\infty(V)$ extracted from 6 Pyr neurons with a nonparametric fitting procedure (balck, iGIF-NP) and by performing a parametric fit in which the smooth rectifier function $\theta_\infty^{\mathrm{Na}}(V)$ (Eq. 5.2) was assumed *a priori* (red, iGIF-Na). The gray area indicates one standard deviation across cells for the iGIF-Na model. In the absence of spikes, the nonlinear part of $\theta_\infty(V)$ is masked (that is, it lies on the right hand side of the diagonal $V = \theta$, dashed black). Spike-triggered movements of the firing threshold unmask, and consequently activate, the nonlinear coupling $\theta_\infty(V)$ by shifting the diagonal to the right (dashed gray). Inset: Maximum log-likelihood (LL, Eq. 5.23) of the GIF (black, $LL = 3.82 \pm 0.29$ bits/spike) and the iGIF-Na model (red, $LL = 5.63 \pm 0.30$ bits/spike). Each set of open circles represent the performance on the same cell. Bar plots indicate mean and one standard deviation across cells. The iGIF-Na model significantly outperforms the GIF model (n=6, paired t-test, $t = -23.59$, $p = 2.5 \cdot 10^{-6}$). **F:** Top: Maximum log-likelihood of the iGIF-NP model as a function of the coupling timescale τ_θ. The optimal timescale τ_θ (red circle) is accurately constrained by the intracellular recordings. Bottom: optimal timescales τ_θ extracted from 6 Pyr neurons. Conventions as in the inset of panel B. **G:** Top: Maximum log-likelihood of the iGIF-Na model as a function of k_i and V_i. The LL increases from dark red to light red. Bottom: the open circles show the optimal parameters extracted from 6 different neurons. The mean and the standard devotional ellipse across cells are shown in red.

Overall, the results reported in Figure 5.4 indicate that, in Pyr neurons, the firing threshold depends on the emission of previous spikes as well as on the subthreshold membrane potential dynamics. Importantly, the timescales on which these two mechanisms operate are different. If on one hand the timescale of the nonlinear coupling θ is relatively short and is consistent with the hypothesis of fast sodium inactivation, threshold changes induced by the emission of previous spikes are characterized by a power-law decay lasting for 5 second and possibly describing slow sodium inactivation (Fleidervish et al., 1996; Pozzorini et al., 2013). Due to this separation of timescales, it is convenient to consider positive spike-triggered movements of the firing threshold in the $V - \theta$ phase plane (Figure 5.4E), as spike-triggered horizontal shifts of the diagonal defining the region in which the membrane potential V equals the firing threshold V_{T} (cf. Eq. 5.3). Since the coupling between membrane potential and firing threshold is nonlinear, this picture suggests that spike-dependent and spike-independent threshold adaptation might interact in a nontrivial manner.

5.2.5 Nonlinear interaction between slow and fast Na$^+$-channel inactivation

To understand the interaction between spike-dependent and spike-independend threshold movements, as well as its implications on single-neuron coding, we analyzed the dynamics of the iGIF-Na model (with parameters extracted from L5 Pyr neurons) in response to three fluctuating currents generated according to Equation 5.6 using different means μ_{I}, a fixed standard deviation $\sigma_{\mathrm{I}} = 0.1$ nA and a temporal correlation of $\tau_{\mathrm{I}} = 3$ ms (Figure 5.5).

Chapter 5. Evidence for a nonlinear coupling between firing threshold and subthreshold potential

In response to a weak input $\mu_I = 60$ pA (Figure 5.5A, gray), the membrane potential fluctuated near the the resting potential and action potentials were occasionally driven by large input fluctuations (Figure 5.5A, black). In this particular regime, the evoked firing rate $f \approx 1$ Hz was very low and threshold movements induced by different action potentials did not build up significantly. Indeed, spike-dependent threshold adaptation $\phi(t) = \sum_{\hat{t}_j} \gamma(t - \hat{t}_j)$ mainly acted as a refractory process by reducing the firing probability after the emission of a previous spike (Figure 5.5A, blue). On average, given the modest mean contribution $\bar{\phi} = T^{-1} \int \phi(t) dt$ of spike-dependent processes to the average firing threshold (Figure 5.5A, dashed gray), action potentials evoked in response to weak inputs were generally initiated at low membrane potentials (Figure 5.5B). Subthreshold membrane potential fluctuations were consequently confined to relatively low voltages, where the coupling between firing threshold and subthreshold membrane potential is weak. That is, where the coupling gain $G_\theta(V) = \frac{d}{dV}\theta_\infty^{\mathrm{Na}}(V)$ is close to 0 (Figure 5.5B). As a result, in this regime, the dynamics of $\theta(t)$ simply implements an additional source of refractoriness by transiently increasing the firing threshold as a direct consequence of high-voltage after-spike resets (Figure 5.5A, red). We concluded that, in Pyr neurons responding to weak inputs, the coupling between subthreshold membrane fluctuations and firing threshold does not play an important role (Figure 5.5A, red).

This result can alternatively be understood by analyzing the dynamics of the iGIF model in the $V - \theta$ plane (Figure 5.5C), where, as already mentioned, spike-dependent changes of the firing threshold effectively shift the diagonal for spike initiation to the right (see Figure 5.4E). Since spike-triggered threshold movements decay according to a power-law (see Figure 5.4C and ref. Pozzorini et al. (2013)), the spike-initiation boundary $V = \theta + \phi(t)$ fluctuates in time over multiple timescales. Insights on the dynamics of the iGIF-Na model, can however be gained by simply considering the magnitude of the average shift $\bar{\phi}$. In contrast to the scenario discussed in Figure 5.3, the iGIF model is stochastic. For this reason, the diagonal $V = \theta + \bar{\phi}$ only approximates the boundary for high firing probability and action potentials can actually originate from a wider region of the phase plane (cf, Eq. 5.10). As shown in Figure 5.5A, for weak inputs evoking low firing rates f, the average contribution of spike-dependent threshold adaptation $\bar{\phi} \propto f$ is close to zero, meaning that the, on average, the phase plane region of high spiking probability is approximately delimited by the identity $V = \theta + \bar{\phi} \approx \theta$ (Figure 5.5C, compare dashed black and solid blue lines). Since in all Pyr neurons included in this study we systematically found that $V_i > V_T^*$ (Figure 5.4G, bottom), one can intuitively understand that, at low firing rates, the nonlinear coupling between firing threshold and membrane potential is not recruited by noting that, on average, the non-constant part of the coupling function $\theta_\infty^{\mathrm{Na}}(V)$ is *masked* on the right-hand side of the diagonal $V = \theta + \bar{\phi}$ (Figure 5.5C).
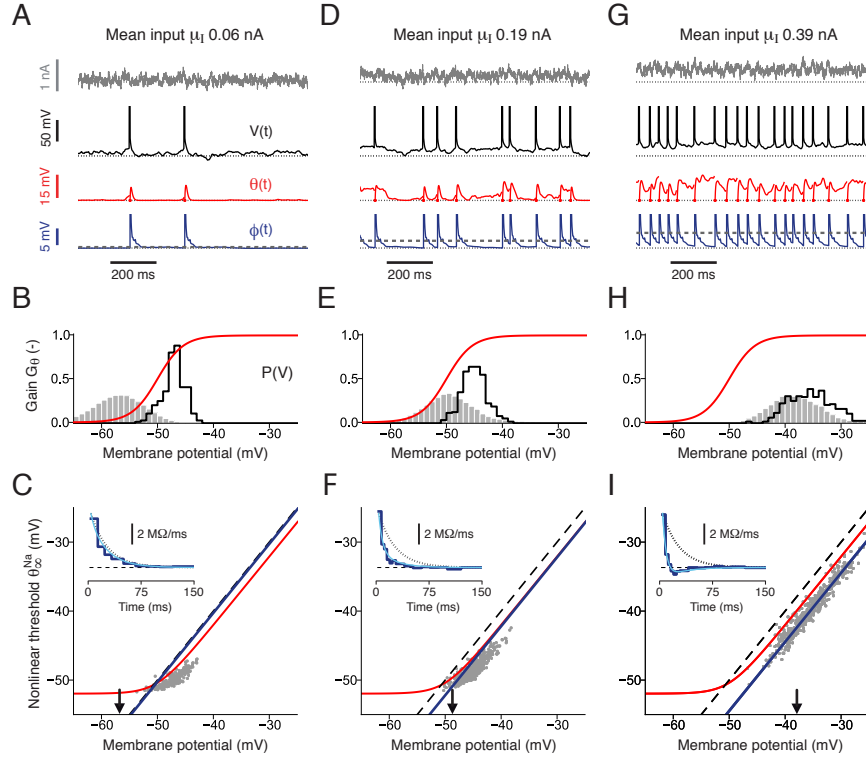
Figure 5.5: **Nonlinear interaction in the iGIF-Na model between spike-dependent and spike-independent threshold adaptation.** The iGIF-Na model dynamics is analyzed by simulating the responses to three fluctuating inputs generated according to Equation 5.6 with different offsets μ_I = 0.06 nA (panel A-C), μ_I = 0.19 nA (panel D-F) and μ_I = 0.39 nA (panel G-I). In all three conditions, the magnitude of the input fluctuations was σ_I = 0.1 nA and the temporal correlation was τ_I = 3 ms. **A:** Input current $I(t)$ (gray), membrane potential $V(t)$ (black), spike-independent threshold adaptation $\theta(t)$ (red), spike-dependent threshold adaptation $\phi(t) = \sum_{\hat{t}} \gamma(t - \hat{t})$ (blue) and average spike-dependent threshold adaptation $\bar{\phi} = T^{-1} \cdot \int_0^T \phi(s)\,ds$ (dashed gray, bottom). The four dotted black lines indicates (from top to bottom): $I = 0$ nA, $V = E_L$, $\theta = V_T^*$ and $\phi = 0$ mV. **B:** Distribution of subthreshold membrane potential fluctuations $P(V)$ (gray) and distribution of voltages at which spikes were initiated $P(V|\text{spike})$ (black). The gain of the firing threshold coupling $G_\theta(V) = \frac{d}{dV}\theta_\infty^{Na}(V)$ is shown as a function of the membrane potential V (red). For weak inputs μ_I, the membrane potential fluctuates within a range where the coupling gain $G_\theta(V)$ vanishes, explaining why, except for the transients induced by high voltage resetting after spikes, $\theta(t)$ is constant (see panel A, red). **C:** Phase plane $\theta - V$. In this regime, the threshold coupling $\theta_\infty^{Na}(V)$ (red) is *masked* on the right-hand side of the diagonal $V = \theta + \bar{\phi}$ (blue line). For comparison, the diagonal $V = \theta$ is also shown (dashed black). Gray dots indicate the phase plane region from where spikes originated. Since spike emission is stochastic and $\phi(t)$ fluctuates in time, the gray dots do not coincide with the diagonal $V = \theta + \bar{\phi}$. The black arrow indicates the mean subthreshold membrane potential (i.e., the mean of P(V) shown in panel B). Inset: The effective linear filter $\kappa_{eff}(t)$ of the iGIF-Na model (light blue) matches the linear filter $\kappa_{GLM}(t)$ computed as a control by fitting the iGIF-Na model data with a GLM (dark blue). For weak inputs, the average gain coupling $\bar{G}_\theta = \int G_\theta(V)P(V)dV$ is almost vanishing. Consequently, the effective filter $\kappa_{eff}(t)$ closely resembles to the membrane filer $\kappa_m(t)$ (dotted black). The dashed black line represents 0 MΩ/ms. **D-F:** iGIF-Na model dynamics in response to a fluctuating input current with mean μ_I = 0.19 nA. Same conventions as in panels A-C. As a result of the increased mean current, the voltage distribution is shifted towards more depolarized potentials (panel D, black line; panel F, black arrow), where the coupling gain G_θ takes intermediate values (panel E). As a result of the increased firing rate $f \approx 10$ Hz,

the average strength of spike-dependent threshold adaptation is also increased (panel D, blue and dashed gray). On average, the region of the phase plane that has to be reached in order to emit a spike (that is, the diagonal $V = \theta + \bar{\phi}$) is consequently shifted to the right (panel F, blue), partially *unmasking* the nonlinear threshold coupling $\theta_\infty^{\text{Na}}(V)$ (panel F, red). In this regime, the nonlinear coupling $\theta(t)$ activates (panel D, red) and significantly shortens the single-neuron integration timescale as seen in $\kappa_{\text{eff}}(t)$ (panel F, inset). **G-I:** iGIF-Na model dynamics in response to a fluctuating input current with mean $\mu_I = 0.39$ nA. The resulting firing rate is $f \approx 20$ Hz. Same conventions as in panels A-C. Increased spike-dependent threshold adaptation (panel G, blue) further shifts the diagonal $V = \theta + \bar{\phi}$ to the right (panel I, blue line). Consequently, the nonlinear coupling is, on average, *unmasked* and the membrane potential fluctuates within a range where the threshold coupling reaches its maximal strength $\bar{G}_\theta \approx \theta_{\text{slope}}^{\text{Na}}$. In this regime, where pyramidal neurons manifest enhanced sensitivity to input fluctuations (see Figure 5.1b), the threshold coupling $\theta(t)$ is strongly active (panel G, red), making the effective filer $\kappa_{\text{eff}}(t)$ biphasic and transforming the single-neuron behavior from *integrate-and-fire* to *resonate-and-fire* (panel F, inset).

Increasing the input strength to $\mu_I = 190$ pA (Figure 5.5D, gray) resulted in a mean firing rate $f \approx 10$ Hz and shifted the membrane potential distribution towards more depolarized potentials (Figure 5.5B, black), where the threshold coupling strength G_θ becomes positive (Fig 5.5E). As a result of increased spike-dependent threshold adaptation, the diagonal $V = \theta + \bar{\phi}$ is shifted towards more depolarized potentials, partially *unmasking* the nonlinear part of the coupling function $\theta_\infty^{\text{Na}}(V)$. Consequently, in this regime, the coupling $\theta(t)$ between firing threshold and membrane potential starts to play a role that goes beyond the simple refractoriness induced by after-spike resets (Figure 5.5D, red).

Further increasing the input strength to $\mu_I = 390$ pA (Figure 5.5G-I) makes the iGIF-Na model fire at a high rate $f \approx 20$ Hz (Figure 5.5G), at which Pyr neurons lose sensitivity to the mean drive μ_I and manifest enhanced sensitivity to input fluctuations (see Figure 5.1B,D). Notably, in this regime, threshold movements triggered by different spikes accumulate in such a way as to completely *unmask* the coupling function $\theta_\infty^{\text{Na}}(V)$ (Figure 5.5I). The strong input μ_I pushes the membrane potential fluctuations to very depolarized values, where the threshold coupling reaches its maximal strength $G_\theta \approx \theta_{\text{slope}}^{\text{Na}}$ (Figure 5.5H). Consequently, following the after-spike reset to $\theta = V_T^*$, the coupling variable $\theta(t)$ rapidly increases to large values where, in contrast to the transient behavior observed in response to weak inputs, it fluctuates until the next spike is emitted (compare the red traces Figure 5.5G, red with Figure 5.5A,D). This result indicates that enhanced sensitivity to input fluctuations, as it is observed in Pyr neurons responding to strong inputs, is mediated by the activation of a coupling mechanism between membrane potential and firing threshold. Indeed, increased input fluctuations translates into faster currents that, in turn, evoke higher firing rates by overcoming the dampening effect induced by fast sodium inactivation (see Figure 5.3 and ref. Platkiewicz and Brette (2011)).

Overall, the results reported in Figure 5.5 provide experimental evidence for the existence of a non-trivial interplay between spike-dependent and nonlinear voltage-dependent threshold movements. In particular, we found that the increased contribution of spike-dependent mechanisms induced by large firing rates, progressively *unmask* (i.e., activates) the nonlinear coupling $\theta_\infty^{\text{Na}}(V)$ (Figure 5.5C,F,I), thus enhancing single-neuron sensitivity to rapid signals.

The functional implications of this interaction, and in particular the link with enhanced sensitivity to input fluctuations, are further investigated in the next section.

5.2.6 In Pyr neurons, nonlinear threshold dynamics adaptively changes the single-neuron behavior from leaky integration to coincidence detection

To unravel the mechanism underlying enhanced sensitivity to input fluctuations, we reduced the iGIF model to a Generalized Linear Model (GLM, Truccolo et al. (2005); Pillow et al. (2008)). In the GLM (Figure 5.6A, see Materials and Methods), the input current $I(t)$ is first passed through a linear filter $\kappa_{\mathrm{eff}}(t)$. In contrast to both the membrane filter $\kappa_{\mathrm{m}}(t)$ and the threshold filter $\kappa_{\theta}(t)$ of the iGIF model, $\kappa_{\mathrm{eff}}(t)$ is not assumed to be an exponential and its shape can be extracted from experimental data (Truccolo et al., 2005; Pillow et al., 2008). As in the iGIF model, an exponential nonlinearity transforms the filtered input into a spiking probability $\lambda_{\mathrm{GLM}}(t)$, according to which action potentials are generated. After each spike, an adaptation process $h_{\mathrm{GLM}}(t)$ is triggered to accounts for the single-neuron spike-history dependency.
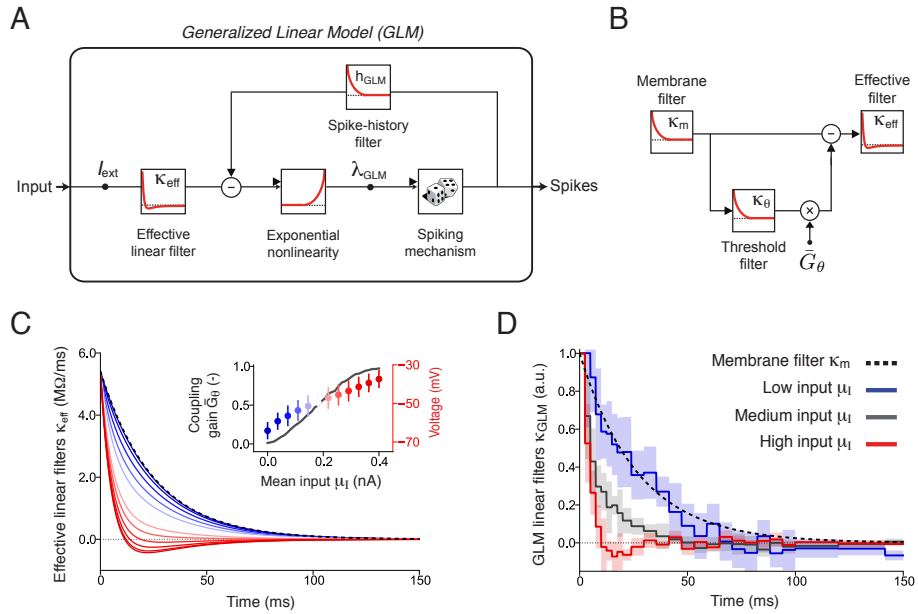
Figure 5.6: **In Pyr neurons, nonlinear threshold dynamics controls a transition from leaky integration to coincidence detection. A:** Schematic representation of the Generalized Linear Model (GLM). The input current $I_{\mathrm{ext}}(t)$ is first low-pass filtered through $\kappa_{\mathrm{eff}}(t)$. Importantly, the linear filter $\kappa_{\mathrm{eff}}(t)$ of the GLM is not constrained to be an exponential function, but can take any shape. The filtered input is transformed by an exponential nonlinearity into a firing intensity $\lambda_{\mathrm{GLM}}(t)$, which defines the probability of emitting a spike. Each time an action potential is fired, a feedback process $h_{\mathrm{GLM}}(t)$ is triggered that phenomenologically accounts for all spike-history effects (e.g., spike-triggered adaptation currents, spike-dependent threshold movements and after-spike reset processes). **B:** The membrane filter $\kappa_{\mathrm{m}}(t)$ and the threshold filter $\kappa_{\theta}(t)$ are combined to compute the effective filter $\kappa_{\mathrm{eff}}(t)$ of a GLM that best describes input filtering in the iGIF model. To map the iGIF model to the GLM, the membrane

filter $\kappa_{\mathrm{m}}(t)$ is first smoothed by $\kappa_\theta(t)$; the resulting function is then rescaled by the average coupling strength $\bar{G}_\theta = \int G_\theta(V)P(V)dV$ and finally subtracted from $\kappa_{\mathrm{m}}(t)$ to obtain $\kappa_{\mathrm{eff}}(t)$ (cf. Eq. 5.5). Since the average coupling strength $\bar{G}_\theta$ is a function of $P(V)$ (which in turn depends on the input strength μ_{I}), the iGIF model predicts that, in Pyr neurons, somatic integration adaptively changes depending on the input statistics. **C:** Effective linear filters $\kappa_{\mathrm{eff}}(t)$ (computed with Eq. 5.5) that best approximate the iGIF model responding to fluctuating currents with mean increasing from $\mu_{\mathrm{I}} = 0$ pA (blue) to $\mu_{\mathrm{I}} = 400$ pA (red). Input fluctuations and temporal correlation were set to $\sigma_{\mathrm{I}} = 100$ pA and $\tau_{\mathrm{I}} = 3$ ms. For $\mu_{\mathrm{I}} = 0$ pA, the membrane potential fluctuates within a region where the coupling strength $G_\theta(V)$ vanishes. Since $\bar{G}_\theta \approx 0$, the effective filter $\kappa_{\mathrm{eff}}(t)$ (dark blue) equals the membrane filer $\kappa_{\mathrm{m}}(t)$ (dashed, black). In this regime Pyr neurons operate as leaky integrators. The average coupling strength $\bar{G}_\theta$ increases with μ_{I} (see inset). The progressive activation of the coupling between firing threshold and membrane potential results into a shrinking of the effective filter $\kappa_{\mathrm{eff}}(t)$. For strong inputs $\mu_{\mathrm{I}} > 300$ pA, $\bar{G}_\theta \to 1$ and the effective filer $\kappa_{\mathrm{eff}}(t)$ becomes biphasic (red). In this regime, Pyr neurons lose sensitivity to the mean drive (that is, $\int_0^\infty \kappa_{\mathrm{eff}}(s)ds \to 0$) and preferentially respond to rapidly fluctuating currents. Inset: The average coupling strength $\bar{G}_\theta$ (left axis, gray line), as well as the mean and the standard deviation of the membrane potential distribution $P(V)$ (right axis, circles with colors used to visualize the filters $\kappa_{\mathrm{eff}}(t)$), are shown as a function of the mean input μ_{I}. **D:** Average effective filters $\kappa_{\mathrm{eff}}(t)$ extracted from six Pyr neurons by fitting the GLM to experimental data. Shaded areas represent one standard deviation across neurons. The experimental data used to compute the $f - \mu_{\mathrm{I}}$ curves (see Figure 5.1) were split in 3 groups depending on the input strength: low (blue, $\mu_{\mathrm{I}} \in [\mu_1, \mu_3]$ pA), medium (gray, $\mu_{\mathrm{I}} \in [\mu_4, \mu_5]$ pA) and high (red, $\mu_{\mathrm{I}} \in [\mu_8, \mu_{10}]$ pA). GLMs were fitted independently on the three datasets. As predicted by the iGIF-Na model (panel C), increasing the input strength μ_{I} switches the single-neuron behavior from leaky integration (blue) to differentiation (red). For comparison, a rescaled version of the average membrane filter $\kappa_{\mathrm{m}}(t)$ of the iGIF-Na (see Figure 5.4B) is shown (dashed black).

In case of a standard GIF model (Mensi et al., 2011b; Pozzorini et al., 2013), where the coupling between membrane potential and firing threshold is absent, it is straightforward to prove that the effective filter $\kappa_{\mathrm{eff}}(t)$ of a GLM that best captures the GIF model response simply corresponds to the membrane filter $\kappa_{\mathrm{m}}(t)$. On the other hand, in case of a nonlinear coupling $\theta_\infty(V)$, the mapping between iGIF model and GLM is more involved and requires the linearization of Equation 5.1 (see Materials and Methods). We simplified the threshold dynamics of the iGIF-Na model by taking the first-order approximation $\theta_\infty^{\mathrm{Na}}(V) \approx \bar{C}_\theta + \bar{G}_\theta \cdot V$, with $\bar{C}_\theta$ being a constant and $\bar{G}_\theta$ being the average coupling strength computed with respect to the membrane potential distribution $P(V)$:

$$\bar{G}_\theta = \int_{-\infty}^{\infty} G_\theta(V)P(V)dV. \tag{5.4}$$

Since in the iGIF-Na model the subthreshold membrane potential dynamics is linear (see Eq. 5.11) and the spiking probability only depends on the difference between firing threshold and membrane potential (see Eq. 5.10), the effective linear filter $\kappa_{\mathrm{eff}}(t)$ that best approximates the response of a iGIF-Na model is given by (Figure 5.6B, see Materials and Methods):

$$\kappa_{\mathrm{eff}}(t) = \kappa_{\mathrm{m}}(t) - \bar{G}_\theta \cdot \int_0^t \kappa_\theta(s)\kappa_{\mathrm{m}}(t - s)ds, \tag{5.5}$$

where $\kappa_{\mathrm{m}}(t) = \frac{R}{\tau_{\mathrm{m}}} \exp\left(-\frac{t}{\tau_{\mathrm{m}}}\right)$ is the membrane filter and $\kappa_\theta(t) = \frac{1}{\tau_\theta} \exp\left(-\frac{t}{\tau_\theta}\right)$ is the threshold filter (see Figure 5.4A). According to Equation 5.5, the nonlinear coupling between membrane

potential and firing threshold is expected to produce to a shunting effect by reducing the magnitude of the effective filter through which somatic integration in performed.

To explore this hypothesis, we further analyzed the results reported in Figure 5.5 by computing the effective linear filters $\kappa_{\mathrm{eff}}(t)$ that best describes the iGIF-Na response to a weak, a medium and a strong input. As already mentioned, in case of a weak drive $\mu_{\mathrm{I}} = 60$ pA, the membrane potential fluctuates within a range where $G_\theta(V)$ vanishes (Figure 5.5B). Consequently, the average coupling strength $\bar{G}_\theta \approx 0$ is extremely weak and, from Equation 5.5, it follows that $\kappa_{\mathrm{eff}}(t) \approx \kappa_{\mathrm{m}}(t)$ (Figure 5.5C, inset). This result indicates that, in Pyr neurons responding to weak inputs, the coupling between membrane potential and firing threshold is not recruited, meaning that somatic input integration is entirely controlled by the passive properties of the membrane. Increasing the input strength to $\mu_{\mathrm{I}} = 190$ pA shifts the membrane potential distribution $P(V)$ towards more depolarized potentials, where $G_\theta(V) > 0$. In this regime, the coupling mechanism is partially recruited and the effective timescale of somatic integration is significantly shortened (Figure 5.5F). Notably, in case of a strong input $\mu_{\mathrm{I}} = 390$ pA at which Pyr neurons undergo firing rate saturation and manifest enhanced sensitivity to input fluctuations (see Figure 5.1B,D), the average coupling reaches its maximal strength $\bar{G}_\theta = \theta_{\mathrm{slope}}^{\mathrm{Na}}$, leading to a resonant filter $\kappa_{\mathrm{eff}}(t)$ (Figure 5.5I). These results were confirmed by fitting a GLM on the iGIF-Na data (insets of Figure 5.5C,F,I) and provide a mechanistic explanation of why, at strong inputs μ_{I}, the firing rate observed in Pyr neurons increases with the magnitude σ_{I} of input fluctuations (Figure 5.1B,D). Moreover, consistent with the fact that Pyr neurons become insensitive to μ_{I}, the maximal coupling strength extracted from six neurons was always very close to $\theta_{\mathrm{slope}}^{\mathrm{Na}} \approx 1$ (Figure 5.4G), implying that, for strong inputs, the area under the filter $\kappa_{\mathrm{eff}}(t)$ vanishes (that is, $\int_0^\infty \kappa_{\mathrm{eff}}(s)\, ds \approx 0$), providing a shunting effect.

Overall, the analytical results obtained by analyzing the iGIF-Na model with parameters extracted from experimental data indicate that increasing the input strength μ_{I} progressively activates the coupling between membrane potential and firing threshold, which in turn switches the single-neuron behavior from leaky integration to coincidence detection (or differentiation) (Figure 5.6C). To provide further evidence, we independently fitted the GLM on three datasets obtained by splitting the experimental data according to the input strength μ_{I}. The resulting GLM filters $\kappa_{\mathrm{GLM}}(t)$ confirmed that, in response to inputs of increasing strength, Pyr neurons progressively shorten the timescale on which the input current is integrated. Moreover, the effective filter $\kappa_{\mathrm{GLM}}(t)$ extracted by fitting a GLM, confirmed that strong inputs are somatically integrated via a biphasic filer (Figure 5.6D).

5.2.7 The iGIF model captures enhanced sensitivity to input fluctuations

The results reported in the previous section indirectly suggest that accounting for a nonlinear interaction between membrane potential and firing threshold might be sufficient to explain enhanced sensitivity to input fluctuations. To confirm this hypothesis, we tested the iGIF-Na model with a set of 5-second currents generated by systematically varying the input

parameters μ_I and σ_I (Figure 5.7). We compared both the transient and the steady-state response of the model against experimental data and found that, despite its relative simplicity, the iGIF-Na model accurately captured the behavior of Pyr neurons over a broad range of input parameters (Figure 5.7A). In particular, the iGIF-Na model exhibited enhanced sensitivity to input fluctuations throughout the entire set of depolarizing currents μ_I that were tested (Figure 5.7B, top) and reproduced the neural response with an average accuracy of $\epsilon_{rate} = 1.38 \pm 0.95$ Hz (Figure 5.7B, bottom). Notably, the iGIF-Na model also captured, at least qualitatively, the complex dependence of the firing threshold on input parameters. Indeed, the voltage threshold at which spikes where initiated in iGIF-Na model was positively correlated with the mean input μ_I (Figure 5.7C) and negatively correlated to σ_I (Figure 5.7D).
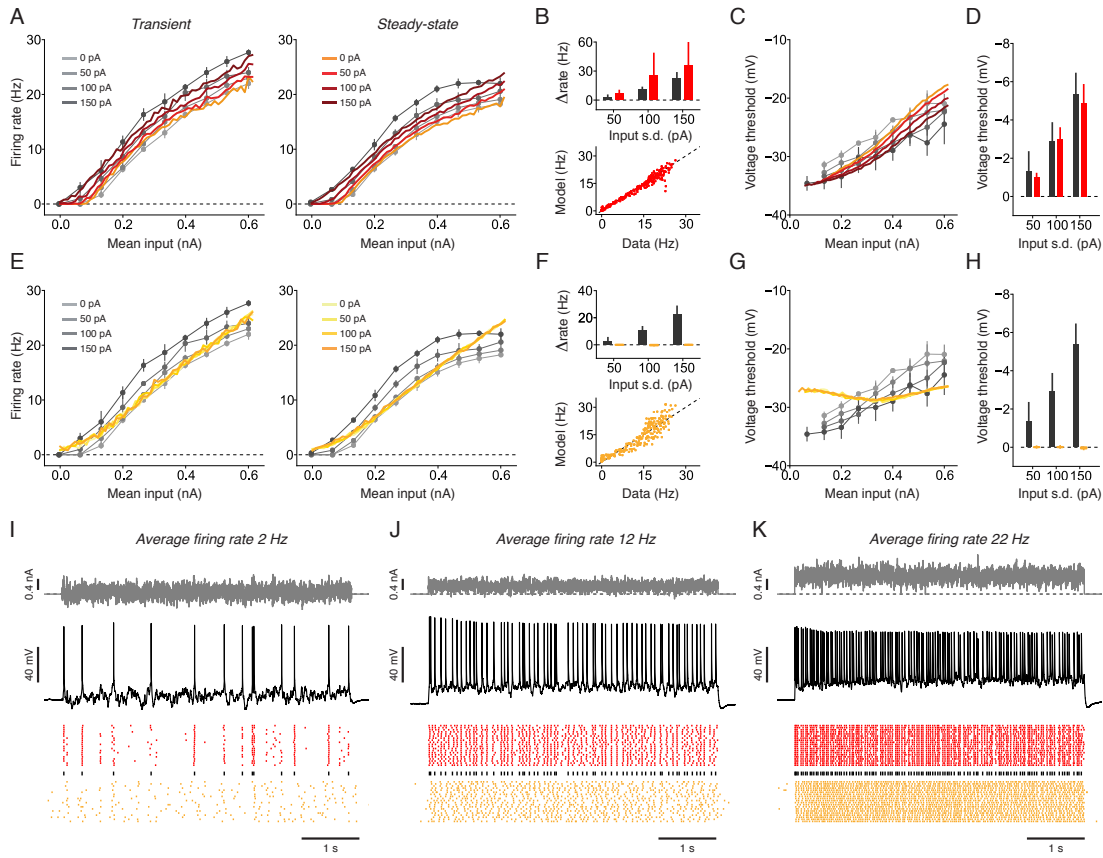
Figure 5.7: **The iGIF-Na model captures the firing rate response observed in Pyr neurons over a broad range of input parameters. A-D:** The iGIF-Na model response (red) is compared against experimental data (gray). **A:** Comparison between $f - \mu_I$ curves observed in a typical Pyr neuron (gray) and produced by the iGIF-Na model (red). Different colors and gray levels indicate the magnitude of input fluctuations σ_I (see legends). For each combination of input parameters (μ_I, σ_I), a 5-second current was tested three times. Gray error bars indicate one standard deviation across repetitions. Left: Transient response quantified by computing the average firing rate f during the first second. Right: Steady-state response computed by discarding the transient response observed during the first second (see Figure 5.1B). **B:** Summary data of results obtained in different neurons (n=6). Top: Percentage change in steady-state firing rate obtained by increasing the input standard deviation σ_I. As

in Figure 5.1D, changes were computed with respect to σ_I=0 pA by taking the average response to the two strongest inputs $\mu_I^{(9)}$ and $\mu_I^{(10)}$. The iGIF-Na model (red) and experimental data (gray) are in nice agreement. Error bars indicate one standard deviation across cells. Bottom: The steady-state firing rate of the iGIF-Na model is compared against experimental data. Each dot represents the performance measured in a single cell for a paritcular input (μ_I, σ_I). **C:** The average firing threshold observed in a typical cell (gray) and produced by the iGIF-Na model (red) are plotted as a function of the mean input μ_I. Different colors and different gray levels indicate the magnitude of input fluctuations (see legends in panel *A*). Gray error bars indicate one standard deviation across recordings. Data are from the same cell as in panel *A*. Note that, in both the model and the experimental data, the firing threshold decreases as a function σ_I. **D:** Summary data of results obtained in different neurons (n=6). Average change in voltage threshold obtained by increasing the input standard deviation σ_I. Changes were computed with respect to $\sigma_I = 0$ by averaging the results obtained for strong depolarizing offsets $\mu_I > \mu_I^{(8)}$. Conventions are as in panel *B*. **E-H:** As a control, the GIF model response (yellow) is compared against experimental data (gray). Different colors indicate different magnitudes of input fluctuations σ_I (see legend in panel E, right). In contrast to the iGIF-Na model (panel *B*, top), the GIF model is not sensitive to σ_I (panel *F*, top). Data are presented as in panels *A-D*. Experimental data were copied from panels *A-D*. **I-K:** Typical raw data used to obtain the results reported in panels *A-H*. **I:** Typical intracellular response (black, middle) evoked by a 5-second current generated with parameters $\mu_I = 60$ pA and $\sigma_I = 150$ pA (top, gray). The spiking response (bottom, black) is well predicted by the iGIF-Na model (red), but not by the GIF model (yellow). Since both models are stochastic, multiple simulations were performed in which the same current was presented to the models. **J:** Same data as in panel *I*, but with a current generated with parameters $\mu_I = 260$ pA and $\sigma_I = 100$. The dashed black line indicates 0 pA (top). **K:** Same data as panel *I*, but with a current generated with parameters $\mu_I = 600$ pA and $\sigma_I = 150$.

To further appreciate the importance of modeling the nonlinear coupling between membrane potential and firing threshold, we also fitted the experimental data with our previous Generalized Integrate-and-Fire model (GIF, Mensi et al. (2011b); Pozzorini et al. (2013), see Materials and Methods). The GIF model differs from the iGIF model simply because its firing threshold dynamics only depends on the spike-history (and not on the membrane potential). As expected, the GIF model could not capture the firing rate dependence on σ_I and was much less accurate than the iGIF model in reproducing the firing rates observed at steady-state ($\epsilon_{\text{rate}} = 2.92 \pm 0.92$ Hz, see Figure 5.7E,F). Finally, the strong mismatch between the firing threshold measured in the experiments and produced by the GIF model (Figure 5.7G,H), highlights the fact that a spiking model in which the firing threshold dynamics simply depends on previous action potentials is not sufficient to explain the activity of Pyr neurons over a wide range of inputs.

5.2.8 The iGIF model outperforms previous models in predicting in the occurrence of individual spikes with millisecond precision

A good single-neuron model should predict the occurrence of individual spikes with millisecond precision (Gerstner and Naud, 2009). As illustrated in Figure 5.7I-K, the iGIF model does not simply model the average firing rate observed in Pyr neurons, but also reproduces the fine temporal structure of the spiking response.

To take into account the fact that single-neurons are stochastic (Mainen and Sejnowski, 1995)

and to avoid problems related to overfitting, we further assessed spike-timing prediction on a new experimental dataset (*test dataset*). This dataset was collected by recording the response to nine repetitive injections of the same fluctuating current $I_{\text{test}}(t)$ and was not used for parameter extraction. To test the model's ability of capturing the single-neuron response to different levels of input fluctuations, the standard deviation of the current $I_{\text{test}}(t)$ was modulated by a slow sinusoidal function (Figure 5.8A, see Materials and Methods). On average, the iGIF model (with parameters extracted from the *f-I dataset* previously used to compute the firing-rate response curves) was able to predict $73.6 \pm 3.3\%$ of the spikes with a precision of ± 4 ms (Figure 5.8B,E). The iGIF model performed well also in predicting the slow firing rate fluctuations induced by the input modulation (Figure 5.8C,F) and the rapid dynamics of the subthreshold membrane potential (Figure 5.8D). As expected, the performance achieved by the GIF model (with parameters extracted form the *f-I dataset*) were significantly lower. In particular, the GIF model was able to predict only $20.9 \pm 5.0\%$ of the spikes (Figure 5.8B,E) and, in agreement with the results in Figure 5.7E-F, it did not capture the slow firing-rate modulation (Figure 5.8C,F).

In previous studies (Mensi et al., 2011b; Pozzorini et al., 2013), we found that the GIF model was able to predict around 80% of the spikes observed in Pyr neurons responding to non-stationary inputs. At first glance, the low performance achieved here might therefore seem surprising. This result can however be understood by comparing the degree of stochasticity (defined by the parameter ΔV, see Materials and Methods) of the GIF and the iGIF model (Figure 5.8G). In both models, ΔV defines the sharpness of the firing threshold and regulates the level of randomness of the spiking process (cf, Eq. 5.10). In particular, both models are deterministic if $\Delta V = 0$ and tend to an homogeneous Poisson process if $\Delta V \rightarrow \infty$. In the ideal case of a perfect model, the parameter ΔV is optimally tuned to capture trial-to-trial variability. In reality, a lack of flexibility in the model biases the estimation of ΔV towards large values (that is, in an oversimplified model, all the single-neuron features that can not be explained are interpreted as a manifestation of randomness). If on one hand, the level of stochasticity observed in the iGIF model was weak ($\Delta V = 0.56$ mV, s.d. 0.10 mV), the values obtained by fitting the GIF model on the *f-I dataset* were always very high ($\Delta V = 7.27$ mV, s.d. 2.34 mV), explaining the low performance achieved by the GIF model in predicting individual spikes.
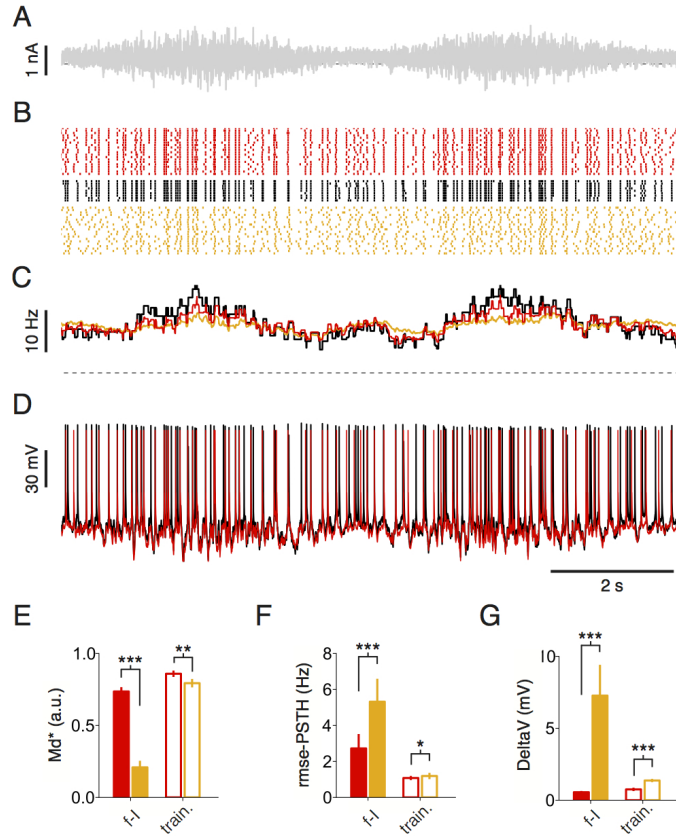
Figure 5.8: **The iGIF-Na model predicts the occurrence of individual spikes of Pyr neurons with a millisecond precision.** The predictive power of both the iGIF model (red) and the GIF model (yellow) was assessed on a new dataset (*test dataset*), which was not used for parameter extraction. **A:** A segment of the 20-second current used to build the *test dataset* is shown. The input current was generated according to a non-stationary Gaussian process with constant mean and sinusoidal standard deviation (cf. Eq. 5.7). The dashed line indicates 0 pA. **B:** Typical spiking response of a Pyr neuron (black raster) to 9 repetitive injections of the current shown in panel *A*. The iGIF model (red) outperforms the GIF model (yellow) in predicting the occurrence of individual spike (results are quantified in panel *E*, filled bars). **C:** PSTHs computed by counting the number of spikes within rectangular windows of 500-ms. The iGIF model (red) outperforms the GIF model (yellow) in predicting the slow rate fluctuations (black) induced by the sinusoidal modulation of the input (results are quantified in panel *F*, filled bars) The dashed line indicates 0 Hz. **D:** Typical intracellular response to a single presentation of the input current shown in panel A (black) compared against the iGIF model prediction (red). **E-G:** Summary data showing the performance of the iGIF (red) and the GIF (yellow) model in predicting the spiking activity of 6 Pyr neurons. Filled bars show the performance of models trained on the experimental dataset used to compute the f-μ_I curves (*f-I dataset*). Empty bars show the performance of models trained on a different dataset obtained by injecting a 120-second current that was generated with the same statistics as the *test dataset* (*training dataset*). Error bars represent one standard deviation across cells. **E:** Spike-timing prediction as quantified by the similarity measure M_d^*. The iGIF model significantly outperforms the GIF model with parameters extracted from the *f-I dataset* (M_d^*=0.74, s.d. 0.03, iGIF; M_d^*=0.21, s.d. 0.05, GIF; $n = 6$, paired Student t-test, $t_5 = -28.22$, $p = 10^{-6}$) and from the *training dataset* (M_d^*=0.86, s.d. 0.02, iGIF; M_d^*=0.79, s.d. 0.03, GIF; $n = 6$, paired Student t-test, $t_5 = -5.68$, $p = 0.0024$). **F:** The prediction error on the PSTH was quantified by computing the root mean squared error (RMSE) between data and model prediction. The iGIF model significantly outperforms the GIF

model with parameters extracted from the *f-I dataset* (ϵ_{rate}=2.72, s.d. 0.80 Hz, iGIF; ϵ_{rate}=5.32, s.d. 1.28 Hz, GIF; n = 6, paired Student t-test, t_5 = 8.72, p = 0.00033) and from the *training dataset* (ϵ_{rate}=1.08, s.d. 0.12 Hz, iGIF; ϵ_{rate}=1.19, s.d. 0.18 Hz, GIF; n = 6, paired Student t-test, t_5 = 3.54, p = 0.01660). **G:** Comparison between the degree of stochasticity of the GIF and the iGIF models as quantified by the parameter ΔV. Regardless of the dataset used to perform parameter extraction, the iGIF model is significantly less stochastic than the GIF model (n = 6, paired Student t-test, t_5 = 7.11, p=0.00085, *f-I dataset*; n = 6, paired Student t-test, t_5 = 7.60, p=0.00062, *training dataset*). Note that the level of stochasticity obtained by fitting the GIF model on the *f-I dataset* is extremely high. This result indicates that the GIF model is not flexible enough to capture the behavior of Pyr neurons over a wide range of input parameters.

To make sure that the success of the iGIF model did not simply result from the aberrant level of stochasticity in the GIF model, we reassessed spike-timing prediction in both models by performing parameter extraction from a new dataset (*training dataset*) obtained by injecting a 120-s current with the same statistics as the *test dataset* (Figure 5.8E-G, empty bars). As expected, the level of stochasticity in the GIF model dramatically decreased (Figure 5.8G), recovering the GIF model's performances to its normal level ($M_d^* = 79.4\%$, s.d. 3.2%). Notably, the iGIF model with parameters extracted from the *training dataset* significantly outperformed the GIF model by predicting 86.0% of spikes ($M_d^* = 86.0\%$, s.d. 2.4%; Figure 5.8E).

Overall, these results indicate that the iGIF model is an excellent spiking model capable of predicting individual spikes with millisecond precision and capturing the activity of Pyr neurons over a wide range on input parameters.

5.3 Discussion

Our main finding is that L5 pyramidal neurons maintain sensitivity to input fluctuations even at large mean inputs due to the adaptive properties of the voltage threshold. Overall this means that pyramidal neurons process their inputs more like coincidence detectors than leaky integrators. Indeed, slow increases of the membrane potential that can result form asynchronous input (or a mean external drive) will lead on average to larger threshold. Consistent with this argument, fI curves measured in pyramidal neurons were characterized by saturation of the firing threshold at relatively low potentials. On the other hand, rapid depolarizations resulting from coincident excitatory inputs will drive the cell more efficiently enhancing temporal coding. Consistent with this explanation, increasing the standard deviation of the input current and consequently increasing the speed at which the subthreshold membrane potential fluctuates was reflected in both lower firing threshold and increased firing rate, even at large mean inputs.

The threshold equation of Platkiewicz and Brette (2010) provides a theory of how different conductances and channels properties modulate the voltage threshold for spike initiation. Therefore, given the biophysical properties of the channels expressed in a particular neuronal types, it is possible to derive an equation for the action potential dynamic. Considering the biophysical properties of Na$^+$ channels reported in a vast number of publications and reported

in a meta analysis (Angelino and Brenner, 2007), Platkiewicz and Brette (2011) concluded that the inactivation properties of sodium channels expressed in the central nervous systems are likely to be, at least in part, the source of the large voltage threshold variability observed *in vivo*.

However, measuring the biophysical properties of sodium currents based on voltage clamp experiments is problematic. Here we take a different approach, all the threshold parameters of the iGIF model, in particular the nature of the nonlinear coupling and the threshold timescale are extracted from intracellular recordings. Based on these results, we can therefore make predictions on certain biophysical quantities, such as k_a, k_i and the dynamics of sodium channel inactivations $\theta_\infty(V)$.

In our model subthreshold coupling accounts for negative correlation between rate of depolarization and firing threshold, while spike-triggered movement of firing threshold, accounts for negative correlation between firing threshold and previous ISIs. Our results are consistent with a model of sodium channel mediated by 3 gating variables $I_{Na} \propto sm^3h$ (Fleidervish et al., 1996) where s implements slow inactivation and, in the iGIF model, is approximated by the stereotypical spike-triggered movement of the firing threshold γ.

To conclude, our data analysis showed that threshold variability was correlated with the membrane potential, depends on the firing rate and on the rate of depolarization. These results strongly suggest that this variability has not to be interpreted as noise but can be explained by the biophysical properties of sodium channels. We fitted a spiking neuron model in which the firing threshold both dependent on the ISI via a spike triggered movement of the firing threshold and is coupled to the subthreshold membrane potential. The results indicate that the firing rate is nonlinearly coupled to the membrane potential in such a way that the the firing threshold adapts to slow fluctuations making the single neuron more sensitive to rapid fluctuations than mean currents. Extending the model with this coupling leads to a better spike timing prediction, a better fit of the fI curve and provides an intuitive explanation of why at large mean currents the output rate is more sensitive to fluctuations than to the mean input. Although, here the iGIF model was used to explain particular phenomena, we believe that it could be used as a biologically plausible model for single neuron dynamics. Indeed, in terms of spike timing perdition, the model outperforms previous models that were considered good. The main advantage of this model is its ability to be precise on a white spectrum of input statistics. A task that, due to the highly non linear dynamics that characterized neurons, in often difficult to achieve.

5.4 Experimental Procedures

5.4.1 Electrophysiological recordings

All procedures in this study were conducted in conformity with the Swiss Welfare Act and the Swiss National Institutional Guidelines on Animal Experimentation for the ethical use

of animals. The Swiss Cantonal Veterinary Office approved the project following an ethical review by the State Committee for Animal Experimentation.

Somatic whole-cell *in vitro* current clamp recordings were performed on 300 μm thick parasagittal acute slices from the right hemispheres of male P13 - P15 mouse brains. Brains were quickly dissected and sliced (HR2 vibratome, Sigmann Elektronik, Germany) in ice-cold dissecting artificial cerebrospinal fluid (ACSF) (in mM: NaCl 124.0, KCl 2.50, $MgCl_2$ 10.0, NaH_2PO_4 1.25, $CaCl_2$ 0.50, D-(+)-Glucose 25.00, $NaHC0_3$ 25.00; pH 7.3 $\pm$ 0.1, aerated with 95% O_2 / 5% CO_2), followed by a 15 minute incubation at 34 °C in standard ACSF (in mM: NaCl 124.0, KCl 2.50, $MgCl_2$ 1.00, NaH_2PO_4 1.25, $CaCl_2$ 2.00, D-(+)-Glucose 25.00, $NaHC0_3$ 25.00; pH 7.40, aerated with 95% O_2 / 5% CO_2). To ensure intact axonal and dendritic arborisation, electrophysiological recordings were conducted in slices cut parallel to the apical dendrites. Recordings in Layer 5 of the primary somatosensory cortex were performed at 32 $\pm$ 1 °C in standard ACSF with an Axon Multiclamp 700B Amplifier (Molecular Devices, USA) using 5 - 7 MΩ borosilicate pipettes, containing (in mM): K^+-gluconate 110.00, KCl 10.00, ATP-Mg^{2+} 4.00, Na^{2+}-phosphocreatine 10.00, GTP-Na^+ 0.30, HEPES 10.00, biocytin 5.00 mg/ml; pH 7.30, 300 mOsm. Cells were visualised using infrared differential interference contrast video microscopy (VX55 camera, Till Photonics, Germany and BX51WI microscope, Olympus, Japan).

While pyramidal cells (n = 6, Pyr) were recorded in C57Bl/6J wild-type mice, fast-spiking interneurons (n = 6, FS) were selected from the GFP-expressing cells in Tg(GAD67-GFP)/J heterozygote knock-in mice (Tamamaki et al., 2003). To estimate the contribution of synaptic transmission, half of the FS cells were recorded in the presence of synaptic blockers (20 μM GABAzine, Tocris Bioscience; 25 μM CNQX, BioTrend; 40 μM AP-5, Tocris Bioscience).

Data were acquired at 10 kHz using an ITC-18 digitising board (InstruTECH, USA) controlled by a custom-written software module operating within IGOR Pro (Wavemetrics, USA). Voltage signals were low-pass filtered (Bessel, 10 kHz) and not corrected for the liquid junction potential. Only cells with an access resistance $\leq$ 20 MΩ (17.7 $\pm$ 2.3 MΩ, n = 6, Py; 17.7 $\pm$ 1.4 MΩ, n = 6, FS) and a drift in the resting membrane potential $\leq$ 8 mV (3.4 $\pm$ 2.8 mV, n = 6, Py; 2.5 $\pm$ 2.1 mV, n = 6, FS) throughout the recording were retained for further analysis.

5.4.2 Current injections

In all the experiments included in this study, neurons were stimulated with *in vivo*-like fluctuating currents $I_{\text{ext}}(t)$ generated according to an Ornstein-Uhlenbeck process:

$$\tau_I \dot{I}_{\text{ext}}(t) = -I_{\text{ext}}(t) + \mu_I + \sqrt{2\tau_I}\sigma_I \cdot \psi(t), \tag{5.6}$$

where $\psi(t)$ is a Gaussian white-noise process with zero mean and unitary variance, τ_I is the correlation timescale, μ_I is the mean current and σ_I defines the magnitude of the fluctuations (that is, the standard deviation of the current). The temporal correlation of the input was fixed to $\tau_I = 3$ ms and input currents $I_{\text{ext}}(t)$ were generated at a sampling rate $\Delta t^{-1} = 10$ kHz.

To measure the impact of input fluctuations on the single-neuron input-ouput transfer function (i.e., the f-μ_{I} curve), we somatically injected a set of 5-second currents with different means μ_{I} and standard deviations σ_{I} (see Equation 5.6). To let the cell recover, injections were performed with interstimuli intervals of 25 seconds. Similar protocols have already been applied in previous studies (Rauch et al., 2003; Higgs et al., 2006; Arsiero et al., 2007). Here, to exhaustively explore the parameter space $(\mu_{\mathrm{I}}, \sigma_{\mathrm{I}})$ and to accurately estimate the experimental f-μ_{I} curves, we considered four different standard deviations $\sigma_{\mathrm{I}} \in \{0, 50, 100, 150\}$ pA and ten different means $\mu_{\mathrm{I}} \in [0, \mu_{\max}]$ nA, with $\mu_{\max}$ begin cell-dependent. Each neuron was stimulated with 40 different inputs that were presented randomly. The entire protocol was repeated 3 times. When stimulated with strong inputs, pyramidal neurons undergo spike failures and can not sustain repetitive firing for long periods of time (Fleidervish et al., 1996). At the beginning of each experiment, the maximum current $\mu_{\max}$ was defined in such a way as to reach saturation of the steady state firing rate while preventing spike failures. For that, neurons were tested with 6-second long noiseless currents (i.e. $\sigma_{\mathrm{I}} = 0$) of increasing magnitude μ_{I}. Cells that could not sustain continuous firing for input currents $\mu_{\mathrm{I}} < 0.4$ nA were discarded. The maximal mean input were $\mu_{\max} \in [0.5, 0.7]$ nA. For fast spiking neurons, the maximal mean current were $\mu_{\max} \in [0.4, 0.8]$ nA.

To evaluate model performance in predicting the occurrence of individual spikes, a different set of experiments was performed. Currents were generated according to Equation 5.6, but in this case, the stochastic process used to generate the input was made non-stationary by modulating the standard deviation σ_{I} with a sinusoidal function

$$\sigma_I(t) = \sigma_0 \left(1 + \Delta\sigma \sin\left(\frac{2\pi}{T} \cdot t \right) \right), \tag{5.7}$$

where $T^{-1} = 0.2$ Hz is the modulation frequency. For each cell, input parameters were calibrated to obtain an average firing rate of 10 Hz, oscillating between 7 and 13 Hz, approximatively. After calibration, input parameters were in the following ranges: $\mu_{\mathrm{I}} \in [120, 190]$ pA, $\sigma_0 \in [120, 190]$ pA and $\Delta\sigma = 0.5$ for pyramidal neurons and $\mu_{\mathrm{I}} \in [70, 180]$ pA, $\sigma_0 \in [80, 180]$ pA and $\Delta\sigma = 0.5$ for fast spiking neurons. Since the spiking responses of both real neurons and GIF models are stochastic, performances were quantified on a *test set* obtained by 9 repetitive injections of the same (i.e. *frozen-noise*) 20-s current generated according to Eqs. 5.6-5.7. For parameter extraction, a *training set* was used in which single neurons were stimulated with a single 120-s-long current having the same statistics as in the *test set* but in which a different realization of the white-noise process $\psi(t)$ was used. All the injections were performed with inter-stimuli intervals of 25 seconds.

5.4.3 Data preprocessing

When acquired with the same electrode used to inject the external input $I_{\mathrm{ext}}(t)$, current-clamp recordings $V_{\mathrm{rec}}(t)$ are biased versions of the true membrane potential $V_{\mathrm{data}}(t)$ (Badel et al., 2008). This bias can in principle be removed using series resistance or bridge balance

compensation. However, perfect calibration of these methods is technically difficult to achieve. Moreover, during long experiments, the electrode properties, and in particular the series resistance R_e, are subject to change (Pozzorini et al., 2013). Quantitative comparison between membrane potentials evoked by input currents having different offsets μ_I requires accurate electrode compensation. Indeed, a non-neutralized series resistance $\tilde{R}_e$ would lead, on average, to a mean input-dependent bias $V_{bias}(\mu_I) = \tilde{R}_e \mu_I$. To avoid this and others problems, for all the *in vitro* recordings included in this study, online series resistance compensation was complemented by offline Active Electrode Compensation (AEC) (Brette et al., 2007; Badel et al., 2008). For that, the same procedure applied in Pozzorini et al. (2013) was used.

Briefly, we first computed the optimal linear filter $K_{opt}(s)$ between a weak current and the evoked subthreshold response. This filter captures the responses of both the electrode $K_e(s)$ and the recorded neuron $K_m(s)$. Consequently, the electrode impulse response $K_e(s)$ was estimated as

$$K_e(s) = K_{opt}(s) - K_m(s), \tag{5.8}$$

where, assuming that neurons operate on relatively long timescales, $K_m(s)$ was approximated by an exponential function fitted on the tail of the optimal linear filter. Knowing $K_e(s)$, subsequent current-clamp recordings $V_{rec}(t)$ were compensated to obtain the *true* membrane potential $V_{data}(t)$:

$$V_{data}(t) = V_{rec}(t) - \int_0^\infty K_e(s) I_{ext}(t-s)\, ds, \tag{5.9}$$

where $I_{ext}(t)$ is the injected current and the convolution integral on the right hand side of the equation approximates the voltage drop across the electrode.

In case of long experiments, estimating the electrode properties at different moments in time can improve the quality of the data by removing drifts due to slow changes in the electrode properties (Pozzorini et al., 2013). For this reason, electrode filters were extracted from 10-s-long subthreshold injections performed before the *training set*, before the *test set* and every twenty injections in the protocol used to measure the f-μ_I curves. Subthreshold input currents were generated according to Equation 5.6 with the following parameters: $\mu_I = 0$ nA, $\sigma_I = 75$ pA and $\tau_I = 3$ ms.

5.4.4 Extracting voltage threshold for spike initiation from *in vitro* recordings

Bifurcation analysis of neuron models capturing smooth spike initiation demonstrates that the concept of voltage threshold (that is, the largest membrane potential that a neuron can reach without emitting a spike) does not have a univocal definition. However, different possible definitions produce very similar results that mainly differ by a shift (Platkiewicz and Brette, 2010). For this reason, our analysis is based on relative variations between the voltage threshold in different conditions, rather than on absolute values. In practice, given an

intracellular recording, different methods exist to estimate the voltage threshold (Sekerli et al., 2004). Here, for each spike in the dataset, the voltage threshold was estimated by measuring the membrane potential at which the depolarization rate dV/dt became larger than a certain value (10 mV/ms for Pyr and Fs neurons). In current-clamp experiments performed with a single electrode, the acquired signal is a biased version of the membrane potential (see Data preprocessing). When comparing the voltage threshold observed by injecting currents with different offsets μ_I, one has to be particularly careful. An uncompensated electrode resistance would indeed translate into an artifactual correlation between input strength (i.e, μ_I) and voltage threshold. Moreover, in case of rapidly fluctuating inputs, the recorded spike shape is also biased (Badel et al., 2008). Overall, while the choice of the specific method used to estimate the voltage threshold was not crucial, removing the electrode bias through AEC was key to achieve the accuracy required to detect a significant dependency of the voltage threshold on the input fluctuations σ_I.

In Figure 5.2c, for each input condition, the depolarization rate preceding the emission of an action potential was extracted from the average spike shape (i.e., from the spike-triggered average of the membrane potential) by performing a linear regression on the time interval $[\hat{t} - 3.5\text{ ms}, \hat{t} - 0.5\text{ ms}]$, with $\hat{t}$ denoting the time at which action potentials were initiated. In Figure 5.2e, the average subthreshold membrane potential was computed by discarding all the data points $\{t | t \in [\hat{t}_j - 2\text{ ms}, \hat{t}_j + 10\text{ ms}]\}$ that were too close to action potentials $\{\hat{t}_j\}$.

5.4.5 Inactivating Generalized Integrate-and-Fire model (iGIF)

The Generalized Integrate-and-Fire (GIF) model introduced in refs. Mensi et al. (2011b); Pozzorini et al. (2013) was augmented with a nonlinear coupling between the subthreshold membrane potential $V(t)$ and the firing threshold $V_\text{T}(t)$. Such a coupling has recently been shown to occur in Hodgkin-Huxley models in which fast sodium channels start to inactivate at subthreshold voltages (Platkiewicz and Brette, 2010). For this reason, we call our model iGIF, where i stands for *inactivating*.

In the model, spikes are produced stochastically according to the conditional firing intensity $\lambda(t)$ defined by the exponential escape rate (Gerstner and van Hemmen, 1992; Jolivet et al., 2006):

$$\lambda(t) = \lambda_0 \exp\left(\frac{V(t) - V_T(t)}{\Delta V}\right), \tag{5.10}$$

where λ_0 is a constant with units s^{-1} and ΔV defines the level of stochasticity. In the limit $\Delta V \to 0$, the model becomes deterministic and action potentials are fired each time the threshold is reached. The dynamics of the subthreshold membrane potential is modeled as a leaky integrator augmented with a spike-triggered current $\eta(s)$ that describes the time course of the net current generated by the intrinsic dynamics of the neuron after a spike. Mathematically,

the membrane potential evolves according to the following first-order differential equation:

$$C\dot{V} = -g_L(V - E_L) + \sum_{\hat{t}_j < t} \eta(t - \hat{t}_j - T_{\text{ref}}) + I_{\text{ext}}, \tag{5.11}$$

where C, g_L and E_L describe the passive properties of the membrane, $\{\hat{t}_1, \hat{t}_2, \hat{t}_3, \ldots\}$ are the spike times and I_{ext} is the external input. Currents triggered by different spikes accumulate and, depending on the sign of $\eta(s)$, produce spike-frequency adaptation or facilitation. The functional shape of $\eta(s)$ depends on neuronal type (Mensi et al., 2011b) and is not assumed *a priori* but is extracted from experimental data. After each spike, the membrane potential is reset to V_{reset} and numerical integration only restarts after an absolute refractory period T_{ref}.

Depending on neuronal type, the voltage threshold for spike initiation is not constant but depends on the occurrence of previous action potentials (Badel et al., 2008; Mensi et al., 2011b; Pozzorini et al., 2013) and also on the depolarization rate of the membrane potential preceding a spike (Azouz and Gray, 2000, 2003). To account for both dependancies, the dynamic threshold is modeled as follows:

$$V_T(t) = V_T^* + \sum_{\hat{t}_j < t} \gamma(t - \hat{t}_j - T_{\text{ref}}) + \theta(t), \tag{5.12}$$

where V_T^* is a constant and $\gamma(s)$ is a function of time describing the movement of the firing threshold after the emission of an action potential. Since the latter term can only account for spike-dependent effects, the model is augmented with an additional state variable $\theta(t)$ implementing a coupling between the dynamics of the firing threshold and that of the subthreshold membrane potential. Based on theoretical results obtained by a systematic reduction of the Hodgkin-Huxley model, it has recently been proposed that this coupling might be nonlinear and could take different forms depending on the underlying biophysical mechanism (Platkiewicz and Brette, 2010). In the iGIF model, the dynamics of the variable θ is defined by a rather general first-order differential equation given by

$$\tau_\theta \dot{\theta} = -\theta + \theta_\infty(V), \tag{5.13}$$

where τ_θ set the characteristic timescale on which the threshold reacts to changes in the membrane potential and $\theta_\infty(V)$ defines the voltage dependent steady-state towards which θ converges. Depending on the particular shape of $\theta_\infty(V)$, Equation 5.13 can in principle capture a dependency of the firing threshold on the depolarization rate preceding a spike (Platkiewicz and Brette, 2010, 2011). To avoid *a priori* assumptions on the biophysical processes underlying the coupling, $\theta_\infty(V)$ is defined as an arbitrary function of the membrane potential and is extracted from experimental data using a new non parametric maximum likelihood method (see Fitting Procedure for iGIF).

Finally, it is worth noting that a spike-triggered movement of the firing threshold could in principle be implemented by incrementing the value of θ after the emission of a spike. However, the timescale on which spike-triggered effects occurs might be different from τ_θ. For this

reason, spike-dependent movements of the firing threshold are modeled by the function $\gamma(s)$ and the state variable θ is reset to $\theta_{\text{reset}} = 0$ mV after each spike.

iGIF-Na model

The iGIF-Na model is defined exactly as the iGIF model except for the fact that the function $\theta_\infty(V)$ defining the coupling between membrane potential and firing threshold is assumed *a priori* to be the smooth linear rectifier $\theta_\infty^{\text{Na}}(V)$ defined in Equation 5.2. This particular function has been shown to accurately capture the voltage-dependence of the firing threshold resulting from Na$^+$-channel inactivation in a standard Hodgkin-Huxley model (Platkiewicz and Brette, 2010, 2011).

GIF model

As a control, we also fitted the experimental data using our previous Generalized Integrated-and-Fire (Mensi et al., 2011b; Pozzorini et al., 2013) in which firing threshold only depends on the spike-history. The GIF model is a particular case of the iGIF model obtained by setting $\theta_\infty(V) = 0$.

5.4.6 iGIF model parameter extraction

Given the input current $I_{\text{ext}}(t)$, the intracellular membrane potential $V_{\text{data}}(t)$, its first-order derivative $\dot{V}_{\text{data}}(t) = [V_{\text{data}}(t + \Delta t) - V_{\text{data}}(t)]/\Delta t$ and the experimental spike train $\{\hat{t}_j\}$, iGIF model parameters were obtained with a new two-steps procedure developed by extending the methods introduced in Mensi et al. (2011b); Pozzorini et al. (2013).

In the first step, all the parameters describing the subthreshold dynamics are extracted by minimizing the sum of squared errors between the voltage derivative observed in the experiment and the one predicted by the model (c.f. Eq. 5.11). To allow convex optimization and avoid *a priori* assumptions on the timescales of adaptation, the spike-triggered current was expanded in a linear combination of basis functions $\eta(s) = \sum_{i=1}^{K} \eta_i b_i^\eta(s)$, where $\{b_i^\eta(s)\}$ is a set of $K = 30$ log-spaced non-overlapping rectangular functions and the parameters $\{\eta_i\}$ define the shape of $\eta(s)$. As in Paninski et al. (2005); Mensi et al. (2011b); Pozzorini et al. (2013), the least-square estimate of the subthreshold parameters $\beta_{\text{sub}}^T = C^{-1} \cdot [g_L, E_L g_L, \eta_1, ..., \eta_K, 1]$ is obtained by solving a multilinear regression problem

$$\hat{\beta}_{\text{sub}} = (X^T X)^{-1} X^T \dot{V}_{\text{data}}, \tag{5.14}$$

where X is a matrix made of vectors $X_t^T = [-V_{\text{data}}(t), 1, \sum_j b_1^\eta(t - \hat{t}_j), ..., \sum_j b_K^{(\eta)}(t - \hat{t}_j), I_{\text{ext}}(t)]$ and $\dot{V}_{\text{data}}$ is a vector containing the membrane potential first-order derivative. Since the model does not capture the voltage trajectory during a spike, all the data points close to action potentials $\{t | t \in [\hat{t}_j - 5 \text{ ms}; \hat{t}_j + T_{\text{ref}}]\}$ were excluded from the fit. Finally, the absolute refractory

period was set to $T_{\text{ref}} = 4$ ms and the voltage reset was estimated by computing the average membrane potential after a spike (i.e. $V_{\text{reset}} = \langle V(\hat{t}_j + T_{\text{ref}}) \rangle_j$). Since a period of absolute refractoriness can also be implemented by setting the first milliseconds of the spike-triggered threshold movement $\gamma(t)$ to high values, the particular choice of T_{ref} is not important.

In the second step, an estimate of the subthreshold membrane potential $\hat{V}(t)$ is obtained by numerically solving Equation 5.11 and the voltage threshold parameters are extracted by extending the non-parametric maximum-likelihood approach of Mensi et al. (2011b); Pozzorini et al. (2013). Again, to avoid *a priori* assumptions on the timescales of spike-dependent adaptation and on the shape of the coupling between firing threshold and subthreshold membrane potential, the two functions $\gamma(s)$ and $\theta_\infty(V)$ were expanded in linear combinations of non-overlapping rectangular basis functions $\gamma(s) = \sum_{i=1}^{K} \gamma_i b_i^{(\gamma)}(s)$ and $\theta_\infty(V) = \sum_{i=1}^{M} \theta_i b_i^{(\theta)}(V)$. For the spike-triggered movement of the firing threshold $\gamma(s)$, the same log-spaced rectangular functions already used for $\eta(s)$ were chosen. For $\theta_\infty(V)$, $M = 11$ regularly spaced rectangular functions $\{b_i^{(\theta)}(V)\}$ were chosen in order to cover the interval $[\min_j \{V(\hat{t}_j)\}, \max_j \{V(\hat{t}_j)\}]$ of voltages in which action potentials were observed. Consequently, after integration of Equation 5.13, the time-dependent voltage threshold is given by

$$V_{\text{T}}(t) = V_{\text{T}}^* + \sum_{i=1}^{K} \gamma_i \cdot \sum_{\hat{t}_j < t} b_i^{(\gamma)}(t - \hat{t}_j - T_{\text{ref}}) + \sum_{i=1}^{M} \theta_i f_i(t; \tau_\theta), \tag{5.15}$$

where $f_i(t; \tau_\theta) = \int_{\hat{t}_{\text{last}} + T_{\text{ref}}}^{t} \tau_\theta^{-1} e^{-\frac{s}{\tau_\theta}} \cdot b_i^{(\theta)}(V(t-s)) ds$ and $\hat{t}_{\text{last}}$ denotes the time of the last spike before t. With the exponential function in Equation 5.10, and assuming that the timescale τ_θ is known, the log-likelihood of the experimental spike train is a convex function of the threshold parameters $\beta_{\text{th}}^{\text{T}} = \Delta V^{-1} \cdot [1, V_{\text{T}}^*, \gamma_1, \ldots, \gamma_K, \theta_1, \ldots, \theta_M]$ and can be written as follows (Paninski, 2004)

$$L(\beta_{\text{th}}; \tau_\theta) = \log p(\{\hat{t}_j\} | \hat{V}(t); \beta_{\text{th}}, \tau_\theta) = \sum_{t \in \{\hat{t}_j\}} Y_t(\tau_\theta) \cdot \beta_{\text{th}} - \Delta T \cdot \sum_{t \in \Omega} \exp(Y_t(\tau_\theta) \cdot \beta_{\text{th}}), \tag{5.16}$$

with $Y_t(\tau_\theta) = [\hat{V}(t), -1, -\sum_j b_1^{(\gamma)}(t - \hat{t}_j - T_{\text{ref}}), \ldots, -\sum_j b_K^{(\gamma)}(t - \hat{t}_j - T_{\text{ref}}), -f_1(t; \tau_\theta), \ldots, -f_M(t; \tau_\theta)]$ being a vector of observables (that implicitly depends on the parameter τ_θ) and $\Omega = \{t | t \notin [\hat{t}_j, \hat{t}_j + T_{\text{ref}}]\}$ a set that excludes all the points falling in the period of absolute refractoriness.

Given the timescale of the coupling τ_θ, the maximum likelihood estimate of the other threshold parameters $\hat{\beta}_{\text{th}}(\tau_\theta) = \underset{\beta_{\text{th}}}{\text{argmax}} \{L(\beta_{\text{th}}; \tau_\theta)\}$ can be obtained as in refs. Mensi et al. (2011b); Pozzorini et al. (2013) by maximizing Equation 5.16 using standard gradient ascent methods. The optimal timescale of the coupling between threshold and membrane voltage $\hat{\tau}_\theta = \underset{\tau_\theta}{\text{argmax}} \{L(\hat{\beta}_{\text{th}}(\tau_\theta); \tau_\theta)\}$ is then obtained by systematically searching in the range $\tau_\theta \in [0.5 \text{ ms}, 15 \text{ ms}]$ the value for which the log-likelihood is maximized. Finally, it is worth noting that even if we do not dispose of a proof of joint convexity, the landscape of the log-likelihood $L(\hat{\beta}_{\text{th}}(\tau_\theta); \tau_\theta)$ was smooth in τ_θ and did not contain local maxima (see Figure 5.4F).

Since the fit of the parameters defining the dynamics of the voltage threshold relies on the estimate of the membrane potential $\hat{V}(t)$, an incorrect estimation of β_{sub} could bias the results obtained for $\hat{\beta}_{\text{th}}$ and $\hat{\tau}_\theta$. To make sure that the functional shapes of $\gamma(s)$ and $\theta_\infty(V)$ could really be attributed to the dynamics of the voltage threshold, all the threshold parameters were also extracted using the experimental membrane potential $V_{\text{data}}(t)$ instead of $\hat{V}(t)$.

Fitting procedure for iGIF-Na

The iGIF-Na model parameters were extracted from experimental data using a maximum likelihood approach closely resembling to the nonparametric method described in the previous section. Briefly, the log-likelihood $L(\beta_{\text{th}}^{\text{Na}}; \tau_\theta, k_{\text{i}}, V_{\text{i}})$ of the iGIF-Na model is convex in $\beta_{\text{th}}^{\text{Na}} = \Delta V^{-1} \cdot [1, V_{\text{T}}^*, \gamma_1, \ldots, \gamma_K, k_{\text{a}}]$. Consequently, given the nonlinear parameters k_{i}, V_{i} and τ_θ, all the other threshold parameters can be easily extracted by solving a convex optimization problem: $\hat{\beta}_{\text{th}}^{\text{Na}}(\tau_\theta, k_{\text{i}}, V_{\text{i}}) = \underset{\beta_{\text{th}}^{\text{Na}}}{\text{argmax}}\{L(\beta_{\text{th}}^{\text{Na}}; \tau_\theta, k_{\text{i}}, V_{\text{i}})\}$. On the other hand, extracting the optimal parameters $\hat{k}_{\text{i}}$, $\hat{V}_{\text{i}}$ and $\hat{\tau}_\theta$ requires the solution of the following nonlinear problem:

$$\underset{(\tau_\theta, k_{\text{i}}, V_{\text{i}})}{\text{argmax}}\left\{L(\hat{\beta}_{\text{th}}^{\text{Na}}(\tau_\theta, k_{\text{i}}, V_{\text{i}}); \tau_\theta, k_{\text{i}}, V_{\text{i}})\right\}. \tag{5.17}$$

Performing an exhaustive search on a three-dimensional space is possible. However, model parameters were extracted by first fixing the coupling timescale τ_θ to the optimal value previously obtained by fitting the iGIF-NP model (see Figure 5.4F) and then performing an exhaustive search for k_{i} and V_{i} (see Figure 5.4G).

5.4.7 iGIF model linearization

In order to linearize the iGIF response, Equation 5.13 is simplified by taking the first-order approximation $\theta_\infty(V) \approx \bar{C}_\theta + \bar{G}_\theta$, with $\bar{C}_\theta$ being a constant and $\bar{G}_\theta$ being the average gain of the coupling between membrane potential and firing threshold (see Eq. 5.4). By integrating Equation 5.13, the linearized threshold dynamics of the iGIF model becomes:

$$V_T(t) = \bar{C}_\theta + \bar{G}_\theta \cdot \int_{\hat{t}_{\text{last}}}^t \kappa_\theta(s) V(t-s) ds + \sum_{\hat{t}_j < t} \gamma(t - \hat{t}_j) + \gamma_{\text{ref}}(t - \hat{t}_{\text{last}}), \tag{5.18}$$

where $\hat{t}_{\text{last}}$ denotes the last spike before time t, $\kappa_\theta(t) = \frac{1}{\tau_\theta}\exp\left(-\frac{t}{\tau_\theta}\right)$ is the threshold filter and the function $\gamma_{\text{ref}}(t)$ describes the transient response induced by the after-spike reset. Analogously, the subthreshold dynamics defined in Equation 5.11 can be rewritten in its integral form as:

$$V(t) = E_{\text{L}} + \int_{\hat{t}_{\text{last}}}^t \kappa_{\text{m}}(s) I(t-s) ds - \sum_{\hat{t}_j < t} \tilde{\eta}(t - \hat{t}_j) - \eta_{\text{ref}}(t - \hat{t}_{\text{last}}), \tag{5.19}$$

where $\kappa_{\mathrm{m}}(t) = \frac{R}{\tau_{\mathrm{m}}}\exp\left(-\frac{t}{\tau_{\mathrm{m}}}\right)$ is the membrane filter, $\tilde{\eta}(t) = \int_0^\infty \kappa_{\mathrm{m}}(s)\eta(t-s)\,ds$ describes the influence of the spike-triggered current $\eta(t)$ on the membrane potential and, similar to $\gamma_{\mathrm{ref}}(t)$, the refractory filter $\eta_{\mathrm{ref}}(t) = (E_{\mathrm{L}} - V_{\mathrm{reset}})\exp\left(-\frac{t}{\tau_{\mathrm{m}}}\right)$ accounts for the transient induced by the spike-after reset $V \to V_{\mathrm{reset}}$.

In the iGIF model, the spiking probability depends on the difference between the membrane potential and the firing threshold (Eq. 5.10). Thus, the different terms appearing in Equations 5.18-5.19 can be combined to obtain a compact expression for the linearized iGIF model intensity $\lambda_{\mathrm{lin}}(t)$:

$$\lambda_{\mathrm{lin}}(t) = \lambda_0 \cdot \exp\left(\frac{E_0 + \int_{\hat{t}_{\mathrm{last}}}^{t}\kappa_{\mathrm{eff}}(s)I_{\mathrm{ext}}(t-s)\,ds + \sum_{\hat{t}_j < t}\xi(t-\hat{t}_j)}{\Delta V}\right), \tag{5.20}$$

where the effective filter $\kappa_{\mathrm{eff}}(t) = \kappa_{\mathrm{m}}(t) - \bar{G}_\theta \cdot \int_0^\infty \kappa_\theta(s)\kappa_{\mathrm{m}}(t-s)\,ds$ provides a phenomenological account of somatic integration and $E_0 = \bar{C}_\theta + E_{\mathrm{L}}$ is a constant. Finally, assuming that the timescales τ_θ and τ_{m} are shorter than the average interspike-interval, the transients induced by the after-spike resets can be absorbed in the effective adaptation filter $\xi(t) = \gamma(t) + \gamma_{\mathrm{ref}}(t) + \int_0^\infty (\delta(s) - \bar{G}_\theta\kappa_\theta(s))\left(\tilde{\eta}(t-s) + \eta_{\mathrm{ref}}(t-s)\right)ds$ that phenomenologically accounts for all processes underlying spike-history dependency.

5.4.8 Generalized Linear Model (GLM)

To confirm the semi-analytical results obtained with the linearized iGIF model, experimental data were fit with a Generalized Linear Model (GLM, Truccolo et al. (2005); Pillow et al. (2008)). In the GLM, spikes are generated stochastically with firing intensity $\lambda_{\mathrm{GLM}}(t)$ defined as:

$$\lambda_{\mathrm{GLM}}(t) = \lambda_0 \cdot \exp\left(C_0 + \int_0^\infty \kappa_{\mathrm{eff}}(s)I_{\mathrm{ext}}(t-s)\,ds + \sum_{\hat{t}_j < t}h_{\mathrm{GLM}}(t-\hat{t}_j)\right), \tag{5.21}$$

where λ_0 has units of s^{-1}, C_0 is a constant, $\kappa_{\mathrm{eff}}(t)$ is an arbitrarily-shaped filter through which the input is integrated and $h_{\mathrm{GLM}}(t)$ accounts for all spike-triggered processes that makes the single-neuron activity history-dependent. GLM parameter extraction is performed using the standard maximum likelihood method (Truccolo et al., 2005; Pillow et al., 2008). For that, both $\kappa_{\mathrm{eff}}(t)$ and $h_{\mathrm{GLM}}(t)$ are expanded in linear combinations of rectangular basis functions. In contrast to the iGIF model, the GLM somatic integration as a linear process described by the filter $\kappa_{\mathrm{eff}}(t)$. The GLM only differs from the linearized iGIF model defined in Equation 5.20 for the absence of both an after-spike reset and an absolute refractory period. Thus, GLM parameter extraction can be performed to verify experimentally the iGIF model predictions about somatic integration (see results in Figure 5.6).

5.4.9 Performance evaluation

To avoid problems related to *overfitting* and allow for a comparison between models that differ in the total number of parameters, all of the performance reported in this study were evaluated on separate data sets that were not used for parameters extraction.

Normalized log-likelihood

A quantitative measure of the quality of both the GIF and the iGIF model is provided by the log-likelihood:

$$L_{\mathrm{model}} = \sum_{t \in \{\hat{t}\}} \log \lambda_{\mathrm{model}}(t) - \int_0^T \lambda_{\mathrm{model}}(t) dt \tag{5.22}$$

where $\lambda_{\mathrm{model}}(t)$ is the conditional firing intensity of the model after parameter optimization, $\{\hat{t}\}$ is the experimental spike train and T is the total duration of the experiment on which the model performance were evaluated. All of the log-likelihoods reported in this study were normalized with respect to an homogeneous Poisson process with firing intensity $\bar{r} = N_{\mathrm{spikes}}/T$ as well as on the total number of spikes:

$$L = \frac{1}{\log(2) \cdot N_{\mathrm{spikes}}} \left(L_{\mathrm{model}} - N_{\mathrm{spikes}}(\log \bar{r} - 1) \right), \tag{5.23}$$

such that L has units of bits per spike.

Spike-timing prediction

Spike-timing prediction was quantified using the spike-train similarity measure M_d^* (Naud et al., 2011). As in our previous studies (Mensi et al., 2011b; Pozzorini et al., 2013), M_d^* was computed using the Kistler coincidence window with a temporal granularity of $\Delta = \pm 4$ ms.

Contributions

S.M. and C.P. conceived the study, designed the experiments, analyzed the data and produced the figures.
C.P. wrote the main part of the manuscript with the help of S.M. and W.G.
O.H. performed the experiments.

Conflict of interest

The authors declare no competing financial interests.

A Temporal whitening by power-law adaptation in neocortical neurons

Spike-frequency adaptation is widespread in the central nervous system, but its functional role remains unclear [1]. In neocortical pyramidal neurons, adaptation manifests itself by an increase in neuronal firing threshold and by adaptation currents triggered after each spike. Combining electrophysiological recordings with modeling, we found that in mice these adaptation processes last for more than 20 seconds and decay over multiple time scales according to a power-law. The power-law decay associated with adaptation mirrors and cancels the temporal correlations of input current received *in-vivo* at the soma of L2/3 somatosensory pyramidal neurons. These findings suggest that, in the cortex, spike-frequency adaptation causes temporal decorrelation of output spikes (*temporal whitening*), an energy efficient coding procedure that, at high signal-to-noise ratio, improves the information transfer.

A.1 Introduction

Neural signaling requires a large amount of metabolic energy (Attwell and Laughlin, 2001). Consequently, neurons are thought to communicate using efficient codes in which redundant information is discarded (Laughlin, 2001). Theories of efficient coding (Barlow, 1961) successfully predict several features of sensory systems. At early stages of visual processing, inputs coming from the external world are *decorrelated* both in space and time (Srinivasan et al., 1982; Dong and Atick, 1995; Dan et al., 1996; Pitkow and Meister, 2012); through sensory adaptation (Wark et al., 2007), codes are dynamically modified so as to maximize information transmission (Wainwright, 1999; Brenner et al., 2000; Fairhall et al., 2001; Maravall et al., 2007); and sensory adaptation on multiple timescales (Fairhall et al., 2001; Baccus and Meister, 2002; Ulanovsky et al., 2004) could possibly reflect the statistics of the external world (Simoncelli

---

[1]This text is copied from Pozzorini et al. (2013), full citation in the bibliography

and Olshausen, 2001).

Sensory adaptation is at least partially due to intrinsic properties of individual neurons and, in particular, to spike-frequency adaptation (SFA). SFA is not only observed at the early stages of sensory processing, but is also widespread in cortical neurons embedded in highly recurrent networks. Often modeled by a single process with one specific timescale (Izhikevich, 2003; Brette and Gerstner, 2005), SFA also occurs on multiple timescales(Spain and Schwindt, 1991; Gilboa et al., 2005; La Camera et al., 2006). In pyramidal neurons of the rat somatosensory cortex, three or more processing steps away from the sensory receptors, SFA is scale-free (Lundstrom et al., 2008), meaning that the effective speed at which individual neurons adapt is not fixed but depends on the input. Scale-free adaptation can be captured by simple threshold models with a power-law decaying spike-triggered process (Drew and Abbott, 2006) that possibly describes the combined action of Na-channel inactivation (Fleidervish et al., 1996; Mickus et al., 1999; Melnick et al., 2004) and ionic channels mediating adaptation currents (Madison and Nicoll, 1984; Schwindt et al., 1989; Sanchez-Vives et al., 2000).

Three questions therefore arise: First, can the temporal features of spike-triggered currents and spike-triggered changes in firing threshold, possibly spanning multiple timescales, directly be extracted from experimental data? Second, can SFA be explained by these spike-triggered effects? And finally, do the timescales of SFA match the temporal statistics of the inputs received by individual neurons? If temporal characteristics of inputs and SFA were matched, SFA could lead to a perfect decorrelation of the information contained in one spike with that of the previous one of the same neuron, a phenomenon called *temporal whitening* (Wang et al., 2003). Temporal whitening in turn implies that, at high signal-to-noise ratio, information transmission is enhanced (Rieke et al., 1999).

A.2   Results

The question of whether SFA is optimally designed for efficient coding can only be addressed if both the dynamics of SFA and the statistical properties of the inputs generated in biologically relevant situations are known. Therefore, the *Results* section is organized as follow. We start with a combined theoretical and experimental approach so as to extract the dynamics of spike-triggered processes and SFA directly from *in-vitro* recordings of cortical neurons. Then, we analyze the synaptically driven membrane potential dynamics recorded *in-vivo* from somatosensory neurons during active whisker sensation (data from (Crochet et al., 2011)). Our overall goal is to study whether adaptation optimally removes the temporal correlations in the input to single neurons embedded in the highly recurrent network of the cortex.

A.2.1   SFA is mediated by two power-law spike-triggered processes

To reveal adaptation on multiple timescales, we stimulated L5 somatosensory pyramidal neurons with sinusoidal noisy currents of period T (see Methods) chosen between 500 ms and 16 s (Figure A.1). Single neurons responded with a firing rate $r(t)$ characterized by fast

fluctuations around a sinusoidal mean $r_{\mathrm{mean}}(t)$ given by the first-order approximation

$$r_{\mathrm{mean}}(t) = r_0 + \hat{H}_{\mathrm{A}}(w) \cdot \Delta I_{\mathrm{mean}} \sin(w t + \hat{H}_\Phi(w)), \tag{A.1}$$

where $w = 2\pi/T$ is the angular frequency of the input modulation, $r_0 \approx 4$ Hz is the average firing rate, $\hat{H}_{\mathrm{A}}(w)$ is the amplitude response and $\hat{H}_\Phi(w)$ is the phase response. In the Fourier domain, the transfer function $\hat{H}(w) = \hat{H}_{\mathrm{A}}(w) e^{i\hat{H}_\Phi(w)}$ constitutes a linear model for the modulation of the output firing rate (Figure A.1).

Since SFA is at least partly due to spike-triggered effects, the simple firing rate picture of Equation A.1 must be complemented by a spike-based description. We therefore used intracellular recordings to fit a generalized leaky integrate-and-fire model (GLIF-ξ) with escape-rate noise (Gerstner and Kistler, 2002) for stochastic spike emission (Figure A.1). To capture spike-triggered adaptation, the model features an *effective* dynamic threshold, described by the function $\xi(s)$. This function (also called effective adaptation *filter* or *kernel*) summarizes the stereotypical sequence of biophysical events triggered by the emission of an action potential and accounts for both adaptation currents and *physiological* changes of the firing threshold. Since the effects induced by consecutive spikes accumulate, the effective dynamic threshold produces SFA. Importantly, the functional shape of $\xi(s)$, like all the other parameters of the model, were extracted from the data (see Methods and ref. (Mensi et al., 2011b)).

As previously reported (Mensi et al., 2011b), neocortical pyramidal neurons adapt their firing rates by means of two distinct biophysical mechanisms that respectively increase the firing threshold and lower the membrane potential after each spike. To get an accurate estimation of the effective adaptation filer $\xi(s)$, we first fitted a two-process GLIF model (Supplementary Fig. S1) that explicitly features both a dynamic threshold and an adaptation current, described by the filters $\gamma(s)$ and $\eta(s)$, respectively (Mensi et al., 2011b) (see Methods). Since in the model the emission of action potentials only depends on the difference between the membrane potential and the firing threshold, spike-triggered currents $\eta(s)$ and movements of the firing threshold $\gamma(s)$ were then be combined to obtain the effective adaptation filter $\xi(s)$ of the more parsimonious model GLIF-ξ (see Methods and Figure A.2).

We found that 22 seconds after the emission of an action potential a small but significant deflection remained in both the spike-triggered current $\eta(t)$ and the moving threshold $\gamma(t)$. Moreover, when displayed on log-log scales, the decay of both adaptation kernels was approximately linear over four orders of magnitude, meaning that both the adaptation current and the moving threshold are characterized by scale-free spike-triggered dynamics (Figure A.2a). Fitting $\eta(t)$ and $\gamma(t)$ with a power-law function (i.e. $f_{\mathrm{PL}}(t) = \alpha_{\mathrm{f}} t^{-\beta_{\mathrm{f}}}$), revealed that both spike-triggered processes have similar scaling exponents ($\beta_\eta = 0.76$, $\beta_\gamma = 0.87$). Consequently, the effective adaptation filter $\xi(t)$ is well described by a truncated power-law

$$\xi_{\mathrm{PL}}(t) = \begin{cases} \alpha_\xi \cdot \left(\frac{t}{T_\xi}\right)^{-\beta_\xi} & \text{if } t > T_\xi \\ \alpha_\xi & \text{if } 0 < t \le T_\xi \end{cases} \tag{A.2}$$

Generalized leaky integrate and fire (GLIF-ξ)
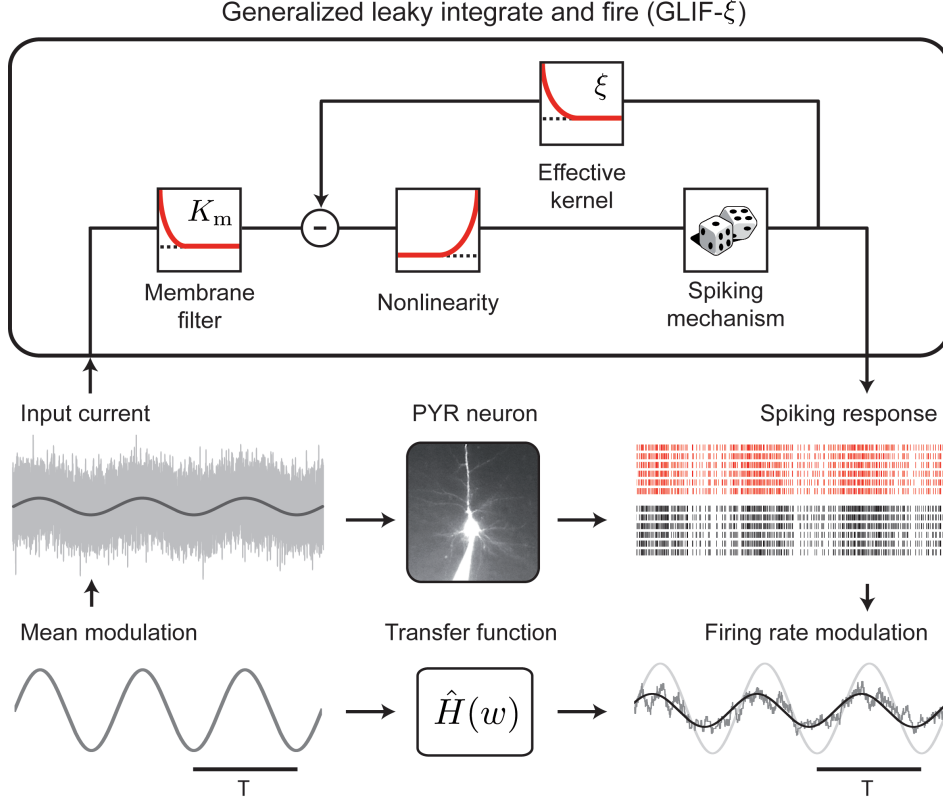
Figure A.1: **Experimental protocol and spiking neuron model GLIF-ξ.** To reveal SFA on multiple timescales, we repeatedly stimulated synaptically isolated L5 pyramidal neurons (*PYR neuron*) with fluctuating currents (*Input current*) generated by adding filtered Gaussian noise to sinusoidal waves with different angular frequencies $w = 2\pi/T$ (*Mean modulation*). The horizontal bars (bottom left and right) indicate the period T of modulation. The single neuron response (*Spiking response*, black) was recorded intracellularly and the firing rate $r(t)$ was estimated by counting the number of spikes in every time bin (*Firing rate modulation*, gray). The periodic oscillations of the firing rate $r_{\mathrm{mean}}(t)$ (*Firing rate modulation*, black) was related to the mean input (*Firing rate modulation*, light gray) with a linear rate model defined in the Fourier domain by the the transfer function $\hat{H}(w)$. We then used the intracellular recordings to fit the Generalized Leaky Integrate & Fire model GLIF-ξ (black-lined box, top). In this model, the input current is first low-pass filtered by the membrane filter $K_m(t)$ and then transformed into a firing intensity by an exponential nonlinearity. Spikes are emitted stochastically (*Spiking response*, red) and trigger an adaptation process described by the effective adaptation kernel $\xi(s)$.

with parameters $\alpha_\xi = 19.2$ mV, $\beta_\xi = 0.93$ and $T_\xi = 8.3$ ms for the average kernel (Figure A.2b) and slightly different values for each individual cell (Supplementary Fig. S2), indicating that scale-free SFA is an intrinsic property of individual neurons and not only of the average over several cells.

In the following, we will refer to a model with a single spike-triggered adaptation filter as GLIF-ξ_L, where GLIF stands for *Generalized Leaky Integrate and Fire* and ξ_L indicates that SFA is implemented by a 22-second *Long* filter obtained by combining the moving threshold

and the spike-triggered current extracted from the experimental data. With the same logic, we denote GLIF-ξ_{PL} a model in which the effective filter $\xi(s)$ is described by the truncated power law ξ_{PL} defined by Equation A.2. A list with all the GLIF-ξ_{PL} model parameters is given in Supplementary Table S1.
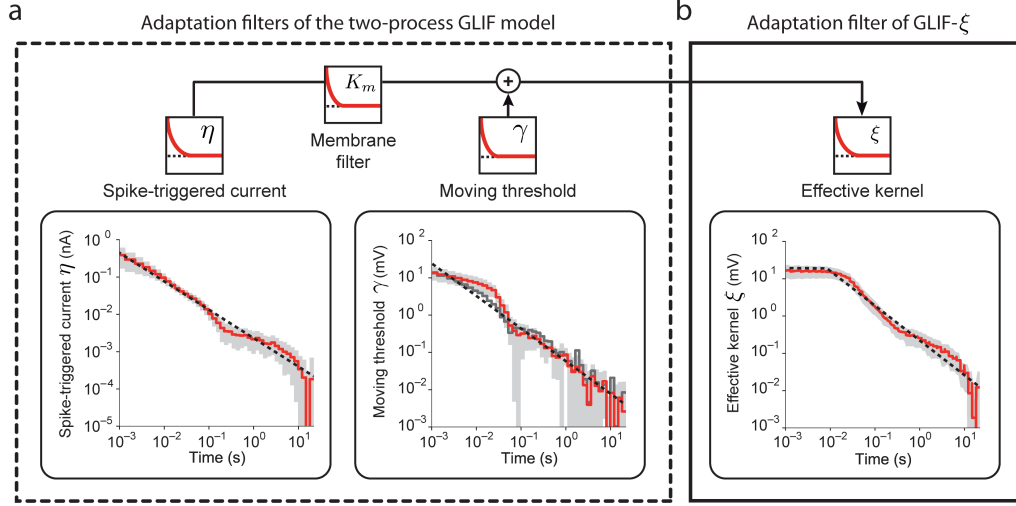

Figure A.2: **Adaptation filter of the GLIF-ξ model extracted from *in-vitro* recordings. a:** Adaptation filters of a two-process GLIF model that accounts for SFA with both a spike-triggered current $\eta(s)$ and a spike-triggered movement of the firing threshold $\gamma(s)$. **Left**: Mean spike-triggered current $\eta(s)$ (red) obtained by averaging the results of different cells ($n = 14$). The dashed black line shows the fit of a power-law function $\eta_{\text{PL}}(s) = \alpha_\eta s^{-\beta_\eta}$ with parameters $\alpha_\eta = 0.44$ nA, $\beta_\eta = 0.76$ and s in milliseconds. **Right**: Mean moving threshold $\gamma(s)$ (red) obtained by averaging the results of different cells ($n = 14$). The dashed black line shows the fit of a power-law function $\gamma_{\text{PL}}(s) = \alpha_\gamma s^{-\beta_\gamma}$ with parameters $\alpha_\gamma = 24.4$ mV, $\beta_\gamma = 0.87$ and s in milliseconds. The dark gray line is a control showing an independent estimation of the average moving threshold $\gamma(t)$ obtained with an alternative fitting procedure (see Methods). **b:** The spike-triggered current $\eta(s)$ and the moving threshold $\xi(s)$ were combined (block diagram) to obtain the effective adaptation filter $\xi(s)$ of the GLIF-ξ model. The mean adaptation filter $\xi_{\text{L}}(s)$ (red, GLIF-ξ_{L}) obtained by averaging the effective spike-triggered adaptation measured in individual cells ($n = 14$, see Supplementary Fig. S2) is shown in red. The optimal fit of a truncated power-law $\xi_{\text{PL}}(s)$ (dashed black, GLIF-ξ_{PL}) yields an exponent $\beta_\xi = 0.93$ (c.f. Eq. A.2). In all panels, the gray area indicates one standard deviation for the distribution of filters across different cells (asymmetric errors are due to log-scales).

A.2.2 Power-law SFA explains neural activity on short timescales

Valid single neuron models should predict the occurrence of individual spikes with a millisecond precision (Jolivet et al., 2008). In response to a single injection of a fluctuating current (Figure A.3a) the neuron emitted spikes that the GLIF-ξ_{L} model was able to predict with a high degree of accuracy (Figure A.3b, red). When the same current was injected repetitively, the spiking responses revealed the stochastic nature of single neurons: certain action potentials were emitted reliably with a high temporal precision, while others did not occur at each repetition or were characterized by larger temporal jitters. The GLIF-ξ_{L} model also captured

this aspect (Figure A.3c). To validate our model, we quantified its predictive power using a similarity measure denoted M_d^* (see Methods and ref. (Naud et al., 2011)). On average, GLIF-ξ_L was able to predict more than 80% of the spikes ($M_d^* = 0.807$, s.d. = 0.04) with a precision of ± 4 ms (Supplementary Fig. S3). Very similar performances, statistically not different (n=12 cells, paired t-test, $t_{11} = 0.30$, p=0.77), were achieved by GLIF-ξ_{PL} ($M_d^* = 0.804$, s.d. = 0.05), indicating that spike-triggered processes are well described by a truncated power-law (Supplementary Fig. S4).

As expected, the subthreshold response observed *in-vitro* was systematically overestimated by GLIF-ξ_L (Figure A.3b, red). This is explained by the fact that GLIF-ξ_L artificially translates spike-triggered currents into effective threshold movements. In a two-process GLIF model, where adaptation currents and threshold movements are described as two distinct features (i.e. when $\eta(t)$ and $\gamma(t)$ are not combined in a single effective kernel), model prediction of the membrane voltage and experimental data were indeed in good agreement (Figure A.3b, gray), confirming the validity of our fitting procedure. In terms of mere spike-timing prediction, the two-process GLIF model and the more parsimonious GLIF-ξ model are equivalent (Figure A.3c). For this reason, we work in the following with single-process model GLIF-ξ.

Overall, the spike time prediction paradigm demonstrates the ability of both GLIF-ξ_L and GLIF-ξ_{PL} to capture the spiking activity of single neurons on the timescale of milliseconds.

A.2.3 Power-law SFA explains neural activity on slow timescales

We wondered whether the 22-second long adaptation filter $\xi(s)$ could also predict the firing rate modulation on the much slower timescale of seconds. To this end, we used the GLIF-ξ_L model fitted on responses to different frequencies of modulation ($0.5 \leq T \leq 16$ s) to predict the firing rates recorded in the second part of the experiment, where one of the two slowest modulations ($T = 8$ or 16 s) was chosen and repetitively presented to the cell. Comparison of the raster plots obtained by injecting the same current in both the neuron and the GLIF-ξ_L model shows that the spiking activity of the real neuron closely resembles the one predicted by the model (Figure A.4a-c). Furthermore, the match between the running-mean PSTHs constructed for the model and the experimental data revealed that both responses share a similar phase advance (Figure A.4d), indicating that our GLIF-ξ_L model is sufficient to capture the characteristic signature of SFA under slow sinusoidal stimulation (Lundstrom et al., 2008). To study the role of the 22-second long adaptation filter of GLIF-ξ_L, we then fitted the same single-process model under the assumption that the adaptation filter $\xi(t)$ has a duration of only 1 second (GLIF-ξ_S, where S stands for *short* adaptation filter). Compared to GLIF-ξ_L, the firing rate predicted by GLIF-ξ_S (Figure A.4e, orange) was in phase with the input (Figure A.4e, dark gray) and not with the spike output of the cells, indicating that GLIF-ξ_S was unable to capture the slow components of SFA (i.e. the model with a short adaptation filter predicted a wrong phase advance). To provide even stronger evidence, we systematically quantified the ability to predict both the mean firing rate r_0 (Figure A.4f) and the phase lead $\hat{H}_\Phi$ (Figure A.4g). Whereas the GLIF-ξ_L model was capable of very good predictions which are in statistical agreement with the experimental data (errors $\Delta r_0 = -0.01$ Hz, s.d. = 0.67; n=12 cells,
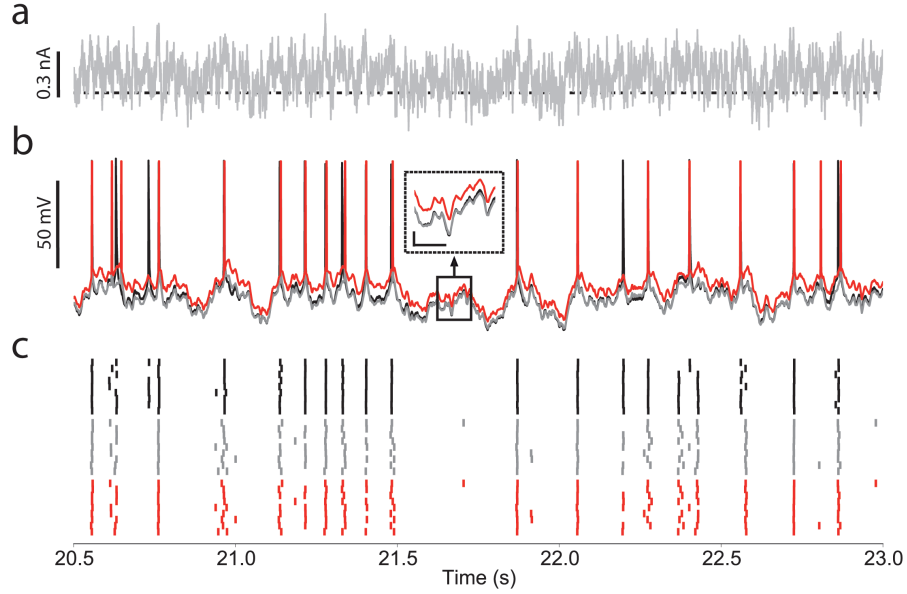
Figure A.3: **The GLIF-ξ model predicts the occurrence of single spikes with a millisecond precision.**
a: Typical 2.5-second segment of injected current. The same fluctuating current is presented several times (*frozen-noise*). The dashed black line represents 0 nA. **b:** The spiking response, but not the subthreshold membrane potential, predicted by the GLIF-ξ_L model (red) is in close agreement with the experimental data (black). In the two-process GLIF model (gray), where spike-triggered currents and threshold movements are modeled by two distinct processes (i.e. $\gamma(s)$ and $\eta(s)$), the dynamics of the subthreshold membrane potential predicted by the model is in excellent agreement with the experimental data. Inset: comparison of subthreshold membrane potential (scale bars: 40 ms, 5 mV). **c:** The raster plots show the spiking response of both the neuron (black) and the GLIF-ξ_L model (red) to repetitive presentation of the same current. By construction, the spiking response of the GLIF-ξ_L model is identical to that of the two-process GLIF model (gray).

Student t-test, $t_{11} = -0.04$, $p = 0.97$ and $\Delta\hat{H}_\Phi = -0.17$ deg, s.d. = 5.7; n=12 cells, Student t-test, $t_{11} = -0.10$, $p = 0.92$), GLIF-ξ_S had the tendency to both overestimate the average firing rate and underestimate the phase advance (errors $\Delta r_0 = 0.47$ Hz, s.d. = 0.72; n=12 cells, Student t-test, $t_{11} = 2.16$, $p = 0.05$ and $\Delta\hat{H}_\Phi = -17.9$ deg, s.d. = 6.5 deg; n=12 cells, Student t-test, $t_{11} = -9.16$, $p < 10^{-6}$), demonstrating that an adaptation filter of 1 second is not sufficient. Finally, we measured the transfer function $\hat{H}(w)$ for both real neurons and spiking models by fitting Equation A.1 on the firing rates observed in response to six frequencies of modulation (Figure A.4h-j). For both real neurons and GLIF-ξ_L, the amplitude response $\hat{H}_A(w)$ was stronger at higher frequencies compared to lower ones revealing high-pass filtering, a characteristic feature of SFA (Figure A.4h). Consistent with observations in L2/3 pyramidal neurons (Lundstrom et al., 2008), plotting on log-log scales the amplitude response $\hat{H}_A$ as a function of the input frequency $f = T^{-1}$, revealed that the gain of L5 pyramidal neurons was approximatively power-law (Figure A.4i). Moreover, the phase response $\hat{H}_\Phi(w)$ was always positive meaning that, for all the frequencies tested in this study, the output firing rate led the input modulation (Figure A.4j). Overall, GLIF-ξ_L was able to capture the features of the trans-

fer function observed in L5 pyramidal neurons. Similar results were obtained with GLIF-ξ_{PL} (Supplementary Fig. S4), confirming that the spike-triggered processes observed *in-vitro* were correctly modeled by a truncated power-law lasting 22 seconds. The experimental results reported in Figure 4h-j are very similar to those obtained in L2/3 pyramidal neurons (Lundstrom et al., 2008) and provide an independent evidence for multiple timescales of adaptation. Overall, these results show that accounting for long-lasting spike-triggered effects with an appropriate adaptation filter is crucial to capture the response of L5 pyramidal neurons on multiple timescales.
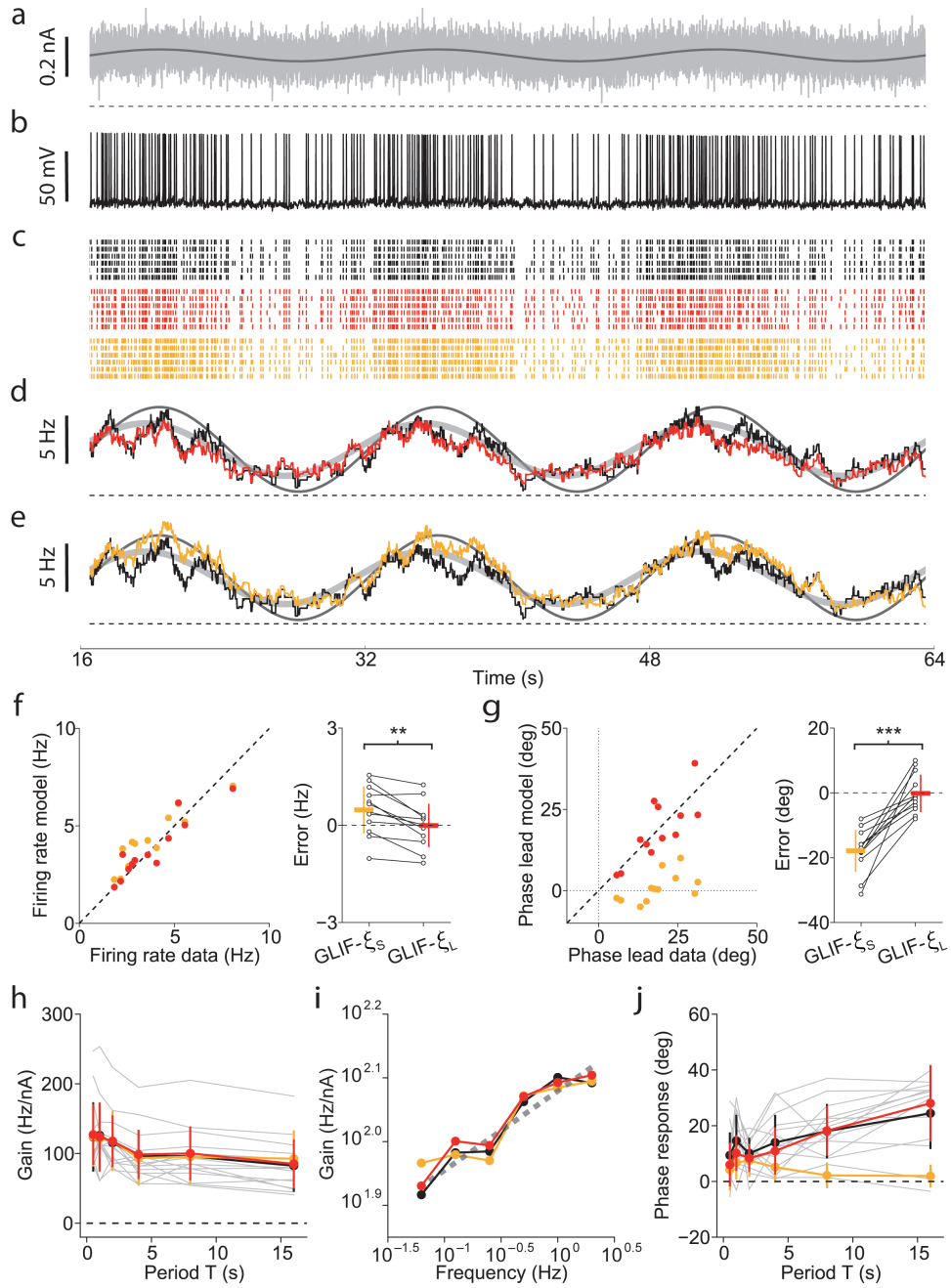
Figure A.4: **The GLIF-ξ model accurately predicts the firing rate response on multiple timescales.**
a: Input current (gray) with slow mean modulation (dark gray). **b:** Membrane potential recorded in a
single trial. **c:** Firing activity (black) obtained by repetitive presentation of the same input current is
compared with predictions of GLIF-ξ_L (red) and GLIF-ξ_S (orange). **d:** Data from *c* were used to build
two PSTHs (black: data, red: GLIF-ξ_L). The two sinusoidal functions represent the input modulation
(dark gray) and the best fit of the experimental data (light gray). **e:** Same as in panel *d* but with the
prediction of GLIF-ξ_S (orange). **f:** Performance in predicting the average firing rate r_0 of new stimuli.
Left: Model predictions are plotted against experimental data. Each dot represents a different cell.

Right: Each couple of open circles shows the prediction errors on the same cell. GLIF-ξ_L (red) is slightly more accurate than GLIF-ξ_S (orange) ($n = 12$, paired t-test, $t_{11} = -4.09$, $p = 0.002$). **g:** Performance in predicting the phase response $\hat{H}_\Phi$ to inputs at $T = 8$ or 16 s. GLIF-ξ_L (red) outperforms GLIF-ξ_S (orange) ($n = 12$ cells, paired t-test, $t_{11} = 6.31$, $p = 6.0 \cdot 10^{-5}$). Conventions as in panel f. **h:** Gain $\hat{H}_A(T)$ as a function of the period $T = 2\pi/w$. **i:** Log-log plot of the gain $\hat{H}_A(f)$ as a function of the input frequency $f = T^{-1}$. Experimental data were fitted by a power-law with scaling exponent $\beta_H = 0.12$ (dashed gray). **j:** Phase response $\hat{H}_\Phi(T)$ as a function of the period $T = 2\pi/w$. In panels h-j, data from individual cells ($n = 14$, gray lines) are averaged (black) and compared with the predictions of GLIF-ξ_L (red) and GLIF-ξ_S (orange). In all panels, error bars indicate one standard deviation and horizontal dashed lines indicate zero.

A.2.4 Power-law SFA is optimally tuned for *temporal whitening*

Our model describes how the net current resulting from dendritic integration is encoded into a spike train at the soma of neocortical pyramidal neurons. To investigate the implications of power-law adaptation, we considered a situation in which a population of N uncoupled GLIF-ξ_{PL} neurons had to encode a common input $I(t) = I_0 + \Delta I(t)$ in the instantaneous firing rate $A(t)$, also called population activity. Note that, since the neurons in our population were all identical and received the same input, the population activity $A(t)$ is identical to the PSTH measured by repetitively injecting the same current into one single cell. For relatively small fluctuations around a mean activity A_0, we can assume that the population operates in a linear regime and responds to an external input fluctuation $\Delta I(t)$ according to the first-order approximation

$$A(t) = A_0 + \int_0^t \Delta I(t-s)H(s)ds + n(t), \tag{A.3}$$

where the impulse response $H(s)$ is the inverse Fourier transform of $\hat{H}(w)$, the noise $n(t)$ is due to stochastic firing in a finite population and both terms depend on the intrinsic properties of the individual neurons and in particular on the precise shape of the adaptation filter $\xi(t)$.

For large populations, the noise term in Equation A.3 becomes negligible and optimal coding is achieved by the removal of temporal correlations potentially present in the input (Atick, 1992; Rieke et al., 1999). This encoding strategy is known as *temporal whitening* and requires the population activity to have a flat power spectrum $A(f) = $ Const. (see Supplementary Text S2).

SFA is known to implement high-pass filtering of the input current (Benda and Herz, 2003; Kondgen et al., 2008). In the particular case of power-law adaptation, the population response is characterized by a power-law gain (Figure A.4h,i and ref. (Lundstrom et al., 2008)) suggesting that, in neocortical pyramidal neurons, spike-triggered processes might be optimally tuned to efficiently encode scale-free signals (i.e. signals that are temporally correlated across multiple timescales). However, the issue of whether the functional role of power-law adaptation is to implement *temporal whitening* can only be solved if the statistical properties of the input received *in-vivo* by neocortical pyramidal neurons are known.

To this end, we analyzed the synaptically driven membrane potential dynamics recorded from

somatosensory pyramidal neurons during active whisker sensation (see Methods). A spectral analysis performed on the data of Crochet et al. 2011 (Crochet et al., 2011) revealed that, at low frequencies, the power spectrum of the subthreshold membrane potential fluctuations was characterized by a power-law decay (Figure A.5a, red), indicating that *natural stimuli* received by somatosensory pyramidal neurons are indeed scale-free.

To provide further evidence, we simulated the activity of a population of GLIF-ξ_{PL} neurons in response to an *in-vivo* like input characterized by a scale-free spectrum (Figure A.5a, black). The statistics of the subthreshold responses obtained in individual GLIF-ξ_{PL} neurons were consistent with the ones observed *in-vivo* (Figure A.5b, gray). Moreover, we found that the power spectrum of the population activity $A(f)$ (Figure A.5b, blue) was much closer to a horizontal line than that of the input, indicating that a population of GLIF-ξ_{PL} neurons efficiently encodes *in-vivo* like signals by removing temporal correlations present in the input. Similar results were obtained with a population of GLIF-ξ_{L} neurons, where the adaptation filter $\xi(t)$ was not an idealized power-law, but the average kernel extracted from intracellular recordings (Figure 5b, gray).

Overall, our results suggest that in neocortical pyramidal neurons, power-law spike-triggered adaptation mirrors and approximately cancels the temporal correlations of signals generated in a biologically relevant situation. This result provides evidence for efficient coding at the level of single neurons embedded in the highly recurrent network of the cortex.

A.3 Discussion

Neocortical pyramidal neurons are known to adapt their firing rate on multiple timescales (La Camera et al., 2006; Lundstrom et al., 2008). Here we found that SFA is due to two separable spike-triggered mechanisms: each time an action potential is fired, both an adaptation current and a movement of the firing threshold are induced. Our results show that these spike-triggered effects are surprisingly long (more than 20 s) and decay with a power-law (Figure A.2), highlighting the fact that SFA does not have a specific timescale. A GLIF model with an effective power-law spike-triggered process simultaneously captured both the fast dynamics critical for the prediction of individual spikes (Figure A.3) and the slow processes that modulate the firing rate (Figure A.4 and Supplementary Fig. S4). Most importantly, we found that, in behaving mice, the currents resulting form dendritic integration and received as input at the soma of pyramidal neurons are characterized by long-range temporal correlations that are partially removed by power-law spike-triggered adaptation (Figure A.5). This final observation indicates that, in cortex, power-law SFA is near-optimally tuned to efficient coding.

A.3.1 Extent of spike-triggered effects

According to our results, 20 seconds after its emission, an individual spike can still affect the firing activity of a neuron. Possibly, spike-triggered effects have an even longer duration. However after 22 seconds the magnitudes of both the moving threshold and the spike-triggered
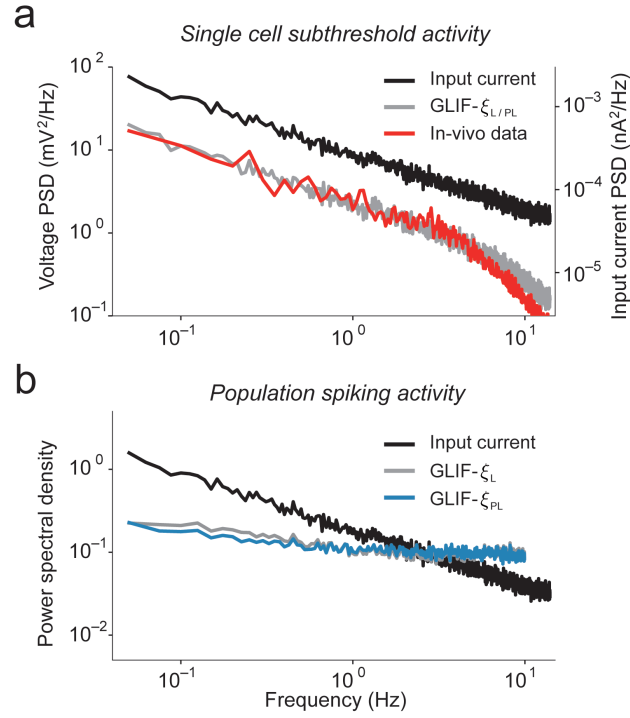
Appendix A. Temporal whitening by power-law adaptation in neocortical neurons

Figure A.5: **Power-law adaptation is near-optimally tuned to perform *temporal whitening*. a:** Power spectral density of the intracellular membrane potential fluctuations recorded *in-vivo* from L2/3 pyramidal neurons (Voltage PSD, red). The power spectrum was computed using 20-second long recordings ($n = 57$) obtained from 7 different cells (data from (Crochet et al., 2011)). Fitting a power law (not shown) on the frequency band $0.05 < f < 2$ Hz yields a scaling exponent $\beta_I = 0.67$. The power spectrum of the scale-free input used to stimulate a population of GLIF-ξ_{PL} neurons ($N = 100$) is shown in black (Input Current PSD). The power spectrum of the subthreshold response of individual GLIF-ξ_{PL} neurons (Voltage PSD, gray) is in good agreement with the *in-vivo* recordings. **b:** The population activity of a group of GLIF-ξ_{PL} neurons in response to an *in-vivo* like input (black, copied from panel *a*) has a nearly flat spectrum $A(f)$ (blue). Similar results were obtained with GLIF-ξ_L neurons (gray). To allow a direct comparison between input and output powers, all the spectra shown in panel *b* were normalized to have the same total power.

current were too small to be measured by our method (for $t > 20$ s, $\eta(t) < 0.1$ pA and $\gamma(t) < 0.01$ mV, see Figure A.2a). Since the effects of consecutive spikes accumulate, these small contributions shaped the single neuron response in a significant way (Figure A.4).

Whereas power-law adaptation was necessary to capture the firing rate fluctuations, a model with spike-triggered processes that only last for 1 second (GLIF-ξ_S) achieved very high performances ($M_d^* = 0.80$, s.d. $= 0.03$) in predicting the occurrence of individual spikes (Supplementary Fig. S3). This fact probably explains why power-law adaptation has not been observed in previous studies where model validation was only based on spike time prediction.

A.3.2 Biophysical implementation of power-law adaptation

Our fitting procedure enabled us to discriminate between adaptation processes implemented by spike-triggered currents and physiological changes of the firing threshold. However, the biophysical details concerning the implementation of power-law dynamics are not part of our model. In principle, power-law relaxations can be approximated by a sums of exponentials covering a wide range of timescales (La Camera et al., 2006; Drew and Abbott, 2006). It is therefore likely that the spike-triggered current $\eta(s)$ we found results from the combined action of multiple ion-channels operating on different timescales like for example Ca-dependent, Na-depedent and high-voltage activated potassium channels. Note, however, that a match of the relative strength of different currents implies a fine-tuned regulation of gene expression levels. In line with this hypothesis, multiple timescales of SFA have been previously modeled by biophysical models with several channels mediating adaptation currents (La Camera et al., 2006; Wang et al., 2003; Lundstrom et al., 2008). Alternatively, scale-free dynamics could also be an intrinsic property of single channels. In particular, the power-law decay we found in the moving threshold $\gamma(s)$ might reflect the scale-free dynamics observed during Na-channel de-inactivation (Toib et al., 1998). In this alternative view, scale-free dynamics is likely to emerge from the presence of multiple inactivated states of ionic-channels (Lowen et al., 1999; Gilboa et al., 2005).

A.3.3 How general is power-law adaptation?

All the *in-vitro* results presented in this paper are from mouse layer 5. We also investigated SFA in L2/3 and obtained very similar results (data not shown). In particular, we found that L2/3 pyramidal neurons adapt by means of power-law filters that closely resemble the ones observed in L5 and cause positive phase lead of the firing rate response to slow sinusoidal currents. These preliminary results suggest that L2/3 and L5 somatosensory pyramidal neurons share similar adaptation mechanisms. We also fitted GLIF models to the data of ref. (Lundstrom et al., 2008) and found that both L2/3 and L5 pyramidal neurons of the rat somatosensory cortex adapt by means of spike-triggered power-law processes (data not shown) indicating that this mechanism is conserved across species and could be a common feature of cortical pyramidal neurons.

A.3.4 Functional implications

Both the moving threshold and the spike-triggered current are characterized by power-law decays with very similar scaling exponents. This suggests that the particular shape of the adaptation filters plays an important role. Neural signaling consumes a large amount of metabolic energy (Attwell and Laughlin, 2001; Laughlin, 2001). The brain should therefore represent information using codes in which redundant information is discarded. According to efficient coding theory, optimality is achieved by adapting to the stimulus statistics and, at high signal-to-noise ratio (SNR), by completely removing correlations that are potentially

present in the signals to be encoded (Barlow, 1961). Efficient coding theory has been used to explain neural processing at early stages of the visual system. In the retina, center-surround receptive fields coupled with nonlinear processing strongly attenuate spatial correlations of natural images (Srinivasan et al., 1982; Pitkow and Meister, 2012). Similarly, in primary visual cortex (V1), spatial decorrelation of features has been found (Simoncelli and Olshausen, 2001). In the temporal domain, neural firing was found to be decorrelated in the lateral geniculate nucleus of the cat (Dan et al., 1996) and pyramidal neurons of V1 adapt on multiple timescales, providing further temporal decorrelation (Wang et al., 2003). However, it remained unclear whether SFA serves for temporal redundancy reduction in the cortex.

To solve this issue, we estimated the statistics of input currents received *in-vivo* at the soma of L2/3 somatosensory pyramidal neurons during active whisker sensation (data from (Crochet et al., 2011)). This current, which reflects spatio-temporal statistics of spike arrivals at the synapses as well as subsequent filtering in the dendritic tree, can be seen as the driving current for spike generation. We found that input currents of pyramidal neurons did not have a preferred timescale but were characterized by scale-free dynamics. Moreover, our numerical simulations indicated that power-law spike-triggered processes are near-optimally tuned to completely remove the temporal correlations revealed by the power-law decay of the input spectrum (Figure A.5). Overall, these results provide evidence for efficient coding in single neocortical neurons stimulated with behaviorally relevant signals.

The GLIF-ξ model implements a form of predictive coding. Indeed, the sum of adaptation processes $\xi(s)$ triggered by past spikes can be interpreted as a linear predictor of the future input. Consistent with predictive coding, further spiking only occurs when the real input exceeds the prediction. In line with our results, it has been shown that predictive coding of scale-free inputs by means of power-law spike-triggered kernels reduces the number of action potentials required to achieve a certain signal-to-noise ratio (Bohte and Rombouts, 2010).

A.3.5 *Temporal Whitening* vs. *Noise-Shaping*

For deterministic signals encoded in absence of noise, efficient coding theory states that redundancy reduction is the optimal solution. However, in presence of noise, complete decorrelation can be detrimental. Redundancy can indeed improve the robustness of a code (Rieke et al., 1999). To assess optimal coding in small populations of neurons, the noise term $n(t)$ associated with stochastic firing (c.f. Eq. A.3) has therefore to be considered.

Previous studies have shown that non-renewal firing activity with negatively correlated inter-spike intervals can achieve higher information rates by *noise-shaping* (Mar et al., 1999; Shin, 2001; Chacron et al., 2004). In this coding strategy, the SNR is increased in the frequency band of the input signal by transferring the effective noise power to other frequencies (see Supplementary Text S2). As already hypothesized in (Avila-Akerberg and Chacron, 2011), we found that at low-frequencies, spike-triggered adaptation resulted in a reduction of noise which was completely counterbalanced by a similar modification of the gain that controls the amplitude of the signal, so that the SNR remained unchanged. Consequently, modifying the adaptation filter $\xi(s)$ did not affect the power spectrum of the effective noise (Supplementary Fig. S5),

indicating that *noise-shaping* is probably not the functional role of power-law adaptation. The question of how this result generalizes to different stimulation paradigms is out of the scope of this study and will be addressed in a future paper.

In computational studies of memory and learning in neural networks, SFA is often neglected and, when considered, it is usually assumed to operate on short timescales. From our perspective, the power-law of spike-triggered adaptation could be helpful in bridging the gap between the millisecond timescale of spike timing and behavioral timescales. Moreover, our results suggest that power-law adaptation causes temporal decorrelation of output spikes, a procedure that, at high signal-to-noise ratio, improves information transfer.

A.4   Acknowledgments

A.5   Author contributions

C.P. and R.N. conceived the study. C.P. designed the experiments, analyzed the data, performed the modeling and wrote the initial draft. S.M. contributed to data analysis and modeling. W.G. supervised the project. All the authors worked on the manuscript.

A.6   Online Methods

A.6.1   *In-vitro* electrophysiological recordings

All animal experiments were performed using published procedures (Lefort et al., 2009; Avermann et al., 2012) in accordance with the rules of the Swiss Federal Veterinary Office. Briefly, somatosensory brain slices were obtained from P14-18 Wild Type mice (C57BL6/J) and whole-cell patch-clamp recordings were performed at 35 C from L5 pyramidal neurons. The pipette solution was comprised of (in mM): 135 K-gluconate, 4 KCl, 4 Mg-ATP, 10 Na2-phosphocreatine, 0.3 Na3-GTP and 10 HEPES (pH 7.3, 290 mOsm). During the experiments, we blocked all excitatory synaptic transmission by adding CNQX (20 μM) and D-AP5 (50 μM) to the bath solution. All electrophysiological data were low-pass Bessel filtered at 10 kHz and digitized at 20 kHz. Measurements were not corrected for the liquid junction potential. Recordings characterized by instabilities in the action potential shape and/or large drifts in the baseline firing rate r_0 were excluded from the dataset upon visual inspection.

A.6.2   Current Injections

To characterize single neurons with the standard tools of linear system analysis, we performed 64-s long experiments in which noisy currents modulated by sinusoidal means were delivered in current-clamp mode. The injected current, denoted I_{ext}, was generated according to the following equation

$$I_{\text{ext}}(t) = I_0 + \Delta I_{\text{mean}} \cdot \sin\left(\frac{2\pi}{T}t\right) + \Delta I_{\text{noise}} \cdot \mathcal{N}(t) \tag{A.4}$$

were I_0 is a constant offset, ΔI_{mean} controls the amplitude of the sinusoidal mean and ΔI_{noise} defines the standard deviation of the noise. The noise $\mathcal{N}(t)$ was generated with an Ornstein-Uhlenbeck process with zero mean, unitary variance and a temporal correlation of 3 ms.

Each experiment consisted of many injections of currents generated according to Equation A.4. In the first half of the experiment (*training set*), we performed six injections using different periods of modulation $T \in \{0.5, 1, 2, 4, 8, 16\}$ in seconds. Stimuli were delivered in random order and, for each of the six injections, a new realization of the noise $\mathcal{N}(t)$ was used. In the second part of the experiment (*test set*), one of the two slowest modulations ($T = 8$ or 16 s) was chosen and more injections were performed. To assess the reliability of single neurons, the same realization of noise $\mathcal{N}(t)$ was used (*frozen-noise*). All the injections were performed with interstimulus intervals of 1 minute.

Before and after each injection, we stimulated the neuron with two additional inputs. The first was a 2.5-s long current composed of a hyperpolarizing step followed, after 500 ms, by a suprathreshold step. We used the response to this stimulus to identify the neuronal type (L5 burst-generating cells were not included in the dataset). The second was a 4-s long subthreshold noisy current generated with an Ornstein-Uhlenbeck process with zero mean and temporal correlation of 3 ms. We used this second injection to characterize the electrode response and perform Active Electrode Compensation (see Data Preprocessing and Supplementary Text S1).

At the beginning of each experiment, we tuned the input parameters I_0, ΔI_{mean} and ΔI_{noise} to obtain a firing rate r_{mean} oscillating periodically between 2 and 6 Hz. Typical values obtained after calibration were comprised in the range 100-450 pA for I_0, 15-30 pA for ΔI_{mean} and 50-150 pA for ΔI_{noise}.

A.6.3   Linear analysis

For each neuron, we estimated the transfer function $\hat{H}(w)$ (Figure A.4h-j) using standard methods already used in previous studies (Lundstrom et al., 2008; Kondgen et al., 2008). Briefly, the experimental spike train $\{\hat{t}_j\}$ was built by selecting the times at which the membrane potential $V(t)$ crossed 0 mV from below. We then obtained the firing rate $r(t)$ by building a histogram of the spike times. The bin size was chosen such that each period of modulation T was divided in 30 bins. For each input frequency $w = 2\pi/T$, we finally obtained the transfer function by minimizing the sum of squared errors (SSE) between the sinusoidal function

$r_{\text{linear}}(t) = C_0 + C_1 \cdot \sin\left(wt + \phi\right)$ and the experimental firing rate $r(t)$, with $\{C_0, C_1, \phi\}$ being the only free-parameters. The transfer functions of GLIF-ξ models (Figure A.4h-j) were obtained with the same method.

A.6.4 Generalized Leaky Integrate-and-Fire model (GLIF-ξ)

The spiking neuron models discussed in this study are generalized leaky integrate-and-fire models equipped with a spike-triggered mechanism for SFA and with escape rate noise for stochastic spike emission (Figure A.1). Spikes are produced according to a point process with conditional firing intensity $\lambda(t)$ which exponentially depends on the momentary distance between the membrane potential $V(t)$ and the *effective* firing threshold $V_T(t)$ (Jolivet et al., 2006):

$$\lambda(t) = \lambda_0 \exp\left(\frac{V(t) - V_T(t)}{\Delta V}\right) \tag{A.5}$$

where λ_0 has units of s^{-1} so that $\lambda(t)$ is in Hz and ΔV defines the sharpness of the threshold. Consequently, the probability of a spike to occur at a time $\hat{t} \in [t; t + \Delta t]$ is

$$P(\hat{t} \in [t; t + \Delta t]) = 1 - \exp\left(-\int_t^{t+\Delta t} \lambda(s)\,ds\right) \approx \lambda(t)\Delta t. \tag{A.6}$$

In the limit of $\Delta V \to 0$, the model becomes deterministic and action potentials are emitted at the moment when the membrane potential crosses the firing threshold. For finite ΔV and a membrane potential at threshold (i.e. when $V = V_T$), λ_0^{-1} defines the mean latency until a spike is emitted.

The subthreshold dynamics is modeled as a standard leaky integrator defined by the following ordinary differential equation for the membrane potential V

$$C\dot{V} = -g_L(V - E_L) + I_{\text{ext}} \tag{A.7}$$

where the three parameters C, g_L and E_L determine the passive properties of the membrane, the *dot* denotes the temporal derivative and I_{ext} is the injected current.

The dynamics of the *effective* firing threshold $V_T(t)$ in Equation A.5 is given by

$$V_T(t) = V_T^* + \sum_{\hat{t}_j < t} \xi(t - \hat{t}_j - T_{\text{ref}}) \tag{A.8}$$

where V_T^* is a constant, $\{\hat{t}_1, \hat{t}_2, \hat{t}_3, \ldots\}$ are the times at which action potentials have been fired and $\xi(s)$ is an effective adaptation filter that accounts for all the biophysical events triggered by the emission of an action potential. According to Equation A.8, each time a spike is emitted, a threshold movement with stereotypical shape $\xi(s)$ is triggered, after a delay of absolute refractoriness T_{ref}. Threshold movements induced by different spikes accumulate and therefore produce SFA, if $\xi > 0$. For $s < 0$, we fixed $\xi(s) = 0$ so that only spikes in the past can affect the momentary value of the firing threshold. Importantly, the adaptation filter $\xi(s)$

153

also accounts for adaptation processes mediated by spike-triggered currents. Consequently, $V_T(t)$ does not describe the *physiological* threshold (i.e. the membrane potential at which action potentials are initiated *in-vitro*) but has to be interpreted as a *phenomenological* model of spike-triggered adaptation. Finally, the functional shape of $\xi(s)$ was not defined *a priori* but was obtained by combining the effects of both spike-triggered currents and spike-triggered movement of the *physiological* threshold which, in turn, were extracted from the experimental data (see Fitting GLIF-ξ on *in-vitro* recordings).

In principle, an absolute refractory period can be included in the adaptation kernel $\xi(s)$. However, here we prefer to work with an explicit reset after a dead time. Each time a spike is emitted the membrane potential is reset to V_r and the numerical integration is restarted after a short period of absolute refractoriness T_{ref}. The GLIF-ξ model only differs from a Generalized Linear Model (Truccolo et al., 2005; Pillow et al., 2008) due to this explicit reset.

The three GLIF-ξ models discussed in the paper differ in the duration and shape of the adaptation filter $\xi(s)$. In GLIF-ξ_L and GLIF-ξ_S, the functional shape of $\xi(s)$ is the one directly extracted from intracellular recordings. In these two models the duration of the adaptation filter is of 22 s and 1 s, respectively. In GLIF-ξ_{PL}, the adaptation filer $\xi(s)$ is modeled as a truncated power law and lasts for 22 s.

A.6.5 Data preprocessing

In-vitro recordings were preprocessed to remove the bias due to the voltage drop across the recording electrode. For that, we performed Active Electrode Compensation (AEC) (Brette et al., 2007) following the procedure described in ref. (Badel et al., 2008). The electrode response was estimated *before*, *during* and *after* each 64-s long injection. Consequently, we were able to remove experimental drifts due to slow changes in the electrode properties (see Supplementary Text S1 and Supplementary Figs. S6-S8).

A.6.6 Fitting the GLIF-ξ model on *in-vitro* recordings

To fit GLIF-ξ models, the method introduced in ref. (Mensi et al., 2011b) was extended to get a more accurate estimate of $\xi(s)$. This was done with an additional hidden variable $I_{\text{drift}}(t)$ able to absorb small drifts that are likely to occur in long recordings.

To get an accurate estimation of the effective adaptation filter $\xi(s)$, *in-vitro* recordings were first fitted with a two-process GLIF model (Supplementary Fig. S1) that explicitly features both a spike-triggered current $\eta(s)$ and a spike-triggered movement of the firing threshold $\gamma(s)$ (Figure A.2). We then obtained the effective adaptation filer $\xi(s)$ by combining $\eta(s)$ and $\gamma(s)$ according to the following formula

$$\xi(t) = \int_0^\infty K_m(t-s)\eta(s)ds + \gamma(t), \tag{A.9}$$

where $K_m(s) = \Theta(s)\frac{R}{\tau_m}e^{-\frac{s}{\tau_m}}$ is the membrane filter, $\Theta(s)$ is the Heaviside step function, $R = g_L^{-1}$ and $\tau_m = RC$. Importantly, the functional shapes of $\eta(s)$ and $\gamma(s)$ were not assumed *a priori* but were directly extracted from the experimental data by the following two-step procedure. In the first step, we extracted the functional shape of $\eta(s)$, together with all the parameters that determines the subthreshold dynamics, by fitting $\dot{V}(t)$ on the experimental voltage derivative $\dot{V}^{(\text{data})}(t) = [V^{(data)}(t + \Delta T) - V^{(data)}(t)]/\Delta T$, where $\Delta T = 0.05$ ms was given by the experimental sampling frequency. Since adaptation currents directly affect the membrane potential dynamics, we fitted $\dot{V}^{(\text{data})}$ with the following model

$$C\dot{V} = -g_L(V - E_L) + I_{\text{ext}} - \sum_{\hat{t}_j < t} \eta(t - \hat{t}_j - T_{\text{ref}}) + I_{\text{drift}}(t), \tag{A.10}$$

where Equation A.7 was extended with a spike-triggered current $\eta(s)$ and the additional term $I_{\text{drift}}(t)$ is an unknown current that averages out at zero over time and captures experimental drifts within individual injections. To avoid any *a priori* assumption on the functional shape of the spike-triggered current, we defined $\eta(s)$ as linear combination of basis functions

$$\eta(s) = \sum_{k=1}^{K} \alpha_k f_k(s), \tag{A.11}$$

where the coefficients α_k control the shape of $\eta(s)$ and $f_k(s) = \text{rect}\left(\frac{s - T_k}{\Delta_k}\right)$ are rectangular functions of width Δ_k and centered at T_k. For GLIF-ξ_L, we used K=45 log-spaced non-overlapping bins with Δ_k ranging from 0.5 ms to 4 s. For GLIF-ξ_S, we set K=30 and $\Delta_k \in [0.5, 200]$ ms. Similarly, we defined $I_{\text{drift}}(t)$ as a piecewise constant function

$$I_{\text{drift}}(t) = \sum_{l=1}^{L} \beta_l \cdot \text{rect}\left(\frac{t - \Delta(l - 0.5)}{\Delta}\right). \tag{A.12}$$

For both GLIF-ξ_L and GLIF-ξ_S, we constrained $I_{\text{drift}}(t)$ to vary slowly in time by choosing a small number of $L = 5$ of regularly spaced bins of size $\Delta = 12.8$ s.

As in ref. (Paninski et al., 2005; Mensi et al., 2011b), given the injected current I_{ext} and the estimate of the membrane potential obtained after electrode compensation $V^{(data)}$ as well as the spike times $\{\hat{t}_j\}$, optimal parameters (minimizing the SSE between $\dot{V}^{(\text{data})}$ and $\dot{V}$ of Eq. A.10) were obtained by solving a multilinear regression problem in discrete time. Since GLIF models do not account for the action potential waveform, all the data points $\{t | t \in [\hat{t}_j - 5\text{ms}; \hat{t}_j + T_{\text{ref}}]\}$ were excluded from the fit. Finally, we fixed the absolute refractory period at $T_{\text{ref}} = 2$ and obtained the voltage reset by averaging the potential recorded T_{ref} milliseconds after the spikes $V_r = \langle V^{(\text{data})}(\hat{t}_j + T_{\text{ref}})\rangle_j$.

Performing parameters extraction in presence of the term $I_{\text{drift}}(t)$ qualitatively affected the results and slightly improved the predictive power of the model (Supplementary Fig. S3). Note, however, that the term $I_{\text{drift}}(t)$ was not part of the model but was just used in the fitting procedure to *absorb* slow changes in the subthreshold potential that could not be explained by spike-triggered processes.

Given the subthreshold dynamics, the second step consisted in estimating the parameters of

the firing threshold. Since adaptation due to spike-triggered currents was already captured by the filter $\eta(s)$, the effective threshold of Equation A.8 was replaced by

$$V_T^{\text{(bio)}}(t) = V_T^* + \sum_{\hat{t}_j < t} \gamma(t - \hat{t}_j - T_{\text{ref}}), \tag{A.13}$$

where $V_T^{\text{(bio)}}(t)$ describes the *physiological* threshold at which action potentials were initiated *in-vitro*. In contrast to $\xi(s)$, $\gamma(s)$ is not a phenomenological model but describes physiological changes of the firing threshold triggered by the emission of previous spikes. Similar to $\eta(s)$, we defined the moving threshold $\gamma(s)$ as a linear combination of rectangular basis function

$$\gamma(s) = \sum_{k=1}^{K} \delta_k f_k(s), \tag{A.14}$$

with $f_k(s)$ as in Equation A.11. Finally, the functional shape of $\gamma(s)$, among with the parameters V_T^* and ΔV, were extracted from experimental data by maximizing the *log-likelihood* of the observed spike-train (Brillinger, 1988):

$$\log L(\theta) = \log p(\{\hat{t}_j\}|V;\theta) = \sum_{\hat{t}_j} \log \lambda_\theta(\hat{t}_j) - \int_\Omega \lambda_\theta(s) ds, \tag{A.15}$$

where $\theta = \{\delta_1, \ldots, \delta_K, V_T^*, \Delta V\}$ are the threshold parameters, $\Omega = \{t | t \notin [\hat{t}_j, \hat{t}_j + T_{\text{ref}}]\}$ is a set that excludes periods of absolute refractoriness and the conditional firing intensity $\lambda_\theta(s)$ is given by

$$\lambda_\theta(t) = \lambda_0 \exp\left(\frac{V(t) - V_T^* - \sum_{\hat{t}_j < t} \gamma(t - \hat{t}_j - T_{\text{ref}})}{\Delta V} \right) \tag{A.16}$$

where $V(t)$ was obtained by integrating Equation A.10 and, without loss of generality, we set $\lambda_0 = \Delta T^{-1}$. With the exponential function in Equation A.16, the *log-likelihood* to maximize is a concave function of θ (Paninski, 2004). Consequently, we could perform the fit in discrete time using standard gradient ascent methods (Truccolo et al., 2005; Pillow et al., 2008; Mensi et al., 2011b).

With this fitting procedure, an inaccurate estimation of the spike-triggered current $\eta(s)$ would affect the measure of the moving threshold $\gamma(s)$. To make sure that the estimation of $\gamma(s)$ we obtained (Figure A.2a, red line) can indeed be attributed to a movement of the physiological threshold, we also extracted the threshold parameters using the experimental membrane potential $V^{\text{(data)}}$, rather than V (Figure A.2a, gray line).

Power-law fit of the effective adaptation filter $\xi(s)$

For GLIF-ξ_{PL}, the effective adaptation filter $\xi_L(s)$ extracted from the intracellular recordings was fitted with a truncated power law $\xi_{\text{PL}}(s)$ (Eq. A.2). The fit was performed in two steps. In the first step, we estimated the magnitude α_ξ and the scaling exponent β_ξ using a least-

square linear regression performed in log-log space. For that, data points were logarithmically resampled and excluded from the fit if $\xi_L(s) < 5 \cdot 10^{-3}$ mV or $s < 5$ ms. In the second step, we obtained the cutoff T_ξ by calculating the intercept between the power-law fitted in the first step and the average value of the extracted kernel $\xi_L(s)$ computed on the first 5 ms. A similar procedure (i.e. least-square linear regression in log-log space with logarithmically resampled points) was used for the power-law fit of the spike-triggered current $\eta(s)$ and the spike-triggered movement of the firing threshold $\gamma(s)$ shown in Figure 2a.

A.6.7 Performance evaluation

Cross-validation

All the performances reported in this study were evaluated on datasets that have not been used for parameter extraction. For the predictions reported in Figure 3 and Figure 4a-g, the model fitted on the first half of the experiment (*training set*) was used to predict the responses observed in the second half (*test set*). Since in certain experiments the average firing rates r_0 observed in the *test set* were slightly different than the ones of the *training set*, the parameter V_T^* was readjusted using the firsts 16 s of all the *test set* injections and models were validated on the responses recorded in the remaining 48 s. According to this procedure, models that do not capture SFA on slow timescales were expected to overestimate the average firing rate r_0. For the predictions reported in Figure 4h-j, a *leave-one-out strategy* was used. In this case, models fitted on the responses to five different periods of modulation were used to predict the sixth one.

Spike-train metrics

To evaluate spike time prediction, we used the similarity measure M_d^* introduced in ref. (Naud et al., 2011). M_d^* quantifies the similarity between two groups of spike trains generated by two stochastic processes and corrects the bias caused by the small number of available repetitions. M_d^* takes values between 0 and 1, where $M_d^* = 0$ indicates that the model is unable to predict any of the observed spikes and $M_d^* = 1$ means that the two groups of spike trains have the same instantaneous firing rate and are statistically indistinguishable. M_d^* can also be interpreted as the number of spikes correctly predicted (here with a precision of ± 4 ms) divided by an estimate of the number of reliable spikes.

A.6.8 Estimating the statistical properties of the input current received *in-vivo* by neocortical pyramidal neurons

To test the hypothesis that power-law adaptation contributes to efficient coding by *whitening* the single neuron output, we measured the power spectrum of the currents $\Delta I(f)$ received as input at the soma of a neocortical pyramidal neuron *in-vivo*. According to Equation A.10, in absence of spikes, the membrane potential $\Delta V(t)$ is a low-pass filtered version of the

input current, where the cutoff frequency $f_c = \tau_m^{-1}$ is defined by the membrane timescale. Consequently, at all frequencies $f \ll f_c$, we have that $\Delta I(f) = \Delta V(f)/R^2$, with $\Delta V(f)$ being the power spectrum of the subthreshold membrane potential fluctuations and R the input resistance.

We estimated $\Delta V(f)$ using 20-second long whole-cell recordings ($n = 57$) of the synaptically driven membrane potential dynamics obtained from 7 different L2/3 pyramidal neurons of behaving mice (data from (Crochet et al., 2011)). All the *in-vivo* recordings were performed in primary somatosensory barrel cortex during active whisker sensation. Further details on the experimental protocol can be found in the original paper (Crochet et al., 2011). Spike-triggered currents last for more than 20 seconds and can in principle affect $\Delta V(f)$ even at very low frequencies. For this reason, only trials with low firing rates $r_0 < 0.5$ Hz were used. However, including recordings with $r_0 > 0.5$ Hz did not affect the results.

A.6.9 Simulating the population response to *in-vivo* like inputs

To obtain the results reported in Figure 5, we simulated a population of $N = 100$ unconnected GLIF-ξ_{PL} neurons in response to 4000-s long currents $I(t)$ characterized by a power spectrum $\Delta I(f) \propto f^{-\beta_{\mathrm{I}}}$, with $\beta_{\mathrm{I}} = 0.67$. Model parameters are given in Supplementary Table S1 and input currents were generated as in ref. (Wang et al., 2003) by numerically solving the following inverse Fourier transform

$$I(t) = I_0 + \mathscr{C} \cdot \int_{-\infty}^{+\infty} \sqrt{\Delta I}(f) \mathscr{N}(f) e^{i(2\pi f t + \phi(f))} df, \tag{A.17}$$

where $\mathscr{N}(f)$ is a Gaussian white-noise process, the phases $\phi(f)$ were independently sampled from a uniform distribution and the scaling factor $\mathscr{C}$ was adjusted to fit the power spectrum of the subthreshold membrane potential fluctuations observed *in-vivo* (see Figure A.5a). To avoid unrealistic large power at slow frequencies, we introduced a cutoff $\Delta I(f) = 0$, for $f < 0.025$ Hz. The highest frequency in the signal was determined by the time step $\Delta T = 0.5$ ms used for numerical simulations. The mean input I_0 was adjusted to obtain a plausible average activity of $A_0 = 4$ Hz, which was consistent with the firing rates obtained *in-vitro*.

The population activity $A(t)$ was constructed by counting the number of spikes falling in bins of 50 ms and its power spectrum $A(f)$ was finally computed using time series of 40 s.

A.6.10 Statistics

The number of cells used for the analysis ($n = 12$ or $n = 14$) was limited due to experimental constraints. Data analysis only started after complete data collection and no data were excluded. Two-sided t-test was used as standard. Normality was verified using the Anderson-Darling test. Multiple comparison correction was not appropriate and therefore not used.

Contributions

This section summarizes my contribution to each of the preceding chapters. It also presents my contribution to another publication not presented in this thesis (Naud et al., 2011).

Chapter 1: I wrote the introduction and produced the figures especially for this thesis.

Chapter 2: I developed the fitting procedure and introduced the GIF model along with Christian Pozzororini and Richard Naud. Experiments were designed by Richard Naud and done by Michael Avermann. I performed the data analysis, produced all the figures and wrote the text in collaboration with Richard Naud and Wulfram Gerstner. This chapter is published in Journal of Neurophysiology under the following name:

"Parameter extraction and classification of three cortical neuron types reveals two distinct adaptation mechanisms"
S. Mensi, R. Naud, C. Pozzorini, M. Avermann, C. C. Petersen & W. Gerstner, 2012
Journal of neurophysiology, 107(6), 1756-1775.

Chapter 3: I designed the conceptual work with Richard Naud and Wulfram Gerstner, performed all the calculations and the numerical simulations and produced the figures. Richard Naud wrote most of the text. This chapter is published in NIPS under the name:

"From Stochastic Nonlinear Integrate-and-Fire to Generalized Linear Models"
S. Mensi, R. Naud & W. Gerstner, 2011
Neural Information Processing Systems (NIPS), pp. 1377-1385.

Chapter 4: The original idea of this article has followed from a discussion with Prof. Christof Koch addressing the feasibility of implementing our fitting procedure in high throughput framework. Christof Koch conceptualized the study and Wulfram Gerstner supervised the project. I performed all the data analysis, numerical simulations, calculations and produced the figures. Christian Pozzorini wrote the main part of the manuscript and performed the active electrode composition on the experimental recordings. Olivier Hagens performed the *in vitro* experiments and Richard Naud helped us with the spike trains similarity measure. We have submitted this chapter to Neuron:

Contributions

"Automated high-throughput parameter extraction for generalized integrate and fire models"
S. Mensi, C. Pozzorini, O. Hagens, R. Naud, C. Koch & W. Gerstner, 2014
Submitted to *Neuron*.

Chapter 5: Christian Pozzorini and I developed and conceptualized this study under the supervision of Wulfram Gerstner. This project is a joint work between Christian Pozzorini and I. We performed the derivation of the results, designed the experimental protocol, analyzed the *in vitro* recordings. Then we developed the new model and its fitting procedure together. Finally we produced the figure and wrote the text. On average Christian Pozzorini is more involved in the data analysis and the writing and I am more responsible for the modeling parts and figures production. Olivier Hagens performed all the *in vitro* experiments. This chapter is a manuscript under preparation.

Appendix: Since I am not first author on the original article (Pozzorini et al., 2013), this chapter is presented as an appendix. However I have contributed to this study in a significant way. I was mainly involved on the data analysis and on the modeling side. The model and the fitting procedure used in this paper are an extension of the one used in Mensi et al. (2011b), so that it makes sense to present this work in this thesis. This paper appears in Nature Neuroscience under the name:

"Temporal whitening by power-law adaptation in neocortical neurons"
C. Pozzorini, R. Naud, S. Mensi & W. Gerstner, 2013
Nature neuroscience, 16(7), 942-948.

Other publication: Naud et al. (2011): I have contributed to the conceptual work of this studies along with Richard Naud, Felipe Gerhard and Wulfram Gerstner. Richard Naud wrote the manuscript, performed simulations and produced the figures. Felipe Gerhard optimized the GLM and produced one figure. This article is published in Neural computations:

"Improved similarity measures for small sets of spike trains"
R. Naud, F. Gerhard, S. Mensi & W. Gerstner, 2011
Neural computation, 23(12), 3016-3069.

Bibliography

L. F. Abbott and C. van Vreeswijk. Asynchronous states in a network of pulse-coupled oscillators. *Phys. Rev. E*, 48:1483–1490, 1993.

P. Achard and E. De Schutter. Complex parameter landscape for a complex neuron model. *PLoS Comput Biol*, 2(7):e94, 2006.

P. R. Adams, D. A. Brown, and A. Constanti. M-currents and other potassium currents in bullfrog sympathetic neurones. *The Journal of Physiology*, 330(1):537–572, 1982.

C. Allen and C. F. Stevens. An evaluation of causes for unreliability of synaptic transmission. *Proceedings of the National Academy of Sciences*, 91(22):10380–10383, 1994.

D. J. Amit and N. Brunel. Model of global spontaneous activity and local structured activity during delay periods in the cerebral cortex. *Cerebral Cortex*, 7(3):237–252, 1997.

E. Angelino and M. P. Brenner. Excitability constraints on voltage-gated sodium channels. *PLoS computational biology*, 3(9):e177, 2007.

M. Arsiero, H.-R. Luscher, B. N. Lundstrom, and M. Giugliano. The impact of input fluctuations on the frequency-current relationships of layer 5 pyramidal neurons in the rat medial prefrontal cortex. *J Neurosci*, 27(12):3274–3284, 2007.

J. J. Atick. Could information theory provide an ecological theory of sensory processing? *Network: Computation in Neural Systems*, 3:213–251, 1992.

D. Attwell and S. B. Laughlin. An energy budget for signaling in the grey matter of the brain. *J. Cereb. Blood Flow Metab.*, 21(10):1133–1145, 2001.

M. Avermann, C. Tomm, C. Mateo, W. Gerstner, and C. Petersen. Microcircuits of excitatory and inhibitory neurons in layer 2/3 of mouse barrel cortex. *J. Neurophysiol.*, 107(11):3116–3134, 2012.

O. Avila-Akerberg and M. J. Chacron. Nonrenewal spike train statistics: causes and functional consequences on neural coding. *Exp. Brain Res.*, 210(3-4):353–371, 2011.

R. Azouz and C. M. Gray. Cellular mechanisms contributing to response variability of cortical neurons in vivo. *Journal of Neuroscience*, 19(6):2209–2223, 1999.

Bibliography

R. Azouz and C. M. Gray. Dynamic spike threshold reveals a mechanism for coincidence detection in cortical neurons in vivo. *Proc. National Academy of Sciences USA*, 97:8110–8115, 2000.

R. Azouz and C. M. Gray. Adaptive Coincidence Detection and Dynamic Gain Control in Visual Cortical Neurons In Vivo. *Neuron*, 37:513–523, 2003.

S. A. Baccus and M. Meister. Fast and slow contrast adaptation in retinal circuitry. *Neuron*, 36 (5):909–919, 2002.

L. Badel, W. Gerstner, and M. J. E. Richardson. Dependence of the Spike-Triggered Average Voltage on Membrane Response Properties. *Neurocomputing*, 69:1062–1065, 2007.

L. Badel, S. Lefort, R. Brette, C. C. H. Petersen, W. Gerstner, and M. J. E. Richardson. Dynamic I-V curves are reliable predictors of naturalistic pyramidal-neuron voltage traces. *Journal of Neurophysiology*, 99(2):656–66, 2008.

W. Bair and C. Koch. Temporal precision of spike trains in extrastriate cortex of the behaving macaque monkey. *Neural Computation*, 8:1185–1202, 1996.

F. Baldissera, B. Gustafsson, and F. Parmiggiani. A model for refractoriness accumulation and secondary range firing in spinal motoneurones. *Biological Cybernetics*, 24(2):61–65, 1976.

G. Baranauskas, A. Mukovskiy, F. Wolf, and M. Volgushev. The determinants of the onset dynamics of action potentials in a computational model. *Neuroscience*, 167(4):1070–1090, 2010.

H. B. Barlow. Possible Principles underlying the transformation of sensory messages. In W. A. Rosenbluth, editor, *Sensory Communication*, pages 217–234. MIT Press, 1961.

J. M. Beck, W. J. Ma, X. Pitkow, P. E. Latham, and A. Pouget. Not noisy, just wrong: the role of suboptimal inference in behavioral variability. *Neuron*, 74(1):30–39, 2012.

J. Benda and A. V. M. Herz. A Universal Model for Spike-Frequency Adaptation. *Neural Computation*, 15(11):2523–2564, 2003.

J. Benda, L. Maler, and A. Longtin. Linear versus nonlinear signal transmission in neuron models with adaptation currents or dynamic thresholds. *Journal of Neurophysiology*, 104 (5):2806–2820, 2010.

P. Berkes, G. Orbán, M. Lengyel, and J. Fiser. Spontaneous cortical activity reveals hallmarks of an optimal internal model of the environment. *Science*, 331(6013):83–87, 2011.

S. M. Bohte and J. O. Rombouts. Fractionally Predictive Spiking Neurons. In *NIPS*, pages 253–261, 2010.

M. Bota and L. W. Swanson. The neuron classification problem. *Brain research reviews*, 56(1): 79–88, 2007.

M. Bota, H.-W. Dong, and L. W. Swanson. From gene networks to brain networks. *Nature neuroscience*, 6(8):795–799, 2003.

Brainscales. The brainscales project. brainscales - brain-inspired multiscale computation in neuromorphic hybrid systems. 2014, available from: http://brainscales.kip.uni-heidelberg.de/.

N. Brenner, W. Bialek, and R. de Ruyter van Steveninck. Adaptive Rescaling Maximizes Information Transmission. *Neuron*, 26:295–701, 2000.

R. Brette and W. Gerstner. Adaptive exponential integrate-and-fire model as an effective description of neuronal activity. *Journal of Neurophysiology*, 94(5):3637–3642, 2005.

R. Brette. Sharpness of spike initiation in neurons explained by compartmentalization. *PLoS computational biology*, 9(12):e1003338, 2013.

R. Brette, Z. Piwkowska, C. Monier, M. Rudolph-Lilith, J. Fournier, M. Levy, Y. Frégnac, T. Bal, and A. Destexhe. High-resolution intracellular recordings using a real-time computational model of the electrode. *Neuron*, 59(3):379–391, 2007.

D. R. Brillinger. Maximum likelihood analysis of spike trains of interacting nerve cells. *Biol. Cybern.*, 59:189–200, 1988.

N. Brunel. Dynamics of sparsely connected networls of excitatory and inhibitory neurons. *Computational Neuroscience*, 8:183–208, 2000.

N. Brunel, V. Hakim, and M. J. Richardson. Single neuron dynamics and computation. *Current opinion in neurobiology*, 25:149–155, 2014.

H. L. Bryant and J. P. Segundo. Spike initiation by transmembrane current: a white-noise analysis. *J Physiol*, 260(2):279–314, 1976.

I. Bureau, F. Von Saint Paul, and K. Svoboda. Interdigitated Paralemniscal and Lemniscal Pathways in the Mouse Barrel Cortex. *PLoS Biology*, 4(12):1, 2006.

M. Carandini and D. Ferster. Membrane potential and firing rate in cat primary visual cortex. *The Journal of Neuroscience*, 20(1):470–484, 2000.

M. Carandini, J. C. Horton, and L. C. Sincich. Thalamic filtering of retinal spike trains by postsynaptic summation. *Journal of Vision*, 7(14):20.1–11, 2007.

J. A. Cardin, R. D. Kumbhani, D. Contreras, and L. A. Palmer. Cellular mechanisms of temporal sensitivity in visual cortex neurons. *The Journal of neuroscience*, 30(10):3652–3662, 2010.

N. T. Carnevale and M. L. Hines. *The NEURON book*. Cambridge University Press, 2006.

M. J. Chacron, B. Lindner, and A. Longtin. Noise shaping by interval correlations increases information transfer. *Phys. Rev. Letters*, 92:80601, 2004.

Bibliography

M. J. Chacron, K. Pakdaman, and A. Longtin. Interspike interval correlations, memory, adaptation, and refractoriness in a leaky integrate-and-fire model with threshold fatigue. *Neural Computation*, 15(2):253–278, 2003.

M. J. Chacron, B. Lindner, and A. Longtin. Threshold fatigue and information transfer. *Journal of Computational Neuroscience*, 23(3):301–311, 2007.

C. Clopath, L. Büsing, E. Vasilaki, and W. Gerstner. Connectivity reflects coding: a model of voltage-based stdp with homeostasis. *Nature Neuroscience*, 13(3):344–352, 2010.

B. W. Connors and M. J. Gutnick. Intrinsic firing patterns of diverse neocortical neurons. *Trends Neurosci*, 13(3):99–104, 1990.

E. P. Cook, J. A. Guest, Y. Liang, N. Y. Masse, and C. M. Colbert. Dendrite-to-soma input/output function of continuous time-varying signals in hippocampal CA1 pyramidal neurons. *J Neurophysiol*, 98(5):2943–2955, 2007.

S. Crochet and C. C. H. Petersen. Correlating whisker behavior with membrane potential in barrel cortex of awake mice. *Nature neuroscience*, 9(5):608–610, 2006.

S. Crochet, J. F. A. Poulet, Y. Kremer, and C. C. H. Petersen. Synaptic mechanisms underlying sparse coding of active touch. *Neuron*, 69(6):1160–1175, 2011.

Y. Dan, J. Atick, and R. C. Reid. Efficient coding of natural scenes in the lateral geniculate nucleus: experimental test of a computational theory. *J. Neurosci.*, 16(10):3351–3362, 1996.

P. Dayan and L. F. Abbott. *Theoretical neuroscience; Computational and Mathematical Modeling of Neural Systems.* The MIT Press; Cambridge, Massachusetts; London, England, 2001.

G. G. de Polavieja, A. Harsch, I. Kleppe, H. P. Robinson, and M. Juusola. Stimulus history reliably shapes action potential waveforms of cortical neurons. *The Journal of neuroscience*, 25(23):5657–5665, 2005.

D. Debanne, E. Campanac, A. Bialowas, E. Carlier, and G. Alcaraz. Axon physiology. *Physiological reviews*, 91(2):555–602, 2011.

A. Destexhe, M. Rudolph, and D. Pare. The high-conductance state of neocortical neurons in vivo. *Nature Reviews Neuroscience*, 4:739–751, 2003.

A. Destexhe and D. Pare. Impact of network activity on the integrative properties of neocortical pyramidal neurons in vivo. *Journal of Neurophysiology 81*, 81:1531–1547, 1999.

L. E. Dobrunz and C. F. Stevens. Heterogeneity of release probability, facilitation, and depletion at central synapses. *Neuron*, 18(6):995–1008, 1997.

B. Doiron, A.-M. M. Oswald, and L. Maler. Interval coding. II. Dendrite-dependent mechanisms. *Journal of Neurophysiology*, 97(4):2744–2757, 2007.

164

D. Dong and J. Atick. Temporal decorrelation: a theory of lagged and nonlagged responses in the lateral geniculate nucleus. *Network*, 6(2):159–178, 1995.

Y. Dong, S. Mihalas, S. S. Kim, T. Yoshioka, S. Bensmaia, and E. Niebur. A simple model of mechanotransduction in primate glabrous skin. *Journal of Neurophysiology*, 109(5): 1350–1359, 2013.

K. Doya, S. Ishii, A. Pouget, and R. P. N. Rao. *Bayesian Brain*. Probabilistic Aproaches to Neural Coding. MIT Press, 2007.

P. J. Drew and L. F. Abbott. Models and properties of power-law adaptation in neural systems. *J. Neurophysiol.*, 96(2):826–833, 2006.

S. Druckmann, Y. Bannitt, A. A. Gidon, F. Schuermann, and I. Segev. A novel multiple objective optimization framework for constraining conductance-based neuron models by experimental data. *Front Neurosci*, 1(1), 2007.

S. Druckmann, T. K. Berger, S. Hill, F. Schürmann, H. Markram, and I. Segev. Evaluating automated parameter constraining procedures of neuron models by experimental and surrogate data. *Biological Cybernetics*, 99(4-5):371–379, 2008.

J. Dunlop, M. Bowlby, R. Peri, D. Vasilyev, and R. Arias. High-throughput electrophysiology: an emerging paradigm for ion-channel screening and physiology. *Nature Reviews Drug Discovery*, 7(4):358–368, 2008.

S. Eldawlatly, R. Jin, and K. G. Oweiss. Identifying functional connectivity in large-scale neural ensemble recordings: a multiscale data mining approach. *Neural computation*, 21(2): 450–477, 2009.

A. L. Fairhall, G. D. Lewen, W. Bialek, and R. R. de Ruyter Van Steveninck. Efficiency and ambiguity in an adaptive neural code. *Nature*, 412(6849):787–792, 2001.

A. A. Faisal, L. P. J. Selen, and D. M. Wolpert. Noise in the nervous system. *Nature Reviews Neuroscience*, 9(4):292–303, 2008.

J.-M. Fellous, P. H. E. Tiesinga, P. J. Thomas, and T. J. Sejnowski. Discovering spike patterns in neuronal responses. *Journal of Neuroscience*, 24(12):2989–3001, 2004.

J. F. Feng. Is the integrate-and-fire model good enough - a review. *Neural Networks*, 14:955–975, 2001.

F. R. Fernandez, T. Broicher, A. Truong, and J. A. White. Membrane voltage fluctuations reduce spike frequency adaptation and preserve output gain in ca1 pyramidal neurons in a high-conductance state. *The Journal of Neuroscience*, 31(10):3880–3893, 2011.

A. Finkel, A. Wittel, N. Yang, S. Handran, J. Hughes, and J. Costantin. Population patch clamp improves data consistency and success rates in the measurement of ionic currents. *Journal of Biomolecular Screening*, 11(5):488–496, 2006.

Bibliography

I. A. Fleidervish and M. J. Gutnick. Kinetics of slow inactivation of persistent sodium current in layer V neurons of mouse neocortical slices. *Journal of Neurophysiology*, 76(3):2125–2130, 1996.

I. A. Fleidervish, A. Friedman, and M. J. Gutnick. Slow inactivation of Na+ current and slow cumulative spike adaptation in mouse and guinea-pig neocortical neurones in slices. *The Journal of Physiology*, 493(Pt 1):83–97, 1996.

N. Fourcaud-Trocme, D. Hansel, C. van Vreeswijk, and N. Brunel. How spike generation mechanisms determine the neuronal response to fluctuating inputs. *Journal of Neuroscience*, 23(37):11628–11640, 2003.

M. G. F. Fuortes and F. Mantegazzini. Interpretation of the repetitive firing of nerve cells. *J. General Physiology*, 45:1163–1179, 1962.

C. D. Geisler and J. M. Goldberg. A stochastic model of repetitive activity of neurons. *Biophys. J.*, 6:53–69, 1966.

L. J. Gentet, M. Avermann, F. Matyas, J. F. Staiger, and C. C. H. Petersen. Membrane potential dynamics of GABAergic neurons in the barrel cortex of behaving mice. *Neuron*, 65(3): 422–435, 2010.

F. Gerhard, T. Kispersky, G. J. Gutierrez, E. Marder, M. Kramer, and U. Eden. Successful reconstruction of a physiological circuit with known connectivity from spiking activity alone. *PLoS computational biology*, 9(7):e1003138, 2013.

G. L. Gerstein and B. Mandelbrot. Random walk models for the spike activity of a single neuron. *Biophysical Journal*, 4(1):41–68, 1964.

W. Gerstner. Time Structure of the Activity in Neural Network Models. *Phys. Rev. E*, 51(1): 738–758, 1995a.

W. Gerstner. A framework for spiking model neurons: The spike response method. *preprint, TU-Muenchen*, xx:xx, 1995b.

W. Gerstner, J. L. VanHemmen, and J. D. Cowan. What matters in neuronal locking? *Neural computation*, 8(8):1653–1676, 1996.

W. Gerstner and W. M. Kistler. *Spiking neuron models : single neurons, populations, plasticity*. Cambridge University Press, Cambridge, U.K., 2002.

W. Gerstner and R. Naud. How Good Are Neuron Models? *Science*, 326(5951):379–380, 2009.

W. Gerstner and J. L. van Hemmen. Associative memory in a network of spiking neurons. *Network: Computation in Neural Systems*, 3(2):139–164, 1992.

S. Gerwinn, J. Macke, M. Seeger, and M. Bethge. Bayesian Inference for Spiking Neuron Models with a Sparsity Prior. *Advances in Neural Information Processing Systems*, pages 1–8, 2008.

M.-O. Gewaltig and M. Diesmann. Nest (neural simulation tool). *Scholarpedia*, 2(4):1430, 2007.

G. Gilboa, R. Chen, and N. Brenner. History-dependent multiple-time-scale dynamics in a single-neuron model. *J. Neurosci.*, 25(28):6479–6489, 2005.

M. Giugliano, P. Darbon, M. Arsiero, H.-R. Luscher, and J. Streit. Single-neuron discharge properties and network activity in dissociated cultures of neocortex. *J Neurophysiol*, 92(2): 977–996, 2004.

C. Gold, D. A. Henze, C. Koch, and G. Buzsáki. On the origin of the extracellular action potential waveform: a modeling study. *Journal of neurophysiology*, 95(5):3113–3128, 2006.

Y. Gutfreund, I. Segev, et al. Subthreshold oscillations and resonant frequency in guinea-pig cortical neurons: physiology and modelling. *The Journal of physiology*, 483(Pt 3):621–640, 1995.

D. Hansel and G. Mato. Existence and stability of persistent states in large neuronal networks. *Phys. Rev. Letters*, 86:4175–4178, 2001.

M. Häusser, N. Spruston, and G. J. Stuart. Diversity and dynamics of dendritic signaling. *Science*, 290(5492):739–744, 2000.

M. Häusser, G. Major, and G. J. Stuart. Differential Shunting of EPSPs by Action Potentials. *Science*, 291:138–141, 2001.

E. Hay, S. Hill, F. Schürmann, H. Markram, and I. Segev. Models of neocortical layer 5b pyramidal cells capturing a wide range of dendritic and perisomatic active properties. *PLoS Computational Biology*, 7(7):e1002107, 2011.

E. Hay, F. Schürmann, H. Markram, and I. Segev. Preserving axosomatic spiking features despite diverse. *J Neurophysiol*, 109:2972–2981, 2013.

D. A. Henze and G. Buzsáki. Action Potential Threshold of Hippocampal Pyramidal Cells vivo is Increased by Recent Spiking Activity. *Neuroscience*, 105(1):121–130, 2001.

A. V. M. Herz, T. Gollisch, C. K. Machens, and D. Jaeger. Modeling single-neuron dynamics and computations: a balance of detail and abstraction. *Science*, 314(5796):80–85, 2006.

M. H. Higgs and W. J. Spain. Kv1 channels control spike threshold dynamics and spike timing in cortical pyramidal neurones. *The Journal of Physiology*, 589(21):5125–5142, 2011.

M. H. Higgs, S. J. Slee, and W. J. Spain. Diversity of gain modulation by noise in neocortical neurons: regulation by the slow afterhyperpolarization conductance. *The Journal of neuroscience*, 26(34):8787–8799, 2006.

A. V. Hill. Excitation and accomodation in nerve. *Proc. R. Soc. B*, 119:305–355, 1936.

B. Hille. *Ionic channels of excitable membranes*. Sinauer, Sunderland, 1992.

Bibliography

A. L. Hodgkin and A. F. Huxley. A quantitative description of membrane current and its application to conduction and excitation in nerve. *J Physiol*, 117(4):500–544, 1952.

A. V. Holden. *Models of the stochastc activity of neurons*, volume 12 of *Lecture notes in Biomothematics*. Springer, Berlin Heidelberg New York, 1976.

D. H. Hubel and T. N. Wiesel. Receptive fields and functional architecture of monkey striate cortex. *The Journal of physiology*, 195(1):215–243, 1968.

B. Hutcheon and Y. Yarom. Resonance, oscillation and the intrinsic frequency preferences of neurons. *Trends in Neurosciences*, 23(5):216–222, 2000.

B. Hutcheon, R. M. Miura, and E. Puil. Subthreshold membrane resonance in neocortical neurons. *Journal of Neurophysiology*, 76(2):683–697, 1996.

Q. J. M. Huys, M. B. Ahrens, and L. Paninski. Efficient estimation of detailed single-neuron models. *J Neurophysiol*, 96(2):872–890, 2006.

E. M. Izhikevich. Resonate-and-fire neurons. *Neural Networks*, 14(6-7):883–894, 2001.

E. M. Izhikevich. Which Model to Use for Cortical Spiking Neurons? *IEEE Transactions on Neural Networks*, 15:1063–1070, 2004.

E. M. Izhikevich. Simple model of spiking neurons. *Neural Networks, IEEE Transactions on*, 14 (6):1569–1572, 2003.

E. M. Izhikevich. *Dynamical systems in neuroscience : the geometry of excitability and bursting*. MIT Press, Cambridge, Mass., 2007.

E. M. Izhikevich and G. M. Edelman. Large-scale model of mammalian thalamocortical systems. *Proceedings of the National Academy of Sciences*, page 712231105, 2008.

E. M. Izhikevich, N. S. Desai, E. C. Walcott, and F. C. Hoppensteadt. Bursts as a unit of neural information: selective communication via resonance. *TRENDS in Neurosciences*, 26(3): 161–167, 2003.

R. Jolivet, T. J. Lewis, and W. Gerstner. Generalized integrate-and-fire models of neuronal activity approximate spike trains of a detailed model to a high degree of accuracy. *Journal of neurophysiology*, 92(2):959–976, 2004.

R. Jolivet, R. Kobayashi, A. Rauch, R. Naud, S. Shinomoto, and W. Gerstner. A benchmark test for a quantitative assessment of simple neuron models. *J Neurosci Methods*, 2007.

R. Jolivet, A. Rauch, H.-R. Luscher, and W. Gerstner. Predicting spike timing of neocortical pyramidal neurons by simple threshold models. *J Comput Neurosci*, 21(1):35–49, 2006.

R. Jolivet, F. Schürmann, T. K. Berger, R. Naud, W. Gerstner, and A. Roth. The quantitative single-neuron modeling competition. *Biological Cybernetics*, 99(4-5):417–426, 2008.

M. Juusola, H. P. Robinson, and G. G. de Polavieja. Coding with spike shapes and graded potentials in cortical networks. *Bioessays*, 29(2):178–187, 2007.

E. R. Kandel, H. Markram, P. M. Matthews, R. Yuste, and C. Koch. Neuroscience thinks big (and collaboratively). *Nature Reviews Neuroscience*, 14(9):659–664, 2013.

Y. Kawaguchi and K. Hama. Two subtypes of non-pyramidal cells in rat hippocampal formation identified by intracellular recording and HRP injection. *Brain Research*, 411(1):190–195, 1987.

J. Keat, P. Reinagel, R. C. Reid, and M. Meister. Predicting every spike: a model for the responses of visual neurons. *Neuron*, 30(3):803–817, 2001.

N. Keren, N. Peled, and A. Korngreen. Constraining compartmental models using multiple voltage recordings and genetic algorithms. *J Neurophysiol*, 94(6):3730–3742, 2005.

B. W. Knight. Dynamics of encoding in a population of neurons. *J. Gen. Physiology*, 59:734–766, 1972.

R. Kobayashi and S. Shinomoto. State space method for predicting the spike times of a neuron. *Physical Review E - Statistical, Nonlinear and Soft Matter Physics*, 75(1 Pt 1):011925, 2007.

R. Kobayashi, Y. Tsubo, and S. Shinomoto. Made-to-Order Spiking Neuron Model Equipped with a Multi-Timescale Adaptive Threshold. *Frontiers in computational neuroscience*, 3 (July):11, 2009.

C. Koch. Cable theory in neurons with active, linearized membranes. *Biological Cybernetics*, 50(1):15–33, 1984.

C. Koch and I. Segev. The role of single neurons in information processing. *Nature Neuroscience*, 3(Supp):1171–1177, 2000.

C. Koch. *Biophysics of computation : information processing in single neurons.* Oxford University Press, New York, 1999.

C. Koch and R. C. Reid. Neuroscience: Observatories of the mind. *Nature*, 483(7390):397–398, 2012.

S. B. Kodandaramaiah, G. T. Franzesi, B. Y. Chow, E. S. Boyden, and C. R. Forest. Automated whole-cell patch-clamp electrophysiology of neurons in vivo. *Nature Methods*, 9(6), 2012.

H. Kondgen, C. Geisler, S. Fusi, X. J. Wang, H. R. Luscher, and M. Giugliano. The Dynamical Response Properties of Neocortical Neurons to Temporally Modulated Noisy Inputs In Vitro. *Cereb Cortex*, 2008.

G. La Camera, A. Rauch, D. Thurbon, H.-R. Lüscher, W. Senn, and S. Fusi. Multiple time scales of temporal response in pyramidal and fast spiking cortical neurons. *J. Neurophysiol.*, 96(6): 3448–3464, 2006.

Bibliography

I. Lampl and Y. Yarom. Subthreshold oscillations and resonant behavior: two manifestations of the same mechanism. *Neuroscience*, 78(2):325–341, 1997.

S. Lang, V. J. Dercksen, B. Sakmann, and M. Oberlaender. Simulation of signal flow in 3d reconstructions of an anatomically realistic neural network in rat vibrissal cortex. *Neural Networks*, 24(9):998–1011, 2011.

L. Lapicque. Recherches quantitatives sur l'excitation electrique des nerfs traitée comme une polarization. *J. Physiol. Pathol. Gen.*, 9:620–635, 1907.

M. Larkum. A cellular mechanism for cortical associations: an organizing principle for the cerebral cortex. *Trends in neurosciences*, 36(3):141–151, 2013.

M. E. Larkum, T. Nevian, M. Sandler, A. Polsky, and J. Schiller. Synaptic integration in tuft dendrites of layer 5 pyramidal neurons: a new unifying principle. *Science*, 325(5941):756–760, 2009.

P. E. Latham, B. J. Richmond, P. G. Nelson, and S. Nirenberg. Intrinsic dynamics in neuronal networks. I. Theory. *J. Neurophysiology*, 83:808–827, 2000.

S. B. Laughlin. Energy as a constraint on the coding and processing of sensory information. *Curr. Opin. Neurobiol.*, 11(4):475–480, 2001.

V. Lawhern, W. Wu, N. Hatsopoulos, and L. Paninski. Population decoding of motor cortical activity using a generalized linear model with hidden states. *Journal of neuroscience methods*, 189(2):267–280, 2010.

S. Lefort, C. Tomm, J. C. F. Sarria, and C. C. H. Petersen. The Excitatory Neuronal Network of the C2 Barrel Column in Mouse Primary Somatosensory Cortex. *Neuron*, 61(2):301–316, 2009.

R. Legenstein and W. Maass. Branch-specific plasticity enables self-organization of nonlinear computation in single neurons. *The Journal of Neuroscience*, 31(30):10787–10802, 2011.

Y.-H. Liu and X.-J. Wang. Spike-frequency adaptation of a generalized leaky integrate-and-fire model neuron. *Journal of computational neuroscience*, 10(1):25–45, 2001.

M. London and M. Häusser. Dendritic Computation. *Annual Reviews of Neuroscience*, 28:503–532, 2005.

A. Losonczy and J. C. Magee. Integrative properties of radial oblique dendrites in hippocampal ca1 pyramidal neurons. *Neuron*, 50(2):291–307, 2006.

S. B. Lowen, L. S. Liebovitch, and J. A. White. Fractal ion-channel behavior generates fractal firing patterns in neuronal models. *Phys. Rev. E Stat. Nonlin. Soft.*, 59(5 Pt B):5970–5980, 1999.

B. N. Lundstrom, M. H. Higgs, W. J. Spain, and A. L. Fairhall. Fractional differentiation by neocortical pyramidal neurons. *Nat. Neurosci.*, 11(11):1335–1342, 2008.

D. V. Madison and R. A. Nicoll. Control of the repetitive discharge of rat CA 1 pyramidal neurones in vitro. *The Journal of Physiology*, 354(1):319–331, 1984.

Z. F. Mainen and T. J. Sejnowski. Reliability of spike timing in neocortical neurons. *Science*, 268(5216):1503–1506, 1995.

Z. F. Mainen and T. J. Sejnowski. Influence of dendritic structure on firing pattern in model neocortical neurons. *Nature*, 382(6589):363–366, 1996.

A. Manwani and C. Koch. Detecting and Estimating Signals in Noisy Cable Structures, I: Neuronal Noise Sources. *Neural Computation*, 11:1797–1829, 1999.

E. J. Mar, C. C. Chow, W. Gerstner, R. W. Adams, and J.J.Collins. Noise-shaping in populations of coupled model neurons. *Proc. Natl. Acad. Sci. USA*, 96:10450–10455, 1999.

M. Maravall, R. S. Petersen, A. L. Fairhall, E. Arabzadeh, and M. E. Diamond. Shifts in Coding Properties and Maintenance of Information Transmission during Adaptation in Barrel Cortex. *PLoS Biol.*, 5(2):e19, 2007.

H. Markram. The blue brain project. *Nature Reviews Neuroscience*, 7(2):153–160, 2006.

H. Markram, M. Toledo-Rodriguez, Y. Wang, A. Gupta, G. Silberberg, and C. Wu. Interneurons of the neocortical inhibitory system. *Nat Rev Neurosci*, 5(10):793–807, 2004.

P. Z. Marmarelis and V. Z. Marmarelis. *Analysis of physiological systems: The white-noise approach.* New York: Plenum Press, 1978.

M. Martina and P. Jonas. Functional differences in Na+ channel gating between fast-spiking interneurones and principal neurones of rat hippocampus. *The Journal of Physiology*, 505 (Pt 3):593–603, 1997.

A. Mauro, F. Conti, F. Dodge, and R. Schor. Subthreshold behavior and phenomenological impedance of the squid giant axon. *J Gen Physiol*, 55(4):497–523, 1970.

D. A. McCormick, Y. Shu1, and Y. Yu. Neurophysiology: Hodgkin and Huxley model ? still standing? *Nature*, 445:E1–E2, 2007.

P. McCullagh and J. A. Nelder. *Generalized Linear Model*, volume 37. Chapman and Hall/CRC, 2nd edition, 1998.

I. V. Melnick, S. F. A. Santos, and B. V. Safronov. Mechanism of spike frequency adaptation in substantia gelatinosa neurones of rat. *J. Physiol.*, 559(Pt 2):383–395, 2004.

S. Mensi, R. Naud, and W. Gerstner. From Stochastic Nonlinear Integrate-and-Fire to Generalized Linear Models. In *Neural Information Processing Systems (NIPS) 2011*, 2011a.

Bibliography

S. Mensi, R. Naud, C. Pozzorini, M. Avermann, C. C. H. Petersen, and W. Gerstner. Parameter Extraction and Classification of Three Cortical Neuron Types Reveals Two Distinct Adaptation Mechanisms. *Journal of Neurophysiology*, 107(December 2011):1756–1775, 2011b.

S. Mensi, C. Pozzorini, O. Hagens, R. Naud, H. Markram, C. Koch, and W. Gerstner. Automated high-throughput parameter extraction for generalized integrate and fire models. *Submitted to Neuron*, -(-), 2014.

T. Mickus, H. y. Jung, and N. Spruston. Properties of slow, cumulative sodium channel inactivation in rat hippocampal CA1 pyramidal neurons. *Biophys. J.*, 76(2):846–860, 1999.

S. Mihalaş and E. Niebur. A generalized linear integrate-and-fire neural model produces diverse spiking behaviors. *Neural Computation*, 21(3):704–718, 2009.

C. Monier, J. Fournier, and Y. Frégnac. In vitro and in vivo measures of evoked excitatory and inhibitory conductance dynamics in sensory cortices. *Journal of Neuroscience Methods*, 169 (2):323–365, 2008.

R. Naud and W. Gerstner. Coding and decoding with adapting neurons: A population approach to the peri-stimulus time histogram. *PLoS computational biology*, 8(10), 2012.

R. Naud, N. Marcille, C. Clopath, and W. Gerstner. Firing patterns in the adaptive exponential integrate-and-fire model. *Biological Cybernetics*, 99(4-5):335–347, 2008.

R. Naud, F. Gerhard, S. Mensi, and W. Gerstner. Improved similarity measures for small sets of spike trains. *Neural Computation*, 23(12):3016–69, 2011.

R. Naud, B. Bathellier, and W. Gerstner. Spike timing prediction with active dendrites. *arXiv preprint arXiv:1311.3586*, 2013.

B. Naundorf, F. Wolf, and M. Volgushev. Unique features of action potential initiation in cortical neurons. *Nature*, 440(7087):1060–1063, 2006.

M. Okatan, M. A. Wilson, and E. N. Brown. Analyzing functional connectivity using a network likelihood model of ensemble neural spiking activity. *Neural Computation*, 17:1927–1961, 2005.

K. Padmanabhan and N. N. Urban. Intrinsic biophysical diversity decorrelates neuronal firing while increasing information content. *Nature Neuroscience*, 13(10), 2010.

L. Paninski. Maximum likelihood estimation of cascade point-process neural encoding models. *Network-Computation in Neural Systems*, 15(4):243–262, 2004.

L. Paninski, J. W. Pillow, and E. Simoncelli. Comparing integrate-and-fire models estimated using intracellular and extracellular data. *Neurocomputing*, 65-66(August 2004):379–385, 2005.

L. Paninski, J. W. Pillow, and E. P. Simoncelli. Maximum likelihood estimation of a stochastic integrate-and-fire neural encoding model. *Neural Comput*, 16(12):2533–2561, 2004.

J. W. Pillow, L. Paninski, V. J. Uzzell, E. P. Simoncelli, and E. J. Chichilnisky. Prediction and decoding of retinal ganglion cell responses with a probabilistic spiking model. *Journal of Neuroscience*, 25(47):11003–11013, 2005.

J. W. Pillow, J. Shlens, L. Paninski, A. Sher, A. M. Litke, E. J. Chichilnisky, and E. P. Simoncelli. Spatio-temporal correlations and visual signalling in a complete neuronal population. *Nature*, 2008.

J. W. Pillow, Y. Ahmadian, and L. Paninski. Model-based decoding, information estimation, and change-point detection techniques for multineuron spike trains. *Neural Computation*, 23(1):1–45, 2011.

X. Pitkow and M. Meister. Decorrelation and efficient coding by retinal ganglion cells. *Nat. Neurosci.*, 15(4):628–635, 2012.

J. Platkiewicz and R. Brette. A threshold equation for action potential initiation. *PLoS computational biology*, 6(7):e1000850, 2010.

J. Platkiewicz and R. Brette. Impact of Fast Sodium Channel Inactivation on Spike Threshold Dynamics and Synaptic Integration. *PLoS Computational Biology*, 7(5):15, 2011.

H. E. Plesser and W. Gerstner. Noise in integrate-and-fire models: from stochastic input to escape rates. *Neural Computation*, 12:367–384, 2000.

P. Poirazi and B. W. Mel. Impact of active dendrites and structural plasticity on the memory capacity of neural tissue. *Neuron*, 29(3):779–796, 2001.

P. Poirazi, T. Brannon, and B. W. Mel. Pyramidal neuron as two-layer neural network. *Neuron*, 37:989–999, 2003.

A. V. Poliakov, R. K. Powers, and M. C. Binder. Functional identification of input-output transforms of motoneurons in cat. *J. Physiology*, 504:401–424, 1997.

J. F. A. Poulet and C. C. H. Petersen. Internal brain state regulates membrane potential synchrony in barrel cortex of behaving mice. *Nature*, 454(7206):881–885, 2008.

C. Pozzorini, R. Naud, S. Mensi, and W. Gerstner. Temporal whitening by power-law adaptation in neocortical neurons. *Nature neuroscience*, 16(7):942–948, 2013.

S. A. Prescott, S. Ratté, Y. De Koninck, and T. J. Sejnowski. Nonlinear interaction between shunting and adaptation controls a switch between integration and coincidence detection in pyramidal neurons. *J Neurosci*, 26(36):9084–9097, 2006.

S. A. Prescott, S. Ratté, Y. De Koninck, and T. J. Sejnowski. Pyramidal neurons switch from integrators in vitro to resonators under in vivo-like conditions. *Journal of Neurophysiology*, 100(6):3030–3042, 2008.

Bibliography

W. Rall. Electrophysiology of a dendritic neuron model. *Biophysical journal*, 2(2):145–167, 1962.

W. Rall. Core conductor theory and cable properties of neurons. *Comprehensive Physiology*, 2011.

S. Ratté, S. Hong, E. De Schutter, and S. A. Prescott. Impact of neuronal properties on network coding: roles of spike initiation dynamics and robust synchrony transfer. *Neuron*, 78(5): 758–772, 2013.

A. Rauch, G. La Camera, H.-R. Luscher, W. Senn, and S. Fusi. Neocortical pyramidal cells respond as integrate-and-fire neurons to in vivo-like input currents. *J Neurophysiol*, 90(3): 1598–1612, 2003.

M. J. E. Richardson, N. Brunel, and V. Hakim. From subthreshold to firing-rate resonance. *Journal of neurophysiology*, 89(5):2538–2554, 2003.

F. Rieke, D. Warland, R. de Ruyter van Steveninck, and W. Bialek. *Spikes: exploring the neural code*. Cambridge: MIT press, 1999.

N. H. Sabah and K. N. Leibovic. Subthreshold oscillatory responses of the Hodgkin-Huxley cable model for the squid giant axon. *Biophys J*, 9(10):1206–1222, 1969.

P. Sah. Ca2+-activated K+ currents in neurones: types, physiological roles and modulation. *Trends in Neurosciences*, 19(4):150–154, 1996.

M. V. Sanchez-Vives, L. G. Nowak, and D. A. McCormick. Cellular mechanisms of long-lasting adaptation in visual cortical neurons in vitro. *J. Neurosci.*, 20(11):4286–4299, 2000.

A. Sawczuk, R. K. Powers, and M. D. Binder. Contribution of outward currents to spike-frequency adaptation in hypoglossal motoneurons of the rat. *Journal of neurophysiology*, 78(5):2246–2253, 1997.

J. Schemmel, J. Fieres, and K. Meier. Wafer-scale integration of analog neural networks. *IEEE International Joint Conference on Neural Networks. Proceedings*, pages 431–438, 2008.

E. Schneidman, B. Freedman, and I. Segev. Ion channel stochasticity may be critical in determining the reliability and precision of spike timing. *Neural Computation*, 10:1679–1703, 1998.

A. Schoen, A. Salehiomran, M. E. Larkum, and E. P. Cook. A compartmental model of linear resonance and signal transfer in dendrites. *Neural computation*, 24(12):3126–3144, 2012.

P. C. Schwindt, W. J. Spain, R. C. Foehring, M. C. Chubb, and W. E. Crill. Slow conductances in neurons from cat sensorimotor cortex in vitro and their role in slow excitability changes. *Journal of Neurophysiology*, 59(2):450–467, 1988a.

P. C. Schwindt, W. J. Spain, R. C. Foehring, C. E. Stafstrom, M. C. Chubb, and W. E. Crill. Multiple potassium conductances and their functions in neurons from cat sensorimotor cortex in vitro. *Journal of Neurophysiology*, 59(2):424–449, 1988b.

P. C. Schwindt, W. J. Spain, and W. E. Crill. Long-lasting reduction of excitability by a sodium-dependent potassium current in cat neocortical neurons. *J. Neurophysiol.*, 61(2):233–244, 1989.

M. Sekerli, C. A. Del Negro, R. H. Lee, and R. J. Butera. Estimating action potential thresholds from neuronal time-series: new metrics and evaluation of methodologies. *Biomedical Engineering, IEEE Transactions on*, 51(9):1665–1672, 2004.

M. N. Shadlen and W. T. Newsome. Noise, neural codes and cortical organization. *Current Opininon in Neurobiology*, 4:569–579, 1994.

J. Shin. Adaptation in spiking neurons based on the noise shaping neural coding hypothesis. *Neural Netw.*, 14(6-7):907–919, 2001.

S. Shoham, L. M. Paninski, M. R. Fellows, N. G. Hatsopoulos, J. P. Donoghue, and R. A. Normann. Statistical encoding model for a primary motor cortical brain-machine interface. *Biomedical Engineering, IEEE Transactions on*, 52(7):1312–1322, 2005.

E. P. Simoncelli and D. J. Heeger. A model of neuronal responses in visual area mt. *Vision research*, 38(5):743–761, 1998.

E. Simoncelli and B. Olshausen. Natural image statistics and neural representation. *Annu. Rev. Neurosci.*, 24(1):1193–1216, 2001.

S. Song, K. D. Miller, and L. F. Abbott. Competitive {H}ebbian learning through spike-time-dependent synaptic plasticity. *Nature Neuroscience*, 3:919–926, 2000.

W. Spain and P. Schwindt. Two transient potassium currents in layer V pyramidal neurones from cat sensorimotor cortex. *J. Physiol.*, 1991.

N. Spruston. Pyramidal neurons: dendritic structure and synaptic integration. *Nature Reviews Neuroscience*, 9(3):206–221, 2008.

M. V. Srinivasan, S. B. Laughlin, and A. Dubs. Predictive coding: a fresh view of inhibition in the retina. *Proceedings of the Royal Society of London. Series B, Biological Sciences*, 216 (1205):427–459, 1982.

R. B. Stein. A theoretical analysis of neuronal variability. *Biophys. J.*, 5:173–194, 1965.

R. B. Stein. Some models of neuronal variability. *Biophysical journal*, 7(1):37–68, 1967.

K. M. Stiefel, B. Englitz, and T. J. Sejnowski. Origin of intrinsic irregular firing in cortical interneurons. *Proceedings of the National Academy of Sciences*, 110(19):7886–7891, 2013.

Bibliography

N. Tamamaki, Y. Yanagawa, R. Tomioka, J.-I. Miyazaki, K. Obata, and T. Kaneko. Green fluorescent protein expression and colocalization with calretinin, parvalbumin, and somatostatin in the GAD67-GFP knock-in mouse. *Journal of Comparative Neurology*, 467(1):60–79, 2003.

T. Tateno and H. P. C. Robinson. Integration of broadband conductance input in rat somatosensory cortical inhibitory interneurons: an inhibition-controlled switch between intrinsic and input-driven spiking in fast-spiking cells. *Journal of Neurophysiology*, 101(2):1056–1072, 2009.

T. Tateno, A. Harsch, and H. P. C. Robinson. Threshold firing frequency - Current relationships of neurons in rat somatosensory cortex: Type 1 and type 2 dynamics. *J. Neurophysiology*, 92: 2283–2294, 2004.

K. Thurley, W. Senn, and H.-R. Lüscher. Dopamine increases the gain of the input-output response of rat prefrontal pyramidal neurons. *Journal of neurophysiology*, 99(6):2985–2997, 2008.

A. Toib, V. Lyakhov, and S. Marom. Interaction between duration of activity and time course of recovery from slow inactivation in mammalian brain Na+ channels. *J. Neurosci.*, 18(5): 1893–1903, 1998.

M. Toledo-Rodriguez, B. Blumenfeld, C. Wu, J. Luo, B. Attali, P. Goodman, and H. Markram. Correlation maps allow neuronal electrical properties to be predicted from single-cell gene expression profiles in rat neocortex. *Cereb Cortex*, 14(12):1310–1327, 2004.

J. Touboul and R. Brette. Spiking Dynamics of Bidimensional Integrate-and-Fire Neurons. *SIAM Journal on Applied Dynamical Systems*, 8(4):1462–1506, 2009.

J. Touboul. Bifurcation Analysis of a General Class of Nonlinear Integrate-and-Fire Neurons. *SIAM Journal on Applied Mathematics*, 68(4):1045–1079, 2008.

J. Touboul and R. Brette. Dynamics and bifurcations of the adaptive exponential integrate-and-fire model. *Biological Cybernetics*, 99(4-5):319–334, 2008.

R. D. Traub, A. Bibbig, F. E. LeBeau, E. H. Buhl, and M. A. Whittington. Cellular mechanisms of neuronal population oscillations in the hippocampus in vitro. *Annu. Rev. Neurosci.*, 27: 247–278, 2004.

A. Treves. Mean-field analysis of neuronal spike dynamics. *Network*, 4:259–284, 1993.

S. J. Tripathy, K. Padmanabhan, R. C. Gerkin, and N. N. Urban. Intermediate intrinsic diversity enhances neural population coding. *Proceedings of the National Academy of Sciences*, 110 (20), 2013.

W. Truccolo, U. T. Eden, M. R. Fellows, J. P. Donoghue, and E. N. Brown. A Point Process Framework for Relating Neural Spiking Activity to Spiking History, Neural Ensemble, and Extrinsic Covariate Effects. *J. Neurophysiol.*, 93(2):1074–1089, 2005.

H. C. Tuckwell. *Introduction to theoretic neurobiology*. Cambridge Univ. Press, Cambridge, 1988.

A. M. Turing. Computing Machinery and Intelligence. *Mind*, 59(236):433–460, 1950.

N. Ulanovsky, L. Las, D. Farkas, and I. Nelken. Multiple time scales of adaptation in auditory cortex neurons. *J. Neurosci.*, 24(46):10440–10453, 2004.

N. G. van Kampen. *Stochastic processes in physics and chemistry*. North-Holland, Amsterdam, 2nd edition, 1992.

M. C. Van Rossum, G. Q. Bi, and G. G. Turrigiano. Stable hebbian learning from spike timing-dependent plasticity. *The Journal of Neuroscience*, 20(23):8812–8821, 2000.

R. D. R. Van Steveninck and W. Bialek. Real-time performance of a movement-sensitive neuron in the blowfly visual system: coding and information transfer in short spike sequences. *Proceedings of the Royal society of London. Series B. Biological sciences*, 234(1277):379–414, 1988.

M. C. Vanier and J. M. Bower. A comparative survey of automated parameter-search methods for compartmental neural models. *J Comput Neurosci*, 7(2):149–171, 1999.

D. V. Vavoulis, V. A. Straub, J. A. Aston, and J. Feng. A self-organizing state-space-model approach for parameter estimation in hodgkin-huxley-type models of single neurons. *PLoS Computational Biology*, 8(3):e1002401, 2012.

M. J. Wainwright. Visual adaptation as optimal information transmission. *Vision Res.*, 39(23): 3960–3974, 1999.

M. M. Waldrop. Computer modelling: Brain in a box. *Nature*, 482(9):456–458, 2012.

X.-J. Wang, Y. Liu, M. V. Sanchez-Vives, and D. A. McCormick. Adaptation and temporal decorrelation by single neurons in the primary visual cortex. *Journal of Neurophysiology*, 89 (6):3279–3293, 2003.

B. Wark, B. N. Lundstrom, and A. Fairhall. Sensory adaptation. *Curr. Opin. Neurobiol.*, 17(4): 423–429, 2007.

S. Weisberg. *Applied Linear Regression*. Wiley/Interscience, 3rd editio edition, 2005.

J. C. Wester and D. Contreras. Biophysical mechanism of spike threshold dependence on the rate of rise of the membrane potential by sodium channel inactivation or subthreshold axonal potassium current. *Journal of computational neuroscience*, pages 1–17, 2013.

J. A. White, J. T. Rubinstein, and A. R. Kay. Channel noise in neurons. *Trends in Neurosciences*, 23:131–137, 2000.

W. B. Wilent and D. Contreras. Stimulus-dependent changes in spike threshold enhance feature selectivity in rat barrel cortex neurons. *The Journal of neuroscience*, 25(11):2983–2991, 2005.

Bibliography

J. Xu, A. Guia, D. Rothwarf, M. Huang, K. Sithiphong, J. Ouang, G. Tao, X. Wang, and L. Wu. A benchmark study with seal chip planar patch-clamp technology. *Assay and Drug Development Technologies*, 1(5):675–684, 2003.

J. Zeng, R. K. Powers, G. Newkirk, M. Yonkers, and M. D. Binder. Contribution of persistent sodium currents to spike-frequency adaptation in rat hypoglossal motoneurons. *Journal of neurophysiology*, 93(2):1035–1041, 2005.

Skander Mensi

Avenue Béthusy 19
1005 Lausanne
Switzerland
☏ +41 (0)79 595 54 03
✉ skander.mensi@epfl.ch
Born: 10.06.1981

Education

2008–present	**Ph.D. Candidate**, *Ecole Polytechnique Fédérale de Lausanne (EPFL)* *School of Life Sciences, Laboratory of Computational Neuroscience (LCN)*. Ph.D. Thesis: A new mathematical framework to understand single neuron computations (Prof. Wulfram Gerstner)
2006–2008	**Master of Science**, *Ecole Polytechnique Fédérale de Lausanne (EPFL)* *School of Life Sciences, Laboratory of Computational Neuroscience (LCN)*. Master Thesis: Simple Neuron Models (Prof. Wulfram Gerstner)
2003–2006	**Bachelor of Science**, *Ecole Polytechnique Fédérale de Lausanne (EPFL)* *School of Life Sciences, Laboratory of Neural Microcircuitry (BMI)*. Bachelor Thesis: Fitting the HH model on real data (Supervisor: Felix Schurmann)
2001–2003	**High school diploma**, *Lausanne*.
1999–2001	**Diplôme de culture général**, *Gymnase de Nyon, Nyon*.

Professional Experience

2012–2013	**Haute école d'arts et de design, HEAD**, *Genève*. Co-organization of workshops in Neurosciences and Arts, in collaboration with Stéphanie Pfister
2006	**Laboratory of Neural Microcircuitry, BMI, EPFL**, *Lausanne*. 3D anatomical reconstruction of cortical neuron morphology using Neurolucida software
2004–2006	**Information Technology Domain (DIT), EPFL**, *Lausanne*. Technical and software support, Call Center & Help Desk

Teaching Experience

2013	**Teaching assistant, EPFL**, *Analye I (Calculus I) for Life Sciences*, Lausanne.
2010–2012	**Teaching assistant, EPFL**, *Neural Networks and Biological Modeling for Physics and Life Sciences*, Lausanne.
2010–2012	**Supervision of bachelor and internship students**, *Laboratory of Computational Neuroscience, LCN, EPFL*, Lausanne.

Extra Professional Experience

2010–present	**Administration for *RezAnimation***, Nyon. Administration for a small center of artistic creation

2009–present	**Treasurer**, *Association Activités Jeunesse Nyon (AAJN)*, Nyon.
	AAJN is promoting creative activities for children and teenagers, such as summer camps, circus courses and creative workshops
2009–present	**Organization of teenager summer camps**, *AAJN*, Nyon.
2004–present	**Co-director & teacher in children Circus**, *Artafou*, Nyon.
	Animation and show creations with 15 children from 8 to 16 years old
2004–present	**Monitor in child & teenager summer camps**, *AAJN*, Nyon.

Awards

2013	Swiss society for neuroscience (SSN), best publication award for *Temporal whitening by power-law adaptation in neocortical neurons* Pozzorini C, Naud R, **Mensi S**, and Gerstner W, Nature Neuroscience 2013
2011	Best student poster award at CNS 2011, Stockholm
2008	Mention of Excellence for master studies (EPFL)

Languages

French	**Mother tongue**
English	**Fluent** (written/spoken)

Computer skills

Programming	Matlab, Python, C/C++, Linux, Bash, Pearl, Latex, Office

Scientific Publications

2013	Pozzorini C, Naud R, **Mensi S**, and Gerstner W Temporal whitening by power-law adaptation in neocortical neurons, *Nature Neuroscience* 2013
2012	**Mensi S**[†], Naud R[†], Pozzorini C, Avermann M, Petersen CC, and Gerstner W Parameter extraction and classification of three cortical neuron types reveals two distinct adaptation mechanisms, *Journal of Neurophysiology* 2012
2011	Naud R, Gerhard F, **Mensi S**, Gerstner W Improved Similarity Measures for Small Sets of Spike Trains, *Neural Computation* 2011
2011	**Mensi S**, Naud R, and Gerstner W From Stochastic Nonlinear Integrate-and-Fire to Generalized Linear Models, *Advances in Neural Information Processing Systems (NIPS)* 2011

Publications in Preparation

2014	**Mensi S**[†], Pozzorini C[†], Hagens O, Koch C, and Gerstner W Automated high-throughput parameter extraction for Generalized Integrate and Fire models, *submitted to Neuron* 2014
2014	**Mensi S**[†], Pozzorini C[†], Hagens O, and Gerstner W Nonlinear threshold dynamics enhances temporal coding in neocortical pyramidal neurons, *in preparation* 2014

---

† Equal contribution

Invited Presentations

2014   Automated high-throughput parameter extraction for Generalized Integrate and Fire models, Allen Institute, Seattle, 2014

2010   Complexity and performance in simple neuron models, Spike-Frequency Adaptation in Neural Systems, Dresden, Germany, 2010

Interests

Electronic   Construction of electronic music instrument (DIY synthesizer, tube amplifier, sound processor)

Music   guitar, electronics, others

Sport   swimming, surf, ski

Poster Presentations

2014   **Mensi S**[†], Pozzorini C[†], Hagens O, and Gerstner W (2014), Nonlinear threshold dynamics implements multiplicative adaptation in pyramidal neurons, *Computational and Systems Neuroscience*, Salt Lake City, UT, USA, 27 Feb - 4 Mar, 2014

2013   Pozzorini C[†], **Mensi S**[†], Hagens O, and Gerstner W (2013), A nonlinear coupling between the firing threshold and the membrane potential enhances coding of rapid signals, *Neuroinformatics 2013*, Stockholm, Sweden, 27 Aug - 29 Aug, 2013

2013   **Mensi S**[†], Pozzorini C[†], Hagens O, and Gerstner W (2013), Evidence for a nonlinear coupling between firing threshold and subthreshold membrane potential, *Computational and Systems Neuroscience*, Salt Lake City, UT, USA, 28 Feb - 5 Mar, 2013

2013   Pozzorini C, Naud R, **Mensi S** and Gerstner W (2013), Temporal decorrelation by power-law adaptation in pyramidal neurons, *Computational and Systems Neuroscience*, Salt Lake City, UT, USA, 28 Feb - 5 Mar, 2013

2011   **Mensi S**, Naud R, Pozzorini C, Avermann M, Petersen C C H, and Gerstner W (2011), Automatic Characterization of Three Cortical Neuron Types Reveals Two Distinct Adaptation Mechanisms, *20th Annual Computational Neuroscience Meeting*, Stockholm, Sweden, 23-28 July 2011,*Best Poster Award*

2011   **Mensi S**, Naud R and Gerstner W (2011), From Stochastic Nonlinear Integrate-and-Fire to Generalized Linear Models, *Advances in Neural Information Processing Systems*, NIPS, Granada, Spain, 2011

2010   Pozzorini P, Naud R, **Mensi S** and Gerstner W (2010), Multiple timescales of adaptation in Single Neuron Models, *Bernstein Conference on Computational Neuroscience*, Berlin, Germany, 27 Sep - 1 Oct, 2010

2010   Naud R, Gerhard F, **Mensi S** and Gerstner W (2010), Improving the Discriminability of Similarity Measures for Small Sets of Spike Trains, *Bernstein Conference on Computational Neuroscience*, Berlin, Germany, 27 Sep - 1 Oct, 2010

2010   **Mensi S**, Naud R, Avermann M, Petersen C and Gerstner W (2010), Complexity and performance in simple neuron models, *Computational and Systems Neuroscience*, Salt Lake City, UT, USA, 25 Feb - 2 Mar, 2010

2009   **Mensi S**, Naud R, Becker TK and Gerstner W (2009). Complexity and performance in simple neuron models. *Frontiers in Neuroinformatics*. Conference Abstract: 2nd INCF Congress of Neuroinformatics, Pilsen, Czech Republic, 2009